

# **Multirate time integration methods and their application for coupled atmosphere-ocean models**

DISSERTATION

zur Erlangung des Doktorgrades der Naturwissenschaften  
(Dr. rer. nat.)

der

Naturwissenschaftlichen Fakultät II  
Chemie, Physik und Mathematik

der Martin-Luther-Universität  
Halle-Wittenberg

vorgelegt von

Herrn Tobias Peter Bauer

Gutachter: Prof. Dr. Martin Arnold  
Prof. Dr. Hans Burchard

Tag der Verteidigung: 17. Januar 2025



Mein Dank gilt all den Menschen, die mich bei dieser Arbeit unterstützt haben.

Danke für den großartigen Austausch, die tollen Gespräche und für das  
entgegengebrachte Vertrauen.





# Contents

<b>Contents</b>	<b>I</b>
<b>List of Abbreviations and Symbols</b>	<b>V</b>
<b>1 Introduction</b>	<b>1</b>
1.1 Advances of multirate methods . . . . .	2
1.2 Outline . . . . .	3
<b>2 Theoretical aspects of geophysical fluid modelling</b>	<b>5</b>
2.1 General assumptions for a geophysical fluid . . . . .	5
2.1.1 Properties of a fluid . . . . .	5
2.1.2 General budget equation for a fluid . . . . .	7
2.2 Conservation laws and equation of state . . . . .	8
2.2.1 Conservation of mass . . . . .	8
2.2.2 Conservation of momentum . . . . .	9
2.2.3 Energy budget . . . . .	11
2.2.4 Equation of state . . . . .	13
2.3 Numerical modelling of geophysical fluids . . . . .	14
2.3.1 Initial-boundary value problem for geophysical fluid models . . . . .	15
2.3.2 Spatial discretisation in geophysical fluid modelling . . . . .	19
2.3.3 Time integration in geophysical fluid modelling . . . . .	20
<b>3 Multirate time integration methods for solving IVPs</b>	<b>23</b>
3.1 One-step methods for initial value problems . . . . .	24
3.1.1 Runge–Kutta methods (RK) . . . . .	24
3.1.2 Generalized additive Runge–Kutta methods (GARK) . . . . .	25
3.2 Multirate time integration methods . . . . .	27
3.2.1 Class of multirate generalized additive Runge–Kutta methods (MGARK) . . . . .	27
3.2.2 Class of multirate infinitesimal step methods (MIS) . . . . .	34
3.3 Interrelations of MGARK and MIS methods . . . . .	40
3.3.1 Formulation of the MNGARK method as GARK method . . . . .	41
3.3.2 The extMIS method formulated as GARK method . . . . .	42

3.3.3	The extMIS method as special case of the MGARK method . . . . .	43
3.3.4	Limits through the investigation of the GARK method . . . . .	45
<b>4</b>	<b>Examples of multirate time integration methods based on their characteristics</b>	<b>47</b>
4.1	Consistency of multirate methods . . . . .	47
4.1.1	Order conditions for Runge–Kutta methods . . . . .	48
4.1.2	Order conditions for generalized additive Runge–Kutta methods . . . . .	49
4.1.3	Order conditions for multirate generalized additive Runge–Kutta methods for $N$ components . . . . .	51
4.1.4	Order conditions for extended multirate infinitesimal step methods . . . . .	53
4.2	Stability of multirate time integration methods . . . . .	57
4.2.1	Stability for Runge–Kutta methods . . . . .	57
4.2.2	Stability of multirate generalized additive Runge–Kutta methods . . . . .	58
4.2.3	Stability of multirate infinitesimal step methods . . . . .	60
4.3	Construction of multirate methods . . . . .	61
4.3.1	MNGARK method – M3GARK135-222 . . . . .	61
4.3.2	Extended MIS method – MIS54 . . . . .	62
<b>5</b>	<b>Numerical realisation of the coupling of atmosphere and ocean models</b>	<b>65</b>
5.1	Coupling conditions and their numerical realisation . . . . .	65
5.1.1	Coupling conditions at the air-sea interface . . . . .	66
5.1.2	Realisation of the coupling conditions in atmosphere and ocean models . . . . .	67
5.2	Coupling approaches for idealised one- and two-dimensional coupled atmosphere- ocean models . . . . .	68
5.2.1	1D idealised coupled atmosphere-ocean model with turbulence closure . . . . .	68
5.2.2	Coupling details for a 2D atmosphere-ocean model . . . . .	71
5.3	The coupling in ICONGETM: a flexible two-way mechanism for a coupled atmosphere- ocean model . . . . .	73
5.3.1	Coupling interfaces in ICON and GETM . . . . .	74
5.3.2	The air-sea interface as exchange grid developed for ICONGETM . . . . .	77
<b>6</b>	<b>Multirate methods and their applications for coupled atmosphere-ocean models</b>	<b>83</b>
6.1	Application of multirate methods to idealised coupled atmosphere-ocean models . . . . .	83
6.1.1	Implementation details for the 1D model . . . . .	84
6.1.2	Simulation results for the 1D model . . . . .	86
6.1.3	Performance evaluation of the applied multirate methods . . . . .	91
6.2	Multirate methods in ICONGETM . . . . .	93
6.2.1	Multirate time integration in ICON, GETM and ICONGETM . . . . .	93
6.2.2	Central Baltic Sea experiment: model setup . . . . .	95
6.2.3	Effects of interactive coupling in the atmosphere . . . . .	95
6.2.4	Coupling effects in the ocean . . . . .	98

<b>7 Summary</b>	<b>101</b>
<b>A Additional Calculus</b>	<b>i</b>
<b>B Physical assumptions and the set of equations</b>	<b>v</b>
<b>C Time averaged set of equations</b>	<b>vii</b>
<b>Bibliography</b>	<b>ix</b>
<b>List of Figures</b>	<b>xxi</b>
<b>List of Tables</b>	<b>xxv</b>
<b>Selbstständigkeitserklärung</b>	<b>xxvii</b>
<b>Lebenslauf</b>	<b>xxix</b>



# List of Abbreviations and Symbols

## Abbreviations for (multirate) time integration methods:

RK	Runge–Kutta methods,
GARK	Generalized additive Runge–Kutta methods,
MGARK	Multirate generalized additive Runge–Kutta methods,
MNGARK	Multirate generalized additive Runge–Kutta methods for $N$ components,
MIS	Multirate infinitesimal step methods,
extMIS	Extended multirate infinitesimal step methods.

Note that the method names are given in American English as in the literature.

## Symbols for set of equations of one-dimensional coupled atmosphere-ocean model:

$q_v, q_{sa}$	Specific humidity and salt content,
$u, v$	x-, y- horizontal velocity components
$\theta$	Potential temperature,
$\theta_q$	Wet equivalent potential temperature,
$k$	Specific turbulent kinetic energy,
$\varepsilon$	Dissipation,
$p$	Pressure,
$f$	Coriolis frequency,
$u_g, v_g$	x-, y-horizontal geostrophic wind velocities
$K_m, K_h$	Turbulent diffusion coefficients for momentum and heat
$\nu^h, \nu^{sa}$	Molecular diffusivities for heat and salt,
$\nu_t$	Eddy diffusivity,
$\nu_t^h, \nu_t^{sa}$	Eddy diffusivities for heat and salt,
$\nu_k, \nu_\varepsilon$	Eddy diffusivities for specific turbulent kinetic energy and dissipation,
$E, P$	Evaporation and Precipitation
SST	Sea surface temperature,
$c_p^A, c_p^O$	Specific heat capacity of air and water,
$l_v$	Specific latent heat capacity for water vapour.



# Chapter 1

## Introduction

Earth system models are developed for investigating all kinds of natural phenomena occurring on our planet. The variety of applications covers areas from the inner core of the Earth up until the ocean, land and atmosphere. In recent years, the most prominent applications are climate development, numerical weather prediction and extreme event modelling with focus on natural hazards. Comprehensive knowledge on climate change, its causes, potential impacts and response options is published in the IPCC reports. The latest contributions for the reports are summarised in the synthesis report, see Calvin et al. (2023)

Individual geophysical models have their main focus on a specific field, e.g. atmosphere, ocean, land, geology, ice, etc. The characteristics of the complex environment on Earth drives the need of a combination of models, i.e. the coupling, to investigate the natural interplay. Coupled models are then used for simulating the effects of the interplay between the individual components.

The core for many coupled Earth system models are atmosphere and ocean models. These individual models are based on the governing equations for geophysical fluid dynamics and describe the conservation laws for mass, momentum and energy. Atmosphere and ocean models are coupled at the air-sea interface, where coupling conditions are fulfilled. These conditions are formulated as flux conditions, i.e. as an equilibrium description of the flow of mass, momentum and energy through the interface. Moreover, the coupling conditions model the physical processes at the interface. Interactive atmosphere-ocean coupling is important for representing the interactions and feedbacks between atmosphere and ocean dynamics, see e.g. Chelton and Xie (2010).

In the framework of this thesis, the new coupled atmosphere-ocean model ICONGETM has been developed and analysed. ICONGETM consists of the next-generation atmosphere model ICON and the coastal ocean model GETM. Applications for coupled atmosphere-ocean models with focus on high-resolution modelling of the interplay between the atmosphere and ocean at the air-sea interface are considered for this thesis. The newly developed model ICONGETM is used to simulate coastal upwelling in the ocean and the influence to the lower atmosphere for the Baltic Sea, see e.g. Bauer et al. (2021).

In a coupled atmosphere-ocean model, the individual atmosphere and ocean models are treated as components or sub-models. Their description through geophysical fluid dynamics refers to solving of initial boundary value problems.

Due to different physical properties of the fluids, water in the ocean or air in the atmosphere, the governing equations are solved on different time scales. Since the atmosphere changes more rapidly than the ocean, the time scale of an atmosphere model is often considered to be smaller than the time scale of an ocean model. For stability and efficiency reasons, the different time scales should be considered by the time integration schemes, i.e. mandatory small time steps for fast dynamics and exploit larger time steps for slower dynamics.

Additionally, the spatial discretisation of the domain and the structure of the governing equations are driving the choice of the integration scheme. Furthermore, integrating coupled models requires investigations on integration schemes, which should also adhere to the solution of coupled models. With evolving computer technology, the complexity of the models is also increased. This must be considered for the integration schemes, especially for coupled models.

Multirate time integration methods are developed for solving coupled initial value problems with different time scales. For this thesis, the application of multirate methods for coupled atmosphere-ocean models are investigated. The structure of coupled atmosphere-ocean models is analysed in order to apply multirate methods, where the characteristics of the integration schemes of the individual components are preserved. Furthermore, it is investigated how the coupling conditions are fulfilled in coupled atmosphere-ocean models and how they can be integrated utilising multirate methods.

The development of multirate methods is reviewed in Section 1.1. Some of the derived methods were influenced by the specific needs of various applications from geophysical fluid dynamics. The main questions concerning the application of multirate methods to coupled models are presented and the outline of this thesis is given in Section 1.2.

**Remark:** *Integration schemes are a key factor for the computing time and resources required for model simulations. State-of-the-art climate simulations are only feasible on super computers with a high power consumption. The computational and energy cost of simulations taking part in the 6th phase of Coupled Model Intercomparison Project (CMIP) is presented in Acosta et al. (2024). The CMIP project investigates prescribed various scenarios of climate change. Each model taking part in the CMIP project contributes to the IPCC assessment reports. Acosta et al. (2024, Table 9) shows Carbon footprints ranging from 24t to 868t of CO<sub>2</sub> for running simulations for the CMIP project per model. Thus, improving the applied integration schemes is of uttermost practical relevance.*

## 1.1 Advances of multirate methods

Multirate methods are an approach for efficient integration of differential equations with different time scales, e.g. advection, diffusion or stiff chemical reactions. The literature stretches mostly over simpler problems than coupled geophysical fluid dynamics.

The main idea of a multirate approach considers the splitting or partitioning of a problem into several parts. The simplest splitting type is a linear combination. Other possibilities are the splitting in linear and non-linear terms, dimensional splitting due to different spatial variables, operator



splitting depending on different physical contributions and component partitioning. These splittings can be of any kind, but are commonly additive. Therefore, the multirate methods discussed in this thesis are for additive split initial value problems.

First discussions on problems with several components on different time scales already took place in the 1980s and 1990s. Multirate linear multistep methods were discussed in Gear and Wells (1984). The time-splitting for elastic equations in atmosphere models was intensively investigated, see e.g. Skamarock and Klemp (1992), Wicker and Skamarock (1998), and Wicker and Skamarock (2002). Symplectic methods for Hamiltonian problems based on additive decompositions were discussed in Araújo et al. (1997).

For Runge–Kutta methods, there exists a variety of methods with different types of splitting, see e.g. Jackiewicz and Vermiglio (2000) for partitioned Runge–Kutta methods and Sandu and Günther (2015) for a generalisation of additive Runge–Kutta methods. Multirate partitioned Runge–Kutta methods were investigated in Günther et al. (2001). Also a multirate approach was found for generalized additive Runge–Kutta methods, see e.g. Günther and Sandu (2016).

Knoth and Wolke (1998) proposed an implicit-explicit method for computing atmospheric reactive flows, where an initial value problem has to be solved in every Runge–Kutta method stage with a free choice integrator. Schlegel et al. (2012) developed a method where the free choice integrator is replaced with an explicit Runge–Kutta method. This was further developed by Sexton and Reynolds (2018) allowing also implicit Runge–Kutta methods instead of only explicit ones.

Other multirate approaches were developed for specific problems, e.g. multirate time-stepping methods for hyperbolic conservation laws (Constantinescu and Sandu 2007), two-step Adams-Bashforth-Moulton split-explicit integrators for compressible atmospheric models (Wicker 2009) and explicit local time-stepping for Maxwell equations (Grote and Mitkova 2010).

With the further development of geophysical fluid dynamics, more time integration schemes considering different time scales are developed. For example, conservative split-explicit time integration methods were investigated for compressible nonhydrostatic equations, see e.g. Klemp et al. (2007). Jebens et al. (2009) developed an explicit two-step peer method for solving the compressible Euler equation.

Multirate methods and their applications are ongoing research. Achievements in recent years can be found in e.g. Connors and Sockwell (2022), where the focus was on multirate discontinuous Galerkin in time frameworks for interface coupled problems. Further examples are the work on multirate partitioned Runge–Kutta methods for coupled Navier-Stokes equations from Kang et al. (2023).

## 1.2 Outline

The application of multirate methods in coupled atmosphere-ocean models is determined by the complexity of the model equations and the time scales of the integration of the individual models. In this thesis, the consideration of the different time scales of the atmosphere and the ocean for the multirate time integration methods applied to coupled atmosphere-ocean models is investigated.

The raised and discussed questions can be summarised as

1. How are the physical processes at a coupling interface modelled, i.e. the coupling conditions applied in a coupled atmosphere-ocean model, and how are they represented in the set of governing equations?
2. Which multirate methods can be applied to coupled models and how is the convergence behaviour of the integration schemes of the individual models adopted in the multirate approach?
3. Which strategies can be applied for the coupling of atmosphere and ocean models and to what extent do these strategies need to be adapted to consider multirate methods?

The first question is addressed independently of the multirate approach. The initial boundary value problems are formulated separately for the individual models. Furthermore, the coupling of atmosphere and ocean models is achieved at the air-sea interface, where the physical processes are modelled. The second question refers to the choice of a suitable multirate method, which is influenced by the structure of the initial boundary value problems and their coupling. For efficiency reasons, only multirate methods with similar convergence behaviour to the integration methods used to solve the individual models should be utilised. Additionally, only multirate methods that take the coupling into account are applied. The third question is determined by the numerical realisation of the coupling, which can be different for each coupled model. These coupling realisations must be adapted, depending on the different time scales, if multirate methods are applied. In order to guide the reader through the chapters, this thesis is structured based on order of the questions raised above. Chapter 2 provides the general theory for geophysical fluid dynamics applied in atmosphere and ocean models. The chapter closes with the concepts of the time integration scheme and the additive coupling of individual models.

Chapters 3 discusses newly developed multirate time integration schemes, which are used for this thesis. At first, the methods are introduced and explained. Furthermore, a series of special cases of the methods and their interrelations to each other are discussed. The convergence analysis of the multirate methods is presented in Chapter 4.

Chapter 5 is showing how atmosphere and ocean models can be coupled with a focus on the numerical aspects for the air-sea interface. The application of multirate methods in the framework of coupled models is discussed in Chapter 6.

Chapter 7 summarises this thesis.

## **Chapter 2**

# **Theoretical aspects of geophysical fluid modelling**

In this chapter, the focus is on a general description to model geophysical fluids on Earth. At first, a general introduction to the theoretical aspects of fluids is given, Section 2.1. Furthermore, the three conservation laws for mass, momentum and energy are discussed, Section 2.2. All these ideas can be applied for a gaseous fluid like the atmosphere as well as a liquid fluid like the ocean. Specific physical needs such as equations of state are explained and applied to the general set of equations. Differences between the atmosphere and ocean are explicitly mentioned. The final part is on general aspects of numerical modelling including a formulation for coupled atmosphere-ocean models, Section 2.3.

### **2.1 General assumptions for a geophysical fluid**

For this section, there is no distinction between the atmosphere and ocean. The properties for an arbitrary fluid are introduced and explained in Section 2.1.1. They are understood as the basis for all further considerations. Furthermore, the general budget equation for a fluid is derived, Section 2.1.2.

#### **2.1.1 Properties of a fluid**

Any fluid can be described through the mass it has, the volume it takes and the energy it stores. Arbitrary volumes are bounded with a surface. In atmospheric and/or oceanic systems the surrounding surfaces can be understood as the interfaces to a different medium. For the atmosphere on Earth, there are the sea surface, the topography over land and the top of the atmosphere. For an ocean on Earth, there are the topography of the bottom of the ocean, called bathymetry, and the sea surface.

A mass or energy change of a fluid can either be stated due to internal processes or an interaction with its surroundings through the various surfaces of the volume, see e.g. Zdunkowski and Bott (2004).

Fluids do not necessarily consist of one substance, e.g. the air in the atmosphere contains oxygen  $O_2$ , carbon dioxide  $CO_2$ , nitrogen  $N$  and even water in several state of matters, i.e. gaseous form (vapour), liquid form (e.g. rain) or ice form (e.g. snow). The water in the ocean contains mainly fresh water and dissolved salt, besides other substances.

Hence, for a general description, it is important to split a fluid into its several substances and components. Such a system is referred to as multiphase system. The following describes the fundamental properties of a fluid:

1. The mass ( $m$ ) of a fluid with  $n \in \mathbb{N}$  different substances is given as

$$m = \sum_{\kappa \in \mathcal{M}} [m_\kappa], \quad (2.1)$$

where  $m_\kappa$  is the mass of substance  $\kappa$  out of the set of  $n$  different substances  $\mathcal{M}$ . Equation (2.1) can be reformulated to

$$1 = \frac{m}{m} = \sum_{\kappa \in \mathcal{M}} \left[ \frac{m_\kappa}{m} \right] = \sum_{\kappa \in \mathcal{M}} [q_\kappa] \quad (2.2)$$

with specific content  $q_\kappa$  of substance  $\kappa$ .

2. The density ( $\rho$ ) of a fluid is defined by

$$\rho = \frac{m}{V} = \sum_{\kappa \in \mathcal{M}} \left[ \frac{m_\kappa}{V} \right] = \sum_{\kappa \in \mathcal{M}} [\rho_\kappa], \quad (2.3)$$

where the volume ( $V$ ) and the partial density ( $\rho_\kappa$ ) of substance  $\kappa$  is used.

3. Each of these substances  $\kappa$  can move with their own velocity ( $\mathbf{v}_\kappa$ ), e.g. rain falls down with a certain speed but the other substances in the atmosphere move with a different speed.
4. In order to find a description for a velocity ( $\mathbf{v}$ ) of the whole fluid, a barycentric velocity is defined by

$$\mathbf{v} = \frac{1}{\rho} \sum_{\kappa \in \mathcal{M}} [\rho_\kappa \mathbf{v}_\kappa] = \sum_{\kappa \in \mathcal{M}} [q_\kappa \mathbf{v}_\kappa]. \quad (2.4)$$

5. The energy of a fluid is described with the total energy ( $E$ ), which is obtained by the summation of kinetic energy ( $K$ ), potential energy ( $\Phi$ ) and internal energy ( $U$ ), i.e.

$$E = K + \Phi + U. \quad (2.5)$$

A substance-wise definition of the total energy is given with a barycentric definition

$$E = \sum_{\kappa \in \mathcal{M}} [q_\kappa \cdot E_\kappa] = \sum_{\kappa \in \mathcal{M}} [q_\kappa (K_\kappa + \Phi_\kappa + U_\kappa)] \quad (2.6)$$

with kinetic energy ( $K_\kappa$ ), potential energy ( $\Phi_\kappa$ ) and internal energy ( $U_\kappa$ ) for substance  $\kappa$ .

### 2.1.2 General budget equation for a fluid

A unified mathematical formulation is introduced for any mass dependent quantity  $\psi$  given over a volume. This has been discussed in many textbooks, see e.g. Baranowski (1975), Kundu et al. (2001), and Lange (2002). For this thesis, the notation of the formulas is unified such that the differences between the atmosphere and ocean are only due to the specific substances or components, indicated by  $\kappa$ .

It is stated that a change in time of quantity  $\psi$  in an arbitrary volume ( $V$ ) is only possible if there are fluxes ( $\lambda_\psi$ ) of  $\psi$  through the surrounding surface ( $\partial V$ ) or inner sources or sinks ( $\sigma_\psi$ ) of  $\psi$ , i.e.

$$\frac{d}{dt} \left( \int_{V(t)} [\rho \psi dV] \right) = - \oint_{\partial V(t)} [\lambda_\psi \cdot \mathbf{n} d\partial V] + \int_{V(t)} [\sigma_\psi dV] \quad (2.7)$$

with an outward-pointing normal vector ( $\mathbf{n}$ ). Applying some calculus, the integral form of the general budget equation is given by

$$\int_{V(t)} \left[ \left( \frac{\partial (\rho \psi)}{\partial t} + \nabla \cdot (\rho \psi \cdot \mathbf{v}_\psi^T) \right) dV \right] = - \int_{V(t)} [\nabla \cdot \lambda_\psi dV] + \int_{V(t)} [\sigma_\psi dV], \quad (2.8)$$

where  $\mathbf{v}_\psi$  represents the velocity of  $\psi$ , see Appendix A.1 for manipulation details. Equation (2.8) is valid for any arbitrary volume ( $V$ ). Henceforth, the differential form of the general budget equation is also valid, i.e.

$$\frac{\partial (\rho \psi)}{\partial t} + \nabla \cdot (\rho \psi \cdot \mathbf{v}_\psi^T) = -\nabla \cdot \lambda_\psi + \sigma_\psi, \quad (2.9)$$

see e.g. Baranowski (1975). If a fluid consists of numerous substances, compare with property 1 from Section 2.1.1, then equation (2.9) holds for each substance  $\kappa$ , i.e.

$$\sum_{\kappa \in \mathcal{M}} \left[ \frac{\partial (\rho_\kappa \psi_\kappa)}{\partial t} + \nabla \cdot (\rho_\kappa \psi_\kappa \cdot \mathbf{v}_\kappa^T) \right] = \sum_{\kappa \in \mathcal{M}} [-\nabla \cdot \lambda_{\psi, \kappa} + \sigma_{\psi, \kappa}], \quad (2.10)$$

where  $\mathbf{v}_\kappa$  represents the velocity,  $\lambda_{\psi, \kappa}$  the flux through the surface of a volume and  $\sigma_{\psi, \kappa}$  the source of substance  $\kappa$ . For

$$\psi = \sum_{\kappa \in \mathcal{M}} [q_\kappa \psi_\kappa], \quad (2.11)$$

the budget equation (2.10) is given by

$$\begin{aligned} \sum_{\kappa \in \mathcal{M}} \left[ \frac{\partial (\rho_\kappa \psi_\kappa)}{\partial t} + \nabla \cdot (\rho_\kappa \psi_\kappa \cdot \mathbf{v}_\kappa^T) \right] \\ = \frac{\partial (\rho \psi)}{\partial t} + \nabla \cdot (\rho \psi \cdot \mathbf{v}^T) + \sum_{\kappa \in \mathcal{M}} \left[ \nabla \cdot (\rho_\kappa \psi_\kappa \cdot (\mathbf{v}_\kappa - \mathbf{v})^T) \right] \\ = \sum_{\kappa \in \mathcal{M}} [-\nabla \cdot \lambda_{\psi, \kappa} + \sigma_{\psi, \kappa}]. \end{aligned} \quad (2.12)$$

Because of equation (2.4) and the definition of the diffusive mass flux for substance  $\kappa$

$$\mathbf{J}_\kappa = \rho_\kappa (\mathbf{v}_\kappa - \mathbf{v}), \quad (2.13a)$$

it follows that

$$\sum_{\kappa \in \mathcal{M}} [\nabla \cdot \mathbf{J}_\kappa] = \nabla \cdot \left( \sum_{\kappa \in \mathcal{M}} [\mathbf{J}_\kappa] \right) = \nabla \cdot \mathbf{0} = 0. \quad (2.13b)$$

This is referred as mass condition in atmospheric modelling, see e.g. Wacker et al. (2006) and Gassmann and Herzog (2015).

Finally, the unified barycentric formulation of the differential form of the general budget equation is given by

$$\frac{\partial (\rho \psi)}{\partial t} + \nabla \cdot (\rho \psi \cdot \mathbf{v}^T) = \sum_{\kappa \in \mathcal{M}} [-\nabla \cdot (\psi_\kappa \mathbf{J}_\kappa^T + \lambda_{\psi, \kappa}) + \sigma_{\psi, \kappa}]. \quad (2.14)$$

This general equation will ease further writings by only defining  $\psi$ ,  $\psi_\kappa$ ,  $\lambda_\kappa$  and  $\sigma_\kappa$ .

## 2.2 Conservation laws and equation of state

The basis for geophysical fluid dynamics are the three conservation laws, i.e. conservation of mass, momentum and energy. They state that there is no change in mass, momentum and energy of a fluid in a closed volume over time. In Sections 2.2.1-2.2.3, the general budget equations for mass, momentum and total energy are derived. The starting point is the general budget equation written in barycentric form, see equations (2.10) and (2.14).

Modelling of physical processes requires validation by measurement data that describe the state of the fluid. Directly measured data are pressure, velocity and temperature. They are often called state or primitive variables. An equation of state relates the state variables of a fluid in thermodynamic equilibrium. For the atmosphere and ocean, the equation of state is presented in Section 2.2.4.

Additional physical assumptions can also be applied to a fluid, e.g. compressible vs. incompressible fluid, Boussinesq approximation and hydrostatic equilibrium. A short explanation is given in Appendix B.

### 2.2.1 Conservation of mass

If there is no change in the total mass in a volume over time, then mass is conserved, i.e. a closed system with respect to mass, cf. Zdunkowski and Bott (2004). Equation (2.7) for mass, i.e.  $\psi = 1$ , simplifies to

$$\frac{d}{dt} \left( \int_{V(t)} [\rho dV] \right) = 0. \quad (2.15)$$

However, transport of mass allows a change at a certain place within the volume. Equation (2.10) reduces then to the budget equation for mass:

$$0 = \sum_{\kappa \in \mathcal{M}} \left[ \frac{\partial \rho_\kappa}{\partial t} + \nabla \cdot (\rho_\kappa \cdot \mathbf{v}_\kappa^T) \right] = \frac{\partial \rho}{\partial t} + \nabla \cdot (\rho \cdot \mathbf{v}^T) = \sum_{\kappa \in \mathcal{M}} [-\nabla \cdot \lambda_\kappa + \sigma_\kappa] \quad (2.16)$$

with  $\psi = \sum_{\kappa \in \mathcal{M}} [q_\kappa \psi_\kappa] = 1$  and  $\psi_\kappa = 1$ , see equations (2.2) and (2.11), and mass condition, equation (2.13b). Since no mass can enter or leave a closed system,  $\nabla \cdot \lambda_\kappa = 0$  holds for each substance  $\kappa$ . Only phase changes can occur, e.g. rain drops can evaporate and become water vapour. They are indicated through source of mass ( $I$ ) i.e.  $\sigma_\kappa = I_\kappa$  for substance  $\kappa$ . Therefore, the right hand side of equation (2.16) simplifies to

$$\sum_{\kappa \in \mathcal{M}} [I_\kappa] = 0,$$

which states that the total amount of sources vanishes. Finally, the budget equations for mass for a single substance  $\kappa$  and for the whole closed system read

$$\frac{\partial \rho_\kappa}{\partial t} + \nabla \cdot (\rho_\kappa \mathbf{v}_\kappa^T) = I_\kappa \quad (2.17a)$$

$$\frac{\partial \rho}{\partial t} + \nabla \cdot (\rho \mathbf{v}^T) = 0. \quad (2.17b)$$

The conservation of mass is applied in atmosphere and ocean models, see e.g. Ullrich et al. (2017) and Klingbeil et al. (2018).

Equation (2.17a) is provided for every substance  $\kappa$  in multiphase models. Equation (2.17b) ensures conservation of total mass in a geophysical model. Hence, the equation for the main substance is replaced with equation (2.17b) because of equation (2.3), i.e. dry air in an atmosphere model and fresh water in an ocean model. Equation (2.17a) is often referred as continuity equation for substance  $\kappa$ .

Theoretical discussions to understand the influence of non-conservative mass approaches for open systems can be found in Bott (2008).

### 2.2.2 Conservation of momentum

Isaac Newton's second law of motion is the basis for the balance of momentum, cf. Kundu et al. (2001) and Zdunkowski and Bott (2003). It states that for conserved mass in a volume, the change of momentum is proportional to the forces applied on the volume. These forces are related to the stress tensor and to external forces. The stress tensor will be split into pressure components and the shear stress tensor. External forces include Coriolis and gravitational force. Other possible forces are neglected in atmosphere and ocean modelling, see e.g. Zdunkowski and Bott (2003).

Applying all these forces gives the equation of motion for each substance  $\kappa \in \mathcal{M}$

$$\rho_\kappa \frac{d\mathbf{v}_\kappa}{dt} = -\nabla p_\kappa - \rho_\kappa \nabla \phi_\kappa - 2\rho_\kappa \boldsymbol{\Omega} \times \mathbf{v}_\kappa + \nabla \cdot \boldsymbol{\tau}_\kappa. \quad (2.18)$$

The right hand side of equation (2.18) is given by the pressure gradient, geopotential, Coriolis term and shear stress tensor, respectively. The derivation can be found for example in Zdunkowski and Bott (2003). A thorough discussion is beyond the scope of this chapter. In addition,

$$\begin{aligned} p &= \sum_{\kappa \in \mathcal{M}} [p_\kappa] & \text{and} & & \boldsymbol{\tau} &= \sum_{\kappa \in \mathcal{M}} [\boldsymbol{\tau}_\kappa], \\ \rho \nabla \phi &= \sum_{\kappa \in \mathcal{M}} [\rho_\kappa \nabla \phi_\kappa] & \text{and} & & \rho \boldsymbol{\Omega} \times \mathbf{v} &= \sum_{\kappa \in \mathcal{M}} [\rho_\kappa \boldsymbol{\Omega} \times \mathbf{v}_\kappa] \end{aligned}$$

hold. The applied geopotential is assumed to be identical for all substances  $\kappa \in \mathcal{M}$ , i.e.

$$\phi = \phi_\kappa = g \cdot z, \quad (2.19)$$

cf. Etling (2008). The budget equation for momentum for a fluid in substance-wise form is then given with equations (2.17a) and (2.18) by

$$\begin{aligned} \sum_{\kappa \in \mathcal{M}} \left[ \frac{\partial (\rho_\kappa \mathbf{v}_\kappa)}{\partial t} + \nabla \cdot (\rho_\kappa \mathbf{v}_\kappa \cdot \mathbf{v}_\kappa^T) \right] &= \sum_{\kappa \in \mathcal{M}} \left[ \rho_\kappa \frac{d\mathbf{v}_\kappa}{dt} + \mathbf{v}_\kappa \left( \frac{\partial \rho_\kappa}{\partial t} + \nabla \cdot (\rho_\kappa \cdot \mathbf{v}_\kappa^T) \right) \right] \\ &= -\nabla p - \rho \nabla \phi - 2\rho \Omega \times \mathbf{v} + \nabla \cdot \boldsymbol{\tau} + \sum_{\kappa \in \mathcal{M}} [\mathbf{v}_\kappa I_\kappa]. \end{aligned} \quad (2.20a)$$

The last part on the right hand side describes the momentum intake by phase changes. Following from equation (2.12) with  $\boldsymbol{\psi}_\kappa = \mathbf{v}_\kappa$  the budget equation for momentum also reads

$$\sum_{\kappa \in \mathcal{M}} \left[ \frac{\partial (\rho_\kappa \mathbf{v}_\kappa)}{\partial t} + \nabla \cdot (\rho_\kappa \mathbf{v}_\kappa \cdot \mathbf{v}_\kappa^T) \right] = \frac{\partial (\rho \mathbf{v})}{\partial t} + \nabla \cdot (\rho \mathbf{v} \cdot \mathbf{v}^T) + \sum_{\kappa \in \mathcal{M}} [\nabla \cdot (\mathbf{v}_\kappa \mathbf{J}_\kappa^T)]. \quad (2.20b)$$

Both equations (2.20a) and (2.20b) define the budget equation for momentum with respect to phase changes due to internal processes in a fluid and diffusive mass fluxes, i.e.

$$\frac{\partial (\rho \mathbf{v})}{\partial t} + \nabla \cdot (\rho \mathbf{v} \cdot \mathbf{v}^T) = -\nabla p - \rho \nabla \phi - 2\rho \Omega \times \mathbf{v} + \nabla \cdot \boldsymbol{\tau} + \sum_{\kappa \in \mathcal{M}} [\mathbf{v}_\kappa I_\kappa - \nabla \cdot (\mathbf{v}_\kappa \mathbf{J}_\kappa^T)]. \quad (2.20c)$$

Note that, since

$$\rho \mathbf{v} \cdot \mathbf{v}^T \gg \sum_{\kappa \in \mathcal{M}} [\mathbf{v}_\kappa \mathbf{J}_\kappa^T] = \sum_{\kappa \in \mathcal{M}} [(\mathbf{v}_\kappa - \mathbf{v}) \mathbf{J}_\kappa^T], \quad (2.21)$$

the latter term is often neglected, see e.g. Lange (2002). Additionally,

$$\sum_{\kappa \in \mathcal{M}} [\mathbf{v}_\kappa I_\kappa] = \sum_{\kappa \in \mathcal{M}} [(\mathbf{v}_\kappa - \mathbf{v}) I_\kappa].$$

Hence, also this term is often neglected, since the velocity differences are relatively small. The differences of both approaches are pointed out in Baranowski (1975) and Lange (2002). However, there are situations in atmosphere models where the the barycentric velocity and the velocity of substance  $\kappa$  deviate, e.g. in tropical cyclones, cf. Bott (2008). Henceforth, equation (2.20c) is reformulated to include the frequently neglected terms, i.e.

$$\frac{\partial (\rho \mathbf{v})}{\partial t} + \nabla \cdot (\rho \mathbf{v} \cdot \mathbf{v}^T) = \sum_{\kappa \in \mathcal{M}} [-\nabla \cdot (\mathbf{v}_\kappa \mathbf{J}_\kappa^T + p_\kappa \mathbb{I} - \boldsymbol{\tau}_\kappa) - \rho_\kappa \nabla \phi - 2\rho_\kappa \Omega \times \mathbf{v}_\kappa + \mathbf{v}_\kappa I_\kappa] \quad (2.22)$$

where the dyadic unit tensor ( $\mathbb{I}$ ) is used. This resembles equation (2.14) with

$$\begin{aligned} \boldsymbol{\psi} &:= \mathbf{v} & \boldsymbol{\psi}_\kappa &:= \mathbf{v}_\kappa \\ \lambda_{\boldsymbol{\psi}, \kappa} &:= p_\kappa \mathbb{I} - \boldsymbol{\tau}_\kappa & \sigma_{\boldsymbol{\psi}, \kappa} &:= -\rho_\kappa \nabla \phi - 2\rho_\kappa \Omega \times \mathbf{v}_\kappa + \mathbf{v}_\kappa I_\kappa. \end{aligned}$$



Neglecting  $\sum_{\kappa \in \mathcal{M}} [\mathbf{v}_\kappa I_\kappa - \nabla \cdot (\mathbf{v}_\kappa \mathbf{J}_\kappa^T)]$  from equation (2.20c) leads to a formulation of the governing equation for barycentric velocity, i.e.

$$\frac{\partial (\rho \mathbf{v})}{\partial t} + \nabla \cdot (\rho \mathbf{v} \cdot \mathbf{v}^T) = -\nabla p - \rho \nabla \phi - 2\rho \boldsymbol{\Omega} \times \mathbf{v} + \nabla \cdot \boldsymbol{\tau}.$$

This equation is often used in atmosphere and ocean models. However, the individual substance velocities in equation (2.20c) must be considered in atmosphere models, especially for heavy precipitation events, cf. Bott (2008). Therefore, if not stated otherwise, the velocities of each substance are considered throughout this thesis.

### 2.2.3 Energy budget

Conservation of energy is interpreted such that energy can neither be created nor destroyed in a closed environment. This refers to a constant total energy ( $E$ ) of a closed system. The total energy is expressed as the sum of kinetic, potential and inner energy, compare with equation (2.5).

Zdunkowski and Bott (2004) demonstrated with a small experiment that it is more convenient to use a description of energy per unit mass, i.e. specific kinetic energy ( $k$ ), specific potential energy ( $\phi$ ), specific internal energy ( $u$ ) and specific total energy ( $e$ ). Conserving energy implies that energy will only be transferred or transformed among the substances  $\kappa$ , i.e.

$$\frac{de}{dt} = \frac{dk}{dt} + \frac{d\phi}{dt} + \frac{du}{dt} = 0 \quad \text{or} \quad \frac{du}{dt} = -\frac{dk}{dt} - \frac{d\phi}{dt}. \quad (2.23)$$

Furthermore, energy can neither be created nor destroyed. Henceforth, in a closed system,

$$\frac{\partial (\rho e)}{\partial t} + \nabla \cdot (\rho e \cdot \mathbf{v}^T) = - \sum_{\kappa \in \mathcal{M}} [\nabla \cdot (e_\kappa \mathbf{J}_\kappa^T)] \quad (2.24)$$

follows from equation (2.14) with  $\psi = e$  and  $\psi_\kappa = e_\kappa$  as well as equation (2.12). However, in general, solar radiation has to be taken into account for atmosphere and ocean models. This yields an additional term, since there is an energy intake, usually at the top of the atmosphere or the sea surface for the ocean. Nevertheless, the equation for specific kinetic energy ( $k$ ) with diffusive mass flux can directly be derived from the conservation of momentum, see Appendix A.2, i.e.

$$\begin{aligned} \frac{\partial (\rho (k + k_d))}{\partial t} + \nabla \cdot (\rho (k + k_d) \cdot \mathbf{v}^T) \\ = \sum_{\kappa \in \mathcal{M}} [-\nabla \cdot (k_\kappa \mathbf{J}_\kappa^T + (p_\kappa \mathbb{I} - \boldsymbol{\tau}_\kappa) \cdot \mathbf{v}_\kappa) + (p_\kappa \mathbb{I} - \boldsymbol{\tau}_\kappa) \cdot \nabla \mathbf{v}_\kappa - \rho_\kappa \mathbf{v}_\kappa \cdot \nabla \phi + k_\kappa I_\kappa]. \end{aligned} \quad (2.25a)$$

Note that, equation (2.11) does only hold in general for specific kinetic energy by defining the specific diffusive kinetic energy ( $k_d$ ), which represents the specific kinetic energy caused by diffusive mass fluxes. The derivation of the specific diffusive kinetic energy ( $k_d$ ) is found in Appendix A.2. The barycentric definition for specific kinetic energy is then given by

$$\sum_{\kappa \in \mathcal{M}} [\rho_\kappa k_\kappa] = \sum_{\kappa \in \mathcal{M}} \left[ \rho_\kappa k + \frac{1}{2} \rho_\kappa (\mathbf{v}_\kappa - \mathbf{v}) \cdot (\mathbf{v}_\kappa - \mathbf{v}) \right] = \rho k + \rho k_d.$$

Comparing with equation (2.14) yields

$$\begin{aligned}\psi &:= k + k_d & \psi_\kappa &:= k_\kappa \\ \lambda_{\psi,\kappa} &:= (p_\kappa \mathbb{I} - \tau_\kappa) \cdot \mathbf{v}_\kappa & \sigma_{\psi,\kappa} &:= (p_\kappa \mathbb{I} - \tau_\kappa) \cdot \nabla \mathbf{v}_\kappa - \rho_\kappa \mathbf{v}_\kappa \cdot \nabla \phi + k_\kappa I_\kappa.\end{aligned}$$

Note that if the velocity differences are considered to be relatively small and neglected, i.e. estimation from equation (2.21), then the specific diffusive kinetic energy is also neglected in equation (2.25a). Thus, equation (2.25a) simplifies to

$$\frac{\partial(\rho k)}{\partial t} + \nabla \cdot (\rho k \cdot \mathbf{v}^T) = -\nabla p \cdot \mathbf{v} + \mathbf{v} \cdot \nabla \cdot \tau - \rho \mathbf{v} \cdot \nabla \phi.$$

The equation for specific potential energy ( $\phi$ ) is given directly by equations (2.14) and (2.19) with no flux through the surface of a volume, i.e.  $\nabla \cdot \lambda_{\psi,\kappa} = 0$  and  $\sigma_{\psi,\kappa} = \rho_\kappa \mathbf{v}_\kappa \cdot \nabla \phi_\kappa$ . Hence,

$$\sum_{\kappa \in \mathcal{M}} \left[ \frac{\partial(\rho_\kappa \phi)}{\partial t} + \nabla \cdot (\rho_\kappa \phi \cdot \mathbf{v}_\kappa^T) \right] = \frac{\partial(\rho \phi)}{\partial t} + \nabla \cdot (\rho \phi \cdot \mathbf{v}^T) = \rho \mathbf{v} \cdot \nabla \phi. \quad (2.25b)$$

The derivation of the equation for specific internal energy ( $u$ ) is based on the first law of thermodynamics, i.e.

$$\frac{du}{dt} = \frac{dq}{dt} + \frac{da}{dt} \quad (2.25c)$$

with specific heat ( $q$ ) changes and specific work ( $a$ ) performed by the fluid. It briefly states that any addition of heat to the fluid and performance of work by the fluid will change the internal energy, see e.g. Zdunkowski and Bott (2004). A general derivation of the specific internal energy highly depends on the structure of the fluid, see e.g. Bannon (2002), Satoh (2003), and Bott (2008). Other aspects such as the second law of thermodynamics are also discussed in atmospheric modelling, see e.g. Gassmann and Herzog (2015). In this thesis, the general derivation is loosely based on Baranowski (1975) and given in Appendix A.3. The assumption that the total energy is conserved in a closed volume states that the internal energy cancels out kinetic and potential energy, cf. equation (2.23). The final equation reads

$$\frac{\partial(\rho u)}{\partial t} + \nabla \cdot (\rho u \cdot \mathbf{v}^T) = \sum_{\kappa \in \mathcal{M}} \left[ -\nabla \cdot (u_\kappa \mathbf{J}_\kappa^T - (p_\kappa \mathbb{I} - \tau_\kappa) \cdot \mathbf{v}_\kappa) - (p_\kappa \mathbb{I} - \tau_\kappa) \cdot \nabla \mathbf{v}_\kappa - k_\kappa I_\kappa \right]. \quad (2.25d)$$

A substance-wise formulation for equation (2.25d) is given by equation (2.14) with

$$\begin{aligned}\psi &:= u & \psi_\kappa &:= u_\kappa \\ \lambda_{\psi,\kappa} &:= -(p_\kappa \mathbb{I} - \tau_\kappa) \cdot \mathbf{v}_\kappa & \sigma_{\psi,\kappa} &:= -(p_\kappa \mathbb{I} - \tau_\kappa) \cdot \nabla \mathbf{v}_\kappa - k_\kappa I_\kappa.\end{aligned}$$

Similar as for specific kinetic energy, equation (2.25d) reads

$$\frac{\partial(\rho u)}{\partial t} + \nabla \cdot (\rho u \cdot \mathbf{v}^T) = \nabla p \cdot \mathbf{v} - \mathbf{v} \cdot \nabla \cdot \tau$$

if the velocity differences are neglected, equation (2.21). For open systems, i.e. with additional heat or radiative fluxes ( $q$ ) through the surface of the volume, equation (2.25d) becomes

$$\begin{aligned} \frac{\partial(\rho u)}{\partial t} + \nabla \cdot (\rho u \cdot \mathbf{v}^T) &= \nabla \cdot \mathbf{q} \\ &+ \sum_{\kappa \in \mathcal{M}} \left[ -\nabla \cdot (u_\kappa \mathbf{J}_\kappa^T - (p_\kappa \mathbb{I} - \boldsymbol{\tau}_\kappa) \cdot \mathbf{v}_\kappa) - (p_\kappa \mathbb{I} - \boldsymbol{\tau}_\kappa) \cdot \nabla \mathbf{v}_\kappa - k_\kappa I_\kappa \right]. \end{aligned}$$

Note that the idea of an open atmosphere is thoroughly discussed in Bott (2008). Additional heat fluxes or solar radiation are not further considered for this thesis, unless stated otherwise.

The total energy budget is described by the budgets for kinetic energy, potential energy and internal energy. Since the kinetic and potential energies are related to the momentum, cf. equation (2.22) with equations (2.25a) and (2.25b), the energy budget is represented by the internal energy in geophysical fluid dynamics. The changes in internal energy are given by the first law of thermodynamics. Temperature ( $T$ ) is reasonable measure for heat and often used to express the general budget equation for internal energy, see e.g. Zdunkowski and Bott (2004).

**Remark:** *The presented equations consider numerous substances for a fluid. With no further a-priori applied assumptions, the same equations can be utilised for any fluid, e.g. for the atmosphere and ocean. Hence, the structure of the equations is identical for atmosphere and ocean models. Applying specific assumptions to the atmosphere and ocean leads to different formulations of the equations, as later seen for ICON and GETM.*

## 2.2.4 Equation of state

The equation of state relates the state variables of a fluid in thermodynamic equilibrium. Feistel (2018) described various formulations of thermodynamic potentials. They allow a general formulation of the thermodynamic properties of a fluid in equilibrium. These potentials are functions depending on state variables, e.g. density ( $\rho$ ), volume ( $V$ ) and temperature ( $T$ ). Notably, these equations depend highly on the characteristics of the fluid, including whether multiple substances are considered.

From such a general equation, the equation of state for a specific fluid is then derived based on geophysical assumptions and is generally defined by

$$p = p(\rho_1, \rho_2, \dots, V, T), \quad (2.26)$$

see e.g. Staniforth (2022). Note that the different substances  $\kappa \in \mathcal{M}$  are represented through their partial densities  $\rho_\kappa$  in equation (2.26). The following introduces the different equations of state commonly applied in atmosphere (Section 2.2.4.1) and ocean (Section 2.2.4.2) models, cf. Cushman-Roisin and Beckers (2011).

### 2.2.4.1 Equation of state for the atmosphere

The equation of state in meteorology is often given by the ideal gas law, i.e.

$$p = \rho RT \quad \text{or} \quad \rho = \frac{p}{RT}. \quad (2.27)$$

This equation describes the state of an ideal gas by relating the mass ( $m$ ), the gas constant ( $R$ ) and temperature ( $T$ ). In general, atmospheric models assume that dry air and water vapour behave like

ideal gases, see e.g. Doms and Baldauf (2013) and Zängl et al. (2015) for the ICON model. The influence of liquid and solid components to density is often neglected, see e.g. Staniforth (2022). Equation (2.27) holds for dry air and water vapour where  $R$  represents the gas constant for dry air ( $R_d$ ) or the gas constant for water vapor ( $R_v$ ), respectively. The partial contributions are added to the total amount. Hence, the gas constant can be formulated as weighted average of  $R_d$  and the  $R_v$ . The combination depends on the time and space dependent specific dry air content ( $q_d$ ), see e.g. Etling (2008).

#### 2.2.4.2 Equation of state for the ocean

The equation of state in oceanography is related to temperature, salinity and pressure. Millero (2010) reported on the history of the equation of state for seawater. There has been a major breakthrough with the international Thermodynamic Equation Of Seawater - 2010 (TEOS-10), see e.g. Ioc et al. (2010) and Feistel (2018). Following Staniforth (2022), the equation of state is given by the reciprocal of the pressure derivative of the Gibbs function. The density can be calculated as function of potential temperature ( $\theta$ ), salinity ( $S$ ) and pressure ( $p$ ), i.e.

$$\rho = \rho(\theta, S, p). \quad (2.28)$$

A variety of algorithms for the calculation of the equation of state are available, see e.g. Ioc et al. (2010) and Roquet et al. (2015). In idealised studies a linearised equation of state can be applied, i.e. the linear equation

$$\rho = \rho_0 (1 + \alpha(\theta - \theta_l) + \beta(S - S_l)), \quad (2.29)$$

see e.g. Burchard et al. (2017).  $\rho_0$ ,  $\theta_l$  and  $S_l$  are constant reference values. The surface mixed layer is the upper part of the ocean beneath the surface where interactions with the atmosphere result in a change of salinity. The lower layer in the ocean is the lower part of the ocean above the bottom where the potential temperature and salinity is nearly constant.

**Remark:** *Potential temperature ( $\theta$ ) is defined as the temperature a fluid parcel would have if it was brought adiabatically to a reference position. In meteorology, this position is usually at a pressure level of 100kPa. In oceanography, this reference position is at the sea surface. A process is referred to as adiabatic, if a system performs work without exchanging heat with its surroundings.*

## 2.3 Numerical modelling of geophysical fluids

The focus of this section is on the application of the conservation laws in atmosphere and ocean models, i.e. the full set of equations which describe the fluid. Moreover, an initial boundary value problem (IBVP) for a coupled atmosphere-ocean model is presented. The structure of this IBVP will then be the basis for the following discussion in this thesis.

The set of equations for the IBVP is described in Section 2.3.1 including a general overview on the

different kinds of boundary conditions. Atmosphere and ocean models use spatial discretisations to define a final set of ordinary differential equations. Section 2.3.2 describes some aspects of spatial discretisations. Furthermore, a short overview of widely used time integration methods are given in Section 2.3.3 followed by general aspects of solving coupled models.

### 2.3.1 Initial-boundary value problem for geophysical fluid models

Modelling an atmosphere or ocean requires an initial boundary value problem in a three-dimensional coordinate system describing the time development of an arbitrary quantity  $\psi$ . For a coupled atmosphere-ocean model, the individual problems are combined. The structure of the set of equations for a coupled atmosphere-ocean model is presented in Section 2.3.1.1. A description and formulation of the boundaries and their conditions in a coupled atmosphere-ocean model is given in Section 2.3.1.2.

#### 2.3.1.1 Set of equations in geophysical fluid dynamics

Adhering to the conservation laws and describing the state of a geophysical fluid with an equation of state, the dynamics can be formulated for a given spatial domain ( $V$ ) and the corresponding conditions for the boundary ( $\partial V$ ). The variables density  $\rho = \rho(\mathbf{x}, t)$ , velocity  $\mathbf{v} = \mathbf{v}(\mathbf{x}, t)$  and internal energy  $u = u(\mathbf{x}, t)$  are representing the overall fluid. For the individual substance  $\kappa$ , the variables are denoted with  $\rho_\kappa = \rho_\kappa(\mathbf{x}, t)$ ,  $\mathbf{v}_\kappa = \mathbf{v}_\kappa(\mathbf{x}, t)$  and  $u_\kappa = u_\kappa(\mathbf{x}, t)$ , respectively. The final set of equations is formulated for the variables of each substance  $\kappa$ . Because of the barycentric definition of the fluid, the equation for one substance can be replaced with the continuity equation for the fluid. The governing equation for dry air is usually replaced in atmosphere modelling, while the governing equation for fresh water is replaced in ocean modelling. Note that the structure of equations (2.17), (2.22) and (2.25d) are identical, i.e. the set of equations can be summarised for an arbitrary geophysical fluid by equations (2.9) or (2.12) and Table 2.1.

Budget equations	$\psi$	$\psi_\kappa$	$\lambda_\kappa$	$\sigma_\kappa$
Mass	1	1	0	$I_\kappa$
Momentum	$\mathbf{v}$	$\mathbf{v}_\kappa$	$p_\kappa \mathbb{I} - \boldsymbol{\tau}_\kappa$	$-\rho_\kappa \nabla \phi - 2\rho_\kappa \boldsymbol{\Omega} \times \mathbf{v}_\kappa + \mathbf{v}_\kappa I_\kappa$
Internal energy	$u$	$u_\kappa$	$-(p_\kappa \mathbb{I} - \boldsymbol{\tau}_\kappa) \cdot \mathbf{v}_\kappa$	$-(p_\kappa \mathbb{I} - \boldsymbol{\tau}_\kappa) \cdot \nabla \mathbf{v}_\kappa - k_\kappa I_\kappa$

Table 2.1: Corresponding variable description for unified formulation of general set of equations based on the conservation laws, i.e. equations (2.17), (2.22) and (2.25d)

A more compact formulation is achieved by defining different operators, i.e. for equation (2.9)

$$\frac{\partial (\rho_\kappa \psi_\kappa)}{\partial t} = -\nabla \cdot (\rho_\kappa \psi_\kappa \cdot \mathbf{v}_\kappa^T) - \nabla \cdot (\lambda_\kappa) + \sigma_\kappa =: f^{\psi_\kappa},$$

for the general differential equation (2.12)

$$\frac{\partial (\rho \psi)}{\partial t} = -\nabla \cdot (\rho \psi \cdot \mathbf{v}^T) + \sum_{\kappa \in \mathcal{M}} [-\nabla \cdot (\psi_\kappa \mathbf{J}_\kappa^T + \lambda_\kappa) + \sigma_\kappa] =: f^\psi$$

and a boundary operator  $\mathcal{B}()$  stating the kind of boundary condition (BC) for  $\psi$

$$\mathcal{B}(\rho\psi) = f_B^\psi, \quad \forall \mathbf{x} \in \partial V.$$

Given initial conditions for the fluid, i.e.

$$\rho(\mathbf{x}, 0) = \rho_0 \quad \text{and} \quad \psi(\mathbf{x}, 0) = \psi_0, \quad \forall \mathbf{x} \in V,$$

the initial boundary value problem (IBVP) is defined by

$$\text{DE :} \quad \frac{\partial(\rho\psi)}{\partial t} = f^\psi \quad (2.30a)$$

$$\text{ES :} \quad p = p(\rho_1, \rho_2, \dots, V, T) \quad (2.30b)$$

$$\text{IC :} \quad \rho(\mathbf{x}, 0) = \rho_0 \quad \text{and} \quad \psi(\mathbf{x}, 0) = \psi_0, \quad \forall \mathbf{x} \in V \quad (2.30c)$$

$$\text{BC :} \quad \mathcal{B}(\rho\psi) = f_B^\psi, \quad \forall \mathbf{x} \in \partial V. \quad (2.30d)$$

with differential equation (DE), equation of state (ES), initial condition (IC) and boundary condition (BC).

The IBVP given in equation (2.30) generally formulates the dynamics of one geophysical fluid. Combining two fluids, e.g. an atmosphere and ocean, results in a coupled IBVP. A coupled atmosphere-ocean problem reads for the atmosphere

$$\frac{\partial(\rho^A \psi^A)}{\partial t} = f^{\psi^A} \quad (2.31a)$$

$$p^A = \rho^A R T^A \quad (2.31b)$$

$$\rho^A(\mathbf{x}, 0) = \rho_0^A \quad \text{and} \quad \psi^A(\mathbf{x}, 0) = \psi_0^A, \quad \forall \mathbf{x} \in V^A \quad (2.31c)$$

$$\mathcal{B}^A(\rho^A \psi^A) = f_B^{\psi^A}, \quad \forall \mathbf{x} \in \partial V^A \quad (2.31d)$$

with a coupling condition

$$\mathcal{C}(\rho^A \psi^A, \rho^O \psi^O) = f_C^{\psi^A, \psi^O} \quad (2.31e)$$

and for the ocean

$$\frac{\partial(\rho^O \psi^O)}{\partial t} = f^{\psi^O} \quad (2.31f)$$

$$\rho^O = \rho^O(\theta^O, S, p^O) \quad (2.31g)$$

$$\rho^O(\mathbf{x}, 0) = \rho_0^O \quad \text{and} \quad \psi^O(\mathbf{x}, 0) = \psi_0^O, \quad \forall \mathbf{x} \in V^O \quad (2.31h)$$

$$\mathcal{B}^O(\rho^O \psi^O) = f_B^{\psi^O}, \quad \forall \mathbf{x} \in \partial V^O. \quad (2.31i)$$

Following the conservation laws, the coupling conditions at the air-sea interface are assuming that mass, momentum and energy are balanced. Figure 2.1 shows the physical processes considered at the boundaries for atmosphere and ocean models.

Water evaporating from the ocean must enter the atmosphere and vice versa for the precipitation from the atmosphere to the ocean. Additionally, balanced momentum and energy implies that any

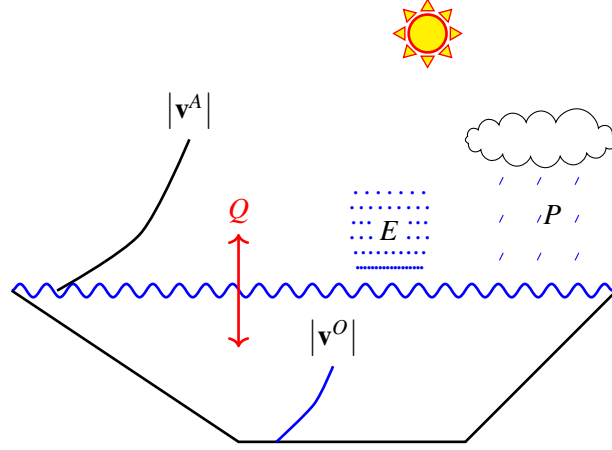


Figure 2.1: Physical processes at the boundaries of the atmosphere and ocean which include the mass transfer due to evaporation ( $E$ ) and precipitation ( $P$ ), the momentum transfer between the fluid velocity ( $\mathbf{v}^A, \mathbf{v}^O$ ) profiles and the energy transfer in terms of heat ( $Q$ ) and radiation (sun).

loss in the atmosphere is added to the ocean and vice versa. The transport of mass, momentum and energy is formulated through fluxes. The energy flux is commonly represented through heat and radiative fluxes. The modelled processes at the sea surface and the corresponding standard parameterisations are explained e.g. in Csanady (2004).

The formulation of the coupling conditions is based on the BCs at the air-sea interface, i.e. by an equilibrium formulation of the exchange of mass (precipitation and evaporation), momentum (wind stress) and energy (heat exchange). This is achieved by equalising the flux formulation at the air-sea interface. Hence, the coupling conditions read

$$f_B^{\psi^A}(\rho^A \psi^A) \equiv f_B^{\psi^O}(\rho^O \psi^O) \quad \text{or} \quad f_C^{\psi^A, \psi^O} = f_B^{\psi^A}(\rho^A \psi^A) - f_B^{\psi^O}(\rho^O \psi^O) = 0, \quad (2.32)$$

see also equation (2.31e). Specific coupling conditions are discussed in Chapter 5.

### 2.3.1.2 Boundary conditions for geophysical fluid models

The boundary ( $\partial V$ ) of the spatial domain ( $V$ ) has to be described by appropriate conditions. The structure of the BC highly depends on the assumptions applied at the boundaries. Moreover, in general, all conservation laws as well as the equation of state must be fulfilled. Therefore, all BCs are time dependent.

In addition to the physical processes at the air-sea interface, Figure 2.1 also shows the vertical boundaries for an ocean model. At the bottom of the sea, the no-slip BCs, i.e.  $\mathbf{v} \equiv \mathbf{0}$ , are applied, see e.g. Cushman-Roisin and Beckers (2011) and Klingbeil et al. (2018). Additionally, the kinematic and dynamic conditions fulfil the hydrostatic assumption, see e.g. Klingbeil et al. (2018), and no mass and energy transfer are considered. Furthermore, there are vertical boundaries over land and at the top in an atmosphere model. The BCs over land are very similar to those at the

bottom of the sea, although the physical processes are described differently.

The BC for mass is provided through assumptions on the mass flux, i.e.

$$\rho(\mathbf{x}, t) \mathbf{v}(\mathbf{x}, t) \cdot \mathbf{n}(\mathbf{x}) = f_B^1(\mathbf{x}, t), \quad \forall \mathbf{x} \in \partial V \quad (2.33)$$

with normal vector ( $\mathbf{n}$ ) pointing outwards of the spatial domain. If no mass leaves or enters the atmosphere or ocean, i.e. there is no mass flux through the boundaries, then  $f_B^1(\mathbf{x}, t) \equiv 0$ . At the sea surface, processes like evaporation or precipitation must be considered.

The conditions for momentum at the bottom of the sea or over land, i.e. kinematic BCs, are based on the assumption that neither air nor water penetrate into land, see Cushman-Roisin and Beckers (2011). This leads to the assumption that the fluid moves tangentially to the boundary, i.e.

$$\mathbf{v}(\mathbf{x}, t) \cdot \mathbf{n}(\mathbf{x}) = 0, \quad \forall \mathbf{x} \in \partial V, \quad (2.34)$$

which is equivalent with a no mass flux condition.

Furthermore, dynamic conditions are applied at the sea surface stating that pressure and shear stress forces are continuous. The pressure in the atmosphere and ocean is assumed to be identical at the sea surface. The shear stress in the atmosphere is directly applied to the ocean, and vice versa. A general formulation is given via the momentum flux, i.e.

$$\left( \rho(\mathbf{x}, t) \mathbf{v}(\mathbf{x}, t) \cdot \mathbf{v}(\mathbf{x}, t)^T + \sum_{\kappa \in \mathcal{M}} [\mathbf{v}_\kappa \mathbf{J}_\kappa^T] + p - \tau \right) \cdot \mathbf{n}(\mathbf{x}) = f_B^v(\mathbf{x}, t), \quad \forall \mathbf{x} \in \partial V. \quad (2.35)$$

The BC for the internal energy is also represented by the fluxes across the boundary, i.e.

$$\left( \rho(\mathbf{x}, t) u(\mathbf{x}, t) \cdot \mathbf{v}(\mathbf{x}, t) + \sum_{\kappa \in \mathcal{M}} [u_\kappa \mathbf{J}_\kappa^T - (p_\kappa \mathbb{I} - \tau_\kappa) \cdot \mathbf{v}_\kappa] \right) \cdot \mathbf{n}(\mathbf{x}) = f_B^u(\mathbf{x}, t), \quad \forall \mathbf{x} \in \partial V. \quad (2.36)$$

Furthermore, the energy BCs are often based on conditions for internal energy. They include heat fluxes and solar radiation.

Following the conservation laws, the same mass, momentum and energy fluxes across the sea surface have to be applied in the atmosphere and in the ocean, which generally states that mass, momentum and energy are not lost at the sea surface. In a coupled atmosphere-ocean model, the processes at the sea surface are then considered as internal processes and are described by the coupling condition, equation (2.31e).

For a global domain, i.e. the full Earth, there are no horizontal BC, since the Earth is assumed to be a sphere. If only a regional domain is of interest, e.g. Europe, Germany, the Baltic Sea, Rostock or Halle(Saale) etc., additional horizontal (lateral) boundary conditions must be provided. For regional models, lateral BCs are usually given through a set of reanalysis data or results from global model simulations. They include the specific contents of the fluid, barycentric velocity and temperature.

Henceforth, all horizontal and vertical BCs for equation (2.31) are usually either Dirichlet ( $f_D$ ) BCs, i.e.

$$\rho(\mathbf{x}, t) \psi(\mathbf{x}, t) = f_D^\psi(\mathbf{x}, t), \quad \forall \mathbf{x} \in \partial V, \quad (2.37a)$$



or Neumann ( $f_N$ ) BCs, here formulated as flux conditions, i.e.

$$\left( \rho(\mathbf{x}, t) \boldsymbol{\psi}(\mathbf{x}, t) \cdot \mathbf{v}(\mathbf{x}, t)^T + \sum_{\kappa \in \mathcal{M}} [\psi_{\kappa} \mathbf{J}_{\kappa}^T + \lambda_{\psi, \kappa}] \right) \cdot \mathbf{n}(\mathbf{x}) = f_N^{\psi}(\mathbf{x}, t), \quad \forall \mathbf{x} \in \partial V. \quad (2.37b)$$

### 2.3.2 Spatial discretisation in geophysical fluid modelling

Appropriate numerical techniques are required to fully conduct a simulation of a geophysical fluid. Examples of numerical approaches are finite differences, finite volumes and spectral element, see e.g. Ullrich et al. (2017) for atmosphere models. For ocean models, Klingbeil et al. (2018) described a commonly used spatial discretisation.

Spatial discretisation in geophysical fluid modelling is split into horizontal and vertical discretisation. Basic ideas and concepts of spatial discretisation are explained in Lauritzen et al. (2011). The horizontal discretisation is represented by a finite number of elements in a model. These elements can be of any shape such as triangles, quadrilaterals, pentagons, hexagons etc., see e.g. Ullrich et al. (2017) for an overview of horizontal discretisation and model grids for the dynamical core model inter-comparison project (DCMIP) 2016.

Each of the prognostic variables from Table 2.1 are then assumed to reside on the corner, edge midpoint or cell midpoint of an element, i.e. the staggering of the variables. Similar choices are also made for the vertical discretisation.

The spatial discretisation highly depends on the staggering of the prognostic variables. Various choices on where a variable lives has been thoroughly investigated as early as in the 1970's. The most common ones are called Arakawa-grids after the first author of Arakawa and Lamb (1977). For the purpose of this thesis, there are two important aspects, horizontal and vertical staggering which are shortly introduced in Section 2.3.2.1. Additionally, some aspects of the vertical discretisation regarding the surface height of the spatial domain are introduced in Section 2.3.2.2.

#### 2.3.2.1 Horizontal and vertical staggering

The usage of an Arakawa-grid describes only the horizontal staggering of the prognostic variables. The most prominent vertical staggering are described by the Lorenz- or Charney-Phillips grids, see e.g. Lauritzen et al. (2011). Both grids separate the position of the vertical component of velocity from the horizontal components. The position of the pressure and temperature variable are different in the grids. Figure 2.2 shows the Arakawa C-grid and Lorenz grid staggering of the prognostic variables for a 1D, 2D and 3D model in a Cartesian coordinate system.

#### 2.3.2.2 Terrain following coordinates vs. cut cells

The vertical staggering is influenced by the two basic vertical discretisation techniques, terrain following coordinates or cut cells. To explain the differences between them, a simple example with a mountain on a flat plane is used, see Figure 2.3.

Terrain following coordinates are a discretisation technique where the vertical layers are following the orography, i.e. the first one is exactly at the surface. Lauritzen et al. (2011, Figure 4.1) shows

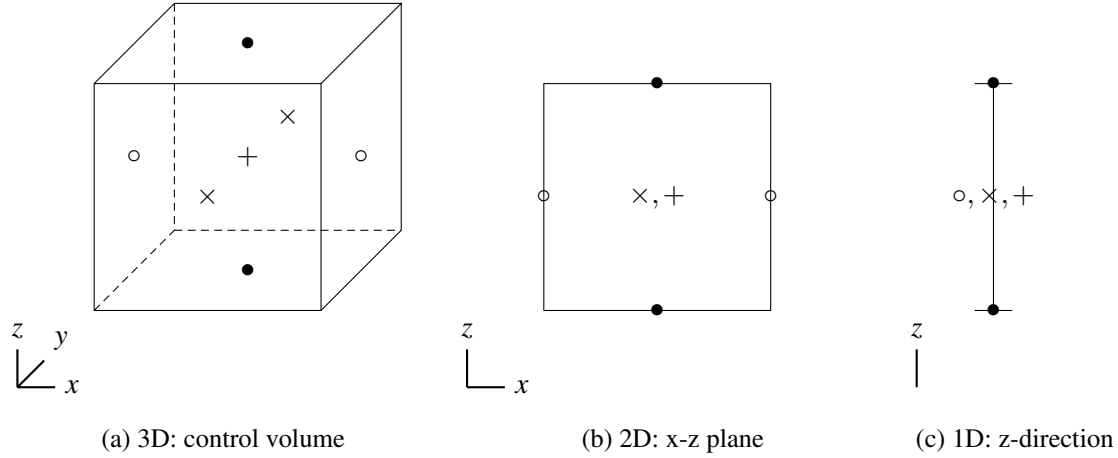


Figure 2.2: Horizontal Arakawa C-grid and vertical Lorenz grid staggering in a Cartesian coordinate system for one, two and three dimensions. The  $\circ$ ,  $\times$  and  $\bullet$  are representing the position of the velocity components in x-, y- and z- direction, i.e.  $u$ ,  $v$  and  $w$ . The  $+$  represents other variables, e.g. density, pressure and temperature.

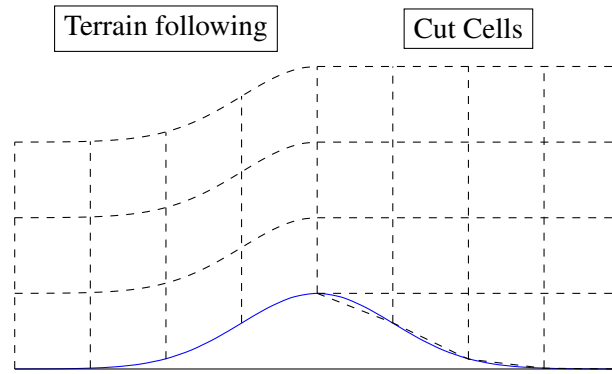


Figure 2.3: Schematic 2D representation of a mountain on a flat plane with the first layers of the vertical discretisation with terrain following coordinates (left side) and cut cells (right side).

two examples of terrain following discretisation. The cut cell technique on the other hand uses a fixed discretisation and cuts out the orography, i.e. smaller elements exist closer to surface. Jähn et al. (2015, Figure 1) shows possible cut cell intersections for a 3D discretisation. If no bathymetry or no topography is considered, then both techniques are equivalent. In Shaw and Weller (2016), a comparison study between both techniques has been discussed.

### 2.3.3 Time integration in geophysical fluid modelling

Given a spatial discretisation including the boundary conditions, ordinary differential equations are formulated for the IBVP from equation (2.31). The set of equations is generally expressed as

$$\frac{\partial(\rho\psi)}{\partial t} = f^\psi(\rho\psi) \quad \text{and} \quad \rho(\mathbf{x}, 0) = \rho_0 \quad \text{and} \quad \psi(\mathbf{x}, 0) = \psi_0, \quad \forall \mathbf{x} \in \partial V. \quad (2.38)$$

These equations are solved with numerical time integration schemes. Examples of such methods are the Crank–Nicholson method, Leapfrog method, Adams–Bashforth method etc., see e.g. Lauritzen et al. (2011). Other methods like Predictor–Corrector schemes are also used, see e.g. Zängl et al. (2015). The applied methods are required to be as efficient as possible to minimise computing resources. Many approaches include a splitting of the right hand side of equation (2.38), see e.g. Skamarock and Klemp (1992) for elastic equations, Klemp et al. (2007) for compressible equations, Zängl et al. (2015) for ICON and Klingbeil et al. (2018) for ocean models.

Many of these ideas have in common that an efficient usage of computing resources is achieved by partitioning the original problem. The overall time integration process is characterised by the convergence and stability behaviour of the utilised methods specifically applied to each part of the problem. The multirate approach is an extension, because in addition to partitioning the system of equations and applying different methods, different time steps are also utilised for each part.

For coupled atmosphere-ocean models, the resulting ordinary differential equations after applying a spatial discretisation to the coupled IBVP can be formulated as a split problem, i.e.

$$\dot{y}^A = \frac{\partial y^A}{\partial t} = f^A(y^A, y^O), \quad y^A(0) = y_0^A \quad (2.39a)$$

$$\dot{y}^O = \frac{\partial y^O}{\partial t} = f^O(y^A, y^O), \quad y^O(0) = y_0^O. \quad (2.39b)$$

The structure of equation (2.39) is described as component-wise partitioning in Bartel and Günther (2020). Note that throughout this thesis, only autonomous ordinary differential equations are considered.

A general formulation for coupled atmosphere-ocean problems in the form of additive split problems is given by

$$\dot{y} = f^{\{s\}}(y) + f^{\{f\}}(y), \quad y(0) = y_0 \quad \text{or} \quad (2.40a)$$

$$\dot{y} = f^{\{s\}}(y) + f^{\{f\}}(y) + f^{\{ff\}}(y), \quad y(0) = y_0 \quad (2.40b)$$

where the superscripts  $\{s\}$ ,  $\{f\}$  and  $\{ff\}$  are representing the slowest component, a fast component and a super fast component, respectively. The curly brackets indicate that the components are integrated on different time scales. If the coupling is assumed to have the same time scale as the slow component, it can be included in the formulation of the slow component, i.e.  $f^{\{s\}}(y)$  in equation (2.40a). This is referred as synchronous coupling since the coupling is synchronised with the slow component. Asynchronous coupling is given if the coupling has a slower time scale than the other parts. Thus, the coupling is separated from the fast and super fast component, i.e. equation (2.40b). For asynchronous coupling of coupled atmosphere-ocean models, the different time scales are given from slow to super fast by the coupling, ocean and atmosphere part, respectively. Although synchronous coupling represents the natural exchange across the interface more accurately, asynchronous coupling is applied in coupled atmosphere-ocean models, because of the minimised coupling at given time points. For example, coupled models apply the coupling at predefined time points usually every hour, three hours or even six hours, see e.g. Döscher et al. (2002), Van Pham et al. (2014), Wang et al. (2015), and Katsafados et al. (2016). A synchronous

coupling was aimed for the coupling in ICONGETM. However, the considered time step for ICON was no common multiplier of the time step from GETM. Hence, the least common multiple was utilised as coupling time step, i.e. the coupling was as often as possible, cf. Bauer et al. (2021).

Asynchronous coupling by time windows and synchronous coupling at time step level is discussed in Marchesiello et al. (2014). Lemarié et al. (2015) presented a stability analysis for the coupling conditions at the air-sea interface for synchronous coupling.

Approaches for coupling atmosphere and ocean models usually focus on simple coupling conditions, i.e. to minimise the access to the variables between the models, see Chapter 5 for more details. With multirate approaches, the time integration can be based on the set of equations of all models and the coupling is then applied during the time integration.

## Chapter 3

# Multirate time integration methods for solving IVPs

In general, initial value problems (IVP) can be integrated with one-step methods, e.g. Runge–Kutta methods (RK), Section 3.1. However, the different time scales shall be considered for coupled problems. Multirate time integration methods use different time steps for different components of the ordinary differential equations (ODE). They have been developed and investigated since the 1980s, see e.g. Gear and Wells (1984), Günther et al. (2001), and Connors and Sockwell (2022). For this thesis, the focus is on RK like multirate methods.

The methods discussed in this thesis are based on additive split ODE with  $N$  different time scales

$$\dot{y} = f(y) = \sum_{\kappa=1}^N \left[ f^{\{\kappa\}}(y) \right]. \quad (3.1)$$

The different temporal scaled components are marked with curly brackets.

Examples for additive split problems in geophysical fluid dynamics with multi temporal scales are advection-diffusion-reaction problems, see e.g. Knoth and Wolke (1998) and Schlegel et al. (2012), convection-diffusion-reaction problems, see Kennedy and Carpenter (2003), or coupled systems such as atmosphere-ocean models, but also stiff and non-stiff problems. Examples in atmosphere and ocean models are found with different waves, e.g. gravity waves are slower than sound waves, see e.g. Dutton (1986) and Etling (2008).

This chapter presents two classes of multirate methods, Section 3.2. The first class, multirate generalized additive Runge–Kutta methods (MGARK), is derived from a generalisation of RK methods for additive split problems applying individual time steps for each component, see Günther and Sandu (2016). The second class of multirate methods, multirate infinitesimal step methods (MIS), have been developed for problems related to the solution of Euler equations where sound waves propagate faster than additive processes, see e.g. Wensch et al. (2009) and Knoth and Wensch (2014). Additionally, the interrelations between different multirate methods are described, Section 3.3.

### 3.1 One-step methods for initial value problems

This section gives an overview about integration methods with one time step, which are used throughout this thesis. The well known class of Runge–Kutta methods is shortly introduced, Section 3.1.1. The generalized additive Runge–Kutta methods (GARK) are presented for additive split problems, Section 3.1.2, and used as the basis for the multirate generalized additive Runge–Kutta method methods in Section 3.2.1.

#### 3.1.1 Runge–Kutta methods (RK)

The time integration of an IVP can be performed with any method. Given some initial conditions, the ordinary differential equations are then written as an initial value problem (IVP), i.e.

$$\dot{y} = f(y), \quad y(t_0) = y_0. \quad (3.2)$$

A general introduction to one-step methods is given in Strehmel et al. (2012) or in other books such as Hairer et al. (1993) and Butcher (2008). A prominent example is the well known class of Runge–Kutta methods (RK).

This section introduces the RK methods with all necessary formulations for this thesis. The details are taken from Strehmel et al. (2012).

##### Definition 3.1.1: (Runge–Kutta methods (RK))

For any autonomous IVP, a RK method reads with time step  $h$

$$Y_i = y_n + h \sum_{j=1}^s [a_{ij} f(Y_j)], \quad i = 1, \dots, s \quad (3.3a)$$

$$y_{n+1} = y_n + h \sum_{i=1}^s [b_i f(Y_i)], \quad (3.3b)$$

where  $y_n$  is the numerical approximation of  $y(t_n)$ ,  $s$  the number of stages,  $\mathbf{A} = (a_{ij})$  the method coefficient matrix and  $\mathbf{b} = (b_i)$  the weight vector.

Each stage  $Y_i$  is defined at time point  $t_n + c_i h$  with time step  $h = t_{n+1} - t_n$ .  $y_{n+1}$  is given by the previous value  $y_n$  plus the linear combination or weighted average of the increments. They are defined as the product of the time step  $h$  and the slopes specified by the problem function  $f$ .

The Butcher tableau  $\begin{array}{c|c} \mathbf{c} & \mathbf{A} \\ \hline & \mathbf{b}^T \end{array}$  is used to describe a specific RK method.  $\mathbf{c}$  is the node vector and is defined throughout this thesis as the summation of the elements in each row of  $\mathbf{A}$ , i.e.

$$c_i = \sum_{j=1}^s [a_{ij}]. \quad (3.4)$$

Definition 3.1.1 is given for general RK methods, i.e. explicit and implicit RK methods. Explicit Runge–Kutta methods (eRK) use the current state to predict the next state of a system. For eRK methods, the summation in equation (3.3a) considers only already calculated stages, i.e.  $a_{ij} = 0$  for  $j \geq i$ . However, these methods have restrictions on the utilised integration step size depending

on the stiffness of the problem equation, see e.g. Hairer and Wanner (1996) and Strehmel et al. (2012). Then implicit Runge–Kutta methods (iRK) are used, which consider both, the current and next state, to find the solution of the problem. In the following sections, especially in Section 3.2, the focus is on explicit Runge–Kutta methods (eRK), since they are used for larger model simulations, e.g. in atmosphere and ocean models.

Figure 3.1 shows an example of the integration process with a three-staged eRK method.

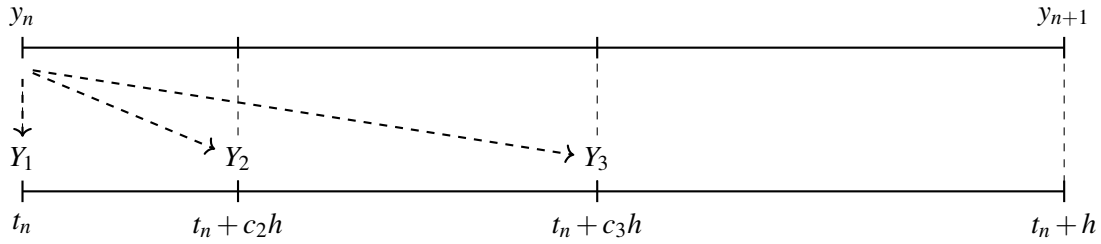


Figure 3.1: Graphical representation of the integration process from  $t_n$  to  $t_{n+1}$  using a three-stage eRK method. The stage values  $Y_i$  are calculated in chronological order. The final  $y_{n+1}$  is then given by a linear combination of the increments of each stage.

### 3.1.2 Generalized additive Runge–Kutta methods (GARK)

A general autonomous additive split initial value problem can be described through

$$\dot{y} = \sum_{\kappa=1}^N [f^{\kappa}(y)], \quad y(0) = y_0. \quad (3.5)$$

Note that in comparison to equation (3.1), the different temporal scales are not considered.

Jackiewicz and Vermiglio (2000) and Kennedy and Carpenter (2003) discussed partitioned and additive Runge–Kutta methods, (PRK) or (ARK), respectively. For these methods, different method coefficients and weight vectors are used for each component of the right hand side of equation (3.5). The class of generalized additive Runge–Kutta methods (GARK) has been introduced as a generalisation to ARK methods, cf. Sandu and Günther (2015), where, additionally, different stage values are allowed for each component of the right-hand side.

**Remark:** The GARK methods are introduced for two reasons. First to derive the first class of multirate methods in the following section and, secondly, for the later performed analysis of the convergence and stability behaviour of the multirate methods.

The general definition for the GARK methods is given in Sandu and Günther (2015, Definition 2.1). However, the focus for this thesis is only on the special case with one stage vector for each component, which is given in Sandu and Günther (2015, Definition 2.2).

#### Definition 3.1.2: (Generalized additive Runge–Kutta methods (GARK))

For any autonomous IVP, a GARK method reads with time step  $h$

$$Y_i^{\kappa} = y_n + h \sum_{\sigma=1}^N \sum_{j=1}^{s^{\sigma}} [a_{ij}^{\kappa\sigma} f^{\sigma}(Y_j^{\sigma})], \quad i = 1, \dots, s^{\kappa}, \quad \kappa = 1, \dots, N \quad (3.6a)$$

$$y_{n+1} = y_n + h \sum_{\kappa=1}^N \sum_{i=1}^{s^\kappa} [b_i^\kappa f^\kappa(Y_i^\kappa)] \quad (3.6b)$$

with  $N \in \mathbb{N}$  additive components, method coefficient matrices  $\mathbf{A}^{\kappa\sigma} = (a_{ij}^{\kappa\sigma})$  and weight vectors  $\mathbf{b}^\kappa = (b_i^\kappa)$  as well as number of stages  $s^\kappa$  for each component  $\kappa$ . The stages  $Y_i^\kappa$  are defined at time points  $t_n + c_i^{\kappa\sigma}h$ , where  $c_i^{\kappa\sigma} = \sum_{j=1}^{s^\sigma} [a_{ij}^{\kappa\sigma}]$ .

If  $\kappa = \sigma$ , then  $\mathbf{A}^{\kappa\sigma}$  is the coefficient matrix for the applied RK method for component  $\kappa$ , in short notation given by  $\mathbf{A}^\kappa$ . Otherwise,  $\mathbf{A}^{\kappa\sigma}$  contains the method coefficients for the numerical coupling mechanism between components  $\kappa$  and  $\sigma$ , see Sandu and Günther (2015). Additionally, internal consistency is defined to ensure all components of the stage value  $Y_i^\kappa$  are calculated at the same internal approximation times, Sandu and Günther (2015).

**Definition 3.1.3: (Internal consistency for GARK methods)**

Any GARK method is said to be internally consistent, if

$$\mathbf{A}^{\kappa,1} \mathbb{1}_{s^1} = \mathbf{A}^{\kappa,2} \mathbb{1}_{s^2} = \dots = \mathbf{A}^{\kappa,N} \mathbb{1}_{s^N} = \mathbf{c}^\kappa, \quad \kappa = 1, 2, \dots, N \quad (3.7)$$

with  $\mathbb{1}_{s^\sigma}$  being a vector of ones of dimension  $s^\sigma$  for  $\sigma = 1, 2, \dots, N$  and node vectors  $\mathbf{c}^\kappa = (c_i^\kappa)$ .

The stages  $Y_i^\kappa$  are then defined at time points  $t_n + c_i^\kappa h$ . The Butcher tableau for an internal consistent GARK methods given by Definition 3.1.2 is stated as follows

$$\begin{array}{c|ccc} \mathbf{c}^1 & \mathbf{A}^{11} & \dots & \mathbf{A}^{1N} \\ \vdots & \vdots & \ddots & \vdots \\ \mathbf{c}^N & \mathbf{A}^{N1} & \dots & \mathbf{A}^{NN} \\ \hline & \mathbf{b}^{1T} & \dots & \mathbf{b}^{NT} \end{array}.$$

Similar as for RK methods, Figure 3.2 shows graphically the integration process for a GARK method for two components, where each of them is integrated with an eRK. There are no restriction on the choice of the method for each component, i.e. the time points for the stages were arbitrarily chosen for Figure 3.2.

Moreover, the focus is on the coupling mechanism between the components, i.e. how the method coefficients  $\mathbf{A}^{\kappa\sigma}$  are chosen. It is assumed that the numerical coupling is of explicit manner, which is required for an explicit method. Otherwise, the method is regarded as implicit. Explicit coupling is guaranteed if  $a_{ij}^{\kappa\sigma} = 0$  for  $c_i^\kappa \leq c_j^\sigma$  for  $\kappa < \sigma$  and if  $a_{ij}^{\kappa\sigma} = 0$  for  $c_i^\kappa < c_j^\sigma$  for  $\kappa > \sigma$ . The method coefficient for the numerical coupling for the very specific example from Figure 3.2 are then given by

$$\mathbf{A}^{12} = \begin{pmatrix} 0 & 0 & 0 \\ \times & 0 & 0 \\ \times & \times & 0 \end{pmatrix} \quad \text{and} \quad \mathbf{A}^{21} = \begin{pmatrix} \times & 0 & 0 \\ \times & \times & 0 \\ \times & \times & \times \end{pmatrix}, \quad (3.8)$$

where the coloured  $\times$  indicates pre-defined coupling values.

Examples of GARK methods are given in Sandu and Günther (2015).



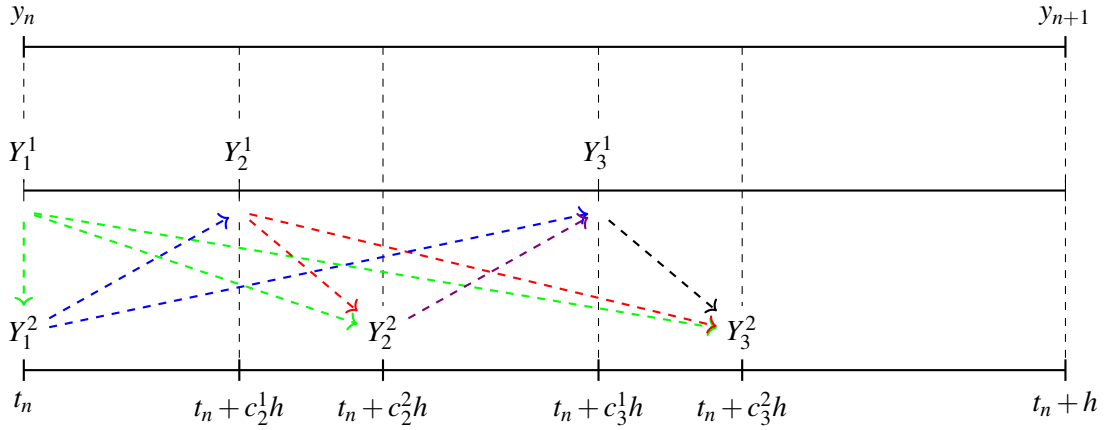


Figure 3.2: Graphical representation of the coupling between the two components of a GARK method in an explicit manner. The coupling is colour coded with green, blue, red, violet and black for the stages and indicate which stages contribute. The stage values  $Y_i^K$  are calculated in chronological order.

## 3.2 Multirate time integration methods

The GARK methods from Section 3.1.2 are formulated for additive split ODE. Since many applications consider different time scales for their components, the GARK framework shall now be formulated for a multirate approach. The class of multirate generalized additive Runge–Kutta methods (MGARK) is introduced in Section 3.2.1.

The multirate infinitesimal step methods (MIS) were investigated for applications with focus on the solution of the compressible Euler equation in the low Mach number regime in Wensch et al. (2009) and Knoth and Wensch (2014). This regime is typical for numerical weather prediction. The class of MIS methods is presented in Section 3.2.2.

### 3.2.1 Class of multirate generalized additive Runge–Kutta methods (MGARK)

A GARK like method for multiple time scaled components is introduced in the following. For problems with an additive splitting in two components, this has been introduced in Günther and Sandu (2016) and later applied to partitioned schemes for fluid-structure interaction, see Bremicker-Trübelhorn and Ortleb (2017).

Section 3.2.1.1 introduces the multirate generalized additive Runge–Kutta methods (MGARK) from Günther and Sandu (2016). A multirate method for multiple time scaled components, which provides more flexibility for coupled atmosphere-ocean models, is newly derived in Section 3.2.1.2.

#### 3.2.1.1 Multirate generalized additive Runge–Kutta methods (MGARK) for 2 components

The class of MGARK methods has been developed for applications with additive splitting in two temporal scaled components where the slow time step is divided into  $M \in \mathbb{N}$  fast time steps with

fractions  $m_k = \frac{h_k}{h}$  and  $\sum_{k=1}^M [h_k] = h$ .

**Definition 3.2.1: (Multirate generalized additive Runge–Kutta methods (MGARK))**

For any autonomous IVP, a MGARK method reads with time step  $h$

$$Y_i^{\{s\}} = y_n + h \sum_{j=1}^{s^{\{s\}}} \left[ a_{ij}^{\{s,s\}} f^{\{s\}} \left( Y_j^{\{s\}} \right) \right] + h \sum_{k=1}^M \sum_{j=1}^{s^{\{f\}}} \left[ m_k a_{ij}^{\{s,f,k\}} f^{\{f\}} \left( Y_j^{\{f,k\}} \right) \right],$$

$$i = 1, \dots, s^{\{s\}} \quad (3.9a)$$

$$Y_i^{\{f,k\}} = y_n + h \sum_{j=1}^{s^{\{s\}}} \left[ a_{ij}^{\{f,s,k\}} f^{\{s\}} \left( Y_j^{\{s\}} \right) \right] + h \sum_{l=1}^{k-1} \sum_{j=1}^{s^{\{f\}}} \left[ m_l b_j^{\{f\}} f^{\{f\}} \left( Y_j^{\{f,l\}} \right) \right]$$

$$+ h \sum_{j=1}^{s^{\{f\}}} \left[ m_k a_{ij}^{\{f,f\}} f^{\{f\}} \left( Y_j^{\{f,k\}} \right) \right], \quad i = 1, \dots, s^{\{f\}}, \quad k = 1, \dots, M \quad (3.9b)$$

$$y_{n+1} = y_n + h \sum_{i=1}^{s^{\{s\}}} \left[ b_i^{\{s\}} f^{\{s\}} \left( Y_i^{\{s\}} \right) \right] + h \sum_{k=1}^M \sum_{i=1}^{s^{\{f\}}} \left[ m_k b_i^{\{f\}} f^{\{f\}} \left( Y_i^{\{f,k\}} \right) \right], \quad (3.9c)$$

where  $\mathbf{A}^{\{s,s\}} = (a_{ij}^{\{s,s\}})$ ,  $\mathbf{b}^{\{s\}} = (b_i^{\{s\}})$  and  $\mathbf{A}^{\{f,f\}} = (a_{ij}^{\{f,f\}})$ ,  $\mathbf{b}^{\{f\}} = (b_i^{\{f\}})$  are the method coefficient matrices and weight vectors for the slow and fast component, respectively. Furthermore,  $\mathbf{A}^{\{f,s,k\}} = (a_{ij}^{\{f,s,k\}})$  and  $\mathbf{A}^{\{s,f,k\}} = (a_{ij}^{\{s,f,k\}})$  are the method coefficients for the numerical coupling mechanism for all fast parts with

$$\sum_{k=1}^M [m_k] = 1. \quad (3.10)$$

The time points of stages  $Y_i^{\{s\}}$  and  $Y_i^{\{f,k\}}$  are given by

$$t_n + c_i^{\{s\}} h \quad \text{and} \quad t_n + \left( \sum_{l=1}^{k-1} [m_l] + m_k c_i^{\{f\}} \right) h,$$

respectively, where  $c_i^{\{s\}} = \sum_{j=1}^{s^{\{s\}}} [a_{ij}^{\{s,s\}}]$  and  $c_i^{\{f\}} = \sum_{j=1}^{s^{\{f\}}} [a_{ij}^{\{f,f\}}]$ . Internal consistency is achieved if

$$\sum_{k=1}^M \left[ m_k \mathbf{A}^{\{s,f,k\}} \cdot \mathbb{1}_{s^{\{f\}}} \right] = \mathbf{c}^{\{s\}} \quad \text{and} \quad \mathbf{A}^{\{f,s,k\}} \cdot \mathbb{1}_{s^{\{s\}}} = \sum_{l=1}^{k-1} [m_l] + m_k \mathbf{c}^{\{f\}} \quad (3.11)$$

holds for all  $k = 1, \dots, M$ .

**Remark:** Günther and Sandu (2016) defined MGARK methods with fixed fast time steps, i.e.  $m_k = \frac{1}{M}$  for all  $k = 1, \dots, M$ . The method has been generalised in Bremicker-Trübelhorn and Ortleb (2017) by allowing different fast time steps as fractions of the slow time step.

The Butcher tableau reads

$$\begin{array}{c|ccc}
 \mathbf{A}^{\{s,s\}} & m_1 \mathbf{A}^{\{s,f,1\}} & m_2 \mathbf{A}^{\{s,f,2\}} & \dots & m_M \mathbf{A}^{\{s,f,M\}} \\
 \mathbf{A}^{\{f,s,1\}} & m_1 \mathbf{A}^{\{f,f\}} & & & \\
 \mathbf{A}^{\{f,s,2\}} & m_1 \mathbb{1}_{s\{f\}} \mathbf{b}^{\{f\}T} & m_2 \mathbf{A}^{\{f,f\}} & & \\
 \vdots & \vdots & \vdots & \ddots & \\
 \mathbf{A}^{\{f,s,M\}} & m_1 \mathbb{1}_{s\{f\}} \mathbf{b}^{\{f\}T} & m_2 \mathbb{1}_{s\{f\}} \mathbf{b}^{\{f\}T} & \dots & m_M \mathbf{A}^{\{f,f\}} \\
 \mathbf{b}^{\{s\}T} & m_1 \mathbf{b}^{\{f\}T} & m_2 \mathbf{b}^{\{f\}T} & \dots & m_M \mathbf{b}^{\{f\}T}
 \end{array} \tag{3.12}$$

with  $\mathbb{1}_{s\{f\}}$  being a vector of  $s^{\{f\}}$  ones, cf. Günther and Sandu (2016, Equation 7) and Bremicker-Trübelhorn and Ortleb (2017, Equation 15). Note that the order of the two components has been reversed in comparison with Günther and Sandu (2016) and Bremicker-Trübelhorn and Ortleb (2017).

Figure 3.3 shows an example of the positioning of the stage values for a MGARK method during a time integration step.

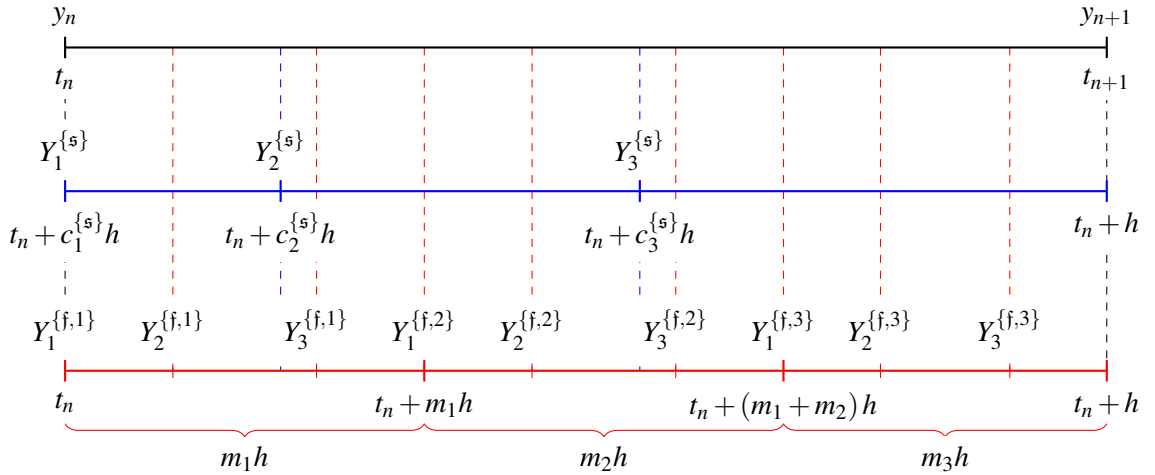


Figure 3.3: Graphical representation of the stage values and their position during the integration of one time step when using a MGARK method. The blue coloured line represents the slow component, while the red coloured the fast component. The fast component is integrated three times in one integration time step of the slow component. The coupling between the two components is not shown. However, for explicit coupling a chronological calculation of the stage values is required. An explicit coupling is graphically represented in Figure 3.2.

Exemplarily, each component is integrated with a three-stage eRK method. The methods do not have to be identical. A coupling scheme is for simplifications not drawn in Figure 3.3. However, an explicit coupling scheme can easily be adapted from Figure 3.2. The matrices for an explicit

coupling for a method like the one presented in Figure 3.3 are then given by

$$\begin{aligned} \mathbf{A}^{\{s,f,1\}} &= \begin{pmatrix} 0 & 0 & 0 \\ \times & \times & 0 \\ \times & \times & \times \end{pmatrix}, \quad \mathbf{A}^{\{s,f,2\}} = \begin{pmatrix} 0 & 0 & 0 \\ 0 & 0 & 0 \\ \times & \times & 0 \end{pmatrix}, \quad \mathbf{A}^{\{s,f,3\}} = \begin{pmatrix} 0 & 0 & 0 \\ 0 & 0 & 0 \\ 0 & 0 & 0 \end{pmatrix}, \\ \mathbf{A}^{\{f,s,1\}} &= \begin{pmatrix} \times & 0 & 0 \\ \times & 0 & 0 \\ \times & \times & 0 \end{pmatrix}, \quad \mathbf{A}^{\{f,s,2\}} = \begin{pmatrix} \times & \times & 0 \\ \times & \times & 0 \\ \times & \times & \times \end{pmatrix}, \quad \mathbf{A}^{\{f,s,3\}} = \begin{pmatrix} \times & \times & \times \\ \times & \times & \times \\ \times & \times & \times \end{pmatrix}. \end{aligned}$$

The  $\times$  represents a coupling value. Each row of  $\mathbf{A}^{\{s,f,k\}}$  shows the coupling from the slow stage values to the fast stage values of fast time interval  $k$  and  $\mathbf{A}^{\{f,s,k\}}$  shows the coupling vice versa. MGARK methods are considered to be explicit if  $a_{ij}^{\{s\}} = 0$  for  $j \geq i$  and if  $a_{ij}^{\{f\}} = 0$  for  $j \geq i$ . Explicit coupling is guaranteed if

$$\begin{aligned} a_{ij}^{\{s,f,k\}} &= 0 \quad \text{for} \quad c_i^{\{s\}} \leq \sum_{l=1}^{k-1} [m_l] + m_k c_j^{\{f\}}, \quad \text{and if} \\ a_{ij}^{\{f,s,k\}} &= 0 \quad \text{for} \quad \sum_{l=1}^{k-1} [m_l] + m_k c_i^{\{f\}} < c_j^{\{s\}} \end{aligned}$$

for all  $k = 1, \dots, M$ .

### 3.2.1.2 Multirate generalized additive Runge–Kutta methods for $N$ components (MNGARK)

The general idea of MGARK methods has been applied to additive split problems with only two components. The motivation for the GARK methods was the derivation of a more general approach for ARK methods, cf. Sandu and Günther (2015). Many applications in geophysical fluid dynamics are utilised with two or more different temporal scaled components. A prominent example is the later introduced ICOSahedral Non-hydrostatic modeling framework (ICON). Another example would be a coupled system with more than two components, e.g. atmosphere-ocean-wave-sea-ice model. This raises the question of a formulation of the class of GARK methods allowing individual time steps for each component. Therefore, the following definition gives the details of the multirate generalized additive Runge–Kutta methods for  $N$  components (MNGARK), i.e. for IVPs with multiple different time scales, see equation (3.1).

For simplifications, it is assumed that the  $N$  components are sorted according to their time scales with the slowest being the first and fastest the  $N^{\text{th}}$  component. Furthermore, the desired (micro) time step for each component is given by

$$\sum_{k=1}^{M^{\{\kappa\}}} [h_k^{\{\kappa\}}] = \sum_{k=1}^{M^{\{\kappa\}}} [m_k^{\{\kappa\}} h] = h \quad \text{or} \quad \sum_{k=1}^{M^{\{\kappa\}}} [m_k^{\{\kappa\}}] = 1 \quad \text{for all} \quad \kappa = 1, 2, \dots, N,$$

where  $M^{\{\kappa\}} \in \mathbb{N}$  is the number of time steps to integrate component  $\kappa$  from  $t_n$  to  $t_n + h$  with time step  $h^{\{\kappa\}}$ .  $M^{\{1\}} = 1$ , since component 1 is assumed to be the slowest component, i.e.  $h^{\{1\}} = h$  and  $M^{\{\kappa+1\}} \geq M^{\{\kappa\}}$ .

**Remark:** A telescopic application of the MGARK method as mentioned in Günther and Sandu (2016, Example 2) is not suitable. It is not guaranteed that each component can be integrated with the same RK method. Furthermore, this would require also that the time scales are given in the same ratio, i.e.  $M^{\{\kappa+1\}} = M^{\{\kappa\}}^2$  for all  $\kappa = 2, \dots, N$  and  $M^{\{2\}} > M^{\{1\}}$ . Henceforth, the telescopic approach is then a special case of this method.

**Definition 3.2.2: (Multirate generalized additive Runge–Kutta methods for  $N$  components (MNGARK))**

For any autonomous IVP, a MNGARK method reads with time step  $h$

$$Y_i^{\{\kappa,k\}} = y_n + h \sum_{\sigma=1}^N \sum_{l=1}^{M^{\{\sigma\}}} \sum_{j=1}^{s^{\{\sigma\}}} \left[ \bar{a}_{ij}^{\{\kappa,\sigma,k,l\}} f^{\{\sigma\}} \left( Y_j^{\{\sigma,l\}} \right) \right] \\ i = 1, \dots, s^{\kappa}, \quad k = 1, \dots, M^{\kappa}, \quad \kappa = 1, \dots, N \quad (3.13a)$$

$$y_{n+1} = y_n + h \sum_{\kappa=1}^N \sum_{k=1}^{M^{\{\kappa\}}} \sum_{i=1}^{s^{\{\kappa\}}} \left[ \bar{b}_i^{\{\kappa,k\}} f^{\{\kappa\}} \left( Y_i^{\{\kappa,k\}} \right) \right] \quad (3.13b)$$

with method coefficient matrices  $\bar{\mathbf{A}}^{\{\kappa,\sigma,k,l\}} = \left( \bar{a}_{ij}^{\{\kappa,\sigma,k,l\}} \right)$  and weight vectors  $\bar{\mathbf{b}}^{\{\kappa,k\}} = \left( \bar{b}_i^{\{\kappa,k\}} \right)$  as well as number of stages  $s^{\{\kappa\}}$  of component  $\kappa$ . For simplifying the writing, a bar has been introduced to differ between the generalised method coefficient matrices and the actually applied coefficients for the components, discussed below, and does not represent a mean value.

The method coefficient matrices and weight vectors are defined by

$$\bar{\mathbf{A}}^{\{\kappa,\sigma,k,l\}} = m_l^{\{\sigma\}} \begin{cases} \mathbf{A}^{\{\kappa\}} & , \kappa = \sigma, \quad k = l \\ \mathbb{1}^{\{\kappa\}} \mathbf{b}^{\{\kappa\}T} & , \kappa = \sigma, \quad k > l \\ \mathbf{0} & , \kappa = \sigma, \quad k < l \\ \mathbf{A}^{\{\kappa,\sigma,k,l\}} & , \kappa \neq \sigma \end{cases} \quad (3.14a)$$

$$\bar{\mathbf{b}}^{\{\kappa,k\}} = m_k^{\{\kappa\}} \mathbf{b}^{\{\kappa\}} \quad (3.14b)$$

with coefficient matrix  $\mathbf{A}^{\{\kappa\}}$  and weight vector  $\mathbf{b}^{\{\kappa\}}$  of applied RK method of component  $\kappa$  and coefficient matrix  $\mathbf{A}^{\{\kappa,\sigma,k,l\}}$  for the coupling from component  $\kappa$  to  $\sigma$ .

The stage values  $Y_i^{\{\kappa,k\}}$  are defined at time points

$$t_n + \left( \sum_{l=1}^{k-1} \left[ m_l^{\{\kappa\}} \right] + m_k^{\{\kappa\}} c_i^{\{\kappa\}} \right) h,$$

where  $c_i^{\{\kappa\}} = \sum_{j=1}^{s^{\{\kappa\}}} \left[ a_{ij}^{\{\kappa,\kappa\}} \right]$  is defined according to equation (3.4).

In order to find the corresponding formulation for Definition 3.2.2, Definition 3.2.1 was reformulated in such a way that the stage values can be expressed with a general equation. This required a more general structure for method coefficient matrices  $\bar{\mathbf{A}}^{\{\kappa,\sigma,k,l\}}$ .

A suitable RK method can be chosen for each component  $\kappa$ . To avoid even more different indices in the method formulation, it is assumed that for each micro time step of the integration of

component  $\kappa$  the same method is applied. Hence, there is no need to integrate each part of each component with the same RK method.

The method can be understood in the sense that every component is integrated and coupled to other components. Furthermore, with the different time scales is each component  $\kappa$   $M^{\{\kappa\}}$  times partly integrated from  $t_n$  till  $t_{n+1}$ . Hence, the interval  $[t_n, t_{n+1}]$  is divided into  $M^{\{\kappa\}}$  parts for each component  $\kappa$ .

Internal consistency has been defined for GARK methods. A similar definition can also be given for MNGARK methods.

**Definition 3.2.3: (Internal consistency for MNGARK methods)**

Any MNGARK method is said to be internally consistent, if

$$\sum_{l=1}^{M^{\{\sigma\}}} \left[ \bar{\mathbf{A}}^{\{\kappa, \sigma, k, l\}} \mathbb{1}_{s^{\{\sigma\}}} \right] = \sum_{l=1}^{k-1} \left[ m_l^{\{\kappa\}} \right] + m_k^{\{\kappa\}} \mathbf{c}^{\{\kappa\}} = \bar{\mathbf{c}}^{\{\kappa, k\}} \quad (3.15)$$

holds for all  $\sigma = 1, 2, \dots, N$  and for each part  $k = 1, 2, \dots, M^{\{\kappa\}}$  of component  $\kappa$  with  $\mathbb{1}^{\{\sigma\}}$  being a vector of ones of dimension  $s^{\{\sigma\}}$  and node vectors  $\bar{\mathbf{c}}^{\{\kappa, k\}}$ .

The structure of an internally consistent MNGARK method for three components, i.e.  $N = 3$  with  $M^{\{1\}} = 1$ ,  $M^{\{2\}} = 3$  and  $M^{\{3\}} = 6$ , is shown as an example in Figure 3.4 and the corresponding Butcher tableau with 54 coupling matrices reads

$$\begin{array}{c|c|c} \mathbf{A}^{\{1\}} & m_l^{\{2\}} \mathbf{A}^{\{1,2,1,l\}} & m_l^{\{3\}} \mathbf{A}^{\{1,3,1,l\}} \\ \hline \mathbf{A}^{\{2,1,k,1\}} & \bar{\mathbf{A}}^{\{2,2,k,l\}} & m_l^{\{3\}} \mathbf{A}^{\{2,3,k,l\}} \\ \hline \mathbf{A}^{\{3,1,k,1\}} & m_l^{\{2\}} \mathbf{A}^{\{3,2,k,l\}} & \bar{\mathbf{A}}^{\{3,3,k,l\}} \\ \hline \mathbf{b}^{\{1\}T} & m_l^{\{2\}} \mathbf{b}^{\{2\}T} & m_l^{\{3\}} \mathbf{b}^{\{3\}T} \\ \hline l = 1, 2, 3 & l = 1, 2, \dots, 6 & \end{array} \quad \begin{array}{l} k = 1, 2, 3 \\ k = 1, 2, \dots, 6 \end{array} \quad (3.16)$$

The different coloured arrows in Figure 3.4 are indicating the coupling from and to a part of a component. However, for visibility reasons not every possible coupling is presented.

Of special interest are explicit methods, i.e. only already calculated stage values are coupled to and from parts of each component. Hence,  $a_{ij}^{\{\kappa\}} = 0$  if  $j \geq i$  for all  $\kappa = \sigma = 1, \dots, N$ . Additionally, explicit coupling is guaranteed if

$$\begin{aligned} a_{ij}^{\{\kappa, \sigma, k, l\}} &= 0 \quad \text{for} \quad \sum_{o=1}^{k-1} \left[ m_o^{\{\kappa\}} \right] + m_k^{\{\kappa\}} c_i^{\{\kappa\}} \leq \sum_{o=1}^{l-1} \left[ m_o^{\{\sigma\}} \right] + m_l^{\{\sigma\}} c_j^{\{\sigma\}}, \quad \kappa < \sigma \\ a_{ij}^{\{\kappa, \sigma, k, l\}} &= 0 \quad \text{for} \quad \sum_{o=1}^{l-1} \left[ m_o^{\{\sigma\}} \right] + m_l^{\{\sigma\}} c_j^{\{\sigma\}} < \sum_{o=1}^{k-1} \left[ m_o^{\{\kappa\}} \right] + m_k^{\{\kappa\}} c_i^{\{\kappa\}}, \quad \kappa > \sigma \end{aligned}$$

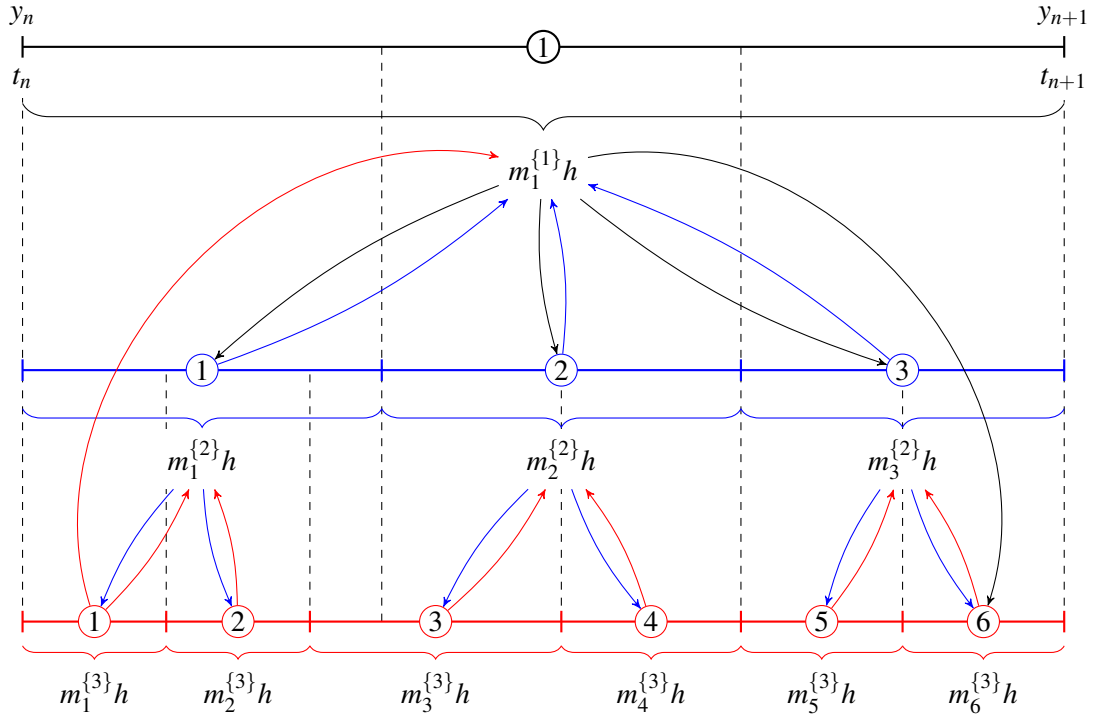


Figure 3.4: Schematic representation of the coupling and time stepping in an MNGARK method with three components, e.g. asynchronous coupling in atmosphere-ocean models. The time step of the **fast** component is divided into three parts according to the time step of the slow component. The time step of the **super fast** component is split into 6 parts. The time steps for each part are shown with curly brackets and described by  $m_k^{\{\kappa\}}h$  and  $h$ .

for all  $\kappa, \sigma = 1, \dots, N$ .

Figure 3.5 shows an example of the stages of an MNGARK in which each part per component is integrated using an eRK method. An explicit coupling would then be given for this specific method by the 54 coupling matrices. The structure of matrices are similar to those from the previous section. Note that if explicit coupling is utilised and internal consistency is assumed, the number of coefficients from these 54 matrices are reducing about 50 %.

There are some properties for MNGARK methods, which are helpful to characterise the range of applications and especially the generality of the method.

**Lemma 3.2.1.** *If  $N \equiv 1$ , then the standard RK method is gained.*

**Lemma 3.2.2.** *If  $N \equiv 2$ , then Definition 3.2.1 is obtained, i.e. the MGARK method published in Günther and Sandu (2016) and Bremicker-Trübelhorn and Ortleb (2017).*

**Lemma 3.2.3.** *If  $M^{\{\kappa\}} \equiv 1$  for all  $\kappa = 1, 2, \dots, N$ , then the standard GARK method with identical time scales for each component is directly given.*

**Lemma 3.2.4.** *If  $M^{\{\kappa\}} = M^{\{2\}^{\kappa-1}}$  for all  $\kappa = 1, 2, \dots, N$  and all  $\mathbf{A}^{\{\kappa\}}$  are identical, then the method fits into the telescopic approach suggested in Günther and Sandu (2016).*

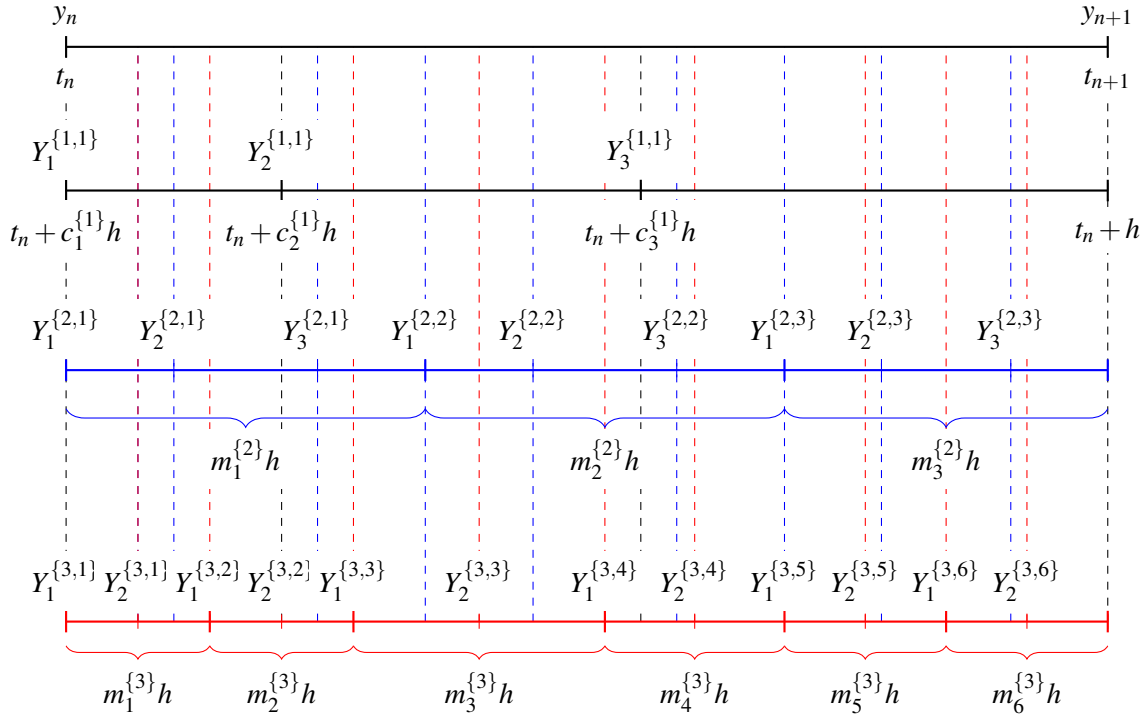


Figure 3.5: Schematic representation of the stage values and time stepping in an MNGARK method with three components. The stage values of each part per component are placed at the corresponding time point. Each part of the slow and fast components is assumed to be integrated with an eRK method with three stages. On the other hand, each part of the super fast component is integrated with an eRK with two stages. The time steps for each part are shown with curly brackets and described by  $m_k^{\{\kappa\}}h$ .

Each lemma can easily be proven by applying the assumption of each theorem to Definition 3.2.2.

### 3.2.2 Class of multirate infinitesimal step methods (MIS)

Multirate infinitesimal step methods (MIS) have been introduced in Wensch et al. (2009) and Knoth and Wensch (2014). These methods are a generalisation of methods introduced in Knoth and Wolke (1998). The idea is to split the ODE additively in two components, i.e.

$$\dot{y} = f^{\{\mathfrak{s}\}}(y) + f^{\{\mathfrak{f}\}}(y), \quad (3.17)$$

where it is assumed that for

$$\dot{y} = c + f^{\{\mathfrak{f}\}}(y) \quad (3.18)$$

an analytical solution is known for any constant  $c$ . This is related to synchronous coupling between slow and fast components, i.e., to equation (2.40a). Section 3.2.2.1 introduces the MIS methods briefly.

The exact solution of the auxiliary ordinary differential equation (3.18) is often not given and,



therefore, replaced by a finite integration scheme which introduces an additional error in the convergence analysis of the whole algorithm. In Schlegel et al. (2012), a method was presented where the auxiliary ordinary differential equation of the method proposed in Knoth and Wolke (1998) is integrated with an explicit Runge–Kutta method. In Sexton and Reynolds (2018), an extension to the method proposed in Schlegel et al. (2012) was presented where any RK method, explicit or implicit, with the first stage given in an explicit manner, has been used for the integration of the auxiliary ordinary differential equation.

A second generalisation was proposed in Sandu (2019) where the method coefficients, which are only applied to the slow part, are defined as time dependent coefficient, i.e. as polynomials in time.

The extended multirate infinitesimal step methods (extMIS) introduced in Section 3.2.2.2 apply arbitrary RK methods for the solution of equation (3.18).

### 3.2.2.1 Multirate infinitesimal step methods (MIS)

This section discusses the multirate infinitesimal step methods (MIS) based on the work published in Wensch et al. (2009) and Knoth and Wensch (2014). The method is defined by the following algorithm taken from Bauer and Knoth (2021).

#### Definition 3.2.4: (Multirate infinitesimal step methods (MIS))

For any autonomous IVP, a MIS method reads with time step  $h$

$$Z_i(0) = y_n + \sum_{j=1}^{i-1} [\alpha_{ij} (Y_j - y_n)] \quad (3.19a)$$

$$\frac{dZ_i(\tau)}{d\tau} = \frac{1}{h} \sum_{j=1}^{i-1} [\gamma_{ij} (Y_j - y_n)] + \sum_{j=1}^{i-1} [\beta_{ij} f^{\{s\}}(Y_j)] + d_i f^{\{f\}}(Z_i(\tau)) \quad (3.19b)$$

$$\begin{aligned} Y_i &= Z_i(h), & i &= 1, \dots, s+1 \\ y_{n+1} &= Y_{s+1}. \end{aligned} \quad (3.19c)$$

In each MIS stage  $i$  an initial value problem has to be solved, where equation (3.19a) represents the initial value and equation (3.19b) the ordinary differential equation. The length of the time interval for the integration in each MIS stage  $i$  is given by  $h$ , which is also the time step to advance from  $y_n$  to  $y_{n+1}$ . Although there are formally  $s+1$  initial value problems, only  $s$  problems have to be solved in reality. The parameters  $\alpha$ ,  $\gamma$  and  $\beta$  are defined as strictly lower triangular matrices with  $(\alpha)_{ij} = \alpha_{ij}$ ,  $(\gamma)_{ij} = \gamma_{ij}$  and  $(\beta)_{ij} = \beta_{ij}$ . Thus, for  $i = 1$ ,  $Y_1 = y_n$ . A method is said to be balanced, if  $(D)_{ii} = d_i = \sum_{j=1}^{i-1} [\beta_{ij}]$  is storing the sum of rows of  $\beta$  and matrix  $D$  is a diagonal matrix, see Wensch et al. (2009, Equation (2.3)). Equation (3.19b) is assumed to be solved exactly, cf. equation (3.18).

A MIS method is completely described by the parameters  $\alpha$ ,  $\beta$  and  $\gamma$ . Additionally, the parameters of the underlying eRK method are given by  $A = R\beta$  and  $b = e_{s+1}^T A$  with  $R = (I_{s+1} - \alpha - \gamma)^{-1}$  and  $s$  RK stages. According to Knoth and Wensch (2014, Section 2c), the time points for stages  $Y_i$  are given by  $t_n + c_i h$ .

**Remark:** A modified formulation for the underlying eRK method parameters is applied, i.e.  $\mathbf{A} \in \mathbb{R}^{s+1 \times s+1}$  where the last column has only zero entries, the last row is containing the weight coefficients and the other entries are the method coefficients. Therefore, the Butcher tableau is reduced to the form  $\mathbf{c} \mid \mathbf{A}$ , where the last entry of the node vector equals one. This allows only eRK methods which are consistent, i.e.  $\mathbf{b}^T \cdot \mathbb{1}_{s+1} = 1$ , cf. Strehmel et al. (2012, Lemma 2.4.1).

A method tableau is simply given by  $\alpha \mid \beta \mid \gamma$ . The integration process is schematically shown in Figure 3.6.

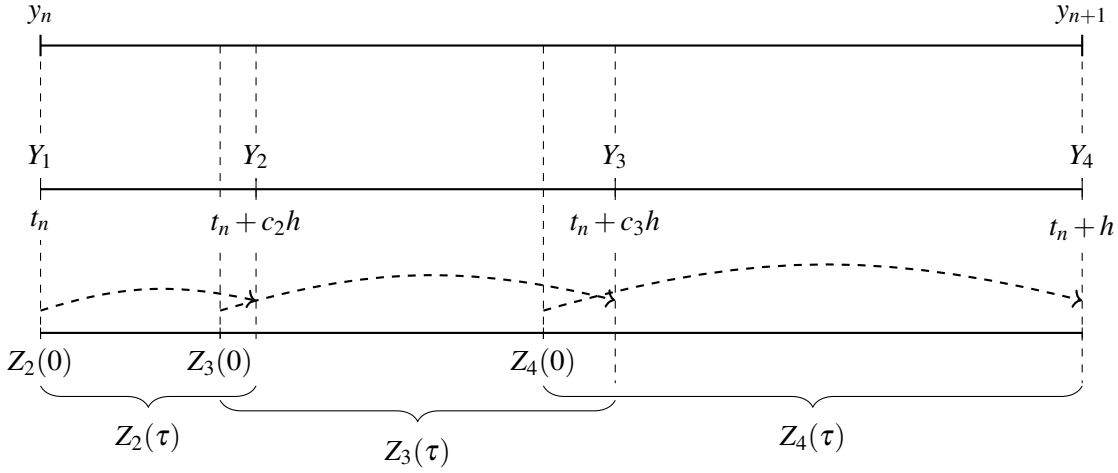


Figure 3.6: Representation of the integration with a three-stage MIS method from  $t_n$  to  $t_n + h$ . The four MIS stages are indicated by  $Y_i$ ,  $i = 1, 2, 3, 4$ . The initial values for the IVP of each MIS stage  $i$  are given by  $Z_i(0)$ , cf. equation (3.19a). The arrows are representing the corresponding integrations.

**Theorem 3.2.1.** For each MIS method, an eRK method is embedded, i.e. by setting  $f^{\{f\}} \equiv 0$ , then equation (3.19) is reduced to the formulation of the embedded eRK method.

This property was given in Knoth and Wolke (1998) and Wensch et al. (2009).

In each MIS stage  $i$  the initial value  $Z_i(0)$  is given as a linear combination of all previously calculated  $Y_j$ ,  $j = 1, \dots, i-1$ . Hence, the integration starts always at an intermediate value and not at  $y_n$ . However, if

$$\alpha = \mathbf{0} \quad \text{or} \quad \alpha = \begin{pmatrix} 0 & & & 0 \\ 1 & 0 & & \\ 0 & 1 & 0 & \\ \vdots & \ddots & \ddots & \ddots \\ 0 & \dots & 0 & 1 & 0 \end{pmatrix},$$

then the integration starts at  $y_n$  or  $Y_{i-1}$ , respectively. Any RK method starts the integration from  $y_n$ . The method introduced in Knoth and Wolke (1998) begins their integration at  $Y_{i-1}$ .

Furthermore, the coupling between both temporal scales is realised in two places, the linear combination of MIS stages values  $Y_i$  through  $\gamma$  as well as the linear combination of the slow component through  $\beta$ .

### 3.2.2.2 Extended multirate infinitesimal step methods (extMIS)

In the following, the strong assumption that the solution of equation (3.19b) is given by an exact integration is weakened due to integrating with an arbitrary RK method for each MIS stage  $i$ . The chosen RK method can either be an explicit or implicit method.

This section is mainly based on Bauer and Knöth (2021). Although this extension is restricted to RK methods, any one-step time integration scheme is applicable.

Throughout this section, subscripted indices will be used for the stages of the MIS method and superscripted indices for the integration of the auxiliary ordinary methods. The Butcher tableau,  $\mathbf{c}_i \mid \mathbf{A}_i$ , represents the utilised RK method in stage  $i$  of the MIS method. Furthermore,  $\mathbf{A}_i$  is the coefficient matrix and  $(\mathbf{A}_i)_{\lambda l} = a_i^{\lambda l}$  represents the RK coefficient of stage  $l$  while integrating the auxiliary ordinary equation in stage  $\lambda$  during the integration in MIS stage  $i$ . The same holds similarly for  $\mathbf{b}_i$ , i.e.  $(\mathbf{b}_i)_l = b_i^l$  as well as for  $\mathbf{c}_i$ , i.e.  $(\mathbf{c}_i)_\lambda = c_i^\lambda$ .

The integration of equation (3.19b) in MIS stage  $i$  with an arbitrary RK method is then given by the following algorithm

$$\begin{aligned}
 Z_i(0) &= y_n + \sum_{j=1}^{i-1} [\alpha_{ij} (Y_j - y_n)], & i &= 1, \dots, s+1 \\
 Z_i^\lambda &= Z_i(0) + h \sum_{l=1}^{s_i} \left[ a_i^{\lambda l} \left( \frac{1}{h} \sum_{j=1}^{i-1} [\gamma_{lj} (Y_j - y_n)] + \sum_{j=1}^{i-1} [\beta_{lj} f^{\{s\}}(Y_j)] + d_i f^{\{f\}}(Z_i^l) \right) \right] \\
 & & \lambda &= 1, \dots, s_i + 1 \\
 Z_i(h) &= Z_i(0) + h \sum_{\lambda=1}^{s_i} \left[ b_i^\lambda \left( \frac{1}{h} \sum_{j=1}^{i-1} [\gamma_{lj} (Y_j - y_n)] + \sum_{j=1}^{i-1} [\beta_{lj} f^{\{s\}}(Y_j)] + d_i f^{\{f\}}(Z_i^\lambda) \right) \right]
 \end{aligned}$$

with time step  $h$ .  $\lambda$  is the index of stages  $s_i$  of the applied RK method. This represents the integration of equation (3.19b) in one RK step. Allowing an even smaller time step, i.e. micro time step  $h_i = \frac{h}{m_i}$  with  $m_i$  being the number of steps in MIS stage  $i$ , the algorithm reads then

$$\begin{aligned}
 Z_i(0) &= y_n + \sum_{j=1}^{i-1} [\alpha_{ij} (Y_j - y_n)], & i &= 1, \dots, s+1 \\
 Z_i^{\mu, \lambda} &= Z_i((\mu - 1) \cdot h_i) \\
 &+ h_i \sum_{l=1}^{s_i} \left[ a_i^{\lambda l} \left( \frac{1}{h} \sum_{j=1}^{i-1} [\gamma_{lj} (Y_j - y_n)] + \sum_{j=1}^{i-1} [\beta_{lj} f^{\{s\}}(Y_j)] + d_i f^{\{f\}}(Z_i^{\mu, l}) \right) \right] \\
 & & \mu &= 1, \dots, m_i \quad \lambda = 1, \dots, s_i + 1 \\
 Z_i(\mu \cdot h_i) &= Z_i((\mu - 1) \cdot h_i) \\
 &+ h_i \sum_{\lambda=1}^{s_i} \left[ b_i^\lambda \left( \frac{1}{h} \sum_{j=1}^{i-1} [\gamma_{lj} (Y_j - y_n)] + \sum_{j=1}^{i-1} [\beta_{lj} f^{\{s\}}(Y_j)] + d_i f^{\{f\}}(Z_i^{\mu, \lambda}) \right) \right].
 \end{aligned}$$

Substituting the integration in equation (3.19) results in the definition of the newly derived extMIS method in recursive form.

**Definition 3.2.5: (Extended extended multirate infinitesimal step methods (extMIS) – recursive)**

Recursive definition of an extMIS method,

$$\begin{aligned} Z_i^{\mu,\lambda} = & y_n + \sum_{j=1}^{i-1} \left[ \left( \alpha_{ij} + \frac{h_i}{h} (\mu - 1 + c_i^\lambda) \gamma_{ij} \right) (Y_j - y_n) \right] \\ & + h_i (\mu - 1 + c_i^\lambda) \sum_{j=1}^{i-1} [\beta_{ij} f^{\{\mathfrak{s}\}}(Y_j)] + h_i d_i \sum_{k=1}^{\mu-1} \sum_{l=1}^{s_i+1} [b_i^l f^{\{\mathfrak{f}\}}(Z_i^{k,l})] \\ & + h_i d_i \sum_{l=1}^{s_i+1} [a_i^{\lambda l} f^{\{\mathfrak{f}\}}(Z_i^{\mu,l})], \quad \mu = 1, \dots, m_i, \quad \lambda = 1, \dots, s_i + 1 \end{aligned} \quad (3.20a)$$

$$Y_i = Z_i^{m_i, s_i+1}, \quad i = 1, \dots, s+1 \quad (3.20b)$$

$$y_{n+1} = Y_{s+1}. \quad (3.20c)$$

Note that, the term  $t_n + h_i (\mu - 1 + c_i^\lambda)$  defines the time point of stage  $Z_i^{\mu,\lambda}$ .

**Remark:** *There are several indices applied in equations or summations throughout this section. Each index is used only for a specific purpose.  $i$  represents the current MIS stage and if  $i$  is already used, then  $j$  is utilised. Furthermore,  $\mu$  is the current time point while integrating the auxiliary ordinary differential equation and if  $\mu$  is already applied, then  $k$  represents the current time point. Moreover,  $\lambda$  shows the current stage during the integration of the auxiliary ordinary differential equation and  $l$  is used if  $\lambda$  is already applied.*

The recursive formulation of the stages  $Y_i$  is replaced with an explicit formulation. Applying a simplified notation for equation (3.20b),

$$\begin{aligned} Y_i = Z_i^{m_i, s_i+1} = & y_n + \sum_{j=1}^{i-1} [(\alpha_{ij} + \gamma_{ij}) (Y_j - y_n)] + h \sum_{j=1}^{i-1} [\beta_{ij} f^{\{\mathfrak{s}\}}(Y_j)] \\ & + h_i d_i \sum_{\mu=1}^{m_i} \sum_{\lambda=1}^{s_i+1} [b_i^\lambda f^{\{\mathfrak{f}\}}(Z_i^{\mu,\lambda})], \end{aligned} \quad (3.21)$$

through

$$\begin{aligned} U_i &= Y_i - y_n \\ \mathcal{A}_i &= h \sum_{j=1}^{i-1} [\beta_{ij} f^{\{\mathfrak{s}\}}(Y_j)] + h_i d_i \sum_{\mu=1}^{m_i} \sum_{\lambda=1}^{s_i+1} [b_i^\lambda f^{\{\mathfrak{f}\}}(Z_i^{\mu,\lambda})] \\ \sigma_{ij} &= \alpha_{ij} + \gamma_{ij} \end{aligned}$$

gives then for equation (3.21)

$$U_i = \sum_{j=1}^{i-1} [\sigma_{ij} U_j] + \mathcal{A}_i$$

and in vector notation

$$\mathbf{U} = (\boldsymbol{\Sigma} \otimes \mathbf{I}_d) \mathbf{U} + \mathcal{A} = ((\mathbf{I}_{s+1} - \boldsymbol{\Sigma}) \otimes \mathbf{I}_d)^{-1} \mathcal{A} = (\mathbf{R}^{-1} \otimes \mathbf{I}_d)^{-1} \mathcal{A} = (\mathbf{R} \otimes \mathbf{I}_d) \mathcal{A},$$

where  $\mathbf{R} = (\mathbf{I}_{s+1} - \mathbf{\Sigma})^{-1} = (\mathbf{I}_{s+1} - \mathbf{\alpha} - \mathbf{\gamma})^{-1}$ . Hence, an explicit form for  $Y_i$  is then given by

$$Y_i = y_n + h \sum_{j=1}^{i-1} \left[ a_{ij} f^{\{\mathbf{s}\}}(Y_j) \right] + \sum_{j=1}^i \sum_{\mu=1}^{m_j} \sum_{\lambda=1}^{s_j+1} \left[ (\mathbf{RD})_{ij} h_j b_j^\lambda f^{\{\mathbf{f}\}}(Z_j^{\mu,\lambda}) \right] \quad (3.22)$$

with the underlying eRK method coefficient matrix  $\mathbf{A} = \mathbf{R}\mathbf{\beta}$  and  $\mathbf{b} = \mathbf{e}_{s+1}^T \mathbf{A}$ . Note that the underlying eRK method is represented by the coefficients  $(\mathbf{A})_{ij} = a_{ij}$ .

Substituting equation (3.22) into equation (3.20a) returns an explicit formulation of the extMIS method from equation (3.20), i.e.

**Definition 3.2.6: (Extended multirate infinitesimal step methods (extMIS) – explicit)**

Explicit definition of an extMIS method,

$$\begin{aligned} Z_i^{\mu,\lambda} = & y_n + h \sum_{j=1}^{i-1} \left[ \left( \mathbf{\alpha A} + \frac{1}{m_i} (\mu - 1 + c_i^\lambda) (\mathbf{A} - \mathbf{\alpha A}) \right)_{ij} f^{\{\mathbf{s}\}}(Y_j) \right] \\ & + \sum_{j=1}^{i-1} \sum_{k=1}^{m_j} \sum_{l=1}^{s_j+1} \left[ \left( \mathbf{\alpha RD} + \frac{1}{m_i} (\mu - 1 + c_i^\lambda) \mathbf{\gamma RD} \right)_{ij} h_j b_j^l f^{\{\mathbf{f}\}}(Z_j^{k,l}) \right] \end{aligned} \quad (3.23a)$$

$$\begin{aligned} & + h_i d_i \sum_{k=1}^{\mu-1} \sum_{l=1}^{s_i+1} \left[ b_i^l f^{\{\mathbf{f}\}}(Z_i^{k,l}) \right] + h_i d_i \sum_{l=1}^{s_i+1} \left[ a_i^{\lambda l} f^{\{\mathbf{f}\}}(Z_i^{\mu,l}) \right] \\ & \mu = 1, \dots, m_i, \quad \lambda = 1, \dots, s_i + 1 \end{aligned}$$

$$Y_i = Z_i^{m_i, s_i+1}, \quad i = 1, \dots, s+1 \quad (3.23b)$$

$$y_{n+1} = Y_{s+1}. \quad (3.23c)$$

Following the approach from Knoth and Wensch (2014, Sec. 2c), the time points for integration stages  $Z_i^{\mu,\lambda}$  are given by

$$t_n + \left( \mathbf{\alpha c} + \frac{1}{m_i} (\mu - 1 + c_i^\lambda) (\mathbf{c} - \mathbf{\alpha c}) \right)_i h. \quad (3.24)$$

Furthermore, a Butcher tableau for this method basically exists of the tableau from Section 3.2.2 and multiple tableau for the integration of the auxiliary ordinary differential equation, i.e.

$$\mathbf{\alpha} \mid \mathbf{\beta} \mid \mathbf{\gamma} \quad \text{and} \quad \mathbf{c}_i \mid \mathbf{A}_i \quad i = 1, \dots, s+1.$$

Note that in each MIS stage  $i$  the applied RK method can differ from each other. Moreover, Figure 3.6 is also valid for this method, since the only difference is the solution of functions  $Z_i(\tau)$ .

**Remark:** Conducting the integration of the auxiliary ordinary differential equation  $m_i$  times can also be achieved by the composition of the applied RK method. The number of time steps will then be equal to one. Equation (3.23) then reads

$$\begin{aligned} Z_i^{1,\lambda} = & y_n + h \sum_{j=1}^{i-1} \left[ \left( \mathbf{\alpha A} + c_i^\lambda (\mathbf{A} - \mathbf{\alpha A}) \right)_{ij} f^{\{\mathbf{s}\}}(Y_j) \right] \\ & + h \sum_{j=1}^{i-1} \sum_{l=1}^{s_j+1} \left[ \left( \mathbf{\alpha RD} + c_i^\lambda \mathbf{\gamma RD} \right)_{ij} b_j^l f^{\{\mathbf{f}\}}(Z_j^{1,l}) \right] + h d_i \sum_{l=1}^{s_i+1} \left[ a_i^{\lambda l} f^{\{\mathbf{f}\}}(Z_i^{1,l}) \right] \end{aligned} \quad (3.25a)$$

$$Y_i = Z_i^{1,s_i+1} \quad (3.25b)$$

$$y_{n+1} = Y_{s+1}. \quad (3.25c)$$

Theorem 3.2.1 states that if the fast component is not existent, the MIS method is reformulated to the embedded / underlying eRK method. This holds also for extMIS methods.

### 3.3 Interrelations of MGARK and MIS methods

The previously introduced methods are related to each other on the basis of additive Runge–Kutta methods. The GARK methods are generalized additive Runge–Kutta methods, i.e. an extension to the RK methods, see Sandu and Günther (2015). Additionally, they have been introduced as generalisation of ARK methods. Moreover, it is stated in Sandu and Günther (2015) that with the GARK methods a more flexible formalism is given compared to classical PRK methods. Furthermore, the MGARK methods have been developed for additive problems with two different temporal scaled components and are formulated in the GARK framework, cf. Günther and Sandu (2016). Bauer and Knoth (2021) discussed how the extMIS methods and their predecessor methods MIS-KW (Knoth and Wolke 1998), recursive flux splitting multirate methods (RFSMR) (Schlegel et al. 2012) and MIS methods (Wensch et al. 2009; Knoth and Wensch 2014) are connected to each other and fit in the GARK structure. It is noteworthy that the extMIS methods are always internal consistent with respect to the GARK methods.

Figure 3.7 graphically presents the relations between the methods and indicates the kind of connection:

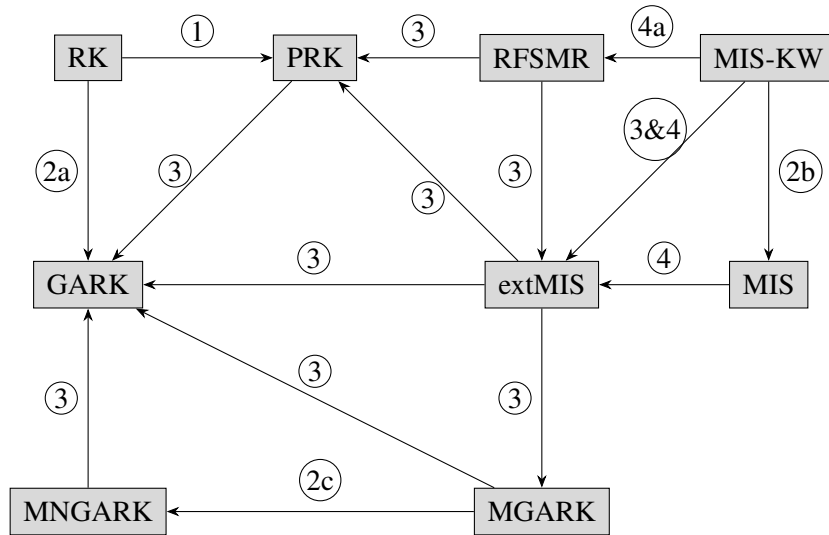


Figure 3.7: Connection of RK type methods to MIS type methods and their generalisations. The different kind of connections are numbered with partitioning ①, generalisation ② with kind (a): additive, (b): interpolation of initial values, (c): multiple components, reformulation (is special case of) ③, applying general RK for inner method ④ with (a): explicit RK

1. Partitioning of problem
2. Generalisation of the method:
  - (a) additive generalisation
  - (b) generalisation with interpolation of initial values
  - (c) generalisation for multiple components
3. Reformulation of method, i.e. method is special case of the other one
4. Applying a RK method for the inner component as well as special case (a) an eRK method.

Following all the mentioned relations, this section explains three specific connections in detail, the formulation of the MNGARK method as GARK method (Section 3.3.1), formulation of the extMIS method as GARK method (Section 3.3.2) and the formulation of the extMIS method as MGARK method (Section 3.3.3). This allows a straightforward derivation of the order theory in the next chapter for the in this thesis introduced multirate time integration methods. Nevertheless, some general limitations of the relations to GARK method are discussed in Section 3.3.4.

### 3.3.1 Formulation of the MNGARK method as GARK method

The connection between the GARK method and MNGARK method is directly derived from equation (3.14) by

$$\mathbf{A}_{kl}^{\kappa\sigma} := \overline{\mathbf{A}}^{\{\kappa,\sigma,k,l\}} \quad \text{and} \quad \mathbf{b}_k^\kappa := \overline{\mathbf{b}}^{\{\kappa,k\}}. \quad (3.26)$$

Note that each entry in the GARK framework  $\mathbf{A}_{kl}^{\kappa\sigma}$  is a block matrix because of the different time scales in the MNGARK framework. Every matrix  $\mathbf{A}^{\kappa\sigma}$  is of size  $(M^{\{\kappa\}} \cdot s^{\{\kappa\}}) \times (M^{\{\sigma\}} \cdot s^{\{\sigma\}})$  and  $\mathbf{b}^\kappa$  is a vector with  $M^{\{\kappa\}} \cdot s^{\{\kappa\}}$  entries.

For the Butcher tableau from equation (3.16), the GARK formulation is given by

$$\begin{array}{ccc} \mathbf{A}^{11} = \mathbf{A}^{\{1\}} & \mathbf{A}^{12} & \mathbf{A}^{13} \\ \mathbf{A}^{12} & \mathbf{A}^{22} & \mathbf{A}^{23} \\ \mathbf{A}^{31} & \mathbf{A}^{32} & \mathbf{A}^{33} \\ \hline \mathbf{b}^{1T} & \mathbf{b}^{2T} & \mathbf{b}^{3T} \end{array}.$$

The first entry shows that the first (slow) component is always integrated directly by the applied RK method. The method coefficients for the numerical coupling mechanism are given by the matrices  $\mathbf{A}^{\kappa\sigma}$  with  $\kappa \neq \sigma$ . A particular result of this connection is the reformulation of the MGARK method as GARK method, i.e. by defining

$$\mathbf{A}^{11} := \mathbf{A}^{\{s,s\}} \quad (3.27a)$$

$$\mathbf{A}^{12} := \left( m_1 \mathbf{A}^{\{s,f,1\}}, m_2 \mathbf{A}^{\{s,f,2\}}, \dots, m_M \mathbf{A}^{\{s,f,M\}} \right) \quad (3.27b)$$

$$\mathbf{A}^{21} := \left( \mathbf{A}^{\{f,s,1\}}, \mathbf{A}^{\{f,s,2\}}, \dots, \mathbf{A}^{\{f,s,M\}} \right)^T \quad (3.27c)$$

$$\mathbf{A}^{22} := \begin{pmatrix} m_1 \mathbf{A}^{\{f,f\}} & & \\ m_1 \mathbb{1}^{\{f\}} \mathbf{b}^{\{f\}T} & m_2 \mathbf{A}^{\{f,f\}} & \\ \vdots & \vdots & \ddots \\ m_1 \mathbb{1}^{\{f\}} \mathbf{b}^{\{f\}T} & m_2 \mathbb{1}^{\{f\}} \mathbf{b}^{\{f\}T} & \dots & m_M \mathbf{A}^{\{f,f\}} \end{pmatrix} \quad (3.27d)$$

$$\mathbf{b}^1 := \mathbf{b}^{\{s\}} \quad (3.27e)$$

$$\mathbf{b}^2 := \left( m_1 \mathbf{b}^{\{f\}T}, m_2 \mathbf{b}^{\{f\}T}, \dots, m_M \mathbf{b}^{\{f\}T} \right)^T. \quad (3.27f)$$

The matrices  $\mathbf{A}^{\{f,s,1\}}$ ,  $\mathbf{A}^{\{f,s,2\}}$ ,  $\mathbf{A}^{\{s,f,1\}}$ ,  $\mathbf{A}^{\{s,f,2\}}$  etc. indicate how the numerical coupling mechanism between the slow and fast component is applied in the MGARK framework. The same coupling mechanism is represented in the coefficient matrices  $\mathbf{A}^{12}$  and  $\mathbf{A}^{21}$  for the GARK framework. However, the coefficients are scaled with the fraction between the fast and slow time step  $m_k$ .

Furthermore, equation (3.27d) shows how a composition of the RK method for the fast component integrated  $M$  times leads to coefficient matrix  $\mathbf{A}^{22}$  of the GARK method. This connection shows that the different time scales from the MGARK method are composed to the time scale of the GARK method. Furthermore, this relation will also allow the application of the convergence theory from the GARK methods, which is discussed in the following chapter.

**Remark:** The GARK method is considered for problems with only one time scale and the superscript is then not given in curly brackets. For the multirate integration methods the curly brackets are applied to indicate different components, time scales and the corresponding method coefficients.

### 3.3.2 The extMIS method formulated as GARK method

The previous section showed how MNGARK methods can be reformulated into GARK methods. Bauer and Knoth (2021) stated how extMIS methods can be formulated as GARK methods, which is summarised in the following.

Applying Definition 3.1.2, a GARK method for an additive split problem for two components is given by

$$Y_i^1 = y_n + h \sum_{j=1}^{s^1} [a_{ij}^{11} f^1(Y_j^1)] + h \sum_{j=1}^{s^2} [a_{ij}^{12} f^2(Y_j^2)] \quad (3.28)$$

$$Y_i^2 = y_n + h \sum_{j=1}^{s^1} [a_{ij}^{21} f^1(Y_j^1)] + h \sum_{j=1}^{s^2} [a_{ij}^{22} f^2(Y_j^2)] \quad (3.29)$$

$$y_{n+1} = y_n + h \sum_{i=1}^{s^1} [b_i^1 f^1(Y_i^1)] + h \sum_{i=1}^{s^2} [b_i^2 f^2(Y_i^2)]. \quad (3.30)$$

The coefficient matrices  $\mathbf{A}^{11}$  and  $\mathbf{A}^{22}$  are for the integration of the first ( $f^1$ ) and second ( $f^2$ ) component, respectively. On the other hand, the matrices  $\mathbf{A}^{12}$  and  $\mathbf{A}^{21}$  represent the coupling between both components. For simplification, in each MIS stage  $i$ , an arbitrary RK method with time step  $h_i = h$  is applied, i.e.  $m_i \equiv 1$ . Equation (3.25) indicates how  $\mathbf{A}^{11} \in \mathbb{R}^{s^1+1 \times s^1+1}$ ,



$\mathbf{A}^{12} \in \mathbb{R}^{s^1+1 \times s^2+1}$ ,  $\mathbf{A}^{21} \in \mathbb{R}^{s^2+1 \times s^1+1}$ , and  $\mathbf{A}^{22} \in \mathbb{R}^{s^2+1 \times s^2+1}$  have to be chosen, i.e.

$$\begin{aligned}
 \mathbf{A}^{11} &= \mathbf{A} \\
 \mathbf{A}^{12} &= \begin{pmatrix} (\mathbf{RD})_{11} \mathbf{b}_1^T & & \mathbf{0} \\ \vdots & \ddots & \\ (\mathbf{RD})_{s+1,1} \mathbf{b}_1^T & \cdots & (\mathbf{RD})_{s+1,s+1} \mathbf{b}_{s+1}^T \end{pmatrix} \\
 \mathbf{A}^{21} &= \begin{pmatrix} (\alpha \mathbf{A})_{11} \mathbb{1}_{s_1+1} & & \mathbf{0} \\ \vdots & \ddots & \\ (\alpha \mathbf{A})_{s+1,1} \mathbb{1}_{s_{s+1}+1} & \cdots & (\alpha \mathbf{A})_{s+1,s+1} \mathbb{1}_{s_{s+1}+1} \end{pmatrix} \\
 &+ \begin{pmatrix} (\mathbf{A} - \alpha \mathbf{A})_{11} \mathbf{c}_1 & & \mathbf{0} \\ \vdots & \ddots & \\ (\mathbf{A} - \alpha \mathbf{A})_{s+1,1} \mathbf{c}_{s+1} & \cdots & (\mathbf{A} - \alpha \mathbf{A})_{s+1,s+1} \mathbf{c}_{s+1} \end{pmatrix} \\
 \mathbf{A}^{22} &= \begin{pmatrix} \mathbf{0} & & \mathbf{0} \\ (\alpha \mathbf{RD})_{21} \mathbb{1}_{s_2+1} \mathbf{b}_1^T & \mathbf{0} & \\ \vdots & \ddots & \ddots \\ (\alpha \mathbf{RD})_{s+1,1} \mathbb{1}_{s_{s+1}+1} \mathbf{b}_1^T & \cdots & (\alpha \mathbf{RD})_{s+1,s} \mathbb{1}_{s_{s+1}+1} \mathbf{b}_s^T & \mathbf{0} \end{pmatrix} \\
 &+ \begin{pmatrix} \mathbf{0} & & \mathbf{0} \\ (\gamma \mathbf{RD})_{21} \mathbf{c}_2 \mathbf{b}_1^T & \mathbf{0} & \\ \vdots & \ddots & \ddots \\ (\gamma \mathbf{RD})_{s+1,1} \mathbf{c}_{s+1} \mathbf{b}_1^T & \cdots & (\gamma \mathbf{RD})_{s+1,s} \mathbf{c}_{s+1} \mathbf{b}_s^T & \mathbf{0} \end{pmatrix} + \begin{pmatrix} d_1 \mathbf{A}_1 & & \mathbf{0} \\ & \ddots & \\ \mathbf{0} & & d_{s+1} \mathbf{A}_{s+1} \end{pmatrix}.
 \end{aligned}$$

**Remark:** The matrix elements are given in the form of a product of a scalar with either a vector or matrix, i.e.  $(\cdot)_{ij}$  denotes an element of a matrix.

The internal consistency is fulfilled, i.e.

$$\begin{aligned}
 \mathbf{c}^1 &= \mathbf{A}^{11} \mathbb{1}_{s^1+1} = \mathbf{A}^{12} \mathbb{1}_{s^2+1} = \mathbf{c} \\
 \mathbf{c}^2 &= \mathbf{A}^{21} \mathbb{1}_{s^1+1} = \mathbf{A}^{22} \mathbb{1}_{s^2+1} = (\tilde{c}_1 \mathbb{1}_{s_1+1}^T + (c - \tilde{c})_1 \mathbf{c}_1^T, \dots, \tilde{c}_{s+1} \mathbb{1}_{s_{s+1}+1}^T + (c - \tilde{c})_{s+1} \mathbf{c}_{s+1}^T)^T,
 \end{aligned}$$

cf. Sandu and Günther (2015, Equation (2.6)). Finally,

$$\mathbf{b}^1 = \mathbf{b} \quad \text{and} \quad \mathbf{b}^2 = \left( \tilde{b}_1 \mathbf{b}_1^T, \tilde{b}_2 \mathbf{b}_2^T, \dots, \tilde{b}_{s+1} \mathbf{b}_{s+1}^T \right)^T.$$

### 3.3.3 The extMIS method as special case of the MGARK method

The MNGARK and extMIS methods can be reformulated as GARK methods. Additionally, the connection of the MIS-KW method with the MGARK method is already pointed out in Günther and Sandu (2016). However, there were no more details provided whether this connection is valid also for the general MIS method. These relations raises the question whether the extMIS method can be reformulated as MGARK method.

To derive the relation between the MGARK and extMIS, there definitions, i.e. equations (3.9) and

(3.23) are compared. From equations (3.9a) and (3.22), it is adopted that the fraction value  $m_i$  from the MGARK method is related to  $(\mathbf{RD})_{ij}$  from the extMIS method. Therefore,  $m_i$  has to be equivalent to  $(\mathbf{RD})_{ij}$  for all  $j \leq i$ , which only holds if  $(\mathbf{RD})_{ij} \equiv (\mathbf{RD})_{ik}$  for all  $k \leq i$ . Thus,

$$\mathbf{R} = (\mathbf{I} - \boldsymbol{\alpha} - \boldsymbol{\gamma})^{-1} = \begin{pmatrix} 1 & & & 0 \\ & 1 & & \\ & & \ddots & \\ 1 & & & 1 \end{pmatrix} \quad \text{and} \quad \boldsymbol{\alpha} + \boldsymbol{\gamma} = \begin{pmatrix} 0 & & & 0 \\ 1 & 0 & & \\ 0 & 1 & 0 & \\ \vdots & \ddots & \ddots & \ddots \\ 0 & \dots & 0 & 1 & 0 \end{pmatrix}.$$

Furthermore, the auxiliary ordinary differential equation has to be solved in each MIS stage  $i$  considering that  $m_i \equiv 1$  for all  $i = 1, \dots, s+1$ , see equation (3.25). Because of equation (3.25a),  $\boldsymbol{\alpha} + c_i^\lambda \boldsymbol{\gamma} = \boldsymbol{\alpha} + \boldsymbol{\gamma}$  for all  $\lambda = 1, \dots, s_i + 1$  and  $i = 1, \dots, s+1$ . Hence, it follows that  $\boldsymbol{\gamma} = \mathbf{0}$  must be chosen. This can also be seen by comparing equations (3.9b) and (3.23a). Thus, only the special case extMIS-KW can be reformulated as MGARK method. This yields the relations:

1. The number of fast integration time steps  $M$  equals  $s+1$ , the number of MIS stages. The time steps are related by  $m_i = d_i$ .
2. The number of RK stages for the slow component is related to the number of MIS stages, i.e.  $s^{\{\mathbf{s}\}} = s$ . For each fast component, the same RK method has to be applied. Hence,  $s^{\{\mathbf{f}\}} = s_i$ , for all  $i = 1, 2, \dots, s+1$ .
3. The coefficient matrices are related by

$$\mathbf{A}^{\{\mathbf{s}, \mathbf{s}\}} = \mathbf{A} \quad \text{and} \quad \mathbf{A}^{\{\mathbf{f}, \mathbf{f}\}} = \mathbf{A}_1 = \mathbf{A}_2 = \dots = \mathbf{A}_{s+1},$$

similar also for the weight coefficients, i.e.

$$\mathbf{b}^{\{\mathbf{s}\}} = \mathbf{b} \quad \text{and} \quad \mathbf{b}^{\{\mathbf{f}\}} = \mathbf{b}_1 = \mathbf{b}_2 = \dots = \mathbf{b}_{s+1}.$$

4. The coefficients for the numerical coupling mechanism are related by

$$a_{ij}^{\{\mathbf{f}, \mathbf{s}, k\}} = \begin{cases} a_{(i-1)j} + c_i^\lambda (a_{ij} - a_{(i-1)j}) & , j < i \\ 0 & , \text{else} \end{cases} \quad \text{and} \\ a_{ij}^{\{\mathbf{s}, \mathbf{f}, k\}} = \begin{cases} b_j^l & , j \leq i \\ 0 & , \text{else} \end{cases}.$$

The indices in each method must also be set in relation: For the MGARK method, the indices for the stage values are  $i$  and  $j$ . For the extMIS method, the indices for the MIS stage values are also  $i$  and  $j$ . However, for the stage values of the fast part, the indices  $i$  and  $l$  are applied. The integration step of the fast component for the MGARK method is represented through index  $k$ .  $\lambda$  is the index for the fast part and index  $j$  for the slow part of the extMIS method. Hence, equation (3.9) is then compared with equation (3.25), i.e.

MGARK:

$$\begin{aligned}
Y_i^{\{s\}} &= y_n + h \sum_{j=1}^{s^{\{s\}}} \left[ a_{ij}^{\{s,s\}} f^{\{s\}} \left( Y_j^{\{s\}} \right) \right] \\
&\quad + h \sum_{k=1}^M \sum_{j=1}^{s^{\{f\}}} \left[ m_k a_{ij}^{\{s,f,k\}} f^{\{f\}} \left( Y_j^{\{f,k\}} \right) \right] \\
Y_i^{\{f,k\}} &= y_n + h \sum_{j=1}^{s^{\{s\}}} \left[ a_{ij}^{\{f,s,k\}} f^{\{s\}} \left( Y_j^{\{s\}} \right) \right] \\
&\quad + h \sum_{l=1}^{k-1} \sum_{j=1}^{s^{\{f\}}} \left[ m_l b_j^{\{f\}} f^{\{f\}} \left( Y_j^{\{f,k\}} \right) \right] \\
&\quad + h \sum_{j=1}^{s^{\{f\}}} \left[ m_k a_{ij}^{\{f,f\}} f^{\{f\}} \left( Y_j^{\{f,k\}} \right) \right] \\
y_{n+1} &= y_n + h \sum_{i=1}^{s^{\{s\}}} \left[ b_i^{\{s\}} f^{\{s\}} \left( Y_i^{\{s\}} \right) \right] \\
&\quad + h \sum_{k=1}^M \sum_{i=1}^{s^{\{f\}}} \left[ m_k b_i^{\{f\}} f^{\{f\}} \left( Y_i^{\{f,k\}} \right) \right],
\end{aligned}$$

extMIS-KW:

$$\begin{aligned}
Y_i &= y_n + h \sum_{j=1}^{i-1} \left[ a_{ij} f^{\{s\}} (Y_j) \right] \\
&\quad + h \sum_{j=1}^i \sum_{l=1}^{s_j+1} \left[ d_j b_j^l f^{\{f\}} (Z_j^{1,l}) \right] \\
Z_i^{1,\lambda} &= y_n + h \sum_{j=1}^{i-1} \left[ \left( \alpha \mathbf{A} + c_i^\lambda (\mathbf{A} - \alpha \mathbf{A}) \right)_{ij} f^{\{s\}} (Y_j) \right] \\
&\quad + h \sum_{j=1}^{i-1} \sum_{l=1}^{s_j+1} \left[ d_j b_j^l f^{\{f\}} (Z_j^{1,l}) \right] \\
&\quad + h \sum_{l=1}^{s_i+1} \left[ d_i a_i^{\lambda l} f^{\{f\}} (Z_i^{1,l}) \right] \\
y_{n+1} &= y_n + h \sum_{i=1}^s \left[ b_i f^{\{s\}} (Y_i) \right] \\
&\quad + h \sum_{i=1}^{s+1} \sum_{\lambda=1}^{s_i+1} \left[ d_i b_i^\lambda f^{\{f\}} (Z_i^{1,\lambda}) \right].
\end{aligned}$$

### 3.3.4 Limits through the investigation of the GARK method

Figure 3.7 represents the relations between the methods discussed throughout this thesis. Additionally, each method is related to the class of GARK methods. This raises the question why multirate methods are investigated. However, there is one important drawback coming with the GARK method, the application to problems with multiple time scales.

Each multirate method is a special case of the GARK framework. Additionally, the method coefficients in the GARK framework are structured and defined through the multirate method coefficients.

If GARK methods are applied to multirate problems, then the different time scales are not considered and the method coefficients are chosen not adhering to the multirate structure. This might causes problems during the integration.

However, investigating the properties of the GARK method and applying the relations / reformulation of the multirate methods, allows a unified, detailed and still unique derivation of the properties. Henceforth, the following chapter discusses the characteristics of multirate methods applying their specialisations to the GARK method.



## Chapter 4

# Examples of multirate time integration methods based on their characteristics

The previous chapter introduced RK and MIS type methods and showed their relations to each other. The analysis of the characteristics of these methods is much simplified through the relations of the methods. Therefore, the consistency and stability behaviour of these methods are discussed in this chapter by using the relations to the GARK methods.

The consistency theory, especially the order conditions, are presented in Section 4.1. The stability behaviour is briefly shown in Section 4.2. The order conditions are used to find examples of MNGARK and MIS methods, which are presented in Section 4.3.

### 4.1 Consistency of multirate methods

The definitions for consistency can be found in various textbooks, see e.g. Hairer et al. (1993) and Strehmel et al. (2012). The here presented definitions are taken from Strehmel et al. (2012). The definitions for consistency and convergence and their corresponding order  $p$  are based on an initial value problem (IVP) given through equation (3.2), i.e.

$$\dot{y} = f(y), \quad y(t_0) = y_0.$$

**Definition 4.1.1: (Consistency of order  $p \in \mathbb{N}$ )**

A one-step method is said to be consistent of order  $p \in \mathbb{N}$ , if for an IVP with sufficiently often continuously differentiable function  $f$  there exists a constant  $c$  and some  $H > 0$  with

$$\|y(t_n + h) - y_{n+1}\| \leq ch^{p+1}, \quad 0 \leq h \leq H \quad (4.1)$$

with  $y_n = y(t_n)$  being the exact initial value and  $y_{n+1}$  being the numerical approximation of  $y(t_n + h)$  by the one-step method where  $h$  is the desired time step.

**Definition 4.1.2: (Convergence of order  $p \in \mathbb{N}$ )**

A one-step method is said to be convergent, if

$$\lim_{h \rightarrow 0} \left[ \max_n \|y(t_n) - y_n\| \right] = 0 \quad (4.2a)$$

with  $y_n$  being the numerical approximation of  $y(t_n)$  by the one-step method. The method has convergence order  $p \in \mathbb{N}$ , if a constant  $c$  independent of time step  $h$  exists and

$$\max_n \|y(t_n) - y_n\| \leq ch^p. \quad (4.2b)$$

Strehmel et al. (2012, Theorem 2.2.1 and Corollary 2.2.2) state the relation of the order of consistency and convergence for one-step methods. As mentioned in Chapter 3, multirate time integration methods are one-step methods. Therefore, the definition for order of convergence of one-step methods can also be applied if an IVP with sufficiently often continuously differentiable function  $f$  is assumed. There are different approaches to derive the order conditions, e.g. Taylor series expansion or using the Leibniz formula for the derivatives of the stage values  $Y_i$  with respect to  $h$  at  $h = 0$ , cf. Hairer et al. (1993, Chapter II.2).

After a brief review of the derivation of the order conditions for RK methods, see Section 4.1.1, the order conditions for GARK methods are presented in Section 4.1.2. All previously introduced methods are related to the GARK framework, see Figure 3.7. Therefore, the order conditions for MNGARK methods (Section 4.1.3) and extMIS methods (Section 4.1.4) are derived from the order conditions for GARK methods. The conditions for the MGARK and MIS methods are presented as special cases of the MNGARK and extMIS methods, respectively.

#### 4.1.1 Order conditions for Runge–Kutta methods

For RK methods, the convergence theory has been discussed throughout many textbooks, e.g. Hairer et al. (1993) and Strehmel et al. (2012). The following only briefly shows the order conditions up to order  $p$  with the corresponding differentials, see e.g. Strehmel et al. (2012). The conditions can be derived by Taylor series expansion of the equations from Definition 3.1.1. For up to order  $p = 4$ , the series expansion results in

$$\begin{aligned} y_{n+1} &= y_n + h \sum_{i=1}^s [b_i f(Y_i)] \\ &= y_n + h \sum_{i=1}^s [b_i] f(y_n) + h^2 \sum_{i=1}^s [b_i c_i] f'(y_n) f'(y_n) \\ &\quad + \frac{h^3}{2} \sum_{i=1}^s [b_i c_i^2] (f'(y_n))^2 f''(y_n) + h^3 \sum_{i=1}^s \sum_{j=1}^s [b_i a_{ij} c_j] f(y_n) (f'(y_n))^2 \\ &\quad + h^4 \sum_{i=1}^s \sum_{j=1}^s \sum_{k=1}^s [b_i a_{ij} a_{jk} c_k] f(y_n) (f'(y_n))^3 \\ &\quad + \frac{h^4}{2} \sum_{i=1}^s \sum_{j=1}^s [b_i a_{ij} c_j^2] (f'(y_n))^2 f''(y_n) f'(y_n) + \frac{h^4}{6} \sum_{i=1}^s [b_i c_i^3] (f'(y_n))^3 f'''(y_n) \\ &\quad + h^4 \sum_{i=1}^s \sum_{j=1}^s [b_i c_i a_{ij} c_j] f(y_n) f'(y_n) f'(y_n) f''(y_n) + \mathcal{O}(h^5). \end{aligned}$$

Furthermore, the conditions up to order  $p = 4$  are then given in simplified notations including the corresponding differentials by

$$\begin{array}{lcl}
 p = 1: & f & \mathbf{b}^T \cdot \mathbb{1} = 1 \\
 p = 2: & f' \langle f \rangle & \mathbf{b}^T \cdot \mathbf{c} = 1/2 \\
 p = 3: & f'' \langle f, f \rangle & \mathbf{b}^T \cdot \mathbf{c}^2 = 1/3 \\
 & f' \langle f' \langle f \rangle \rangle & \mathbf{b}^T \cdot \mathbf{A}\mathbf{c} = 1/6
 \end{array} \quad \left| \quad \begin{array}{lcl}
 p = 4: & f''' \langle f, f, f \rangle & \mathbf{b}^T \cdot \mathbf{c}^3 = 1/4 \\
 & f'' \langle f, f' \langle f \rangle \rangle & \mathbf{b}^T \cdot \text{diag}(\mathbf{c}) \mathbf{A}\mathbf{c} = 1/8 \\
 & f' \langle f'' \langle f, f \rangle \rangle & \mathbf{b}^T \cdot \mathbf{A}\mathbf{c}^2 = 1/12 \\
 & f' \langle f' \langle f' \langle f \rangle \rangle \rangle & \mathbf{b}^T \cdot \mathbf{A}\mathbf{A}\mathbf{c} = 1/24
 \end{array} \right. \quad (4.3)$$

with denoting  $f = f(y_n)$  and using angle brackets for the differentials. The number of convergence conditions per order  $p$  are given in Strehmel et al. (2012, Table 2.4.3). For order  $p = 1$ , only the consistency condition remains, cf. Strehmel et al. (2012, Lemma 2.4.1). One additional condition must be fulfilled for order  $p = 2$ . Order  $p = 3$  requires two further conditions, order  $p = 4$  additional four conditions and order  $p = 5$  additional 9 conditions.

**Remark:** Strehmel et al. (2012, Table 2.4.2) shows additionally to the order conditions up to order  $p = 5$  also the tree development. A derivation of the tree development for RK methods can also be found in Butcher (2010).

#### 4.1.2 Order conditions for generalized additive Runge–Kutta methods

The order conditions for GARK methods are discussed in detail in Sandu and Günther (2015). The work was based on the theory using  $N$ -trees from Araújo et al. (1997). All the conditions up to order  $p = 4$  are given by Sandu and Günther (2015, Theorem 2.6). Using a similar notation as in Sandu and Günther (2015, Equation 2.9), then the conditions read

$$\begin{array}{lcl}
 p = 1: & f^{\kappa} & \mathbf{b}^{\kappa T} \cdot \mathbb{1}^{\kappa} = 1 \\
 p = 2: & f^{\kappa'} \langle f^{\sigma} \rangle & \mathbf{b}^{\kappa T} \cdot \mathbf{c}^{\kappa\sigma} = 1/2 \\
 p = 3: & f^{\kappa''} \langle f^{\sigma}, f^{\nu} \rangle & \mathbf{b}^{\kappa T} \cdot \text{diag}(\mathbf{c}^{\kappa\sigma}) \mathbf{c}^{\kappa\nu} = 1/3 \\
 & f^{\kappa'} \langle f^{\sigma'} \langle f^{\nu} \rangle \rangle & \mathbf{b}^{\kappa T} \cdot \mathbf{A}^{\kappa\sigma} \mathbf{c}^{\sigma\nu} = 1/6 \\
 p = 4: & f^{\kappa'''} \langle f^{\sigma}, f^{\nu}, f^{\mu} \rangle & \mathbf{b}^{\kappa T} \cdot \text{diag}(\mathbf{c}^{\kappa\sigma}) \text{diag}(\mathbf{c}^{\kappa\nu}) \mathbf{c}^{\kappa\mu} = 1/4 \\
 & f^{\kappa''} \langle f^{\sigma}, f^{\nu'} \langle f^{\mu} \rangle \rangle & \mathbf{b}^{\kappa T} \cdot \text{diag}(\mathbf{c}^{\kappa\sigma}) \mathbf{A}^{\kappa\nu} \mathbf{c}^{\nu\mu} = 1/8 \\
 & f^{\kappa'} \langle f^{\sigma''} \langle f^{\nu}, f^{\mu} \rangle \rangle & \mathbf{b}^{\kappa T} \cdot \mathbf{A}^{\kappa\sigma} \text{diag}(\mathbf{c}^{\sigma\nu}) \mathbf{c}^{\sigma\mu} = 1/12 \\
 & f^{\kappa'} \langle f^{\sigma'} \langle f^{\nu'} \langle f^{\mu} \rangle \rangle \rangle & \mathbf{b}^{\kappa T} \cdot \mathbf{A}^{\kappa\sigma} \mathbf{A}^{\sigma\nu} \mathbf{c}^{\nu\mu} = 1/24
 \end{array} \quad (4.4)$$

$\forall \kappa, \sigma, \nu, \mu = 1, \dots, N$  and  $\mathbf{c}^{\kappa\sigma} = \mathbf{A}^{\kappa\sigma} \mathbb{1}^{\sigma}$  with  $\mathbb{1}^{\sigma}$  being a vector of ones of dimension  $s^{\sigma}$ , respectively.

Furthermore, the numbers of conditions are highly dependent on the number of components  $N$ . Table 4.1a gives the number of conditions without any simplifying assumptions and how they evolve up to order  $p = 5$ . For  $N = 1$  the number of conditions are identical to the number of conditions for RK methods, since only one component is considered and, therefore, the GARK method reduces to a RK method. Application of internal consistency as a simplifying assumption, i.e. equation (3.7), decreases the number of condition for convergence order  $p$ . The conditions are

$p \backslash N$	1	2	3	$N$
1	1	2	3	$N$
2	1	4	9	$N^2$
3	2	16	54	$2 \cdot N^3$
4	4	64	324	$4 \cdot N^4$
5	9	288	2187	$9 \cdot N^5$

(a) Without simplifying assumptions

$p \backslash N$	1	2	3	$N$
1	1	2	3	$N$
2	1	2	3	$N$
3	2	6	12	$N + N^2$
4	4	18	48	$N + 2 \cdot N^2 + N^3$
5	9	62	219	$N + 3 \cdot N^2 + 4 \cdot N^3 + N^4$

(b) With internal consistency

Table 4.1: Number of conditions up to order  $p = 5$  for GARK w/o internal consistency as simplifying assumption.

then

$$\begin{aligned}
p = 1: & \quad f^\kappa & \mathbf{b}^{\kappa T} \cdot \mathbb{1}^\kappa & = 1 \\
p = 2: & \quad f^{\kappa'} \langle f^\kappa \rangle & \mathbf{b}^{\kappa T} \cdot \mathbf{c}^\kappa & = 1/2 \\
p = 3: & \quad f^{\kappa''} \langle f^\kappa, f^\kappa \rangle & \mathbf{b}^{\kappa T} \cdot \mathbf{c}^{\kappa 2} & = 1/3 \\
& \quad f^{\kappa'} \langle f^{\sigma'} \langle f^\sigma \rangle \rangle & \mathbf{b}^{\kappa T} \cdot \mathbf{A}^{\kappa\sigma} \mathbf{c}^\sigma & = 1/6 \\
p = 4: & \quad f^{\kappa'''} \langle f^\kappa, f^\kappa, f^\kappa \rangle & \mathbf{b}^{\kappa T} \cdot \mathbf{c}^{\kappa 3} & = 1/4 \\
& \quad f^{\kappa''} \langle f^\kappa, f^{\sigma'} \langle f^\sigma \rangle \rangle & \mathbf{b}^{\kappa T} \cdot \text{diag}(\mathbf{c}^\kappa) \mathbf{A}^{\kappa\sigma} \mathbf{c}^\sigma & = 1/8 \\
& \quad f^{\kappa'} \langle f^{\sigma''} \langle f^\sigma, f^\sigma \rangle \rangle & \mathbf{b}^{\kappa T} \cdot \mathbf{A}^{\kappa\sigma} \mathbf{c}^{\sigma 2} & = 1/12 \\
& \quad f^{\kappa'} \langle f^{\sigma'} \langle f^{\nu'} \langle f^\nu \rangle \rangle \rangle & \mathbf{b}^{\kappa T} \cdot \mathbf{A}^{\kappa\sigma} \mathbf{A}^{\sigma\nu} \mathbf{c}^\nu & = 1/24
\end{aligned} \tag{4.5}$$

$\forall \kappa, \sigma, \nu = 1, \dots, N$  and  $\mathbf{c}^\kappa = \mathbf{A}^{\kappa\sigma} \mathbb{1}^\sigma$  with  $\mathbb{1}^\sigma$  being a vector of ones of dimension  $s^\sigma$ , respectively.

These conditions have been discussed in Sandu and Günther (2015, Remark 5). Table 4.1b shows the number of conditions of convergence order  $p$  with internal consistency and, additionally, how the numbers evolve depending on the number of components. Further simplifying assumptions, such as for the construction of higher order RK methods, as given by Hairer et al. (1993, Equations (7.12)-(7.14)), will reduce the number of conditions even further.

Note that, in Sandu and Günther (2015) the number of conditions have only be given up to order  $p = 4$ . In an attempt to find methods of order  $p = 5$ , the number of conditions were calculated. Henceforth, Table 4.1 shows the number of conditions till order  $p = 5$  to indicate the development of the number of higher order conditions. Nevertheless, throughout this thesis only the methods up to order  $p = 4$  are considered.

In the following, internal consistency is always applied since the discussed methods can fulfil this condition. Hence, equation (4.5) and the corresponding numbers from Table 4.1b are relevant for this thesis.



### 4.1.3 Order conditions for multirate generalized additive Runge–Kutta methods for $N$ components

The forward reformulation of the MNGARK methods into GARK methods allows the application of their convergence theory. Following equations (4.4) and (3.26), the order conditions up to order  $p = 4$  with corresponding differentials are

$$\begin{aligned}
 p = 1 : \\
 f^{\{\kappa\}} & \sum_{k=1}^{M^{\{\kappa\}}} \left[ \bar{\mathbf{b}}^{\{\kappa,k\}T} \cdot \mathbb{1}_{\{\kappa\}} \right] = 1 \\
 p = 2 : \\
 f^{\{\kappa\}'} \langle f^{\{\sigma\}} \rangle & \sum_{k=1}^{M^{\{\kappa\}}} \sum_{l=1}^{M^{\{\sigma\}}} \left[ \bar{\mathbf{b}}^{\{\kappa,k\}T} \cdot \bar{\mathbf{A}}^{\{\kappa,\sigma,k,l\}} \mathbb{1}_{\{\sigma\}} \right] = 1/2 \\
 p = 3 : \\
 f^{\{\kappa\}''} \langle f^{\{\sigma\}}, f^{\{\nu\}} \rangle & \sum_{k=1}^{M^{\{\kappa\}}} \sum_{l=1}^{M^{\{\sigma\}}} \sum_{o=1}^{M^{\{\nu\}}} \left[ \bar{\mathbf{b}}^{\{\kappa,k\}T} \cdot \text{diag} \left( \bar{\mathbf{A}}^{\{\kappa,\sigma,k,l\}} \mathbb{1}_{\{\sigma\}} \right) \right. \\
 & \left. \bar{\mathbf{A}}^{\{\kappa,\nu,k,o\}} \mathbb{1}_{\{\nu\}} \right] = 1/3 \\
 f^{\{\kappa\}'} \langle f^{\{\sigma\}'} \langle f^{\{\nu\}} \rangle \rangle & \sum_{k=1}^{M^{\{\kappa\}}} \sum_{l=1}^{M^{\{\sigma\}}} \sum_{o=1}^{M^{\{\nu\}}} \left[ \bar{\mathbf{b}}^{\{\kappa,k\}T} \cdot \bar{\mathbf{A}}^{\{\kappa,\sigma,k,l\}} \bar{\mathbf{A}}^{\{\sigma,\nu,l,o\}} \mathbb{1}_{\{\nu\}} \right] = 1/6 \\
 p = 4 : \\
 f^{\{\kappa\}'''} \langle f^{\{\sigma\}}, f^{\{\nu\}}, f^{\{\mu\}} \rangle & \sum_{k=1}^{M^{\{\kappa\}}} \sum_{l=1}^{M^{\{\sigma\}}} \sum_{o=1}^{M^{\{\nu\}}} \sum_{q=1}^{M^{\{\mu\}}} \left[ \bar{\mathbf{b}}^{\{\kappa,k\}T} \cdot \text{diag} \left( \bar{\mathbf{A}}^{\{\kappa,\sigma,k,l\}} \cdot \mathbb{1}_{\{\sigma\}} \right) \right. \\
 & \left. \text{diag} \left( \bar{\mathbf{A}}^{\{\kappa,\nu,k,o\}} \cdot \mathbb{1}_{\{\nu\}} \right) \bar{\mathbf{A}}^{\{\kappa,\mu,k,q\}} \cdot \mathbb{1}_{\{\mu\}} \right] = \frac{1}{4} \\
 f^{\{\kappa\}''} \langle f^{\{\nu\}'} \langle f^{\{\mu\}} \rangle, f^{\{\sigma\}} \rangle & \sum_{k=1}^{M^{\{\kappa\}}} \sum_{l=1}^{M^{\{\sigma\}}} \sum_{o=1}^{M^{\{\nu\}}} \sum_{q=1}^{M^{\{\mu\}}} \left[ \bar{\mathbf{b}}^{\{\kappa,k\}T} \cdot \text{diag} \left( \bar{\mathbf{A}}^{\{\kappa,\sigma,k,l\}} \cdot \mathbb{1}_{\{\sigma\}} \right) \right. \\
 & \left. \bar{\mathbf{A}}^{\{\kappa,\nu,k,o\}} \bar{\mathbf{A}}^{\{\nu,\mu,o,q\}} \cdot \mathbb{1}_{\{\mu\}} \right] = \frac{1}{8} \\
 f^{\{\kappa\}'} \langle f^{\{\sigma\}''} \langle f^{\{\nu\}}, f^{\{\mu\}} \rangle \rangle & \sum_{k=1}^{M^{\{\kappa\}}} \sum_{l=1}^{M^{\{\sigma\}}} \sum_{o=1}^{M^{\{\nu\}}} \sum_{q=1}^{M^{\{\mu\}}} \left[ \bar{\mathbf{b}}^{\{\kappa,k\}T} \cdot \bar{\mathbf{A}}^{\{\kappa,\sigma,k,l\}} \right. \\
 & \left. \text{diag} \left( \bar{\mathbf{A}}^{\{\sigma,\nu,l,o\}} \cdot \mathbb{1}_{\{\nu\}} \right) \bar{\mathbf{A}}^{\{\sigma,\mu,l,q\}} \cdot \mathbb{1}_{\{\mu\}} \right] = \frac{1}{12} \\
 f^{\{\kappa\}'} \langle f^{\{\sigma\}'} \langle f^{\{\nu\}'} \langle f^{\{\mu\}} \rangle \rangle \rangle & \sum_{k=1}^{M^{\{\kappa\}}} \sum_{l=1}^{M^{\{\sigma\}}} \sum_{o=1}^{M^{\{\nu\}}} \sum_{q=1}^{M^{\{\mu\}}} \left[ \bar{\mathbf{b}}^{\{\kappa,k\}T} \cdot \bar{\mathbf{A}}^{\{\kappa,\sigma,k,l\}} \right. \\
 & \left. \bar{\mathbf{A}}^{\{\sigma,\nu,l,o\}} \bar{\mathbf{A}}^{\{\nu,\mu,o,q\}} \cdot \mathbb{1}_{\{\mu\}} \right] = \frac{1}{24}
 \end{aligned} \tag{4.6}$$

for all  $\kappa, \sigma, \nu, \mu = 1, 2, \dots, N$ .

In case of internal consistency, see Definition 3.2.3, the conditions are simplified to

$$\begin{aligned}
 p = 1 : \\
 f^{\{\kappa\}} & \sum_{k=1}^{M^{\{\kappa\}}} \left[ \bar{\mathbf{b}}^{\{\kappa,k\}T} \cdot \mathbb{1}_{\{\kappa\}} \right] = 1 \\
 p = 2 : \\
 f^{\{\kappa\}'} \langle f^{\{\sigma\}} \rangle & \sum_{k=1}^{M^{\{\kappa\}}} \left[ \bar{\mathbf{b}}^{\{\kappa,k\}T} \cdot \bar{\mathbf{c}}^{\{\kappa,k\}} \right] = 1/2 \\
 p = 3 : \\
 f^{\{\kappa\}''} \langle f^{\{\sigma\}}, f^{\{\nu\}} \rangle & \sum_{k=1}^{M^{\{\kappa\}}} \left[ \bar{\mathbf{b}}^{\{\kappa,k\}T} \cdot \bar{\mathbf{c}}^{\{\kappa,k\}2} \right] = 1/3 \\
 f^{\{\kappa\}'} \langle f^{\{\sigma\}'} \langle f^{\{\nu\}} \rangle \rangle & \sum_{k=1}^{M^{\{\kappa\}}} \sum_{l=1}^{M^{\{\sigma\}}} \left[ \bar{\mathbf{b}}^{\{\kappa,k\}T} \cdot \bar{\mathbf{A}}^{\{\kappa,\sigma,k,l\}} \bar{\mathbf{c}}^{\{\sigma,l\}} \right] = 1/6 \\
 p = 4 : \\
 f^{\{\kappa\}'''} \langle f^{\{\sigma\}}, f^{\{\nu\}}, f^{\{\mu\}} \rangle & \sum_{k=1}^{M^{\{\kappa\}}} \left[ \bar{\mathbf{b}}^{\{\kappa,k\}T} \cdot \bar{\mathbf{c}}^{\{\kappa,k\}3} \right] = \frac{1}{4} \\
 f^{\{\kappa\}''} \langle f^{\{\nu\}'} \langle f^{\{\mu\}} \rangle, f^{\{\sigma\}} \rangle & \sum_{k=1}^{M^{\{\kappa\}}} \sum_{l=1}^{M^{\{\sigma\}}} \left[ \bar{\mathbf{b}}^{\{\kappa,k\}T} \cdot \text{diag}(\bar{\mathbf{c}}^{\{\kappa,k\}}) \bar{\mathbf{A}}^{\{\kappa,\sigma,k,l\}} \bar{\mathbf{c}}^{\{\sigma,l\}} \right] = \frac{1}{8} \\
 f^{\{\kappa\}'} \langle f^{\{\sigma\}''} \langle f^{\{\nu\}}, f^{\{\mu\}} \rangle \rangle & \sum_{k=1}^{M^{\{\kappa\}}} \sum_{l=1}^{M^{\{\sigma\}}} \left[ \bar{\mathbf{b}}^{\{\kappa,k\}T} \cdot \bar{\mathbf{A}}^{\{\kappa,\sigma,k,l\}} \bar{\mathbf{c}}^{\{\sigma,l\}2} \right] = \frac{1}{12} \\
 f^{\{\kappa\}'} \langle f^{\{\sigma\}'} \langle f^{\{\nu\}'} \langle f^{\{\mu\}} \rangle \rangle \rangle & \sum_{k=1}^{M^{\{\kappa\}}} \sum_{l=1}^{M^{\{\sigma\}}} \sum_{o=1}^{M^{\{\nu\}}} \left[ \bar{\mathbf{b}}^{\{\kappa,k\}T} \cdot \bar{\mathbf{A}}^{\{\kappa,\sigma,k,l\}} \bar{\mathbf{A}}^{\{\sigma,\nu,l,o\}} \bar{\mathbf{c}}^{\{\nu,o\}} \right] = \frac{1}{24}
 \end{aligned} \tag{4.7}$$

for all  $\kappa, \sigma, \nu, \mu = 1, 2, \dots, N$ . The conditions for higher order are given in the same manner as up to order  $p = 4$ . They can be easily written down using equations (4.4) and (3.26). Since MNGARK methods can be reformulated as GARK methods, the number of order conditions corresponds to the number of order conditions for GARK methods.

As special case, the conditions for convergence of the MGARK method are given for  $N = 2$  components. The order conditions are presented in Günther and Sandu (2016, Table 1-2) and Bremicker-Trübelhorn and Ortleb (2017, Theorem 2) up to order  $p = 3$ . In Bremicker-Trübelhorn and Ortleb (2017), they have been derived using the order conditions from the GARK method and equation (3.27). For order  $p = 3$  this lead to 21 conditions. Comparing with the number of conditions from Table 4.1b, there is one extra condition. This special condition comes with equation (3.10), which has to be fulfilled for order  $p = 1$ . Since, this condition already belongs to the method definition, it does not need to be accounted as convergence condition. Hence, the number of convergence conditions are identical to the number of convergence conditions for GARK methods.

#### 4.1.4 Order conditions for extended multirate infinitesimal step methods

In this section, the order conditions up to order  $p = 4$  for the class of extMIS methods will be presented. Note that in Bauer and Knoth (2021) this has been already documented. The approach in Bauer and Knoth (2021) was the application of the order conditions from PRK methods.

The derivation of the order conditions is presented following the relations to the internal consistent GARK method, i.e. applying equation (4.5), see also Section 3.3.2. Additionally, if the applied RK methods are of sufficient order, then the conditions for the extMIS method simplify to the conditions of the general MIS method. Hence, this approach recovers also the conditions for the MIS method from Wensch et al. (2009) and Knoth and Wensch (2014). They have derived only the conditions for up to order  $p = 3$ . Henceforth, the here presented approach for the calculation of the order conditions of the extMIS method applies also for the order conditions of the MIS method.

The resulting formulas for the order conditions are identical to the ones presented in Bauer and Knoth (2021). In order to avoid repeating the full text from Bauer and Knoth (2021), only the final conditions are presented. The derivation is presented in Bauer and Knoth (2021).

The abbreviations  $f^{\{\mathfrak{s}\}} = f^{\{\mathfrak{s}\}}(y_n)$  and  $f^{\{\mathfrak{f}\}} = f^{\{\mathfrak{f}\}}(y_n)$  as well as  $F = f^{\{\mathfrak{s}\}} + f^{\{\mathfrak{f}\}}$  will be used. Moreover, the consistency for the utilised RK methods in MIS stage  $i$  will always be assumed, i.e.

$$\sum_{\lambda=1}^{s_i+1} [b_i^\lambda] = \mathbf{b}_i^T \cdot \mathbb{1}_{s_i+1} = 1.$$

**For order  $p = 1$ :**

$$F : \mathbf{b}^T \cdot \mathbb{1}_s = 1 \quad (4.8a)$$

The remaining condition is the classical order one condition for a RK method, cf. equation (4.3).

**For order  $p = 2$ :**

$$\begin{aligned} f^{\{\mathfrak{s}\}}' \langle F \rangle : \mathbf{b}^T \cdot \mathbf{c} &= \frac{1}{2} \\ f^{\{\mathfrak{f}\}}' \langle F \rangle : \frac{1}{2} \tilde{\mathbf{b}}^T \cdot (\mathbf{c} + \tilde{\mathbf{c}}) + \sum_{i=1}^{s+1} \left[ \tilde{b}_{i \frac{1}{m_i}} (\mathbf{b}_i^T \cdot \mathbf{c}_i - \frac{1}{2}) (c_i - \tilde{c}_i) \right] &= \frac{1}{2} \end{aligned} \quad (4.8b)$$

If  $\mathbf{b}_i^T \cdot \mathbf{c}_i = \frac{1}{2}$  for every RK method in MIS stage  $i$ , which is the standard order condition for a RK method, cf. equation (4.3), the second condition from equation (4.8b) reduces to the additional MIS condition for order two, cf. Wensch et al. (2009, Equation (3.7)), i.e.

$$\tilde{\mathbf{b}}^T \cdot (\mathbf{c} + \tilde{\mathbf{c}}) = 1.$$

For order  $p = 3$ :

$$\begin{aligned}
f^{\{\mathfrak{s}\}''} \langle F, F \rangle : \quad & \mathbf{b}^T \cdot \mathbf{c}^2 &= \frac{1}{3} \\
f^{\{\mathfrak{f}\}''} \langle F, F \rangle : \quad & \frac{1}{3} \tilde{\mathbf{b}}^T \cdot (\mathbf{c}^2 + \mathbf{c}\tilde{\mathbf{c}} + \tilde{\mathbf{c}}^2) + \sum_{i=1}^{s+1} \left[ \tilde{b}_i \frac{1}{m_i} (\mathbf{b}_i^T \cdot \mathbf{c}_i - \frac{1}{2}) (c_i^2 - \tilde{c}_i^2) \right] \\
& + \sum_{i=1}^{s+1} \left[ \tilde{b}_i \frac{1}{m_i^2} (\mathbf{b}_i^T \cdot \mathbf{c}_i^2 - \mathbf{b}_i^T \cdot \mathbf{c}_i + \frac{1}{6}) (c_i - \tilde{c}_i)^2 \right] &= \frac{1}{3} \\
f^{\{\mathfrak{s}\}'} \langle f^{\{\mathfrak{s}\}'} \langle F \rangle \rangle : \quad & \mathbf{b}^T \cdot \mathbf{A}\mathbf{c} &= \frac{1}{6} \\
f^{\{\mathfrak{s}\}'} \langle f^{\{\mathfrak{f}\}'} \langle F \rangle \rangle : \quad & \frac{1}{2} \mathbf{b}^T \cdot \mathbf{RD}(\mathbf{c} + \tilde{\mathbf{c}}) + \sum_{i=1}^{s+1} \left[ (\mathbf{b}^T \cdot \mathbf{RD})_i \frac{1}{m_i} (\mathbf{b}_i^T \cdot \mathbf{c}_i - \frac{1}{2}) (c_i - \tilde{c}_i) \right] &= \frac{1}{6} \\
f^{\{\mathfrak{f}\}'} \langle f^{\{\mathfrak{s}\}'} \langle F \rangle \rangle : \quad & \frac{1}{2} \tilde{\mathbf{b}}^T \cdot (\mathbf{I} + \boldsymbol{\alpha}) \mathbf{A}\mathbf{c} + \sum_{i=1}^{s+1} \left[ \tilde{b}_i \frac{1}{m_i} (\mathbf{b}_i^T \cdot \mathbf{c}_i - \frac{1}{2}) (\mathbf{A}\mathbf{c} - \boldsymbol{\alpha}\mathbf{A}\mathbf{c})_i \right] &= \frac{1}{6} \\
f^{\{\mathfrak{f}\}'} \langle f^{\{\mathfrak{f}\}'} \langle F \rangle \rangle : \quad & \frac{1}{2} \tilde{\mathbf{b}}^T \cdot (\boldsymbol{\alpha} + \frac{\boldsymbol{\gamma}}{2}) \mathbf{RD}(\mathbf{c} + \tilde{\mathbf{c}}) + \frac{1}{6} \tilde{\mathbf{b}}^T \cdot \mathbf{D}(\mathbf{c} + 2\tilde{\mathbf{c}}) \\
& + \sum_{i=1}^{s+1} \sum_{j=1}^{i-1} \left[ \tilde{b}_i \frac{1}{m_j} (\mathbf{b}_j^T \cdot \mathbf{c}_j - \frac{1}{2}) \left( (\boldsymbol{\alpha}\mathbf{RD})_{ij} + \frac{1}{2} (\boldsymbol{\gamma}\mathbf{RD})_{ij} \right) (c_j - \tilde{c}_j) \right] \\
& + \frac{1}{2} \sum_{i=1}^{s+1} \sum_{j=1}^{i-1} \left[ \tilde{b}_i \frac{1}{m_i} (\mathbf{b}_i^T \cdot \mathbf{c}_i - \frac{1}{2}) (\boldsymbol{\gamma}\mathbf{RD})_{ij} (c_j + \tilde{c}_j) \right] \\
& + \sum_{i=1}^{s+1} \sum_{j=1}^{i-1} \left[ \tilde{b}_i \frac{1}{m_i} (\mathbf{b}_i^T \cdot \mathbf{c}_i - \frac{1}{2}) \frac{1}{m_j} (\mathbf{b}_j^T \cdot \mathbf{c}_j - \frac{1}{2}) (\boldsymbol{\gamma}\mathbf{RD})_{ij} (c_j - \tilde{c}_j) \right] \\
& + \sum_{i=1}^{s+1} \left[ (\tilde{\mathbf{b}}^T \cdot \mathbf{D})_i \frac{1}{m_i} (\mathbf{b}_i^T \cdot \mathbf{c}_i - \frac{1}{2}) c_i \right] \\
& + \sum_{i=1}^{s+1} \left[ (\tilde{\mathbf{b}}^T \cdot \mathbf{D})_i \frac{1}{m_i^2} \left( \frac{1}{3} - \mathbf{b}_i^T \cdot \mathbf{c}_i + \mathbf{b}_i^T \cdot \mathbf{A}_i \mathbf{c}_i \right) (c_i - \tilde{c}_i) \right] &= \frac{1}{6}
\end{aligned} \tag{4.8c}$$

Furthermore, if every RK method in MIS stage  $i$  is at least of order three, then the conditions simplify to

$$\begin{aligned}
f^{\{\mathfrak{s}\}''} \langle F, F \rangle : \quad & \mathbf{b}^T \cdot \mathbf{c}^2 &= \frac{1}{3} \\
f^{\{\mathfrak{f}\}''} \langle F, F \rangle : \quad & \tilde{\mathbf{b}}^T \cdot (\mathbf{c}^2 + \mathbf{c}\tilde{\mathbf{c}} + \tilde{\mathbf{c}}^2) &= 1 \\
f^{\{\mathfrak{s}\}'} \langle f^{\{\mathfrak{s}\}'} \langle F \rangle \rangle : \quad & \mathbf{b}^T \cdot \mathbf{A}\mathbf{c} &= \frac{1}{6} \\
f^{\{\mathfrak{s}\}'} \langle f^{\{\mathfrak{f}\}'} \langle F \rangle \rangle : \quad & \mathbf{b}^T \cdot \mathbf{RD}(\mathbf{c} + \tilde{\mathbf{c}}) &= \frac{1}{3} \\
f^{\{\mathfrak{f}\}'} \langle f^{\{\mathfrak{s}\}'} \langle F \rangle \rangle : \quad & \tilde{\mathbf{b}}^T \cdot (\mathbf{I} + \boldsymbol{\alpha}) \mathbf{A}\mathbf{c} &= \frac{1}{3} \\
f^{\{\mathfrak{f}\}'} \langle f^{\{\mathfrak{f}\}'} \langle F \rangle \rangle : \quad & 3\tilde{\mathbf{b}}^T \cdot (\boldsymbol{\alpha} + \frac{\boldsymbol{\gamma}}{2}) \mathbf{RD}(\mathbf{c} + \tilde{\mathbf{c}}) + \tilde{\mathbf{b}}^T \cdot \mathbf{D}(\mathbf{c} + 2\tilde{\mathbf{c}}) &= 1
\end{aligned} \tag{4.8d}$$

The conditions up to order  $p = 3$  were also derived in Wensch et al. (2009) for the general MIS method with an analytical integration of the auxiliary ordinary differential equation. Henceforth, an analytical integration is not required if RK methods of the desired overall order are chosen for the inner stages  $i$ .

For order  $p = 4$ :

The order conditions for the underlying explicit RK method are

$$\begin{aligned}
f^{\{\mathfrak{s}\}'''} \langle F, F, F \rangle : \quad & \mathbf{b}^T \cdot \mathbf{c}^3 &= \frac{1}{4} \\
f^{\{\mathfrak{s}\}''} \langle F, f^{\{\mathfrak{s}\}'} \langle F \rangle \rangle : \quad & \mathbf{b}^T \cdot \text{diag}(\mathbf{c}) \mathbf{A}\mathbf{c} &= \frac{1}{8} \\
f^{\{\mathfrak{s}\}'} \langle f^{\{\mathfrak{s}\}''} \langle F, F \rangle \rangle : \quad & \mathbf{b}^T \cdot \mathbf{A}\mathbf{c}^2 &= \frac{1}{12} \\
f^{\{\mathfrak{s}\}'} \langle f^{\{\mathfrak{s}\}'} \langle f^{\{\mathfrak{s}\}'} \langle F \rangle \rangle \rangle : \quad & \mathbf{b}^T \cdot \mathbf{A}\mathbf{A}\mathbf{c} &= \frac{1}{24}
\end{aligned} \tag{4.8e}$$

Assuming that the auxiliary ordinary differential equations are solved with arbitrary RK methods of at least order four, then there are 14 additional conditions, i.e.

$$\begin{aligned}
f^{\{f\}'''} \langle F, F, F \rangle : & \quad \tilde{\mathbf{b}}^T \cdot \text{diag}(\mathbf{c}^2 + \tilde{\mathbf{c}}^2)(\mathbf{c} + \tilde{\mathbf{c}}) &= 1 \\
f^{\{s\}'''} \langle F, f^{\{f\}'} \langle F \rangle \rangle : & \quad \mathbf{b}^T \cdot \text{diag}(\mathbf{c}) \mathbf{RD}(\mathbf{c} + \tilde{\mathbf{c}}) &= \frac{1}{4} \\
f^{\{f\}''} \langle F, f^{\{s\}'} \langle F \rangle \rangle : & \quad \tilde{\mathbf{b}}^T \cdot (\text{diag}(2\mathbf{c} + \tilde{\mathbf{c}}) \mathbf{A} + \text{diag}(\mathbf{c} + 2\tilde{\mathbf{c}}) \boldsymbol{\alpha} \mathbf{A}) \mathbf{c} &= \frac{3}{4} \\
f^{\{f\}''} \langle F, f^{\{f\}'} \langle F \rangle \rangle : & \quad 2\tilde{\mathbf{b}}^T \cdot \text{diag}(\mathbf{c} + \tilde{\mathbf{c}}) \boldsymbol{\alpha} \mathbf{RD}(\mathbf{c} + \tilde{\mathbf{c}}) \\
& \quad + \frac{4}{3} \tilde{\mathbf{b}}^T \cdot \text{diag}(\mathbf{c} + \frac{1}{2}\tilde{\mathbf{c}}) \boldsymbol{\gamma} \mathbf{RD}(\mathbf{c} + \tilde{\mathbf{c}}) \\
& \quad + \tilde{\mathbf{b}}^T \cdot \text{diag}(\mathbf{c} + \frac{1}{3}\tilde{\mathbf{c}}) \mathbf{D} \mathbf{c} + \tilde{\mathbf{b}}^T \cdot \text{diag}(\frac{5}{3}\mathbf{c} + \tilde{\mathbf{c}}) \mathbf{D} \tilde{\mathbf{c}} &= 1 \\
f^{\{s\}'} \langle f^{\{f\}''} \langle F, F \rangle \rangle : & \quad \mathbf{b}^T \cdot \mathbf{RD}(\mathbf{c}^2 + \tilde{\mathbf{c}}\mathbf{c} + \tilde{\mathbf{c}}^2) &= \frac{1}{4} \\
f^{\{f\}'} \langle f^{\{s\}''} \langle F, F \rangle \rangle : & \quad \tilde{\mathbf{b}}^T \cdot (\mathbf{I} + \boldsymbol{\alpha}) \mathbf{Ac}^2 &= \frac{1}{6} \\
f^{\{f\}'} \langle f^{\{f\}''} \langle F, F \rangle \rangle : & \quad 4\tilde{\mathbf{b}}^T \cdot (\boldsymbol{\alpha} + \frac{1}{2}\boldsymbol{\gamma}) \mathbf{RD}(\mathbf{c}^2 + \tilde{\mathbf{c}}\mathbf{c} + \tilde{\mathbf{c}}^2) \\
& \quad + \tilde{\mathbf{b}}^T \cdot \mathbf{D}(\mathbf{c}^2 + 2\tilde{\mathbf{c}}\mathbf{c} + 3\tilde{\mathbf{c}}^2) &= 1 \\
f^{\{s\}'} \langle f^{\{s\}'} \langle f^{\{f\}'} \langle F \rangle \rangle \rangle : & \quad \mathbf{b}^T \cdot \mathbf{ARD}(\mathbf{c} + \tilde{\mathbf{c}}) &= \frac{1}{12} \\
f^{\{s\}'} \langle f^{\{f\}'} \langle f^{\{s\}'} \langle F \rangle \rangle \rangle : & \quad \mathbf{b}^T \cdot \mathbf{RD}(\mathbf{I} + \boldsymbol{\alpha}) \mathbf{Ac} &= \frac{1}{12} \\
f^{\{s\}'} \langle f^{\{f\}'} \langle f^{\{f\}'} \langle F \rangle \rangle \rangle : & \quad 3\mathbf{b}^T \cdot \mathbf{RD}(\boldsymbol{\alpha} + \frac{1}{2}\boldsymbol{\gamma}) \mathbf{RD}(\mathbf{c} + \tilde{\mathbf{c}}) + \mathbf{b}^T \cdot \mathbf{RDD}(\mathbf{c} + 2\tilde{\mathbf{c}}) &= \frac{1}{4} \\
f^{\{f\}'} \langle f^{\{s\}'} \langle f^{\{s\}'} \langle F \rangle \rangle \rangle : & \quad \tilde{\mathbf{b}}^T \cdot (\mathbf{I} + \boldsymbol{\alpha}) \mathbf{AAc} &= \frac{1}{12} \\
f^{\{f\}'} \langle f^{\{s\}'} \langle f^{\{f\}'} \langle F \rangle \rangle \rangle : & \quad \tilde{\mathbf{b}}^T \cdot (\mathbf{I} + \boldsymbol{\alpha}) \mathbf{ARD}(\mathbf{c} + \tilde{\mathbf{c}}) &= \frac{1}{6} \\
f^{\{f\}'} \langle f^{\{f\}'} \langle f^{\{s\}'} \langle F \rangle \rangle \rangle : & \quad 3\tilde{\mathbf{b}}^T \cdot (\boldsymbol{\alpha} + \frac{1}{2}\boldsymbol{\gamma}) \mathbf{RD}(\mathbf{I} + \boldsymbol{\alpha}) \mathbf{Ac} + \tilde{\mathbf{b}}^T \cdot \mathbf{D}(\mathbf{I} + 2\boldsymbol{\alpha}) \mathbf{Ac} &= \frac{1}{4} \\
f^{\{f\}'} \langle f^{\{f\}'} \langle f^{\{f\}'} \langle F \rangle \rangle \rangle : & \quad \frac{1}{2} \tilde{\mathbf{b}}^T \cdot (\boldsymbol{\alpha} + \frac{1}{2}\boldsymbol{\gamma}) \mathbf{RD}(\boldsymbol{\alpha} + \frac{1}{2}\boldsymbol{\gamma}) \mathbf{RD}(\mathbf{c} + \tilde{\mathbf{c}}) \\
& \quad + \frac{1}{6} \tilde{\mathbf{b}}^T \cdot (\boldsymbol{\alpha} + \frac{1}{2}\boldsymbol{\gamma}) \mathbf{RDD}(\mathbf{c} + 2\tilde{\mathbf{c}}) \\
& \quad + \frac{1}{4} \tilde{\mathbf{b}}^T \cdot \mathbf{D}(\boldsymbol{\alpha} + \frac{1}{3}\boldsymbol{\gamma}) \mathbf{RD}(\mathbf{c} + \tilde{\mathbf{c}}) + \frac{1}{24} \tilde{\mathbf{b}}^T \cdot \mathbf{DD}(\mathbf{c} + 3\tilde{\mathbf{c}}) &= \frac{1}{24}
\end{aligned} \tag{4.8f}$$

**Remark:** The conditions for order  $p = 4$  are written assuming a RK method of at least order four. Moreover, the full summation form is not written for readability. However, they have been derived in order to find the presented conditions. Furthermore, the procedure for the derivation of the order conditions can also be repeated for higher order convergence. However, the number of conditions increases drastically, cf. Table 4.1b.

As already mentioned, if a RK method of sufficient order is chosen for the fast component, the order conditions for MIS methods are recovered. The main reason are the sums in the order conditions, see equations (4.8b) and (4.8c). For example, in equation (4.8c) for order  $p = 3$  there are the following differences

$$\frac{1}{m_i} \left( \mathbf{b}_i^T \cdot \mathbf{c}_i - \frac{1}{2} \right), \quad \frac{1}{m_i^2} \left( \mathbf{b}_i^T \cdot \mathbf{c}_i^2 - \mathbf{b}_i^T \cdot \mathbf{c}_i + \frac{1}{6} \right), \quad \text{and} \quad \frac{1}{m_i^2} \left( \frac{1}{3} - \mathbf{b}_i^T \cdot \mathbf{c}_i + \mathbf{b}_i^T \cdot \mathbf{A}_i \mathbf{c}_i \right). \tag{4.9}$$

It can be adapted that there are two possibilities for vanishing the differences and, therefore, the sums, which will recover the additional conditions of a standard MIS method. First, if the number of steps in each MIS stage  $i \rightarrow \infty$ , which can be interpreted as an exact integration. Secondly, if

the applied RK method for MIS stage  $i$  is of the same order as the MIS method. Both opportunities indicate that the solution of equation (3.19b) does not need to be given analytically. Equation (4.9) shows also that the arbitrary number of steps  $m_i$  influences the method parameters  $\alpha$ ,  $\gamma$  and  $\beta$  at least linearly. However, assuming order  $p = 2$  for a RK method in stage  $i$  results in second order degree polynomial influence of  $m_i$ . Moreover, choosing at least a third order RK method for stage  $i$ , then equation (4.9) vanishes, i.e. for order  $p = 3$  equation (4.8d) is recovered. This suggests that the influence through  $m_i$  scales always the difference of the order condition formula versus the desired value with  $1/m_i^q$ , where  $q$  is the corresponding polynomial exponent. Additionally, with a significantly large number of time steps  $m_i$  in MIS stage  $i$ , the overall influence towards the MIS method parameters is very low, especially for higher order polynomials for  $m_i$ .

Following the connection of the extMIS method to MIS-KW method, the conditions for order  $p = 4$  for the MIS-KW method can be derived. The MIS-KW method is written as special case of a extMIS method when utilising parameter

$$\alpha = \begin{pmatrix} 0 & & & & 0 \\ 1 & 0 & & & \\ 0 & 1 & 0 & & \\ \vdots & \ddots & \ddots & \ddots & \\ 0 & \dots & 0 & 1 & 0 \end{pmatrix}, \quad \gamma = \mathbf{0}.$$

The 14 additional conditions from equation (4.8f) are reduced to five additional conditions,

$$\begin{aligned} f^{\{f\}''} \langle F, f^{\{s\}'} \langle F \rangle \rangle : & \quad \tilde{\mathbf{b}}^T \cdot \text{diag}(2\mathbf{c} + \tilde{\mathbf{c}}) \mathbf{A} \mathbf{c} + \tilde{\mathbf{b}}^T \cdot \text{diag}(\mathbf{c} + 2\tilde{\mathbf{c}}) \alpha \mathbf{A} \mathbf{c} = \frac{3}{4} \\ f^{\{s\}'} \langle f^{\{f\}''} \langle F, F \rangle \rangle : & \quad \tilde{\mathbf{b}}^T \cdot (\mathbf{I} + \alpha) \mathbf{A} \mathbf{c}^2 = \frac{1}{6} \\ f^{\{s\}'} \langle f^{\{f\}'} \langle f^{\{s\}'} \langle F \rangle \rangle \rangle : & \quad \mathbf{b}^T \cdot \mathbf{R} \mathbf{D} (\mathbf{I} + \alpha) \mathbf{A} \mathbf{c} = \frac{1}{12} \\ f^{\{f\}'} \langle f^{\{s\}'} \langle f^{\{s\}'} \langle F \rangle \rangle \rangle : & \quad \tilde{\mathbf{b}}^T \cdot (\mathbf{I} + \alpha) \mathbf{A} \mathbf{A} \mathbf{c} = \frac{1}{12} \\ f^{\{f\}'} \langle f^{\{f\}'} \langle f^{\{s\}'} \langle F \rangle \rangle \rangle : & \quad 3\tilde{\mathbf{b}}^T \cdot \alpha \mathbf{R} \mathbf{D} (\mathbf{I} + \alpha) \mathbf{A} \mathbf{c} + \tilde{\mathbf{b}}^T \cdot \mathbf{D} (\mathbf{I} + 2\alpha) \mathbf{A} \mathbf{c} = \frac{1}{4} \end{aligned}$$

A straight forward calculation can show that all other conditions from equation (4.8f) are met. In the future, it is of interest to develop a theory based on trees for the derivation of the order conditions of the (extended) MIS method. Although, the order conditions from the GARK method were applied, a tree structure has not been recognised, yet.

**Remark:** Naumann and Wensch (2019) gave the order conditions of the multirate finite step methods, if an explicit Euler method is applied as RK method in each MIS stage. Equation (4.8b) yields the same conditions as provided in Naumann and Wensch (2019, Table 1) if the additional MIS condition is met, i.e.

$$\sum_{i=1}^{s+1} \left[ \tilde{b}_i \frac{1}{m_i} (c_i - \tilde{c}_i) \right] = 0. \quad (4.10)$$

This condition and all other conditions from Naumann and Wensch (2019, Table 1) are obsolete, if  $m_i \rightarrow \infty$ , which is also stated in Naumann and Wensch (2019). As already mentioned, if the applied RK methods in each MIS stage are of sufficient order, all the additional conditions from Naumann

and Wensch (2019) vanish as well. However, for understanding the influence of the additional MIS condition, it is noteworthy that these conditions from Naumann and Wensch (2019) are useful. On the other hand, the conditions given in Naumann and Wensch (2019, Table 1) were restricted to the explicit and symplectic Euler methods. All the conditions for multirate finite step methods are derived, if the extMIS conditions are based on RK methods with non-sufficient order. Hence, this section additionally shows a procedure for the derivation of the conditions for multirate finite step methods, i.e. these methods can be understood as a special version of extMIS methods.

## 4.2 Stability of multirate time integration methods

Additionally to consistency, the stability of a method shall be analysed for characterising a method. For linear problems, a stability analysis is often conducted using the Dahlquist equation, a prominent test equation,

$$\dot{y} = \lambda y, \quad (4.11)$$

where  $\lambda \in \mathbb{C}$  is an arbitrary parameter.

Due to the different time scales for split problems, valid stability information shall be derived for multirate methods. The multirate methods introduced in Chapter 3 are based on eRK methods. However, there are so called stiff problems, where their solution not necessarily converges for all methods, especially explicit methods. Examples of such problems can be found in the literature, e.g. chemical reaction systems, diffusion problems or even a combination of them, see e.g. Hairer and Wanner (1996). For geophysical fluid dynamics such problems play also an important role and are investigated, e.g. for atmospheric reactive flows see Knoth and Wolke (1998), for atmosphere ocean coupling see Lemarié et al. (2015) and Zhang et al. (2020).

The following introduces some definitions for investigating the stability of the methods used throughout this thesis, Section 4.2.1. Additionally, it is described how the stability for multirate GARK methods (Section 4.2.2) and MIS methods (Section 4.2.3) can be investigated depending on the structure of applications.

### 4.2.1 Stability for Runge–Kutta methods

The stability theory for Runge–Kutta methods is well known and can be found in many textbooks, cf. e.g. Hairer and Wanner (1996) and Strehmel et al. (2012). The following gives a short overview of the stability theory for linear problems and is loosely taken from Strehmel et al. (2012). Applying an arbitrary RK method to integrate equation (4.11), yields generally a linear equation system

$$(\mathbf{I} - h\lambda \mathbf{A}) \mathbf{Y} = \mathbb{1} y_n,$$

where identity matrix  $\mathbf{I}$  and RK method coefficient matrix  $\mathbf{A}$  are building the linear equation system matrix and  $\mathbf{Y}$  is containing all  $s$  stage values. The solution is only given if matrix  $\mathbf{I} - h\lambda \mathbf{A}$  is regular. Furthermore, applying the solution to the RK method, i.e. equation (3.3b) results in

$$y_{n+1} = \left( 1 + h\lambda \mathbf{b}^T (\mathbf{I} - h\lambda \mathbf{A})^{-1} \mathbb{1} \right) y_n = R(h\lambda) y_n, \quad (4.12)$$

where  $R(h\lambda)$ ,  $h\lambda \in \mathbb{C}$ , is called stability function. Corollary 8.2.2 in Strehmel et al. (2012) states that the stability function approximates the exponential function with order  $p$  if the RK method converges with order  $p$ .

**Remark:** *The exponential function is the solution of equation (4.11).*

The stability function is used to define stability terms.

**Definition 4.2.1: (A-stability)**

A RK method is said to be A-stable, if

$$|R(z)| \leq 1 \quad \text{for all } z \in \mathbb{C} \text{ with } \operatorname{Re} z \leq 0. \quad (4.13a)$$

A-stable methods with  $|R(z)|$  very close to one, or even one, are damping stiff components very slowly. It is, therefore, more desirable to use methods which are L-stable.

**Definition 4.2.2: (L-stability)**

A RK method is said to be L-stable, if it is A-stable and

$$\lim_{\operatorname{Re} z \rightarrow -\infty} |R(z)| = 0. \quad (4.13b)$$

In addition to A-stability, a weaker  $A(\alpha)$ -stability can also be defined.

**Definition 4.2.3: ( $A(\alpha)$ -stability)**

A RK method is said to be  $A(\alpha)$ -stable, if for all  $\alpha \in (0, \frac{\pi}{2})$

$$|R(z)| \leq 1 \quad \text{for all } z \in \mathbb{C} \text{ and } \operatorname{Re} z \leq 0 \text{ with } |\arg(z) - \pi| \leq \alpha \quad (4.13c)$$

holds. Furthermore, the stability region of a RK method is given by the set

$$S := \{z \in \mathbb{C} : |R(z)| \leq 1\}. \quad (4.13d)$$

## 4.2.2 Stability of multirate generalized additive Runge–Kutta methods

For MGARK methods, the stability analysis follows the GARK stability analysis, see Günther and Sandu (2016). Henceforth, the stability analysis for GARK methods can be applied directly for MGARK methods. However, there are some specifications for MGARK methods, which are described at the end of this section. Furthermore, the stability concept is also valid for MNGARK methods.

### 4.2.2.1 Stability of GARK methods

The stability theory for GARK methods has been given in Sandu and Günther (2015). The linear stability analysis is similar to the one for RK methods, except of the applied test equation

$$\dot{y} = \sum_{\kappa=1}^N [\lambda^{\kappa} y].$$



The resulting stability function is then a  $N$ -dimensional complex function, i.e.  $R$  depends on  $z^1, z^2, \dots, z^N$  with  $z^\kappa = h\lambda^\kappa \in \mathbb{C}$ . The details of this function are given in Sandu and Günther (2015). To present an idea how the complexity of the stability function evolves, the stability function for PRK methods is given by

$$R(z^1, z^2, \dots, z^N) = 1 + \sum_{\kappa=1}^N [z^\kappa \mathbf{b}^{\kappa T}] \cdot \left( \mathbf{I} - \sum_{\kappa=1}^N [z^\kappa \mathbf{A}^\kappa] \right)^{-1} \mathbb{1}.$$

This equation has been presented as a special case for the GARK methods, see Sandu and Günther (2015, Example 4).

Furthermore, a nonlinear stability analysis for GARK methods is presented in Sandu and Günther (2015). For this, the concept of algebraically stable GARK methods is introduced, following Sandu and Günther (2015, Definition 4.1).

**Definition 4.2.4: (Algebraically stable GARK methods)**

A GARK method is algebraically stable if the weight vectors are nonnegative

$$\mathbf{b}^\kappa \geq \mathbf{0} \quad \text{for all } \kappa = 1, 2, \dots, N \quad (4.14a)$$

and the matrix

$$\mathbf{P} = \left( \mathbf{A}^{\sigma\kappa T} \text{diag}(\mathbf{b}^\sigma) + \text{diag}(\mathbf{b}^\kappa) \mathbf{A}^{\kappa\sigma} - \mathbf{b}^\kappa \mathbf{b}^{\sigma T} \right)_{1 \leq \kappa, \sigma \leq N} \geq \mathbf{0} \quad (4.14b)$$

is nonnegative definite.

Of special interest are stability-decoupled methods.

**Definition 4.2.5: (Stability-decoupled GARK method)**

A GARK method is stability-decoupled if

$$\mathbf{b}^\kappa \mathbf{b}^{\sigma T} = \mathbf{A}^{\sigma\kappa T} \text{diag}(\mathbf{b}^\sigma) + \text{diag}(\mathbf{b}^\kappa) \mathbf{A}^{\kappa\sigma} \quad \text{for all } \kappa \neq \sigma \quad \text{and } \kappa, \sigma = 1, 2, \dots, N. \quad (4.15)$$

As stated in Sandu and Günther (2015), the interaction of the different components does not influence the overall nonlinear stability of stability-decoupled GARK methods. Hence, it is recommended to apply these type of GARK methods for coupled problems.

**Remark:** Sandu and Günther (2015) also discuss the nonlinear stability analysis for dispersive and coercive functions in detail.

**4.2.2.2 Stability of MGARK/MNGARK methods**

Following the ideas of the previous section, the focus here is on the specification of the nonlinear stability analysis for MGARK methods. Especially, equation (4.15) for stability-decoupled GARK methods reduces if  $\mathbf{b}^{\{f\}} > \mathbf{0}$ :

$$\mathbf{A}^{\{f,s,\lambda\}} = \mathbb{1}^{\{s\}} \mathbf{b}^{\{s\} T} - \text{diag}(\mathbf{b}^{\{f\}})^{-1} \mathbf{A}^{\{f,s,\lambda\}} \text{diag}(\mathbf{b}^{\{s\}}) \quad (4.16)$$

for all  $\lambda = 1, 2, \dots, M$  for MGARK methods, cf. Günther and Sandu (2016, Equation (13)). Note that the specific notation of the MGARK method from Section 3.2.1.1 is used in equation (4.16). However, for MNGARK methods, there is no such reduction. Nevertheless, it can be derived, using the notation and block matrices from Section 3.2.1.2, such that equation (4.15) reads

$$\mathbf{b}^{\{\kappa\}} \mathbf{b}^{\{\sigma\}T} = \mathbf{A}^{\{\sigma, \kappa, l, k\}T} \text{diag}(\mathbf{b}^{\{\sigma\}}) + \text{diag}(\mathbf{b}^{\{\kappa\}}) \mathbf{A}^{\{\kappa, \sigma, k, l\}} \quad (4.17)$$

for all  $\kappa \neq \sigma$  and  $\kappa, \sigma = 1, 2, \dots, N$  as well as  $k = 1, 2, \dots, M^{\{\kappa\}}$  and  $l = 1, 2, \dots, M^{\{\sigma\}}$ . Equations (4.15) - (4.17) have in common that for stability-decoupled methods the coefficients for the numerical coupling mechanism in one direction highly depend on the coefficients in the opposite direction.

**Remark:** Note that for efficiency reasons, it is recommended to consider explicit coupling methods, as also previously mentioned in Section 3.1.2. Throughout the work of Günther and Sandu (2016), explicit coupled methods are called decoupled methods, which shall not be confused with stability-decoupled methods.

### 4.2.3 Stability of multirate infinitesimal step methods

In Section 3.3 and Bauer and Knoth (2021), it is shown that extMIS methods can be formulated as GARK methods. Applying the idea of algebraically stable GARK methods to the reformulated version of the extMIS methods is rather cumbersome. In order to estimate a reasonably good method, the stability concept for the MIS method as described in Wensch et al. (2009), Knoth and Wensch (2014), and Bauer and Knoth (2021) is providing a simpler approach. A linear representative example for the compressible Euler equation has been applied as test equation, i.e.

$$\frac{\partial u}{\partial t} + U \frac{\partial u}{\partial x} = -c_S \frac{\partial \Pi}{\partial x} \quad \text{and} \quad \frac{\partial \Pi}{\partial t} + U \frac{\partial \Pi}{\partial x} = -c_S \frac{\partial u}{\partial x},$$

see Wensch et al. (2009) or Knoth and Wensch (2014, Equation (10)) with x-horizontal component of velocity ( $u$ ), Exner function ( $\Pi$ ) as well as speed of sound ( $c_S$ ) and a constant advection velocity ( $U$ ). This equation is a linearised continuous one-dimensional compressible inviscid equation. To obtain a finite dimensional test problem, all spatial differential operators are replaced by finite differences and then transformed into Fourier space. The pressure and divergence terms are discretised by central differences, the advection term by third order up-winding. The stability is tested for the CFL range  $U\Delta t < \frac{1}{6}c_S\Delta t$  and 40 Fourier modes. Therefore, a MIS method is tailored for this special application where the spectra lies near the imaginary axis. The stability region can be calculated accordingly to Knoth and Wensch (2014).

The main advantage of this specific method is a larger CFL number for speed of sound ( $C_S$ ) with a given Mach number or ratio of  $\frac{C_A}{C_S} < \frac{1}{6}$  with CFL number for advection ( $C_A$ ). Even a  $C_S$  as high as 50 is possible for a Mach number as low as  $\frac{1}{6}$ .



### 4.3.2 Extended MIS method – MIS54

MIS54 is an example of a MIS method of order four with five stages. Table 4.2 gives the parameters  $\alpha$ ,  $\gamma$  and  $\beta$  for the MIS54 method with five stages and order four. Note that the method has been published in Bauer and Knoth (2021). The description is also taken to some extent from Bauer and Knoth (2021).

$\alpha_{ij}$		$\gamma_{ij}$		$\beta_{ij}$	
$\alpha_{21}$	-0.056843003311023	$\gamma_{21}$	0.168489083931286	$\beta_{21}$	0.219579314792533
$\alpha_{31}$	0.071035715986068	$\gamma_{31}$	-0.025097850341834	$\beta_{31}$	-0.032864918414060
$\alpha_{32}$	0.050143439731979	$\gamma_{32}$	0.025515704040468	$\beta_{32}$	0.634699918767414
$\alpha_{41}$	0.021491523917140	$\gamma_{41}$	0.106139356407192	$\beta_{41}$	-0.241761887431829
$\alpha_{42}$	0.287530720188756	$\gamma_{42}$	0.264445452990869	$\beta_{42}$	-0.120631540663984
$\alpha_{43}$	0.239030810792355	$\gamma_{43}$	0.402246482358727	$\beta_{43}$	0.374686620841487
$\alpha_{51}$	0.027558616966568	$\gamma_{51}$	-0.031464053194458	$\beta_{51}$	-0.058474324094343
$\alpha_{52}$	0.382675659910308	$\gamma_{52}$	-0.068258296801680	$\beta_{52}$	0.351217252190521
$\alpha_{53}$	0.177185696263246	$\gamma_{53}$	0.027558616966568	$\beta_{53}$	0.309657030167295
$\alpha_{54}$	-0.314894383613333	$\gamma_{54}$	0.015830368641068	$\beta_{54}$	0.168604799122988
$\alpha_{61}$	0.065158401284120	$\gamma_{61}$	0.150547662349659	$\beta_{61}$	-0.056205055946158
$\alpha_{62}$	0.079591607322196	$\gamma_{62}$	0.088610905686011	$\beta_{62}$	-0.068390330952311
$\alpha_{63}$	0.459806401597571	$\gamma_{63}$	0.067880982803316	$\beta_{63}$	-0.086209210260269
$\alpha_{64}$	0.086725275506356	$\gamma_{64}$	-0.297416190393485	$\beta_{64}$	0.034904705602768
$\alpha_{65}$	0.439945196292364	$\gamma_{65}$	0.148246909195494	$\beta_{65}$	0.448964988009822

Table 4.2: MIS method parameters with 5 stages and order four, (MIS54)

**Remark:** In Knoth and Wensch (2014), the MIS methods were derived by solving an optimisation problem which combined the stability properties with the small integration time interval  $\sum_{i=1}^{s+1} [d_i]$ . Additionally to good stability, the aim was the minimisation of this time interval.

The MIS54 method was chosen by visualising the stability region for each of 100 different methods of order four according to the stability approach described in Section 4.2.3. The corresponding stability region is given in Figure 4.1a. The stability region of this method has considerably expanded the regions compared to methods given in Knoth and Wensch (2014).

Figure 4.1b shows the order convergence of the MIS54 method, where the auxiliary ordinary differential equation was solved with different methods. The cold bubble downburst benchmark example as described in Knoth and Wensch (2014) was used for the calculation of the error convergence. The calculation was performed for time steps ranging from  $2^{-6}$  to  $2^2$  seconds. The integration was conducted for 900 s. No background wind was applied. The error was derived by comparison with an eRK method of order four with a time step of 0.0001 s. Although each time step was applied for each numerical test, the Runge–Kutta method with order two only converged for a time step of 0.25 s or less.

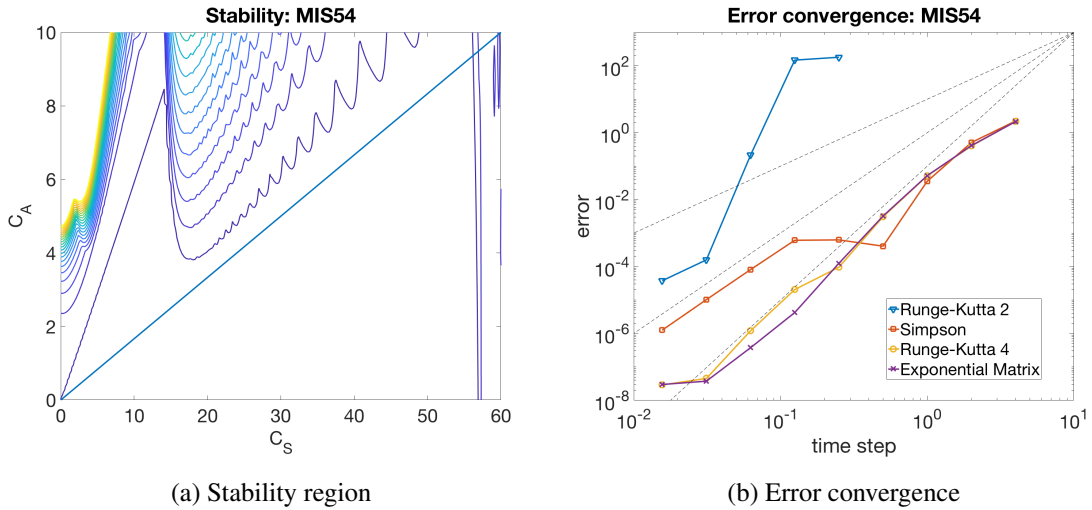


Figure 4.1: Results of MIS54 method

Furthermore, for some time steps, the method converges with a higher order, see e.g. Runge–Kutta method with order two and time step 0.0625 s and Simpson’s method with time step 0.5 s. This is related to the number of fast integration time steps applied for each MIS stage. Equation (4.9) states that the number of fast integration time steps influences quadratically the order conditions for order three and a RK method of order two applied for the fast integration. However, if this number is sufficiently large, then there is almost no influence. Moreover, with a further decrease of the time step, the number of fast integration time steps was also reduced. Therefore, the solution then converges more slowly. This can also be seen by the fast integration with the Simpson method.

This characteristic allows the application of a RK method of reduced order for fast integration without an increase in error as long as the number of fast time steps is large enough, see also Section 4.1.4. This is exemplarily justified by the application of the Simpson’s method for time steps larger than 0.5 s.

Furthermore, Figure 4.1b also shows that the MIS54 method converges with order four by utilising an exponential integrator for the auxiliary ordinary differential equation.

During this test, there has been no change of the RK method applied for the integration in each MIS stage. However, this is not required.

**Remark:** A constant time step  $h$  is used in geophysical fluid dynamics. Therefore, step size controlling with embedded methods is not considered throughout this thesis. However, in geophysical fluid dynamics efficiency is a very important aspect for the development of models and methods. The largest possible time step is chosen such that stable results can still be guaranteed. Henceforth, efficiency is based on the required amount of computation time and not on the time-step. However, this also requires that the method is implemented in the most efficient way.



## Chapter 5

# Numerical realisation of the coupling of atmosphere and ocean models

The air-sea interface is the joint boundary of the atmosphere and ocean. In atmosphere models, the air-sea interface is treated by boundary conditions (BCs), equation (2.31d), similarly for ocean models, equation (2.31i). The physical processes at the air-sea interface, e.g. precipitation, evaporation, wind stress or heat exchange are represented in models by the corresponding fluxes and are time-dependent. For coupled atmosphere-ocean models, the coupling condition, equation (2.31e), is described by an equilibrium formulation of the flow of mass, momentum and energy through the air-sea interface.

In preparation for the development of the realistic three-dimensional coupled atmosphere-ocean model ICONGETM, the mathematical details of the coupling between atmosphere and ocean are first studied in an idealised one-dimensional setting. In Section 5.1, coupling conditions are formulated based on the definition of the physical processes at the air-sea interface. Furthermore, general approaches for the realisation of the coupling of atmosphere and ocean models are also introduced and discussed in Section 5.1. The physics and derivation of a one-dimensional idealised coupled atmosphere-ocean model is described in Section 5.2 and specific coupling approaches for one-dimensional and two-dimensional coupled atmosphere-ocean models are explained. The approach realised for the coupled model ICONGETM is presented in Section 5.3 and discussed by means of a simulation setup for the Central Baltic Sea.

### 5.1 Coupling conditions and their numerical realisation

The coupling conditions based on the formulation of the fluxes at the air-sea interface for atmosphere and ocean models are presented in Section 5.1.1. Common physical and mathematical approaches for modelling the air-sea interface in coupled atmosphere-ocean models are discussed in Section 5.1.2.

### 5.1.1 Coupling conditions at the air-sea interface

The flux formulation of the physical processes at the air-sea interface for atmosphere and ocean models is introduced. These fluxes are the basis for the development of the coupling conditions. At first, the mass flux is formulated. Water is exchanged at the air-sea interface, i.e. fresh water is evaporated from the ocean to the atmosphere and rain drops are precipitated from the atmosphere into the ocean. Salt is not transported from the ocean into the atmosphere. Hence, ocean models balance the salt content at the air-sea interface. This causes an increase in salinity if fresh water evaporates. If there is precipitation into the ocean the salinity decreases, see e.g. Esau (2014) and Nurser and Griffies (2019). This flux exchange reads

$$\mathbf{J}_{saS} \cdot \mathbf{n} = -q_{saS}(E - P)$$

with diffusive mass flux for salinity  $\mathbf{J}_{saS}$ , surface specific salt content ( $q_{saS}$ ), evaporation ( $E$ ) and precipitation ( $P$ ). For details on the salt and fresh water balance see e.g. Beron-Vera et al. (1999). The structure of the horizontal momentum fluxes is given by the formulation of Neumann conditions at the air-sea interface, i.e. equation (2.37b). Furthermore, they are commonly parameterised in atmosphere and ocean models applying by

$$\tau_x = -\rho C_m^d |\mathbf{v}_h| (u - u_S), \quad \text{and} \quad \tau_y = -\rho C_m^d |\mathbf{v}_h| (v - v_S)$$

with bulk transfer coefficients for momentum ( $C_m^d$ ), horizontal velocity ( $\mathbf{v}_h$ ) and surface horizontal velocities ( $u_S, v_S$ ).

Similarly also for the specific heat fluxes, i.e. the sensible heat flux ( $Q_s$ ) is parameterised by

$$Q_s = -\rho C_h^d |\mathbf{v}_h| c_p (T - T_S)$$

with bulk transfer coefficients for heat ( $C_h^d$ ), specific heat capacity at constant pressure ( $c_p$ ) and a surface temperature ( $T_S$ ). The latent heat flux ( $Q_l$ ) is parameterised by

$$Q_l = -\rho C_h^d |\mathbf{v}_h| l_v (q_v - q_{vS})$$

with specific latent heat capacity for water vapor ( $l_v$ ), specific humidity ( $q_v$ ) and saturated specific humidity at the air-sea interface  $q_{vS}$  which depends on the temperature  $T_S$ .

The coupling conditions at the air-sea interface are then formulated through equalising the fluxes. The resulting non-linear system of equations reads

$$\mathbf{J}_{sa} \cdot \mathbf{n} = -q_{saS}(E - P) \tag{5.1a}$$

$$\tau_x^A(u_S) = \tau_x^O(u_S) \tag{5.1b}$$

$$\tau_y^A(v_S) = \tau_y^O(v_S) \tag{5.1c}$$

$$Q_s^A(T_S) + Q_l^A(T_S) = Q_s^O(T_S) + Q_l^O(T_S). \tag{5.1d}$$

This set of equations must be solved for  $u_S, v_S, T_S$  and  $q_{saS}$ , which are unknown to the individual models, but required to calculate the fluxes above. Because of dependencies such as  $q_{vS} = q_{vS}(T_S)$  or the weighted average

$$c_p = q_d c_{pd} + q_v c_{pv}$$



with specific heat capacity at constant pressure for dry air ( $c_{pd}$ ) and water vapour ( $c_{pv}$ ) as well as specific dry air content ( $q_d$ ) and water vapour content ( $q_v$ ), the set of equations is non-linear. The fluxes are then calculated after solving the non-linear system of equations for  $u_S$ ,  $v_S$ ,  $T_S$  and  $q_{saS}$  and are provided to the atmosphere and ocean models. Note that solar radiation is neglected for this analysis, which leads to additional terms for the specific heat flux.

For the details of the formulation of the fluxes in ICON see Doms et al. (2013) and Zängl et al. (2015) and for GETM see Burchard and Bolding (2002). Note that atmosphere and ocean models can apply different formulations of the fluxes at the air-sea interface and thus of the resulting coupling.

### 5.1.2 Realisation of the coupling conditions in atmosphere and ocean models

The coupling conditions in coupled atmosphere-ocean models are defined by the fluxes across the air-sea interface. Three common approaches in coupled atmosphere-ocean models are:

1. No coupling, i.e. fluxes derived from simplifying assumptions and in terms of independent reanalysis data
2. Simple coupling based on simplifying assumptions but using state variables from the atmosphere and ocean
3. Fully consistent coupling, i.e. solving the non-linear system of equations (5.1).

In the event of no coupling, the no-slip condition for the air-sea interface, i.e.  $u_S \equiv v_S \equiv 0$ , is assumed for atmosphere models, cf. Doms et al. (2013). Furthermore, a parameterised or pre-calculated sea surface temperature is provided. Meteorological data are used to calculate the fluxes at the air-sea interface for ocean models implying also no-slip conditions, see e.g. Klingbeil et al. (2018). These kind of data is usually given through reanalysis data provided by weather services, e.g. the German Weather Service (DWD) or European Centre for Medium-Range Weather Forecasts (ECMWF).

The second approach for coupling of atmosphere and ocean models also applies no-slip conditions, but state variables are exchanged between the atmosphere and ocean. Hence, the ocean sea surface temperature is provided to the atmosphere and meteorological variables to the ocean within the coupled model. The fluxes are calculated by the atmosphere and ocean model in terms of these updated quantities. Some application scenarios consider a one-way coupling, i.e. the variables of only one model are provided. If variables between both models are exchanged, the coupling is called two-way.

In the latter case, the flux calculation by the atmosphere and ocean models shall be consistent. If it is not ensured, there can be an inconsistency at the coupling interface during the simulation. To guarantee a consistent flux calculation at the air-sea interface, the calculated fluxes must be provided to both models, i.e. the fluxes calculated on the atmosphere side are provided to the ocean side or vice versa, see e.g. Bauer et al. (2021). A second flux calculation approach at the coupling interface is presented in Karsten et al. (2024). Here, the atmosphere and ocean models provide the

required variables. The flux calculation is conducted at the air-sea interface based on the formulas from Doms et al. (2013). The fluxes are then provided to the atmosphere and ocean models. This ensures a conservative and consistent transport of mass, momentum and energy with respect to the applied no-slip conditions, i.e.  $u_S \equiv v_S \equiv 0$ , and the sea surface temperature from the ocean model.

It is important to note that only the third approach mentioned above solves the non-linear system of equations (5.1) for the coupling conditions. No further assumptions are required, i.e. no parameterisation must be applied. This allows a more accurate formulation of the physical processes at the air-sea interface. For example, the no-slip condition implies that the velocity of the ocean does not influence the wind velocity.

The first two described approaches are applied to ICONGETM. The third approach is utilised for the idealised one-dimensional coupled atmosphere-ocean model in the upcoming section. However, there is a fourth possible approach, which is not discussed further in this thesis. If a differential equation of time for the physical processes at the air-sea interface can be derived, the coupling conditions can be included in the differential equations of the initial boundary value problem for the coupled atmosphere-ocean model. Numerical aspects, such as consistency and stability, of this approach have been investigated by Lemarié et al. (2015), Beljaars et al. (2017), and Zhang et al. (2020).

## 5.2 Coupling approaches for idealised one- and two-dimensional coupled atmosphere-ocean models

The approaches for idealised one- and two-dimensional coupled atmosphere-ocean models are discussed in this section. The analysis of the coupling for these idealised coupled models is later used for development of the coupled model ICONGETM.

A one-dimensional idealised coupled atmosphere-ocean model is explained in detail in Section 5.2.1. The set of governing equations and the coupling conditions are fully derived for this model.

Possible different spatial discretisation for atmosphere and ocean models requires an interpolation of the exchanged quantities at the air-sea interface. The interpolation at the air-sea interface for two-dimensional coupled atmosphere-ocean models considering one horizontal and the vertical direction is explained in Section 5.2.2.

### 5.2.1 1D idealised coupled atmosphere-ocean model with turbulence closure

The common basis for atmosphere and ocean models is the non-hydrostatic compressible set of equations for a geophysical fluid, i.e. equation (2.14) formulated for the prognostic variables in Table 2.1. There are a variety of assumptions applied to this general set of equations to gain the model equations for a one-dimensional idealised coupled atmosphere-ocean model. The assumptions mentioned in the following can be found in various text books, e.g. Stull (1988), Lange (2002), and Etling (2008), and are briefly summarised in Appendix B.

Dry air and water vapour are the considered substances for the atmosphere as well as fresh water

and salt for the ocean. The set of equations is simplified by the following assumptions which will hold for both, the atmosphere and ocean:

- No internal source for each substance since only dry air ( $d$ ), water vapour ( $v$ ), fresh water ( $f$ ) and salinity ( $sa$ ) are applied. The only phase change, which is considered, is the evaporation at the air-sea interface of fresh water, i.e.  $I_v + I_f = 0$  and  $I_d = I_{sa} = 0$ . No precipitative fluxes are applied, as well as no salinity flux at the boundaries of the ocean.
- Both fluids are described as horizontally homogeneous, i.e. there are no horizontal velocity gradients. Additionally, the hydrostatic approximation is applied, see Appendix B.2. Note that a mass conserving fluid with horizontal homogeneity and hydrostatic assumption becomes incompressible. Hence, the one dimensional idealised coupled atmosphere-ocean model is incompressible.
- There are no radiative processes considered as well as other heat fluxes from the surroundings of the atmosphere and ocean.
- Model simulations shall be compared to measurements. However, they are representing an averaged quantity. Thus, modelling of averaged quantities is required. Hence, Reynolds averaging is applied. For more details see Appendix C or Etling (2008). For the sake of readability, the averaging of a quantity is not explicitly labelled.

Applying all simplifications, the set of equations for a one-dimensional atmosphere and ocean model is given by

Atmosphere	Ocean
$\frac{\partial q_v}{\partial t} - \frac{\partial}{\partial z} \left( K_h \frac{\partial q_v}{\partial z} \right) = 0$	$\frac{\partial q_{sa}}{\partial t} - \frac{\partial}{\partial z} \left( (v_t^h + v^{sa}) \frac{\partial q_{sa}}{\partial z} \right) = 0$
$\frac{\partial u}{\partial t} - \frac{\partial}{\partial z} \left( K_m \frac{\partial u}{\partial z} \right) = -\frac{1}{\rho} \frac{\partial p}{\partial x} + f \cdot v$	$\frac{\partial u}{\partial t} - \frac{\partial}{\partial z} \left( (v_t + v) \frac{\partial u}{\partial z} \right) = -\frac{1}{\rho} \frac{\partial p}{\partial x} + f \cdot v$
$\frac{\partial v}{\partial t} - \frac{\partial}{\partial z} \left( K_m \frac{\partial v}{\partial z} \right) = -\frac{1}{\rho} \frac{\partial p}{\partial y} - f \cdot u$	$\frac{\partial v}{\partial t} - \frac{\partial}{\partial z} \left( (v_t + v) \frac{\partial v}{\partial z} \right) = -\frac{1}{\rho} \frac{\partial p}{\partial y} - f \cdot u$
$\frac{\partial \theta_q}{\partial t} - \frac{\partial}{\partial z} \left( K_h \frac{\partial \theta_q}{\partial z} \right) = 0$	$\frac{\partial \theta}{\partial t} - \frac{\partial}{\partial z} \left( (v_t^h + v^h) \frac{\partial \theta}{\partial z} \right) = 0.$

Note that for the atmosphere the wet equivalent potential temperature ( $\theta_q$ ) is applied as a representative for the energy component, while for the ocean the potential temperature ( $\theta$ ) is used as it will be later used in ICON and GETM, respectively. The set of equations for the atmosphere can be found in a similar form in Weng and Taylor (2003). For the ocean, they are described in Burchard and Petersen (1999) and have been applied in the water column model GOTM, see Burchard et al. (1999).

The pressure gradient in the atmosphere is given by a geostrophic wind, see e.g. Weng and Taylor (2003). Hence,

$$\frac{1}{\rho} \frac{\partial p}{\partial x} = f \cdot v_g \quad \text{and} \quad \frac{1}{\rho} \frac{\partial p}{\partial y} = -f \cdot u_g. \quad (5.2)$$

Note that the resulting equations only model the vertical transport of water vapour, salt and temperature due to turbulence.

The turbulent diffusion coefficient for momentum ( $K_m$ ) and for heat ( $K_h$ ) are defined according to Weng and Taylor (2006). Additionally, the eddy diffusivities  $v_t$  and  $v_t^h$  as well as the molecular diffusivities  $v$ ,  $v^h$  and  $v^{sa}$  are defined according to Burchard et al. (1999). In both, the atmosphere and ocean, the turbulent diffusion coefficients and diffusivities are obtained in terms of specific turbulent kinetic energy ( $k$ ) and dissipation ( $\epsilon$ ). The second order  $k$ - $\epsilon$  turbulence closure scheme is applied and requires two additional equations (one for specific turbulent kinetic energy ( $k$ ) and dissipation ( $\epsilon$ )) for the atmosphere and ocean. They read

Atmosphere	Ocean
$\frac{\partial k}{\partial t} = P_s + P_b - \epsilon + \frac{\partial}{\partial z} \left( \frac{K_m}{\sigma_k} \frac{\partial k}{\partial z} \right)$	$\frac{\partial k}{\partial t} = P_s + P_b - \epsilon + \frac{\partial}{\partial z} \left( \frac{v_t}{\sigma_k} \frac{\partial k}{\partial z} \right)$
$\frac{\partial \epsilon}{\partial t} = c_1 \frac{\epsilon}{k} (P_s + P_b) - c_2 \frac{\epsilon^2}{k} + c_3 \frac{\partial}{\partial z} \left( \frac{K_m}{\sigma_\epsilon} \frac{\partial \epsilon}{\partial z} \right)$	$\frac{\partial \epsilon}{\partial t} = c_1 \frac{\epsilon}{k} (P_s + P_b) - c_2 \frac{\epsilon^2}{k} + c_3 \frac{\partial}{\partial z} \left( \frac{v_t}{\sigma_\epsilon} \frac{\partial \epsilon}{\partial z} \right)$

with shear production ( $P_s$ ) and buoyancy production ( $P_b$ ). The shear and buoyancy production and the  $k$ - $\epsilon$  scheme parameters  $c_1$ ,  $c_2$ ,  $c_3$ ,  $\sigma_k$  and  $\sigma_\epsilon$  are defined according to Umlauf and Burchard (2003).

**Remark:** Weng and Taylor (2003) and Weng and Taylor (2006) have utilised different turbulence closure schemes for their one-dimensional atmosphere model experiments. ICON also applies a different turbulence closure scheme. The  $k$ - $\epsilon$  scheme was chosen for the atmosphere and ocean models so that the same turbulence closure scheme is applied. For more details on turbulence closure schemes, see e.g. Umlauf and Burchard (2003).

The coupling conditions are defined by balancing the fluxes at the air-sea interface. However, it is assumed that there is no exchange of specific turbulent kinetic energy and dissipation at the air-sea interface. Hence, boundary conditions for the specific turbulent kinetic energy and dissipation are formulated based on  $k$ - $\epsilon$  turbulence closure scheme. The coupling conditions for this one-dimensional coupled atmosphere-ocean model read

$$q_{sa} \rho^A K_h \frac{\partial q_v}{\partial z} = -\rho^O \left( v_t^h + v^h \right) \frac{\partial q_{sa}}{\partial z} \quad (5.3a)$$

$$-\rho^A K_m \frac{\partial u^A}{\partial z} = -\rho^O (v_t + v) \frac{\partial u^O}{\partial z} \quad (5.3b)$$

$$-\rho^A K_m \frac{\partial v^A}{\partial z} = -\rho^O (v_t + v) \frac{\partial v^O}{\partial z} \quad (5.3c)$$

$$-\rho^A \left( c_p^A K_h \frac{\partial \theta_q^A}{\partial z} + l_v K_h \frac{\partial q_v}{\partial z} \right) = -\rho^O \left( v_t^h + v^h \right) c_p^O \frac{\partial \theta^O}{\partial z}. \quad (5.3d)$$

The equations are defined by the formulation of the Neumann boundary conditions from equation (2.37b). For readability, the variables  $u_S$ ,  $v_S$ ,  $T_S$  and  $q_{saS}$  are neglected from equation (5.3). In comparison to the equations from Section 5.1.1, no parameterisation is used. In this one-dimensional setting no horizontal interpolation is required at the air-sea interface.

### 5.2.2 Coupling details for a 2D atmosphere-ocean model

The two-dimensional models considered here are slice models, which assume only one horizontal direction. The Eady model is a two-dimensional atmosphere model, see e.g. Cullen (2008), Cotter and Holm (2013), Visram et al. (2014), and Yamazaki et al. (2017). The slice model option of the GETM model is an example for a two-dimensional ocean model, see Burchard and Bolding (2002). In comparison to the coupling in the one-dimensional idealised atmosphere-ocean model from the previous section, an interpolation at the air-sea interface must now be considered. Thus, the main purpose of this section is the discussion on how the coupling conditions are applied at the air-sea interface in a two-dimensional atmosphere-ocean model.

Any two-dimensional slice model applies a one-dimensional horizontal discretisation, which basically is a definition of grid points along a horizontal line. Because of different horizontal discretisations in the atmosphere and ocean models, the air-sea interface shall be discretised considering the different spatial discretisations, i.e. an exchange grid must be defined. Therefore, a spatial interpolation at the air-sea interface is required. Interpolation methods of choice are usually nearest-neighbour, bilinear or conservative methods, see e.g. Balaji et al. (2019). In geophysical fluid dynamics, the most obvious choice is a conservative method, since a conservative treatment of the fluxes at the air-sea interface is required.

A conservative interpolation takes the area of each grid cell from the source grid and calculates the fraction of the contribution to the destination grid. Hence, an incidence matrix  $\mathbf{I} \in \mathbb{R}_0^{+N_d \times N_s}$  storing the fractions can be applied with  $N_s$  and  $N_d$  being the number of grid cells on the source and destination side, respectively. The following equation defines an area weighted conservative interpolation

$$\phi_{d_i} \cdot A_{d_i} = \sum_{j=1}^{N_s} \left[ (\mathbf{I})_{ij} \cdot A_{s_j} \cdot \phi_{s_j} \right], \quad i = 1, 2, \dots, N_d, \quad (5.4)$$

where  $\phi$  represents the data to be interpolated and  $A_{s_i}$  and  $A_{d_j}$  the area of grid cells  $i$  and  $j$ . The subscription  $s$  and  $d$  are representing the source and destination side, respectively.

**Remark:** *The column-sum of the incidence matrix is less than or equal to one. The only columns with a sum less than one are those where not every source grid element contributes to the destination grid, i.e. the source grid element is outside of the destination grid, cf. Figure 5.1. The incidence matrix for the interpolation from the atmosphere to the ocean side is not identical with the incidence matrix for the interpolation from the ocean to the atmosphere side. Henceforth, the interpolation is not reversible. Therefore, the incidence matrix must be calculated for each interpolation direction.*

Since a conservative interpolation is weighted through the cell area of the source and destination discrete grid structure, the to be interpolated value have to be a quantity related to an area, e.g. pressure and flux etc.

Henceforth, the procedure for applying the coupling conditions shall be provided in three steps:

1. the interpolation of the variables to an exchange grid from the atmosphere and ocean component,

2. solving the coupling conditions on the exchange grid, and
3. interpolating back to the atmosphere and ocean.

The following is a more general formulation of Bauer et al. (2021, Section 3.3), who focused on the exchange grid in the model ICONGETM. However, the approach is transferable to many coupling scenarios.

Based on the information provided by the discretisation from the atmosphere and ocean models, an exchange grid can be derived. The exchange grid is created by overlaying both grids and calculation of the intersection points. Figure 5.1, taken and modified from Bauer et al. (2021), shows an exemplary exchange grid situation for a one-dimensional air-sea interface in a two-dimensional coupled atmosphere-ocean model.

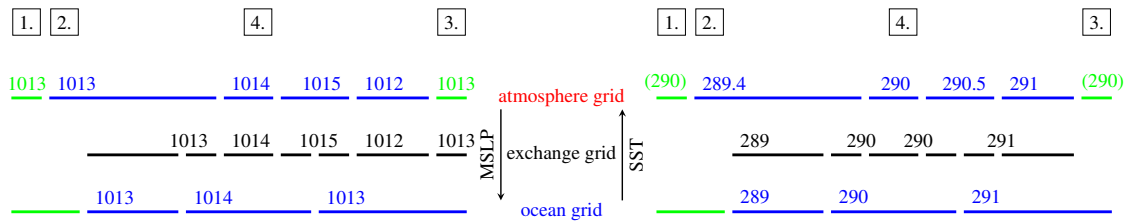


Figure 5.1: Schematic representation of the interpolation between atmosphere and ocean slice models. In the atmosphere and ocean grids active ocean cells are coloured in blue and land cells in green. As shown for the transfer of mean sea level pressure (MSLP in hPa) and sea surface temperature (SST in K), the exchange grid can consist of different cells for each direction. The four possible combinations of land/ocean masks are indicated. On land (cases 1 and 3) an atmosphere-internal SST (here 290 K) must be applied. This atmosphere-internal SST is also considered for fractions of ocean cells not covered by the ocean domain (case 2).

As indicated in Figure 5.1, the overlay of the different model grids yields four possible combinations of land/ocean masks:

1. land cells on atmosphere and ocean side,
2. ocean cell on atmosphere and land cell on ocean side,
3. land cell on atmosphere and ocean cell on ocean side,
4. ocean cells on atmosphere and ocean side.

Elements of case 1 are excluded from the exchange grid, since no data exchange is required. Case 4 elements are included, since both sides show water cells. For case 2 holds that a fraction of the atmospheric water cell is utilised for the interpolation to the exchange grid. In Figure 5.1, the contribution of the second element of the atmosphere to the exchange grid is 0.8. In case of the regridding in the other direction, the non-covered ocean grid cell part of the atmospheric water cell must be filled with corresponding pre-calculated data. Whether the elements of case 3 belong to

the exchange grid depends on the direction of interpolation. Henceforth, two different exchange grids are created and used, one for the interpolation from the atmosphere to the ocean, which includes the elements of case 3, and one vice versa, excluding elements of case 3, see Figure 5.1. Any interpolation method can then be applied, although a conservative interpolation method is highly recommended, as mentioned previously.

An exchange grid requires two incidence matrices for the interpolation from one side to the other, one for the interpolation to the exchange grid and one from the exchange grid. Hence, a fully two-way coupled interpolation requires two exchange grids and corresponding incidence matrices must be calculated. Equation (5.4) is applied twice per direction. The incidence matrix for the interpolation from the exchange grid is filled only with zeros or ones. The column sum is always equal to one, i.e. one exchange grid element always contributes to only one destination grid element. By multiplying the incidence matrices for the interpolation to and from the exchange grid, the incidence matrix for the direct conservative interpolation from the atmosphere / ocean side to the ocean / atmosphere side is gained, respectively.

**Remark:** *The additional work load covered by the overall coupled model can be split into two parts. The incidence matrices and the interpolation weights have to be calculated only once during the initialisation of the model. The actual interpolation is then carried out multiple times during the time integration using the pre-calculated incidence matrices and interpolation weights. Henceforth, the most expensive part is again the solving of the coupling conditions for the air-sea interface at each coupling time step.*

### 5.3 The coupling in ICONGETM: a flexible two-way mechanism for a coupled atmosphere-ocean model

The coupled atmosphere-ocean model ICONGETM was developed for considering the physical process, especially for applications in the Baltic Sea area. A consistent flux calculation at the air-sea interface is utilised. Due to different horizontal spatial discretisations, a conservative interpolation using the exchange grid philosophy is applied, as suggested in the previous section.

The coupling interfaces in ICON and GETM are summarised in Section 5.3.1 with focusing on the set of equations and the horizontal discretisation. The coupling mechanism utilised in the coupled model ICONGETM is presented in Section 5.3.2. Furthermore, the advantages and disadvantages of the coupling approach are discussed.

**Remark:** *The implementation was realised using the special coupling software library Earth System Modelling Framework (ESMF). The variables calculated by ICON and GETM were interpolated to an exchange grid. Some additional variable manipulations, e.g. scaling or averaging, is carried out at the exchange grid. The final step is then the conservative interpolation to the horizontal grids ICON and GETM.*

### 5.3.1 Coupling interfaces in ICON and GETM

Except of the actual coupling conditions, the horizontal discretisation is the key element for the coupling at the air-sea interface. The spatial discretisation is completely different in each model. Henceforth, it is important to emphasise that the formulation of the set of governing equations for each model is also a factor for understanding how the coupling conditions have to be applied. Therefore, the horizontal discretisation of the models ICON and GETM are presented after a brief introduction of the governing equations. They are shown here, since GETM applies the concept of a free surface, which ICON does not. This will lead to a conceptional problem for the coupling and is discussed later on. For the two-dimensional model, this problem was ignored in the previous section due to focusing on the concept of interpolation at an interface.

Some of the presented aspects are taken from Bauer et al. (2021). However, the realisation of the coupling interface in ICON and in GETM is explained in detail in this section.

#### 5.3.1.1 Coupling interface in ICON

The German Weather Service (DWD) and the Max Planck Institute for Meteorology (MPI-M) have developed in a joint project the non-hydrostatic dynamical core for the ICOSahedral Non-hydrostatic modeling framework (ICON). The derivation of the set of equations is explained in Zängl et al. (2015). They have been summarised in Ullrich et al. (2017) for the dynamical core model inter-comparison project (DCMIP) 2016. Henceforth, the first section shows the final implemented set of equations and the horizontal grid structure.

#### Set of equations in ICON

ICON solves the two-dimensional vector-invariant momentum equations on an icosahedral (triangular) grid with Arakawa C-grid staggering and terrain-following vertical discretisation. Zängl et al. (2015) stated that the derivation of the set of equations is based on the work in Gassmann and Herzog (2008). The final formulation has been modified with respect to the horizontal grid structure, see Zängl et al. (2015, equations (3)-(6)) and reads

$$\frac{\partial \rho}{\partial t} + \nabla \cdot (\rho \cdot \mathbf{v}^T) = 0 \quad (5.5a)$$

$$\frac{\partial v_n}{\partial t} + \frac{\partial k_h}{\partial n} + (\zeta + f) v_t + w \frac{\partial v_n}{\partial z} = -c_{pd} \theta_v \frac{\partial \Pi}{\partial n} + F(v_n) \quad (5.5b)$$

$$\frac{\partial w}{\partial t} + \mathbf{v}_h \cdot \nabla w + w \frac{\partial w}{\partial z} = -c_{pd} \theta_v \frac{\partial \Pi}{\partial z} - g \quad (5.5c)$$

$$\frac{\partial (\rho \theta_v)}{\partial t} + \nabla \cdot (\rho \theta_v \cdot \mathbf{v}^T) = Q \quad (5.5d)$$

with prognostic variables density ( $\rho$ ), horizontal velocity component normal to the triangle edges ( $v_n$ ), the vertical component of velocity ( $w$ ) and virtual potential temperature ( $\theta_v$ ). Furthermore, the horizontal specific kinetic energy  $k_h = \frac{1}{2} (v_n^2 + v_t^2)$ , vorticity ( $\zeta$ ), Coriolis frequency ( $f$ ), reconstructed tangential velocity component ( $v_t$ ), specific heat capacity at constant pressure for dry air ( $c_{pd}$ ), Exner function ( $\Pi$ ), source term for horizontal momentum  $F(v_n)$ , horizontal velocity ( $\mathbf{v}_h$ ),



gravitational acceleration ( $g$ ) and diabatic heat-source terms ( $Q$ ) are applied. Additionally, Zängl et al. (2015) stated that in accordance with the model code, it is assumed that  $(v_t, v_n, w)$  form a right-handed system. The parameterisation is based on the physics from the COSMO model, see Doms et al. (2013) and Zängl et al. (2015).

**Remark:** Equation (2.14) was derived as a general formulation of an differential equation for any geophysical fluid. The set of equations are usually differently formulated when focusing on a specific geophysical fluid. Hence, the set of equations in ICON were reformulated to the present form.

### Horizontal grid structure

The horizontal grid structure has been explained in Bauer et al. (2021) and the following is based on that description. However, the original documentation can be found in Linardakis et al. (2011). The very first assumption for the horizontal grid is that the Earth is approximated as a sphere. Furthermore, the horizontal grid structure is based on the projection of an icosahedron on the sphere. The edges of each triangle of the icosahedron can now be interpreted as parts of great circles on the sphere, see Figure 5.2.

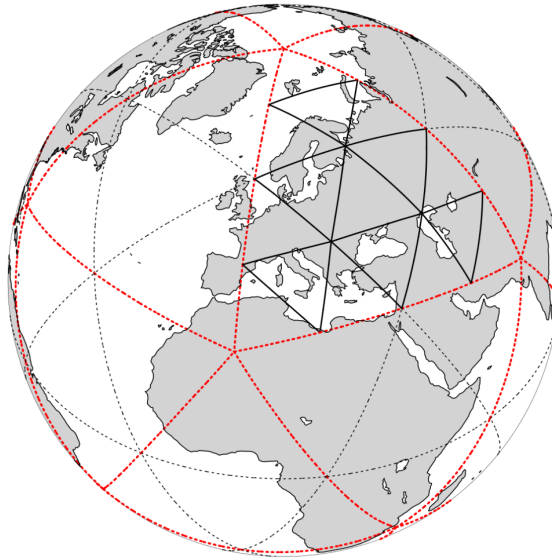


Figure 5.2: Illustration of the grid construction procedure. The original spherical icosahedron is shown in red, denoted as R1B00. In this example, the initial division (black dotted), followed by one subsequent edge bisection yields a R2B01 grid (solid lines), see Prill et al. (2019).

A refinement of the grid, i.e. to increase the resolution by using smaller triangles, is achieved by a combination of two steps. The first step is an initial division of the original icosahedron triangle edges by  $n \in \mathbb{N}$ . The second step are  $b \in \mathbb{N}$  bisections of the remaining smaller triangles. The final grid is then described by  $RnBb$ .

The number of triangles on the sphere for a  $RnBb$  grid is given by  $20n^24^k$ , see Zängl et al. (2015).

The effective grid resolution is given by

$$\sqrt{\frac{\pi}{5}} \frac{r_E}{n^{2k}} \quad (5.6)$$

with Earth radius ( $r_E$ ).

**Remark:** An icosahedron consists of 20 equilateral triangles. After the initial division and the bisections, the gained triangles on the sphere are not equilateral. Using the concepts of springs for optimisation of the grid from Tomita et al. (2002), the triangle vertices are shifted so that the edges are of similar lengths. This also holds for the area of the triangles.

Table 1 in Zängl et al. (2015) shows different R2Bb grids with effective grid resolutions.

The DWD applies an R3B07 grid for global weather forecast simulations, which has an effective resolution of 13.15 km. For Europe, a finer resolved grid with about 6.58 km resolution is applied. The area of a triangle is calculated using the formula for spherical trigonometry. This coincides with the assumption that all triangle edges are considered as parts of a great circle.

### 5.3.1.2 Coupling interface in GETM

The General Estuarine Transport Model (GETM) is an ocean model developed for coastal and regional applications. The full set of equations is given in detail in Burchard and Bolding (2002).

#### Set of governing equations in GETM

The hydrostatic set of equations with the Boussinesq approximation and the eddy viscosity assumption are used in GETM, see e.g. Bryan (1969) and Blumberg and Mellor (1987). A detailed description and derivation is given in Burchard and Bolding (2002), which is summarised in the following.

$$\begin{aligned} \frac{\partial u}{\partial t} + \frac{\partial}{\partial z}(uw) - \frac{\partial}{\partial z} \left( (v_t + v) \frac{\partial u}{\partial z} \right) + \alpha \left( \frac{\partial u^2}{\partial x} + \frac{\partial}{\partial y}(uv) - \frac{\partial}{\partial x} \left( 2A_h^M \frac{\partial u}{\partial x} \right) \right. \\ \left. - \frac{\partial}{\partial y} \left( A_h^M \left( \frac{\partial u}{\partial y} + \frac{\partial v}{\partial x} \right) \right) - fv - \int_z^\zeta \left[ \frac{\partial b}{\partial x} \right] dz' \right) = -g \frac{\partial \zeta}{\partial x}, \end{aligned} \quad (5.7a)$$

$$\begin{aligned} \frac{\partial v}{\partial t} + \frac{\partial}{\partial z}(vw) - \frac{\partial}{\partial z} \left( (v_t + v) \frac{\partial v}{\partial z} \right) + \alpha \left( \frac{\partial}{\partial x}(vu) + \frac{\partial v^2}{\partial y} - \frac{\partial}{\partial x} \left( 2A_h^M \frac{\partial v}{\partial y} \right) \right. \\ \left. - \frac{\partial}{\partial x} \left( A_h^M \left( \frac{\partial u}{\partial y} + \frac{\partial v}{\partial x} \right) \right) + fu - \int_z^\zeta \left[ \frac{\partial b}{\partial y} \right] dz' \right) = -g \frac{\partial \zeta}{\partial y}, \end{aligned} \quad (5.7b)$$

$$\frac{\partial u}{\partial x} + \frac{\partial v}{\partial y} + \frac{\partial w}{\partial z} = 0. \quad (5.7c)$$

$$\frac{\partial \theta}{\partial t} + \nabla \cdot (v\theta) - \frac{\partial}{\partial x} \left( A_h^\theta \frac{\partial \theta}{\partial x} \right) - \frac{\partial}{\partial y} \left( A_h^\theta \frac{\partial \theta}{\partial y} \right) - \frac{\partial}{\partial z} \left( v_t^\theta \frac{\partial \theta}{\partial z} \right) = \frac{1}{c_p \rho_0} \frac{\partial I}{\partial z}. \quad (5.7d)$$

Here,  $u$  and  $v$  are the horizontal velocity components in  $x$  and  $y$  direction, respectively.  $w$  is the vertical velocity component. The vertical coordinate  $z$  ranges from the bottom,  $\eta$  as height function  $-H(x,y)$  for the bathymetry, to the surface  $\zeta(t,x,y)$ . The non-linear free surface  $\zeta$  is computed by a split-explicit mode-splitting technique with drying-and-flooding capability, see the review about numerics of coastal ocean models, Klingbeil et al. (2018). Note that symbol  $\zeta$  in GETM represents the free surface while in ICON vorticity.

Additionally, the viscosities  $\nu$  and  $\nu_t$ , i.e. the kinematic and vertical eddy viscosities, respectively, must be parameterised. The Coriolis frequency ( $f$ ) and gravitational acceleration ( $g$ ) are treated as constants. Horizontal mixing is parameterised by terms containing the horizontal eddy viscosity  $A_h^M$ , see Blumberg and Mellor (1987) for details. The buoyancy ( $b$ ) is defined as

$$b = -g \frac{\rho - \rho_0^O}{\rho_0^O} \quad (5.8)$$

with the density ( $\rho$ ) and a reference density of the ocean ( $\rho_0^O$ ).

Potential temperature ( $\theta$ ) is calculated by equation (5.7d), which contains also a source term for absorption of solar radiation with the solar radiation at depth  $z$  given using specific heat capacity of water ( $c_p^O$ ). The radiation  $I$  in the upper water column is parameterised according to Paulson and Simpson (1977). Similar to the velocity, mixing in equation (5.7d) is parameterised with horizontal diffusivity  $A_h^\theta$  as well as the vertical eddy diffusivity of heat ( $\nu_t^h$ ).

In hydrostatic 3D models, the vertical velocity is calculated by means of equation (5.7c). Due to this, mass conservation and free surface elevation can easily be obtained.

The non-dimensional  $\alpha \in [0, 1]$  incorporates drying and flooding processes in the equations. The value of  $\alpha$  depends on the water depth, for details see Burchard and Bolding (2002) and Burchard et al. (2004).

### Horizontal grid structure

The horizontal grid in GETM is based on the general regular latitude-longitude structured grid defined through prime meridian in London. The whole grid can also be applied through Cartesian coordinates. A rectangular cell of the regular latitude-longitude grid is defined through the surrounding great circles in east and west and rhumb lines in north and south. The number of grid cells is gained by dividing the model domain length with the desired resolution in latitude and longitude direction.

Additionally, curvilinear horizontal grids are also supported by rotation of the regular grid.

The area of a grid element is calculated using spherical trigonometry.

**Remark:** Since GETM is generally applied as regional coastal ocean model in mid-latitude areas, the singularities of the grid structure at the North and South pole are not an issue.

### 5.3.2 The air-sea interface as exchange grid developed for ICONGETM

The previously introduced horizontal discretisations of ICON and GETM are now used to discuss the final discretisation of the air-sea interface. The geometrical details of the coupling interface

are discussed, including the characteristics of the exchange grid. The interpolation steps during the simulation are discussed for state variables and flux data.

The details of the described realisation of the air-sea interface as an exchange grid in ICONGETM are taken from Bauer et al. (2021).

### 5.3.2.1 Coupling via the exchange grid structure

The horizontal grid in ICON is an unstructured grid. In GETM, the horizontal grid is structured. Using the exchange grid (XGrid) philosophy described in Section 5.2.2 leads to an unstructured grid consisting of triangles, quadrilaterals, pentagons or hexagons. A triangulation is applied to gain only triangles, see Figure 5.3, taken from Bauer et al. (2021), for a schematic representation of such an XGrid.

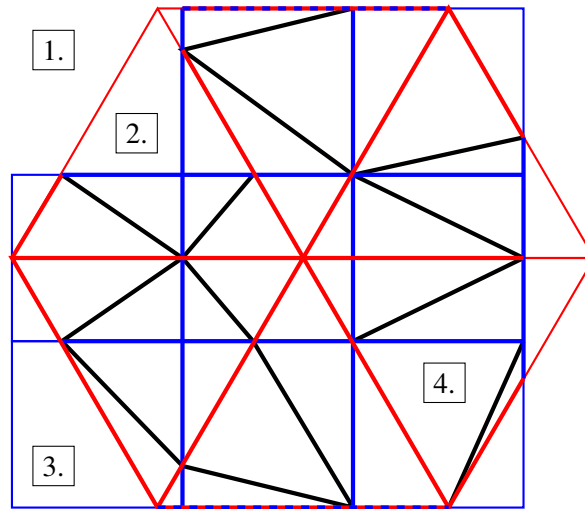


Figure 5.3: 2D exchange grid formed by a triangular atmosphere (red) and a rectangular ocean (blue) grid. The exchange grid consists of edges from the original triangular and rectangular grids (thick red and blue) and additional edges from the triangulation (black). Assuming that only water cells are shown, the four possible combinations of land/ocean masks are labeled. Here the exchange grid is shown for the interpolation from the ocean to the atmosphere grid, therefore, excluding the elements of case 3.

The four different land/sea masking combinations are also shown. In ICONGETM, such an XGrid is calculated using the ESMF\_XGRID class from the ESMF library. Applying equation (5.4) for conservative interpolation, requires the knowledge of the area of the grid elements. The coupling approach described in Section 5.1.1 states that the coupling conditions are met at coupling interface, i.e. numerical realised at the XGrid.

Due to the deeply nested implementation of the parameterisation of the air-sea fluxes in ICON, this strategy could not be followed in ICONGETM. The implementation of the flux calculation in ICON has been developed over the last decades, since they are based on the COSMO model code. Reorganising the implementation of ICON was beyond the scope of this thesis. Therefore, the calculation of the air-sea fluxes is still conducted by ICON and interpolated to GETM. The

list of exchangeable variables is given in Bauer et al. (2021, Table 1). This is the second approach described in Section 5.1.2.

However, since the fluxes at the air-sea interface are not calculated adhering to the coupling conditions, there is a modelling error at the air-sea interface. The error is assumed to be relatively small, especially since the prescribed sea surface temperature (SST) is replaced with the SST from GETM, which is then used for the calculation of the fluxes in ICON. This coupling approach also has a time lag issue. The calculated fluxes are based on the SST from the previous coupling time point. Hence, the smallest possible coupling time step is recommended and applied in the demonstration example in Bauer et al. (2021).

Although the interpolation is carried out in a conservative manner, there are some issues with respect to the land classification used for ICON and GETM.

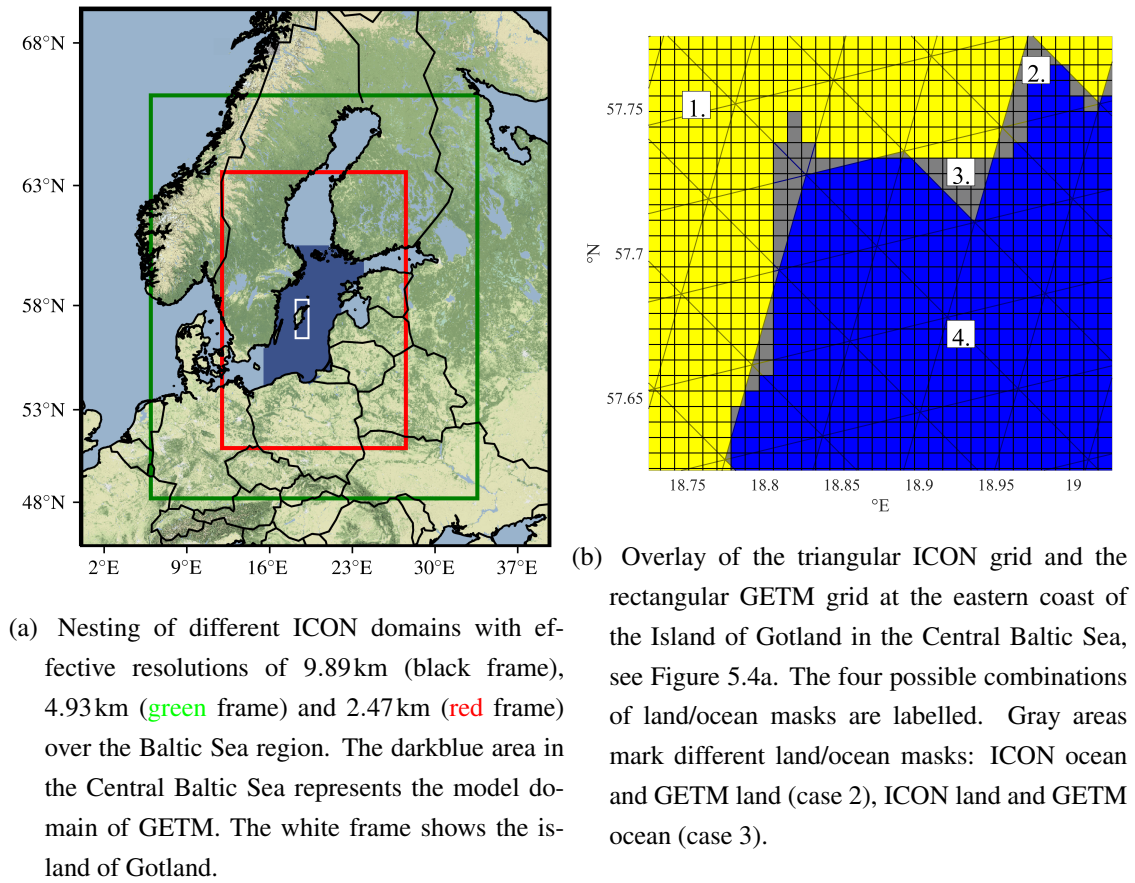


Figure 5.4: Overview of domain for the Central Baltic Sea application and the applied horizontal discretisation in ICON and GETM.

Figures 5.4a and 5.4b are taken from Bauer et al. (2021). They show the horizontal grids of ICON and GETM applied the simulation described in Bauer et al. (2021). The issue with land/ocean masking or land classification is a drawback from applying different grids and resolutions. The discretisation of the surface of the Earth leaves a list of grid elements which are marked as land or ocean. ICON marks a grid element as ocean if at least 50% of the area of a grid element consists of sea water. In ocean models, the land classification is described via the model domain. More details

on the land classification can be found in Bauer et al. (2021). Henceforth, the ICON variables living on grid elements of case 2, see Figures 5.3 or 5.4b, are updated with the contribution of the corresponding GETM grid element variable and the fraction of the ICON variable based on the remaining grid element area. Ideally, the ocean area from the ICON grid element corresponds exactly to the GETM grid elements area. Since the land classification in ICON is user-provided, an update of the land masking should be prepared by the user.

Although the air-sea interface is considered to be horizontally, there is also a minor problem with the vertical direction in the current implementation in the ICONGETM code.

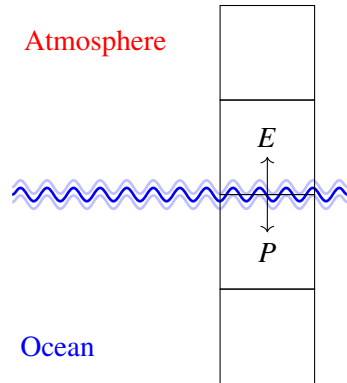


Figure 5.5: Schematic overview of the sea level change in comparison to a fixed a vertical discretisation.

GETM applies the strategy of a free surface, see Section 5.3.1.2. This shifts the air-sea interface in the vertical direction up and down around  $z = 0$ . The vertical discretisation in ICON does not assume such time-varying position of the air-sea interface. Possible reasons for a sea level change are precipitation ( $P$ ), evaporation ( $E$ ), river in flows, temperature ( $T$ ) rise of the water, post glacial movements and many more. A study for the Baltic Sea for example can be found in Gräwe et al. (2019). To overcome this problem, an adaptive vertical discretisation is recommended. However, this is currently not planned for ICON. The error due to the sea level change is relatively small since the changes in the sea level are about 2 mm/a for the Baltic Sea and globally 1.62 mm/a, cf. Dangendorf et al. (2014) and Gräwe et al. (2019).

**Remark:** *Although the coupling scheme developed for ICONGETM is currently not perfectly designed with all the addressed issues, it is safe to assume that the simulation results will improve. The main reason is that the boundary conditions over the ocean in ICON simulations are much more realistic, than any prescribed constant value. The results from the simulation over the Central Baltic Sea support this, see the upcoming Chapter 6.*

A thorough discussion, why the calculation of all fluxes at the coupling interface is recommended, can be found in Bauer et al. (2021, Section 5) and is neglected for the scope of this thesis. An alternative approach has been discussed in Section 5.1.2.

### 5.3.2.2 Interpolation between ICON and GETM

In ICONGETM, the air-sea fluxes are taken from the atmosphere model ICON, because of the very complex and deeply nested implementation in the original ICON model code. Hence, the coupling conditions at the air-sea interface are not met on the exchange grid. Therefore, the interpolation from the source grid to the destination grid via the exchange grid is directly achieved by utilising equation (5.4) twice. Henceforth, the interpolation in ICONGETM can be summarised by

$$\phi_{d_i} \cdot A_{d_i} = \sum_{j=1}^{N_x} \sum_{k=1}^{N_s} \left[ \left( \mathbf{I}^{dx} \right)_{ij} \cdot \left( \mathbf{I}^{xs} \right)_{jk} \cdot A_{s_k} \cdot \phi_{s_k} \right] \quad i = 1, 2, \dots, N_d, \quad (5.9)$$

where  $\phi$  represents the data to be interpolated and  $A_{s_k}$  and  $A_{d_i}$  the area of source and destination grid cells  $i$  and  $k$ . The subscripts and superscripts  $s$ ,  $x$  and  $d$  are representing the source, exchange grid and destination side, respectively.  $N$  is the corresponding number of grid elements, while  $\mathbf{I}$  is the incidence matrix for the interpolations.

The area of the horizontal grids in ICON and GETM are calculated by applying spherical trigonometry. The ESMF\_XGRID library assumes that all grid element edges are components of great circles. This contradicts to GETM grid edges. However, the interpolation by equation (5.9) is not affected by this issue, if and only if the area calculated for the model domains are provided to the ESMF\_XGRID. Otherwise, the area is calculated by the ESMF library with the assumption that each grid edge is on a great circle.

As sketched in Figure 5.1, the interpolation of the state variable mean sea level pressure (MSLP) from ICON to GETM is straight-forward in principle, because ICON provides all quantities over the whole domain. However, in case sea surface fluxes are exchanged, there are two issues if the land/sea masks do not match between ICON and GETM. First, there is a physical inconsistency, when surface fluxes parametrised over land cells in ICON are transferred to ocean cells in GETM (case 3). Second, when ICON applies sea surface fluxes in ocean areas that are represented by land in GETM (case 2), the fluxes are not conserved in the global atmosphere-ocean-system. This latter case demonstrates that the conservative interpolation via the exchange grid is not sufficient to guarantee a conservative flux exchange.

Figure 5.1 sketches also the interpolation of the sea surface temperature (SST) from GETM to ICON. The update of an ICON ocean cell that is partly covered by a GETM land cell (case 2) needs some remarks. For the contribution from a GETM land cell to an ICON ocean cell, the SST value of the ICON cell is applied.





## Chapter 6

# Multirate methods and their applications for coupled atmosphere-ocean models

The previously described coupling techniques are differing between how the fluxes at boundaries are provided and how a two-way feedback mechanism for the modelled physical processes at the air-sea interface is achieved. Two problems occur for coupled models. First, a spatial interpolation is required if the horizontal discretisation of the atmosphere and ocean at the air-sea interface is different. Second, a timing issue occurs while integrating the atmosphere and ocean model on different time scales, see Bauer et al. (2021). While the previous chapter explained among others how the interpolation at the air-sea interface can be applied, this chapter presents how multirate methods are utilised for coupled models to overcome the time scaling issue.

The details of the numerical implementation for the one-dimensional coupled atmosphere-ocean model from Section 5.2.1 are described in Section 6.1. Additionally, the details of the simulation of a coupled idealised experiment are shown.

Furthermore, the application of multirate methods in the coupled model ICONGETM is discussed in Section 6.2. Moreover, the results of the simulation with ICONGETM over the Central Baltic Sea are also presented.

### 6.1 Application of multirate methods to idealised coupled atmosphere-ocean models

This section discusses the application of multirate methods to idealised coupled atmosphere-ocean models. The one-dimensional coupled model introduced in Section 5.2.1 is used. A detailed description of the implementation of the one-dimensional model is presented in Section 6.1.1. The simulation results of the coupled experiment are discussed in Section 6.1.2. Benchmark experiments for one-dimensional atmosphere and ocean models from the literature, see e.g. Burchard et al. (1999), Umlauf and Burchard (2005), and Weng and Taylor (2006), are used to compare

the simulation results of coupled experiment. The application of the multirate methods is demonstrated and their performance is evaluated in Section 6.1.3.

### 6.1.1 Implementation details for the 1D model

The one-dimensional idealised coupled atmosphere-ocean model from Section 5.2.1 has been implemented in MATLAB<sup>®</sup>. The code can be found on Zenodo, see Bauer (2024).

The atmosphere model is based on the example studies from Cuxart et al. (2006), Weng and Taylor (2006), and Svensson et al. (2011). The studies apply the same set of equations and discuss the results based on different set of parameters. Especially the work from Cuxart et al. (2006) and Svensson et al. (2011) indicate that the applied one-dimensional model can be regarded as benchmark example. The ocean model is based on the entrainment examples from the GOTM model. For details on the entrainment experiment see Umlauf and Burchard (2005). The implemented one-dimensional coupled atmosphere-ocean model is given by the set of equations from Section 5.2.1, the coupling conditions from equation (5.3), the following described spatial discretisation and given boundary conditions.

The method of lines is applied. A non-necessarily identical equidistant splitting of the calculation domain is utilised, i.e.  $\Delta z = \text{const}$ . For the atmosphere and ocean side the chosen spacing is  $\Delta z = 1 \text{ m}$  and  $\Delta z = 0.5 \text{ m}$ , respectively. The vertical staggering is based on the Lorenz grid, cf. Figure 2.2c. No horizontal discretisation is required. Figure 6.1 sketches the vertical discretisation and staggering at the air-sea interface.

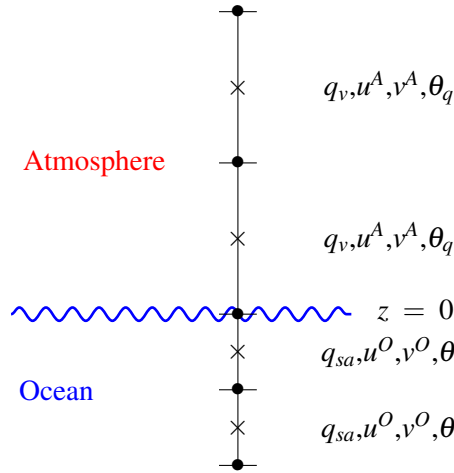


Figure 6.1: Vertical discretisation at the air-sea interface for the one-dimensional idealised coupled atmosphere-ocean model.

The atmospheric quantities  $q_v, u^A, v^A$  and  $\theta_q$  and the ocean quantities  $q_{sa}, u^O, v^O$  and  $\theta$  are living in the centre of a layer,  $\times$  in Figure 6.1. The specific turbulent kinetic energy ( $k$ ) and dissipation ( $\varepsilon$ ) components are defined at layer interfaces,  $\bullet$  in Figure 6.1.

For the vertical derivative, the central differential quotient is applied as discrete spatial operator.

However, at the boundaries, i.e. at the bottom of the sea, the sea surface and top of the atmosphere, the central differential quotient is replaced by a one-sided second order differential quotient which also helps to formulate the parameterisation at the boundaries.

At the air-sea interface, i.e. at  $z = 0$ , the coupling conditions are valid in a single point. Therefore, no horizontal interpolation at the air-sea interface is required.

The boundary conditions at the ocean bottom and the top of the atmosphere can be summarised by

Atmosphere (top)	Ocean (bottom)
$q_v = 0$	$(v_t^h + v^{sa}) \frac{\partial q_{sa}}{\partial z} = 0 \text{ ms}^{-1}$
$u = 8 \text{ ms}^{-1}$	$u = 0 \text{ ms}^{-1}$
$v = 0 \text{ ms}^{-1}$	$v = 0 \text{ ms}^{-1}$
$\theta_q = 268 \text{ K}$	$\theta = 277.15 \text{ K}$
$K_m \frac{\partial k}{\partial z} = 0 \text{ m}^3/\text{s}^3$	$v_k \frac{\partial k}{\partial z} = 0 \text{ m}^3/\text{s}^3$
$K_m \frac{\partial \varepsilon}{\partial z} = 0 \text{ m}^3/\text{s}^4$	$v_\varepsilon \frac{\partial \varepsilon}{\partial z} = -(c_\mu^0)^3 v_\varepsilon \frac{k^{3/2}}{\kappa(z+z_0)^2}.$

At the bottom of the ocean ( $z = -50 \text{ m}$ ), the no-slip conditions are applied. Additionally, the no flux condition for salinity as well as specific turbulent kinetic energy ( $k$ ) is assumed. This results in a flux condition for the dissipation ( $\varepsilon$ ), cf. Burchard and Petersen (1999).

Furthermore, the coupling conditions do not include the turbulent quantities, because it is assumed that no turbulent energy is transferred through the air-sea interface. Hence, boundary conditions at the air-sea interface for  $k$  and  $\varepsilon$  must be provided. For the ocean with no-free surface, the boundary conditions are given by

$$v_k \frac{\partial k}{\partial z} = 0 \text{ m}^3/\text{s}^3$$

$$v_\varepsilon \frac{\partial \varepsilon}{\partial z} = -(c_\mu^0)^3 v_\varepsilon \frac{k^{3/2}}{\kappa(z+z_0)^2}.$$

For the atmosphere, the original benchmark experiment from Weng and Taylor (2006) integrated also the specific turbulent kinetic energy ( $k$ ) at the air-sea interface. Hence, there is only one boundary condition for  $\varepsilon$ , which is given through the assumption that the production balances the dissipation, i.e.

$$P_s + P_b - \varepsilon = 0 \text{ m}^2/\text{s}^3$$

with shear production ( $P_s$ ) and buoyancy production ( $P_b$ ).

For the top of the atmosphere ( $z = 400 \text{ m}$ ), the applied conditions are Dirichlet conditions for the state quantities,  $q_v$ ,  $u^A$  and  $v^A$ ,  $\theta_q$ . The no-flux conditions are used for the turbulent quantities  $K_m \frac{\partial k}{\partial z}$  and  $K_m \frac{\partial \varepsilon}{\partial z}$ .

The coupled atmosphere-ocean model is then defined as IBVP by the set of equations from Section 5.2.1, the state equations, Section 2.2.4, the coupling conditions from equation (5.3) and the here presented boundary conditions. The initial conditions are taken from the literature, cf. Burchard et al. (1999), Umlauf and Burchard (2005), and Weng and Taylor (2006).

### 6.1.2 Simulation results for the 1D model

The results of the simulation of the one-dimensional coupled atmosphere-ocean model introduced in the previous section are discussed in the following. The simulations were carried out with the classical Runge–Kutta method of fourth order (RK4), the M3GARK135-222 method and the MIS54 method from Section 4.3. All methods were applied equally, i.e. the results of the simulations were compared.

For the sake of simplicity, the results are presented in a similar way as the benchmark examples in the literature, see Burchard et al. (1999) and Weng and Taylor (2006). At first, it is shown that the implemented atmosphere and ocean models produce the results from the literature. The results from the coupled experiment are discussed with focusing on the air-sea interface.

#### Single Atmospheric boundary layer experiment

Weng and Taylor (2006) discussed a simple stably stratified atmospheric boundary layer (ABL) model with a specified cooling rate and no-slip conditions at the air-sea interface. The study includes various combinations of the parameters cooling rate (e.g.  $0.25 \text{ K h}^{-1}$ ), geostrophic wind (e.g.  $u_g = 8 \text{ m s}^{-1}$ ,  $v_g = 0 \text{ m s}^{-1}$ ) and surface roughness length (e.g.  $z_A = 0.1 \text{ m}$ ). For this thesis, the A2 parameter combination from Weng and Taylor (2006) has been applied. The simulation results from this experiment, see Figure 6.2, are comparable with the presented results in Weng and Taylor (2006).

**Remark:** *Although the development of a stable stratified boundary layer is achieved in this experiment, there is a main difference to the results from Weng and Taylor (2006, Figure 2). The height, where the boundary layer ends, is different. The A2 experiment shows a boundary layer height of approximately 175 m in Weng and Taylor (2006). A boundary layer height of approximately 290 m shows the experiment conducted for this thesis. However, this is explained by the fact that the applied turbulence closure schemes are different and the boundary layer height is very sensitive to turbulent quantities, e.g. specific heat flux ( $w'\theta'$ ), shear stress ( $\tau$ ) or turbulent kinetic energy, cf. Cuxart et al. (2006).*

#### Single Entrainment experiment

The entrainment experiment from the GOTM model documentation has been chosen as a benchmark experiment for the one-dimensional ocean model. It is an ideal scenario to verify the model against available experiments, see Umlauf and Burchard (2005). A constant horizontal momentum flux is applied at the air-sea interface and the no-flux condition is applied for the specific heat flux. The simulation shows how an accelerated thin near-surface layer is gradually entraining into the stratified non-turbulent interior region, see Figure 6.3.

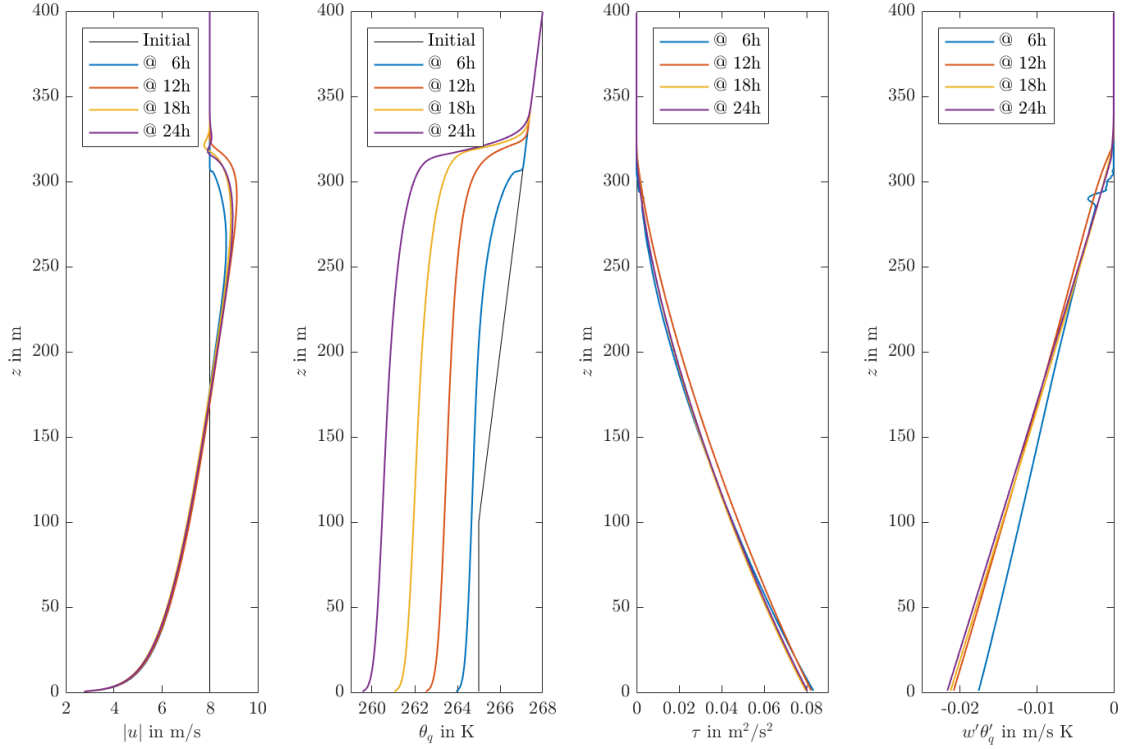


Figure 6.2: Results of the one-dimensional atmospheric boundary layer experiment. A stable boundary layer is achieved.

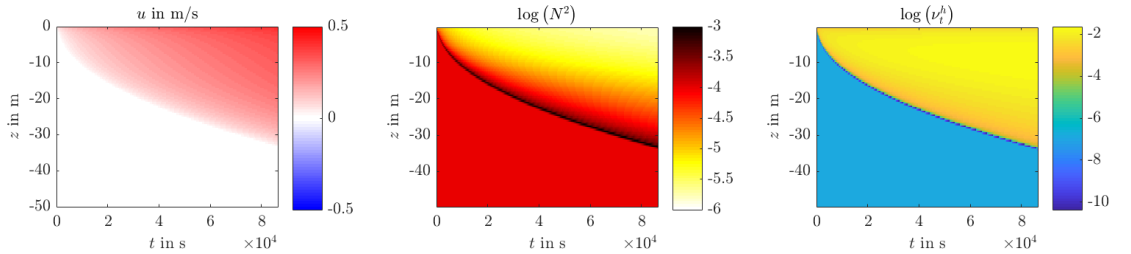


Figure 6.3: Results of the implemented entrainment experiment. There are no significant differences to the result from Burchard et al. (1999) and Umlauf and Burchard (2005).

Note that the results of this experiment are very well comparable to the results given in the GOTM model documentation.

### Coupled Atmospheric Boundary Layer - Entrainment experiment

Both single experiments were used in a coupled scenario. As preparation for the coupled experiment, two small changes had to be applied to the single Entrainment experiment. The Coriolis frequency and gravitational acceleration are set to the values of the atmospheric boundary layer experiment. This ensures that both one-dimensional models are set to same position on Earth since the Coriolis frequency and gravitational acceleration are not necessarily identical everywhere.

At first, the entrainment experiment was repeated with the applied changes. The results are shown in Figure 6.4.

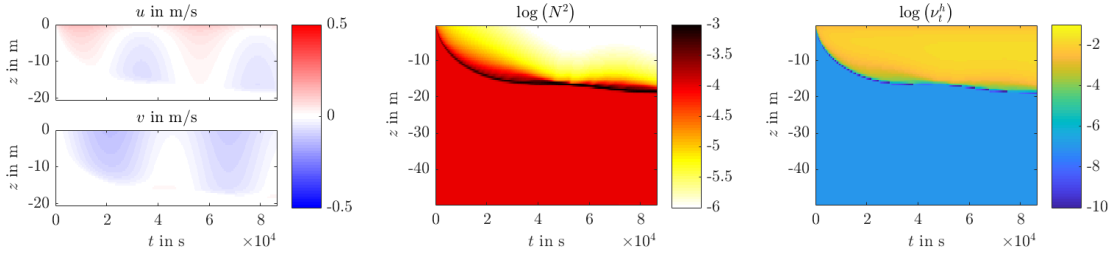


Figure 6.4: Results of the implemented entrainment experiment with applied Coriolis frequency and gravitational acceleration from the atmospheric boundary layer experiment. Due to the applied Coriolis frequency, there is a velocity in both directions. The acceleration of the thin near-surface layer is not as deep into the stratified non-turbulent interior region.

Due to the changing of the Coriolis frequency and gravitational acceleration, the results of the ocean model differ to the original entrainment experiment. Adding Coriolis frequency to the original experiment leads to evolving velocities in zonal and meridional directions. Furthermore, it is shown that the accelerated thin near-surface layer is gradually entraining not as deep into the stratified non-turbulent interior region, c.f. Figure 6.3 and Figure 6.4.

Moreover, in the coupled experiment, the coupling conditions at the air-sea interface, i.e. equation (5.3), were solved at each time step.

In comparison to the single case, the boundary layer height is significantly lower in the coupled experiment. The same holds for the velocity, wet equivalent potential temperature, shear stress and heat flux. The stable stratified atmospheric boundary layer is achieved. However the boundary layer height after 24 h is less high compared to the single case, cf. Figure 6.2 and Figure 6.5.

For the ocean, the main difference is that the acceleration of the thin near-surface layer into the stratified non-turbulent interior region is even less deep than in the single experiment. Furthermore, the squared Brunt-Väisälä frequency

$$N^2 = -\frac{g}{\rho_0} \frac{\partial \rho}{\partial z}$$

becomes negative close to the air-sea interface. This is explained by the loss of fresh water due to evaporation at the air-sea interface since the atmosphere was assumed to be dry.

The coupling conditions were not solved when  $N^2 < 0$  close to the air-sea interface and a constant stability function for the calculation of the vertical eddy viscosity was used. However, if a non-constant stability function was implemented according to Burchard and Petersen (1999, Equations (16) and (17)), the coupling conditions were solved.

Figure 6.7 shows how velocity (left panel), temperature (centre panel) and various fluxes (right panel) at the air-sea interface are evolving over time. Shortly after the initialisation phase, the velocity is significantly decreasing towards zero. However, the no-slip condition is never reached. A small increasing over time is observed after approximately one hour.

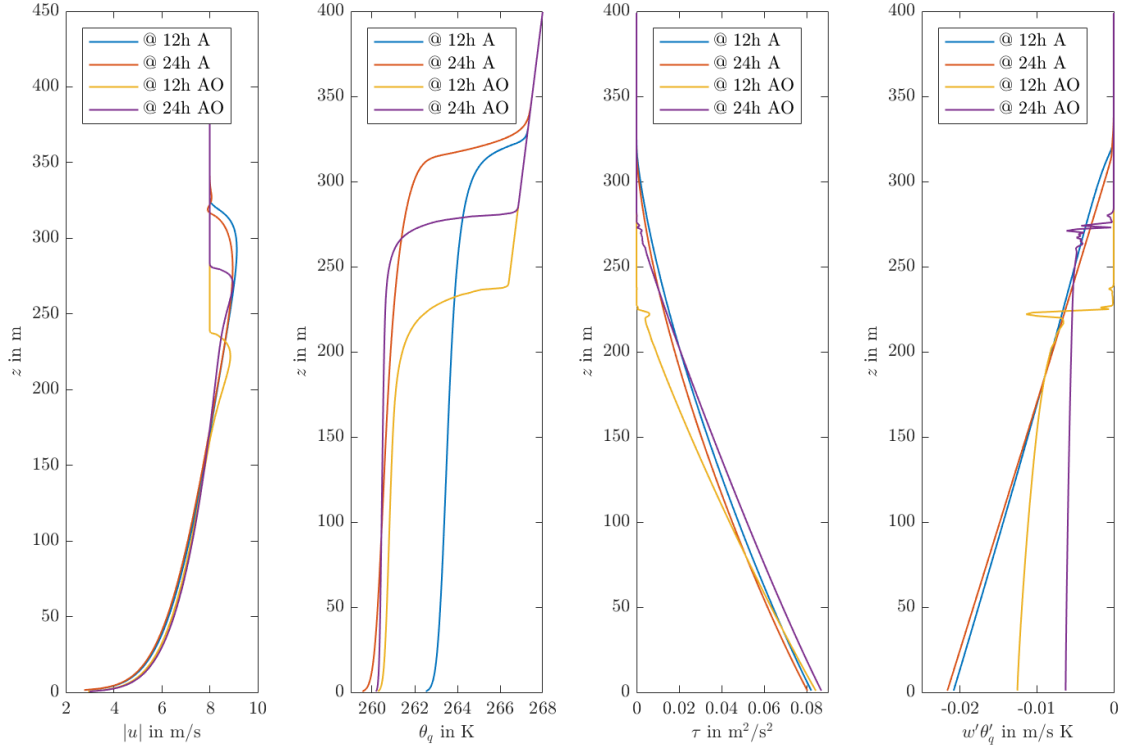


Figure 6.5: Results of the coupled one-dimensional atmospheric boundary layer experiment. The boundary layer height is significantly lower than for the single experiment. The same holds for the velocity, wet equivalent potential temperature, shear stress and heat flux.

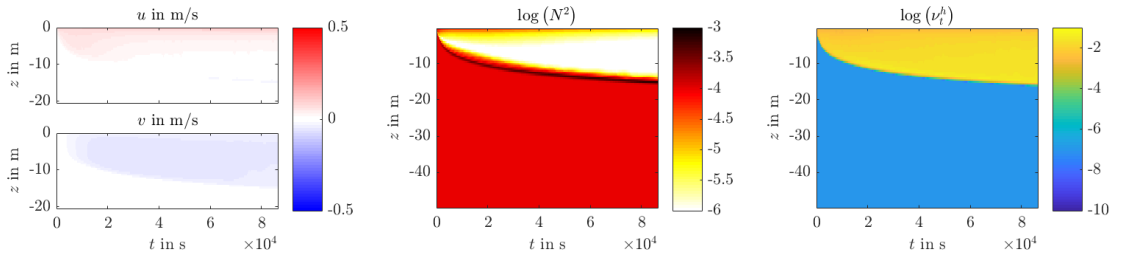


Figure 6.6: Results of the coupled one-dimensional entrainment experiment. The acceleration of the thin near-surface layer into the stratified non-turbulent interior region is even less deep than in the single experiment. Close to the air-sea interface, the Brunt-Väisälä frequency becomes negative and, therefore, only the real component of the logarithm is drawn.

The sea surface temperature is more than 18K higher compared to the original experiments. Hence, there is no cooling for the atmosphere. However, after approximately one hour the temperature is decreasing very slowly. The specific heat flux presented on the right panel in Figure 6.7 shows a strong trend towards zero. This suggests an asymptotic behaviour for the sea surface temperature over time. Additionally, the mass fluxes also show a decreasing towards zero, similar to

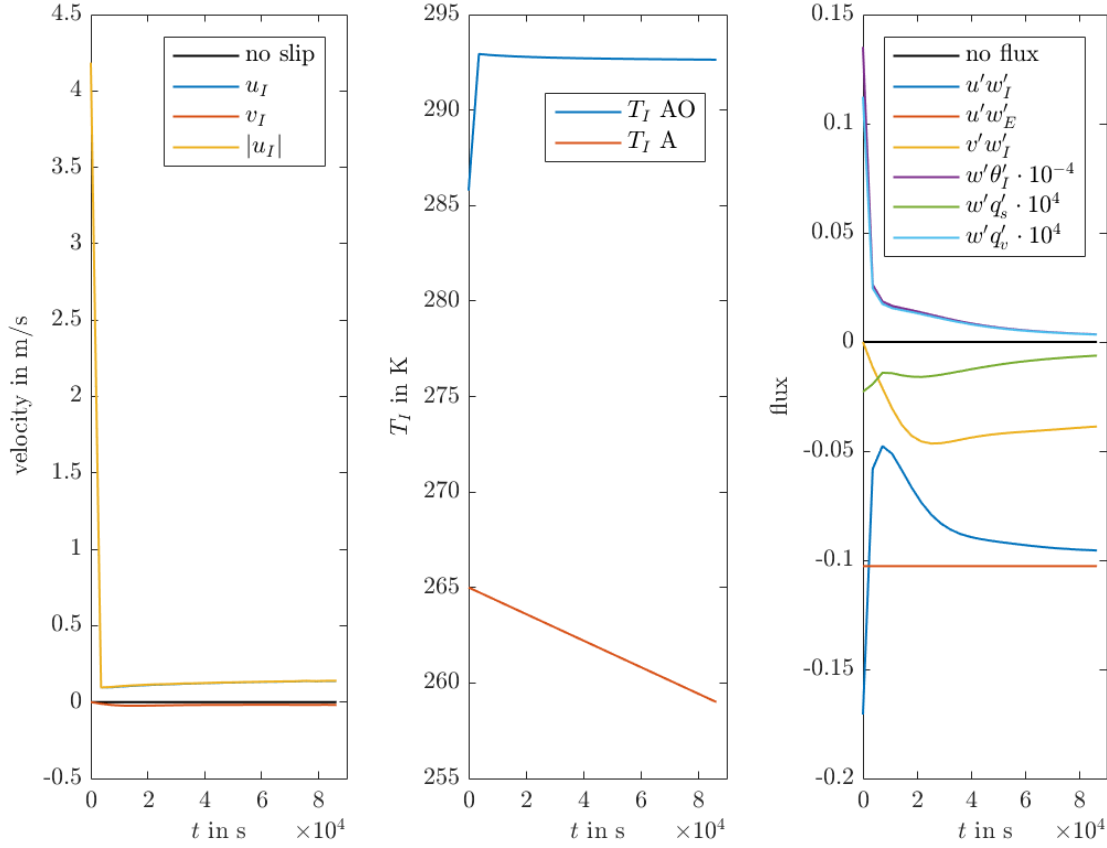


Figure 6.7: Results of the coupling at the air-sea interface in comparison to the boundary conditions from the original experiments. The no-slip (left panel) and no flux (right panel) condition are also shown as well as the constant cooling (centre panel). The velocity, temperature and various fluxes at the air-sea interface are presented over time.

the specific heat flux. Thus, the atmospheric layer at the air-sea interface is almost saturated. The water vapour is only vertically uplifted by turbulence. Hence, fresh water will further be evaporated, if turbulence in the atmosphere uplifts the water vapour.

Another interesting effect is observed for the momentum flux. Although the constant momentum flux applied in the original entrainment experiment (marked as  $uw_E$ ) is not recovered, the zonal momentum flux seems to trend towards a very similar value. However, due to the applied Coriolis frequency, there is also a meridional momentum flux approximately half of the zonal momentum flux.

Comparing the simulated air-sea interface values with the boundary conditions from the original experiments, it can be indicated that the conditions from the entrainment experiment might be closely recovered if the simulation is continued.



### 6.1.3 Performance evaluation of the applied multirate methods

The different results between the single and coupled atmosphere and ocean experiments are discussed in the previous section. This section focus on the efficiency of each experiment w/o multirate methods. Since efficiency is not based on the number of function evaluations or on the time step itself, the overall simulation time for a solution is evaluated. All different simulations were carried out on the same computer.

Following the results of the benchmark simulations from the literature, the CFL criterium is used to approximate the time steps for the atmosphere and ocean models. The expected velocities and the resolution of the different horizontal spatial discretisations in the atmosphere and ocean models lead to CFL numbers, which require a time step of approximately 0.1 s and 1 s, respectively. Hence, a multirate method applied in the sense that the ocean model is treated as slow part is recommended. The model can either be integrated in the structure of asynchronous or synchronous coupling, see equation (2.40). The synchronous structure is chosen for all experiments. The coupling is utilised with the same time scale of the ocean model.

Each experiment was simulated with the classical Runge–Kutta method of fourth order (RK4). Furthermore, the M3GARK135-222 method and the MIS54 method from Section 4.3 were used as a multirate method.

Technically, there are no limitations on how the slow and fast components shall be chosen. For example, additive (Sandu and Günther (2015)), operator (Bazavov (2022)) or split-explicit (Knoth and Wensch (2014)) splitting are possible approaches. However, for coupled atmosphere-ocean models it is recommended to integrate rapidly changing parts as fast component. The splitting into the slow, fast and super fast component for the M3GARK135-222 method was chosen such that:

- slow part:** coupling conditions and non-turbulent quantities from the ocean model,
- fast part:** turbulent quantities from the ocean model and non-turbulent quantities from the atmosphere model,
- super fast part:** turbulent quantities from the atmosphere model.

Atmosphere	Ocean
$\frac{\partial q_v}{\partial t} = \frac{\partial}{\partial z} \left( K_h \frac{\partial q_v}{\partial z} \right)$	$\frac{\partial q_{sa}}{\partial t} = \frac{\partial}{\partial z} \left( (v_t^{sa} + v^{sa}) \frac{\partial q_{sa}}{\partial z} \right)$
$\frac{\partial u}{\partial t} = \frac{\partial}{\partial z} \left( K_m \frac{\partial u}{\partial z} \right) + f \cdot (v - v_g)$	$\frac{\partial u}{\partial t} = \frac{\partial}{\partial z} \left( (v_t + v) \frac{\partial u}{\partial z} \right) - \frac{1}{\rho} \frac{\partial p}{\partial x} + f \cdot v$
$\frac{\partial v}{\partial t} = \frac{\partial}{\partial z} \left( K_m \frac{\partial v}{\partial z} \right) - f \cdot (u - u_g)$	$\frac{\partial v}{\partial t} = \frac{\partial}{\partial z} \left( (v_t + v) \frac{\partial v}{\partial z} \right) - \frac{1}{\rho} \frac{\partial p}{\partial y} - f \cdot u$
$\frac{\partial \theta_q}{\partial t} = \frac{\partial}{\partial z} \left( K_h \frac{\partial \theta_q}{\partial z} \right)$	$\frac{\partial \theta}{\partial t} = \frac{\partial}{\partial z} \left( (v_t^h + v^h) \frac{\partial \theta}{\partial z} \right)$
$\frac{\partial k}{\partial t} = P_s + P_b - \varepsilon + \frac{\partial}{\partial z} \left( \frac{K_m}{\sigma_k} \frac{\partial k}{\partial z} \right)$	$\frac{\partial k}{\partial t} = P_s + P_b - \varepsilon + \frac{\partial}{\partial z} \left( \frac{v_t}{\sigma_k} \frac{\partial k}{\partial z} \right)$
$\frac{\partial \varepsilon}{\partial t} = c_1 \frac{\varepsilon}{k} (P_s + P_b) - c_2 \frac{\varepsilon^2}{k} + c_3 \frac{\partial}{\partial z} \left( \frac{K_m}{\sigma_\varepsilon} \frac{\partial \varepsilon}{\partial z} \right)$	$\frac{\partial \varepsilon}{\partial t} = c_1 \frac{\varepsilon}{k} (P_s + P_b) - c_2 \frac{\varepsilon^2}{k} + c_3 \frac{\partial}{\partial z} \left( \frac{v_t}{\sigma_\varepsilon} \frac{\partial \varepsilon}{\partial z} \right)$

The right hand side of the equations are coloured according to the slow, fast and super fast splitting.

For the MIS54 method, the ocean model and the coupling conditions are considered to be the slow part while the atmosphere model is the fast part which was integrated with the simple Euler method.

The time steps for each experiment were chosen as follows,

	RK4	M3GARK135-222	MIS54 + $m_i$
Entrainment	3.0 s	15 s	6.0 s + 4
ABL-A2	0.1 s	0.5 s	0.2 s + 2
no coupling	0.1 s	0.5 s	1.0 s + 5
coupled	0.1 s	0.4 s	1.0 s + 8

where  $m_i$  is the number of fast time step evaluation for one slow time step for the MIS54 method. The coupling conditions were evaluated at each slow time step, especially since synchronous coupling was applied.

Applying the RK4 method for all experiments, the smaller time step from the ABL-A2 experiment must be applied for the coupled experiments as well. Thus, the ocean model is integrated much more frequent than necessary during the coupled experiments, which is not efficient.

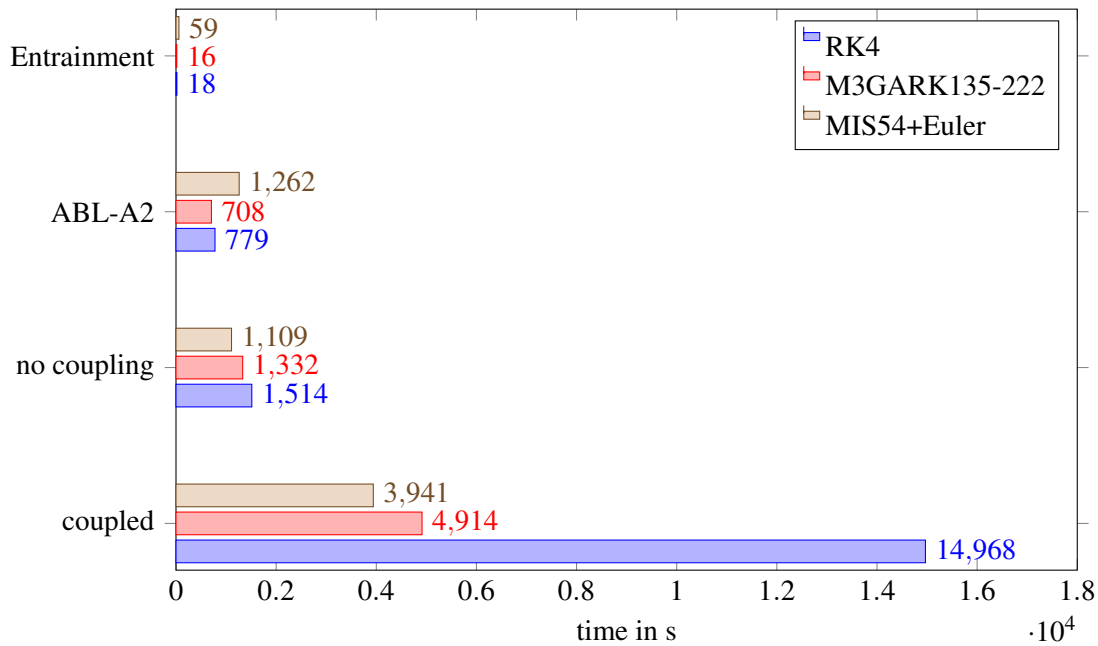


Figure 6.8: Simulation time for each experiment and applied method.

Figure 6.8 shows how the simulation time is evolved for each experiment. Note that each experiment was conducted at least three times and the average simulation time is shown.

At first, the multirate methods were applied to the single experiments (Entrainment + ABL-A2). The splitting was chosen such that the turbulent quantities were considered to be the super fast part for the M3GARK135-222 method and the fast part for MIS54+Euler method. The computation time applying multirate methods show a decrease of approximately 10% for the M3GARK135-222 method and a larger increase for the MIS54+Euler method compared to the RK4 method.

Hence, the chosen splitting for the MIS54 method is not suitable for the single experiments.

For the coupled experiments, the multirate methods showed a significant improvement of the computation time. This is expected, since the atmosphere and ocean models are integrated with their desired time step. The large differences between the single and coupled experiment show the influence of solving the coupling conditions at the small time step. Henceforth, the most expensive part is solving the coupling conditions at each time step, i.e. the overhead for solving the non-linear system of equations at the air-sea interface is significant.

The application of the M3GARK135-222 method showed a decrease of approximately 66 % of the computation compared to the RK4 method in the coupled case. However, the MIS54 method was even faster and required approximately 25 % of the simulation time of the RK4 method. The reason is the much larger time step for the slow component. Therefore, the expansive solving of the coupling conditions were not as often conducted as for the M3GARK135-222 and RK4 method. Overall, solving conditions at each coupling time step for more accurate simulation results comes with a longer simulation time. Applying multirate methods will significantly reduce the simulation time compared to standard methods, which in the end is more efficient.

**Remark:** *This section focuses on the application of multirate methods for a one-dimensional coupled atmosphere-ocean model. A two-dimensional model was developed and successfully tested. The results confirmed the performance of the multirate methods observed in the one-dimensional case.*

## 6.2 Multirate methods in ICONGETM

The previous section discussed the application of multirate method for a one-dimensional coupled atmosphere-ocean model. This section focuses on the coupled model ICONGETM.

Before the details of the multirate approach in ICONGETM are discussed, a brief summary of the time integration applied for ICON and GETM is presented, Section 6.2.1. The conducted experiment over the Central Baltic Sea with ICONGETM has been published in Bauer et al. (2021). The configuration is summarised in Section 6.2.2. Furthermore, the simulation results from Bauer et al. (2021) are presented to demonstrate the improvement of the model results due to the coupling. Sections 6.2.3 and Section 6.2.4 summarises the simulation results for the atmosphere and ocean, respectively.

### 6.2.1 Multirate time integration in ICON, GETM and ICONGETM

The time integration scheme utilised for ICON is described in Zängl et al. (2015). In general, a two-time-level predictor-corrector scheme is applied. Additionally, a time splitting between tracer advection, horizontal diffusion, fast physic parameterisations and the dynamical core is utilised, see Zängl et al. (2015). This is already a multirate approach, i.e. for the integration of ICON multiple time steps are considered. The user can control these time steps to some extend. The details of the implementation of the time integration scheme in ICON are not necessarily important for

this work. They can be found in Zängl et al. (2015).

Burchard (2002) and Burchard et al. (2004) described the temporal discretisation applied in GETM. A splitting into a baroclinic and a fast barotropic mode has been utilised, i.e. internal and external system, respectively. The time scales for the baroclinic and barotropic modes depend on the CFL number for the advection and the vertical spatial resolution, respectively. The method from Blumberg and Mellor (1987) has been adopted, since the free surface elevation is well resolved, which is a requirement for flooding and drying processes, cf. Burchard et al. (2004). Hence, a multirate approach for the integration of GETM is applied. For the details of mode splitting and the time integration in GETM, see e.g. Klingbeil et al. (2018).

Multirate schemes are applied for the integration of ICON and GETM. However, due to effort for restructuring the implementation of new multirate methods, an user-specified multirate method is not applied to the coupled model ICONGETM. Therefore, the question raises whether a multirate approach is already applicable for ICONGETM because the ICON and GETM do.

Bartel and Günther (2020) investigated whether component-wise partitioning, cf. equation (2.39), in multirate schemes is consistent and converges.

**Theorem 6.2.1.** *Consistency of fully-decoupled multirate schemes - Bartel and Günther (2020, Theorem 1)*

*Given the coupled ODE-IVP (2.39), where  $f^O$  and  $f^A$  are Lipschitz with respect to the sought solution. Furthermore, two basic integration schemes of order  $p$  are applied: one for  $f^O$  with macro time step  $H$ , a second for  $f^A$  with fixed multirate factor  $m \in \mathbb{N}$  steps of size  $h$ . If these integration schemes are combined with two extrapolation procedures for the coupling variables of order  $p - 1$ , the resulting fully decoupled multirate scheme has order  $p$*

A fully decoupled multirate approach is given when the slow and fast variables are integrated in parallel using extrapolated waveforms based on information from the initial data of the current macro step at time  $t$ . The proof can be found in Bartel and Günther (2020). Bartel and Günther (2020, Corollary 1 and 2) follow the ideas of Bartel and Günther (2020, Theorem 1) for slowest-first and fastest first multirate schemes. With all three theorems / corollaries it can be stated that if the time integration methods of the atmosphere and ocean models in a coupled model are at least of order  $p$  and the applied inter- / extrapolation method for the coupling variables is of order  $p - 1$ , the overall multirate scheme is of order  $p$ .

Following these ideas, the time integration scheme applied to the model ICONGETM is of order  $p$  if the time integration schemes of ICON and GETM are of order  $p$  and the interpolation at the air-sea interface via the ESMF exchange grid is of order  $p - 1$ . Moreover, ICONGETM inherits the lowest order of the time integrations schemes applied to ICON and GETM. Since the interpolation in ICONGETM is conducted with the first-order conservative interpolation method from the ESMF library, see Bauer et al. (2021), the overall convergence of ICONGETM can only be of order  $p = 2$ . However, the time integration scheme in GETM is based on explicit and implicit RK approach, which implies even only order  $p = 1$ .

Generally speaking, this can be compared to the additional coupling conditions from the multirate methods for order  $p = 1$ . Since for order  $p = 1$ , no additional condition must be fulfilled for mul-

tirate methods, it can be stated that ICONGETM converges at least with order  $p = 1$ .

However, a thorough investigation whether an even higher order applies to ICONGETM was not conducted. An analytical investigation requires a detailed analysis of the time integration schemes implemented for ICON and GETM. Furthermore, additional multirate conditions for order  $p \geq 2$  have to be derived for these time integration schemes.

### **6.2.2 Central Baltic Sea experiment: model setup**

The configuration of the ICONGETM model is described in this section. Note that the following has been taken and summarised from Bauer et al. (2021).

For demonstration purposes, the developed model ICONGETM has been applied to the Central Baltic Sea, see Figure 5.4a. High-resolution uncoupled, one-way and two-way coupled simulations were carried out and compared. The modelling period July 1 – 21, 2012 is chosen.

The general spatial and temporal discretisation of ICON and GETM was explained in Section 5.3. More details on the exact horizontal resolution and time steps applied can be found in Bauer et al. (2021). The exchanged variable at the air-sea interface are listed in Bauer et al. (2021, Table 1).

The boundary data for ICON were provided through the 6-hourly IFS data from ECMWF. Initial conditions are also obtained by interpolation from IFS data.

For GETM, at the open boundaries, hourly data for temperature, salinity, sea surface elevation and normal depth-averaged velocity from the Baltic Sea setup of Gräwe et al. (2019) are prescribed. Furthermore, the freshwater discharge of the five major rivers entering the model domain is prescribed, for details see Chrysagi et al. (2021). The initial temperature and salinity distribution for the present study was obtained by continuing the original simulations of Holtermann et al. (2014) and subsequent distance-weighted nudging with available measurements from the HELCOM database ([www.helcom.fi](http://www.helcom.fi)) below 50m depths. During a spin-up period from 20 May – 30 June 2012, GETM is run uncoupled.

In the uncoupled simulation, GETM calculates the air-sea fluxes according to the bulk parameterisation of Kondo (1975) in terms of hourly meteorological CFSv2 data, see Saha et al. (2014), read from file. During the one- and two-way coupled simulations the coupling is processed with process the air-sea fluxes from ICON.

### **6.2.3 Effects of interactive coupling in the atmosphere**

The coupled simulation results are compared to the uncoupled simulations to investigate the effects of the two-way feedback coupling in the atmosphere. The results presented in this section have been taken and summarised from Bauer et al. (2021).

In the uncoupled and one-way coupled simulations, ICON uses its prescribed internal sea surface temperature (SST), which does not show any pronounced temperature gradients due to oceanic eddies or coastal upwelling. Short-term and small-scale variations are only considered in the two-way coupled ICONGETM run, see Figure 6.9, with the SST simulated and provided in high-resolution by GETM.

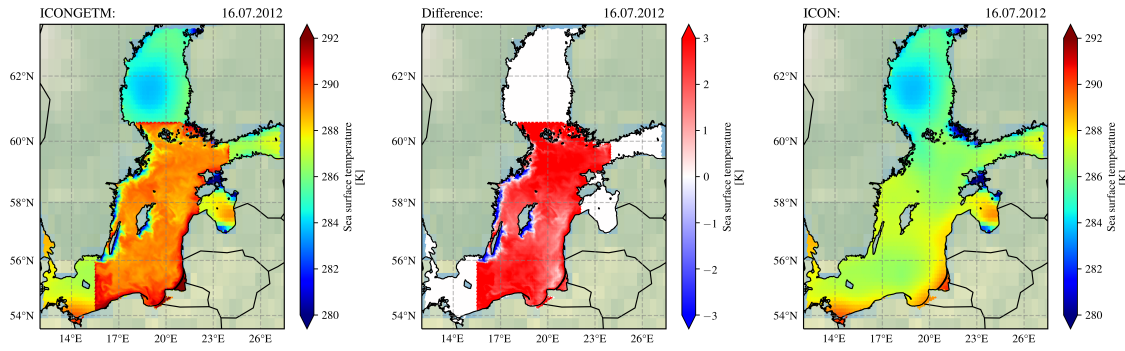


Figure 6.9: Daily mean sea surface temperature (SST) from the two-way coupled ICONGETM run (left panel), and the uncoupled/one-way coupled ICON run (right panel), as well as the difference (central panel; ICONGETM minus ICON) for 16 July 2012. Outside the domain of simulated SST in the Central Baltic Sea, the two-way coupled ICONGETM run also uses the prescribed ICON-internal SST.

The ICON-internal SST is between 0.5 K and 2 K colder. The overall warmer surface of the Baltic Sea in the two-way coupled ICONGETM run causes a predominantly warmer lower troposphere. As a result, the daily mean 2 m temperature is about 0.5 K to 2 K higher, cf. Figure 6.10.

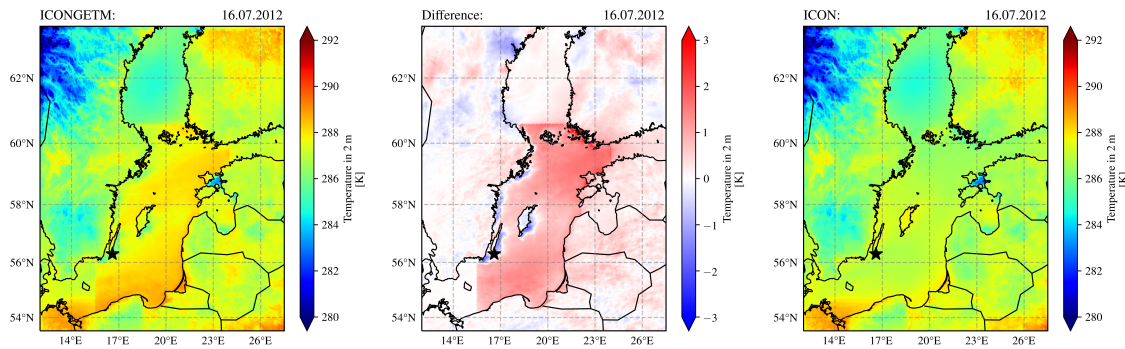


Figure 6.10: Daily mean 2 m air temperature from the two-way coupled ICONGETM simulation (left panel) and the uncoupled/one-way coupled ICON simulation (right panel), as well as the difference (central panel; ICONGETM minus ICON) for 16 July 2012.

However, over the upwelling regions, where cold deep water has risen to the surface, only the two-way coupled ICONGETM run is able to reproduce the cooling in the 2 m temperatures of between minus 1 K to 2 K against the surroundings. Thus, the two-way coupled atmosphere-ocean simulation provides a more realistic representation of actual weather conditions. This is also reflected when comparing the model results with air temperature measured onboard the RV Meteor off the island of Gotland during the above-mentioned field campaign, see Figure 6.11. In the uncoupled ICON simulation the temperature is significantly underestimated by up to 2.5 K. In contrast, the values from the two-way coupled ICONGETM run are in a much better agreement with the measurements. The temporal development agrees also more with the observations, see Figure 6.11, especially after 10 days of simulations. The average deviation between the modelled and mea-

sured temperature in the period from 01 July till 21 July 2012 is decreased from 1.9 K for the uncoupled to 1.6 K for the two-way coupled simulation. This represents an improvement of about 15%. On the other hand, the Pearson correlation coefficient is only slightly improved from 0.7 for the uncoupled to 0.72 for the two-way coupled simulation. Figure 6.11 indicates that the coupled ICONGETM system needs some spin-up time to adapt to the coupling, before the improvement with respect to the uncoupled simulation becomes visible. Within the period from 10 July till 21 July 2012, the average deviation between the modelled and measured temperature decreases from 2.0 K for the uncoupled to 1.5 K for the two-way coupled simulation. Thus, after the spin-up, the model results are significantly improved due to the coupling by 25%. The exclusion of the spin-up period also increases the correlation coefficients to 0.73 for the uncoupled and to 0.75 for the two-way coupled simulation.

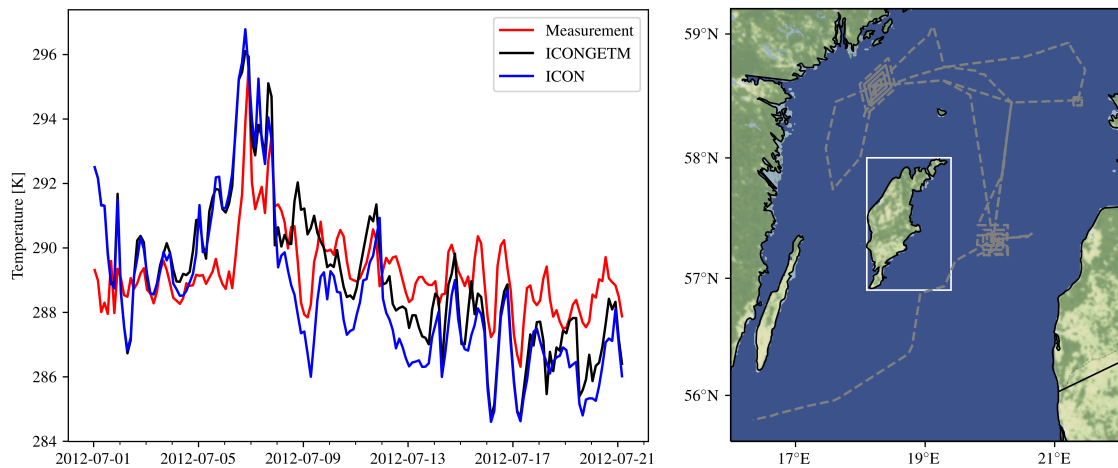


Figure 6.11: Air temperature in the Central Baltic Sea over the period July 1 – 21, 2012 (left panel). Compared are 3-hourly measurements in 29.1 m onboard the RV Meteor, ship track shown on the right panel, with model results from the two-way coupled ICONGETM and uncoupled/one-way coupled ICON simulations, respectively. The white frame shows the island of Gotland, similar to Figure 5.4a.

Similar results were found for the wind field, pressure systems and vertical temperature profiles, for more details see Bauer et al. (2021).

The weather conditions leading to the upwelling event are therefore more pronounced in the two-way coupled model run. The effects of the interactive atmosphere-ocean coupling on the boundary layer dynamics are most evident for the upwelling regions. Hence, the evolution / stratification of the marine boundary layer are reproduced more realistically. Similarly, also the boundary layer wind conditions, in particular over upwelling regions, are better represented using two-way atmosphere-ocean coupling.

### 6.2.4 Coupling effects in the ocean

As in the previous section, the coupled simulation results are compared to the uncoupled simulations to investigate the coupling effects in the ocean. The results have been also taken and summarised from Bauer et al. (2021).

In Figure 6.12, the sea surface temperature (SST) from all model simulations are compared to satellite data.

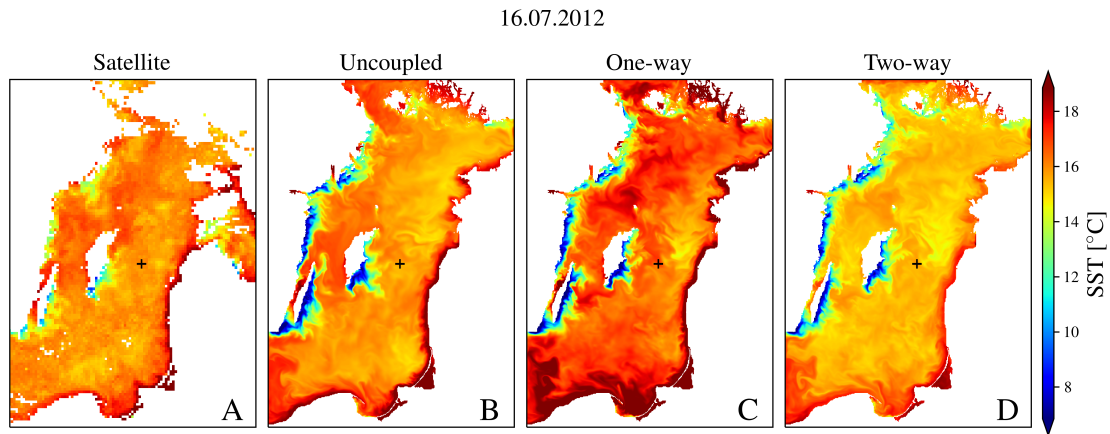


Figure 6.12: Daily mean sea surface temperature from satellites (A) and simulated by GETM in the uncoupled (B), one-way (C) and two-way (D) coupled simulation for 16 July 2012. The colourbar is identical to Figure 6.9. The SST derived from satellite data was provided by the Federal Maritime and Hydrographic Agency of Germany (BSH).

Due to the forcing with meteorological reanalysis data, the SST from the uncoupled simulation shows best agreement with the satellite data and most pronounced upwelling activity. The SST from the two-way coupled simulation is only slightly colder, but is clearly overestimated in the one-way coupled simulation. This overestimation results from a continuous increase of near surface temperature, see Figure 6.13 for the evolution in the Eastern Gotland Basin.

The evolution indicates that the surface heat flux (not shown) used in the one-way coupled GETM simulation is overestimated after 12 July 2012. For the one-way coupled simulation, the heat flux provided by ICON is calculated in terms of the too cold ICON-internal SST, see Figure 6.9. In the uncoupled and two-way coupled simulations, the surface heat flux is calculated in terms of the SST from GETM, either within GETM or ICON, respectively. Henceforth, the fluxes are adapting more conveniently to the warming ocean.

**Remark:** With ICONGETM, consisting of the state-of-the-art operational atmosphere model ICON and the established coastal ocean model GETM, a new model especially suited for high-resolution studies was developed. The key results of this simulations are an overall better agreement of the modelled and measured temperature close to the air-sea interface in the atmosphere and ocean, cf. Bauer et al. (2021). Generally speaking, two-way coupled atmosphere-ocean simulations are highly recommended in order to investigate, understand and reproduce the nature of the physics close to the air-sea interface.



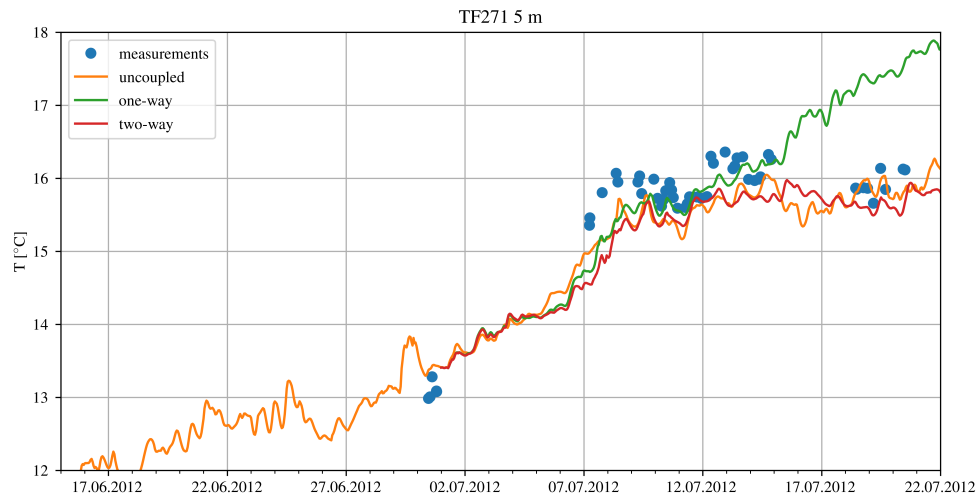


Figure 6.13: Temperature in 5 m depth at station TF271 from CTD measurements and the three model simulations. The one- and two-way coupled simulations are started at 1 July 2012, after the uncoupled spin-up period.

The example simulation showed an overhead of approximately 15 % compared to uncoupled simulations. The majority is spent for the initialisation. Although the calculation of the incidence matrices and interpolation weights must be carried out only once, cf. Section 5.3, the very high horizontal resolution requires very large matrices. However, any coupled model simulation with only an overhead of 15 % can be regarded as well performing. The advantage of applying a conservative flux data exchange at the coupling interface compared to uncoupled simulations is dominating over the increased computational costs.



## Chapter 7

### Summary

Various aspects of applying multirate methods to coupled atmosphere-ocean models were discussed in this thesis. The set of equations describing the dynamics of a geophysical fluid was introduced. Such coupled model is formulated as multiphase system with a spatially distributed interface. Each phase can have a different time scale. Multirate methods are an appropriate choice for solving coupled initial boundary value problems with different time scales.

The aspects of geophysical fluid dynamics were presented in the beginning, see Chapter 2. The principals of formulating the conservation of mass, conservation of momentum, the energy budget and the equation of state were discussed. The focus was on the general formulation of the model equations for a fluid containing multiple substances. Moreover, the initial boundary value problem for a coupled atmosphere-ocean model is presented.

Two different categories of multirate methods were discussed, the class of multirate generalized additive Runge–Kutta methods (MGARK) and multirate infinitesimal step methods (MIS), see Chapter 3. Both of them are suitable for additive split problems, i.e. an additive coupling or a linear combination of components. The MGARK category was further developed applying an arbitrary number of components, i.e. the multirate generalized additive Runge–Kutta methods for  $N$  components (MNGARK). Additionally, the MIS method was extended to overcome the problem of knowing the analytical solution of the auxiliary ordinary differential equation, i.e. the extended multirate infinitesimal step method (extMIS). Moreover, it is shown how the methods are directly related. The discussed connections between the methods were exploited to derive a consistency and stability theory of these methods, see Chapter 4. It was shown that the convergence behaviour of multirate methods is strongly related to the convergence of the individual components and by the ratio of the different time steps. The presented examples of multirate methods are of explicit manner.

The increasing complexity of any Earth system model requires efficient coupling techniques and time integration schemes. A key element are the coupling conditions modelling the physical processes at the interface, usually an equilibrium description. This leads to a system of non-linear equations, which must be solved in every time step. Henceforth, the modelling of the interface is often simplified to avoid expensive computations. Various numerical approaches for the coupling at spatially distributed model interfaces were explained with focus on the air-sea interface, see

---

Chapter 5. The models ICON and GETM were used as examples of state-of-the-art atmosphere and ocean models, respectively. The newly developed coupled model ICONGETM is used to discuss a coupling approach for complex models.

Two main aspects, the importance of the coupling at the air-sea interface and the advantages of using multirate methods, are described in Chapter 6. The influence of a coupling approach including a multirate time integration scheme has been demonstrated for an idealised coupled one-dimensional atmosphere-ocean model. Additionally, the simulation with ICONGETM shows a greatly improved agreement with measurements than individual simulations with ICON and GETM. Thus, the significance of coupled atmosphere-ocean simulations is shown. Additionally, the multirate scheme applied in ICONGETM has been discussed.

In general, multirate methods can be used for coupled atmosphere-ocean models. The choice of the multirate method is not necessarily influenced by the coupling itself. However, the modelling of the physical processes of the coupling and the numerical realisation is a decisive element for investigations at the air-sea interface. Multirate methods will be particularly interesting for coupled atmosphere-ocean models developed in the future.

Formulating coupled Earth system models and integrating them with multirate methods is an efficient approach for simulating the natural phenomena on our planet. The complexity of Earth system models increases with the more detailed modelling of the nature. Thus, final coupled models with multirate approaches can then be applied to simulate natural phenomena in an efficient way.

# Appendix A

## Additional Calculus

### A.1 Some manipulations of the general budget equation

Some manipulations on the left hand side of the general budget equation for a quantity  $\psi$  with density ( $\rho$ ) are shown, i.e.

$$\begin{aligned} \frac{d}{dt} \left( \int_{V(t)} [\rho \psi dV] \right) &= \int_{V(t)} \left[ \frac{\partial (\rho \psi)}{\partial t} dV \right] + \oint_{\partial V(t)} [\rho \psi \cdot \mathbf{v}_\psi \cdot \mathbf{n} d\partial V] \\ &= \int_{V(t)} \left[ \left( \frac{\partial (\rho \psi)}{\partial t} + \nabla \cdot (\rho \psi \cdot \mathbf{v}_\psi^T) \right) dV \right]. \end{aligned} \quad (\text{A.1})$$

This calculus also shows the connection to the Lagrange form of the budget equation. The general interpretation of the Lagrange form is that the change of an arbitrary volume element along a path is observed.

### A.2 Derivation of the budget equation for specific kinetic energy

The budget equation for specific kinetic energy based on the equation of motion (2.18), and equation (2.17a) reads

$$\begin{aligned} &\sum_{k \in \mathcal{M}} \left[ \frac{\partial (\rho_k k_k)}{\partial t} + \nabla \cdot (\rho_k k_k \cdot \mathbf{v}_k^T) \right] \\ &= \sum_{k \in \mathcal{M}} \left[ \mathbf{v}_k \cdot \left( \frac{\partial (\rho_k \mathbf{v}_k)}{\partial t} + \nabla \cdot (\rho_k \mathbf{v}_k \cdot \mathbf{v}_k^T) \right) - k_k \cdot \left( \frac{\partial \rho_k}{\partial t} + \nabla \cdot (\rho_k \cdot \mathbf{v}_k^T) \right) \right] \\ &= \sum_{k \in \mathcal{M}} [\mathbf{v}_k \cdot (-\nabla p_k - \rho_k \cdot \nabla \phi_k - 2\rho_k \cdot \Omega \times \mathbf{v}_k + \nabla \cdot \boldsymbol{\tau}_k) + k_k I_k] \\ &= -\rho \mathbf{v} \cdot \nabla \phi + \sum_{k \in \mathcal{M}} [\mathbf{v}_k \cdot (-\nabla p_k + \nabla \cdot \boldsymbol{\tau}_k) + k_k I_k]. \end{aligned} \quad (\text{A.2})$$

This equation considers each individual substance. The very first component of the right hand side is the change in kinetic energy related to potential energy, i.e. all the other components of the right hand side state the energy of the motion. The next part describes the energy related to the pressure

and shear stress of the motion. The last additive component states the change in energy due to internal phase changes, i.e. processes such as evaporation or precipitation.

Moreover, in meteorology and oceanography it is also of interest how the specific kinetic energy of a fluid with respect to velocity ( $\mathbf{v}$ ) evolves. Therefore,

$$\begin{aligned} \frac{\partial(\rho k)}{\partial t} + \nabla \cdot (\rho k \cdot \mathbf{v}^T) &= \mathbf{v} \cdot \left( \frac{\partial(\rho \mathbf{v})}{\partial t} + \nabla \cdot (\rho \mathbf{v} \cdot \mathbf{v}^T) \right) - k \cdot \left( \frac{\partial \rho}{\partial t} + \nabla \cdot (\rho \cdot \mathbf{v}^T) \right) \\ &= -\rho \mathbf{v} \cdot \nabla \phi + \mathbf{v} \cdot (-\nabla p + \nabla \cdot \boldsymbol{\tau}) \\ &\quad + \sum_{k \in \mathcal{M}} \left[ \mathbf{v} \cdot ((\mathbf{v}_k - \mathbf{v}) I_k - \nabla \cdot ((\mathbf{v}_k - \mathbf{v}) \mathbf{J}_k^T)) \right]. \end{aligned} \quad (\text{A.3})$$

There is a remarkable difference between equations (A.2) and (A.3). This difference is caused by the difference of the velocity of each substance to the barycentric velocity. Some models do not consider the velocity difference between the substances and, therefore, neglect diffusive effects. The barycentric definition of specific kinetic energy will help to categorise these difference. Hence,

$$\begin{aligned} \sum_{k \in \mathcal{M}} [\rho_k k_k] &= \sum_{k \in \mathcal{M}} \left[ \frac{1}{2} \cdot \rho_k (\mathbf{v} \cdot \mathbf{v} + 2 \cdot \mathbf{v} \cdot (\mathbf{v}_k - \mathbf{v}) + (\mathbf{v}_k - \mathbf{v}) \cdot (\mathbf{v}_k - \mathbf{v})) \right] \\ &= \sum_{k \in \mathcal{M}} \left[ \rho_k k + \frac{1}{2} \cdot \rho_k (\mathbf{v}_k - \mathbf{v}) \cdot (\mathbf{v}_k - \mathbf{v}) \right] = \rho k + \rho k_d. \end{aligned} \quad (\text{A.4})$$

The second term on the right hand side shows the specific kinetic energy related to the diffusive mass flux. There are situations in meteorology where this diffusive specific kinetic energy becomes more prominent, e.g. in tropical cyclones, cf. Bott (2008).

$$\begin{aligned} \sum_{k \in \mathcal{M}} \left[ \frac{\partial(\rho_k k_k)}{\partial t} + \nabla \cdot (\rho_k k_k \cdot \mathbf{v}_k^T) \right] &- \frac{\partial(\rho k)}{\partial t} - \nabla \cdot (\rho k \cdot \mathbf{v}^T) \\ &= \frac{\partial(\rho k_d)}{\partial t} + \nabla \cdot (\rho k_d \cdot \mathbf{v}^T) + \sum_{k \in \mathcal{M}} [\nabla \cdot (k_k \mathbf{J}_k^T)]. \end{aligned} \quad (\text{A.5})$$

The difference between equations (A.2) and (A.3) gives the barycentric definition of specific diffusive kinetic energy ( $k_d$ ), i.e.

$$\begin{aligned} \frac{\partial(\rho k_d)}{\partial t} + \nabla \cdot (\rho k_d \cdot \mathbf{v}^T) &= \sum_{k \in \mathcal{M}} \left[ (\mathbf{v}_k - \mathbf{v}) \cdot \left( -\nabla p_k + \nabla \cdot \boldsymbol{\tau}_k + \frac{1}{2} (\mathbf{v}_k - \mathbf{v}) I_k \right) \right] \\ &\quad + \sum_{k \in \mathcal{M}} [\mathbf{v} \cdot (\nabla \cdot ((\mathbf{v}_k - \mathbf{v}) \mathbf{J}_k^T))]. \end{aligned} \quad (\text{A.6})$$

The final budget equation for the specific kinetic energy with diffusive mass flux reads

$$\begin{aligned}
 & \frac{\partial(\rho k)}{\partial t} + \nabla \cdot (\rho k \cdot \mathbf{v}^T) + \frac{\partial(\rho k_d)}{\partial t} + \nabla \cdot (\rho k_d \cdot \mathbf{v}^T) \\
 &= -\rho \mathbf{v} \cdot \nabla \phi + \mathbf{v} \cdot (-\nabla p + \nabla \cdot \boldsymbol{\tau}) \\
 &+ \sum_{k \in \mathcal{M}} [\mathbf{v} \cdot ((\mathbf{v}_k - \mathbf{v}) I_k - \nabla \cdot ((\mathbf{v}_k - \mathbf{v}) \mathbf{J}_k^T))] \\
 &+ \sum_{k \in \mathcal{M}} \left[ (\mathbf{v}_k - \mathbf{v}) \cdot \left( -\nabla p_k + \nabla \cdot \boldsymbol{\tau}_k + \frac{1}{2} (\mathbf{v}_k - \mathbf{v}) I_k \right) \right] \\
 &+ \sum_{k \in \mathcal{M}} [\mathbf{v} \cdot (\nabla \cdot ((\mathbf{v}_k - \mathbf{v}) \mathbf{J}_k^T))] - \sum_{k \in \mathcal{M}} [\nabla \cdot (k_k \mathbf{J}_k^T)] \\
 &= -\rho \mathbf{v} \cdot \nabla \phi + \mathbf{v} \cdot (-\nabla p + \nabla \cdot \boldsymbol{\tau}) + \sum_{k \in \mathcal{M}} [\mathbf{v} \cdot (\mathbf{v}_k - \mathbf{v}) I_k] \\
 &+ \sum_{k \in \mathcal{M}} \left[ (\mathbf{v}_k - \mathbf{v}) \cdot \left( -\nabla p_k + \nabla \cdot \boldsymbol{\tau}_k + \frac{1}{2} (\mathbf{v}_k - \mathbf{v}) I_k \right) \right] \\
 &- \sum_{k \in \mathcal{M}} [\nabla \cdot (k_k \mathbf{J}_k^T)].
 \end{aligned} \tag{A.7}$$

Reformulating equation (A.7) to gain the general form of equation (2.14) requires the usage of  $\nabla \cdot (\mathbb{T} \cdot \mathbf{a}) = \mathbb{T} \cdot \nabla \mathbf{a} + \mathbf{a} \cdot (\nabla \cdot \mathbb{T})$ , where  $\mathbb{T}$  is a tensor of order two and  $\mathbf{a}$  is a tensor of order one. Finally,

$$\begin{aligned}
 & \frac{\partial(\rho(k + k_d))}{\partial t} + \nabla \cdot (\rho(k + k_d) \cdot \mathbf{v}^T) \\
 &= \sum_{k \in \mathcal{M}} [-\nabla \cdot (k_k \mathbf{J}_k^T + (p_k \mathbb{I} - \boldsymbol{\tau}_k) \cdot \mathbf{v}_k) + (p_k \mathbb{I} - \boldsymbol{\tau}_k) \cdot \nabla \mathbf{v}_k - \rho_k \mathbf{v}_k \cdot \nabla \phi + k_k I_k].
 \end{aligned} \tag{A.8}$$

### A.3 Derivation of the budget equation for specific internal energy

The derivation of the budget equation for specific internal energy is extensively described in Baranowski (1975), Groot and Mazur (1984), and Zdunkowski and Bott (2004). The usual way to derive the equation is to define the budget equation for specific total energy and calculate the difference from budget equations for specific kinetic energy and specific potential energy.

$$\sum_{k \in \mathcal{M}} \left[ \frac{\partial(\rho_k e_k)}{\partial t} + \nabla \cdot (\rho_k e_k \cdot \mathbf{v}_k^T) \right] = \frac{\partial(\rho e)}{\partial t} + \nabla \cdot (\rho e \cdot \mathbf{v}^T) + \sum_{k \in \mathcal{M}} [\nabla \cdot (e_k \mathbf{J}_k^T)] = 0 \tag{A.9}$$

and

$$\begin{aligned}
 & \frac{\partial(\rho e)}{\partial t} + \nabla \cdot (\rho e \cdot \mathbf{v}^T) \\
 &= \frac{\partial(\rho(k + k_d + \phi + u))}{\partial t} + \nabla \cdot (\rho(k + k_d + \phi + u) \cdot \mathbf{v}^T) \\
 &= \sum_{k \in \mathcal{M}} [-\nabla \cdot (k_k \mathbf{J}_k^T + (p_k \mathbb{I} - \boldsymbol{\tau}_k) \cdot \mathbf{v}_k) + (p_k \mathbb{I} - \boldsymbol{\tau}_k) \cdot \nabla \mathbf{v}_k - \rho_k \mathbf{v}_k \cdot \nabla \phi + k_k I_k] \\
 &+ \rho \mathbf{v} \cdot \nabla \phi + \frac{\partial(\rho u)}{\partial t} + \nabla \cdot (\rho u \cdot \mathbf{v}^T) = - \sum_{k \in \mathcal{M}} [\nabla \cdot (e_k \mathbf{J}_k^T)].
 \end{aligned} \tag{A.10}$$

Moreover, for specific internal energy

$$\frac{\partial(\rho u)}{\partial t} + \nabla \cdot (\rho u \cdot \mathbf{v}^T) = \sum_{\kappa \in \mathcal{M}} [-\nabla \cdot (u_\kappa \mathbf{J}_\kappa^T - (p_\kappa \mathbb{I} - \boldsymbol{\tau}_\kappa) \cdot \mathbf{v}_\kappa) - (p_\kappa \mathbb{I} - \boldsymbol{\tau}_\kappa) \cdot \cdot \nabla \mathbf{v}_\kappa - k_\kappa I_\kappa]. \quad (\text{A.11})$$

A substance-wise formulation is adapted by the barycentric definition of the internal energy and adding the diffusive mass flux for each substance  $\kappa$  to equation (2.25d), i.e.

$$\sum_{k \in \mathcal{M}} \left[ \frac{\partial(\rho_k u_k)}{\partial t} + \nabla \cdot (\rho_k u_k \cdot \mathbf{v}_k^T) \right] = \sum_{k \in \mathcal{M}} [-\nabla \cdot (-(p_k \mathbb{I} - \boldsymbol{\tau}_k) \cdot \mathbf{v}_k) - (p_k \mathbb{I} - \boldsymbol{\tau}_k) \cdot \cdot \nabla \mathbf{v}_k - k_k I_k]. \quad (\text{A.12})$$

However, this requires the knowledge of all the aspects of the total energy.



## Appendix B

# Physical assumptions and the set of equations

This section introduces the assumptions compressibility, hydrostatic equilibrium and Boussinesq approximation and discusses their influence on the general set of equations. A thorough explanation on applications of these assumptions is beyond the scope of this thesis and can be found in the literature, see e.g. Lange (2002) and Cushman-Roisin and Beckers (2011). The following briefly introduces them.

### B.1 Compressible vs. incompressible fluid

A compressible fluid has the property that its volume decreases as the pressure on its surrounding surfaces increases. Additionally, all physical substances are compressible, but the compressibility of liquids and solids is much smaller than for gases. Although all fluids are compressible, some models assume a constant density, i.e. there is no temporal change in density,  $\frac{d\rho}{dt} = 0$ . Hence, equation (2.17b) is simplified to

$$\frac{\partial \rho}{\partial t} + \nabla \cdot (\rho \cdot \mathbf{v}^T) = \frac{d\rho}{dt} + \rho \nabla \cdot \mathbf{v} = \rho \nabla \cdot \mathbf{v} = 0. \quad (\text{B.1})$$

In Kundu et al. (2001), Holton (2004), and Etling (2008) different ways of introducing incompressible fluids can be found. Let a fluid be incompressible, then equation (2.14) simplifies to

$$\rho \frac{d\psi}{dt} = \sum_{\kappa \in \mathcal{M}} [-\nabla \cdot (\psi_{\kappa} \cdot \mathbf{J}_{\kappa}^T + \lambda_{\kappa}) + \sigma_{\kappa}]. \quad (\text{B.2})$$

### B.2 Hydrostatic equilibrium

In case of a fluid is motionless, i.e.  $\mathbf{v}_{\kappa} \equiv \mathbf{0}$  holds for all substances  $\kappa$ , the conservation of momentum, equation (2.22) simplifies to

$$\mathbf{0} = \sum_{\kappa \in \mathcal{M}} [-\nabla p_{\kappa} - \rho_{\kappa} \cdot \nabla \phi] = -\nabla p - \rho \cdot \nabla \phi. \quad (\text{B.3})$$

Because of the definition of the geopotential, see equation (2.19), the following holds,

$$\frac{\partial p}{\partial z} = -\rho g. \quad (\text{B.4})$$

If a fluid fulfils equation (B.4), then it is said to be hydrostatically balanced. Equation (B.4) defines a relation between the vertical derivative of the pressure with the density and gravitational acceleration, cf. Kundu et al. (2001), Zdunkowski and Bott (2003), Holton (2004), Etling (2008), and Cushman-Roisin and Beckers (2011). Note that a hydrostatically balanced fluid must not necessarily be motionless. If equation (B.3) holds, then the fluid is hydrostatically balanced, but not vice versa.

The hydrostatic assumption states that equation (B.4) is assumed to be valid, otherwise a fluid is said to be non-hydrostatic.

### B.3 Boussinesq approximation

The ideas of the Boussinesq approximation is discussed in Cushman-Roisin and Beckers (2011). The main idea is related to the fact, that the density varies only gently around a constant mean value  $\rho_0$ , i.e.

$$\rho = \rho_0 + \rho'(x, y, z, t) \quad (\text{B.5})$$

with  $|\rho'| \ll \rho$ , see Cushman-Roisin and Beckers (2011, equation (3.16)). Equation (2.17b) is then reformulated to

$$\frac{\partial \rho}{\partial t} + \nabla \cdot (\rho \cdot \mathbf{v}) = \rho_0 \nabla \cdot \mathbf{v} + \rho' \nabla \cdot \mathbf{v} + \frac{d\rho'}{dt} = 0. \quad (\text{B.6})$$

Due to the fact that  $\rho'$  varies gently it is safe to assume  $\frac{d\rho'}{dt} \approx 0$ . Furthermore, since  $|\rho'| \ll \rho$ , the remaining most dominant part is

$$\nabla \cdot \mathbf{v} = 0. \quad (\text{B.7})$$

The budget equation of momentum, see Section 2.2.2 equation (2.20a), is simplified to

$$\begin{aligned} \sum_{\kappa \in \mathcal{M}} \left[ \frac{\partial (\rho_\kappa \mathbf{v})}{\partial t} + \nabla \cdot (\rho_\kappa \mathbf{v} \cdot \mathbf{v}^T) \right] &= \sum_{\kappa \in \mathcal{M}} \left[ \rho_\kappa \cdot \frac{d\mathbf{v}}{dt} + \mathbf{v} \cdot \left( \frac{\partial \rho_\kappa}{\partial t} + \nabla \cdot (\rho_\kappa \cdot \mathbf{v}) \right) \right] \\ &= \rho \frac{d\mathbf{v}}{dt} = -\nabla p - \rho \cdot \nabla \phi - 2 \cdot \Omega \times \rho \mathbf{v} + \nabla \cdot \tau. \end{aligned} \quad (\text{B.8})$$

Furthermore, due to equation (B.7), divergence of shear stress ( $\tau$ ) is simplified to

$$\nabla \cdot \tau = \mu \cdot \nabla^2 \mathbf{v}. \quad (\text{B.9})$$

# Appendix C

## Time averaged set of equations

All geophysical fluid model simulations shall be compared to measurements. However, they are usually representing an averaged quantity. Thus, an averaging of modelled quantities is also necessary. Time-averaging a quantity  $\psi = \psi(\mathbf{x}, t)$  over a period  $T$  is given for a mean time  $t_0$  by

$$\overline{\psi(\mathbf{x}, t_0)} = \frac{1}{T} \cdot \int_{t_0 - \frac{T}{2}}^{t_0 + \frac{T}{2}} [\psi(\mathbf{x}, t) dt]. \quad (\text{C.1})$$

For further details and other averaging options, e.g. spatial and ensemble averaging, see e.g. Lange (2002), Etling (2008), and Cushman-Roisin and Beckers (2011).

### C.1 Reynolds averaging

Modelling a sufficiently long time-averaged quantity is referred to Reynolds averaging. A quantity is split into a time-averaged and disturbed component, i.e.

$$\psi(\mathbf{x}, t) = \overline{\psi(\mathbf{x}, t_0)} + \psi'(\mathbf{x}, t). \quad (\text{C.2})$$

Following equation (C.1),

$$\overline{\psi(\mathbf{x}, t_0)} = \frac{1}{T} \cdot \int_{t_0 - \frac{T}{2}}^{t_0 + \frac{T}{2}} [\overline{\psi(\mathbf{x}, t_0)} + \psi'(\mathbf{x}, t) dt] = \overline{\psi(\mathbf{x}, t_0)} + \frac{1}{T} \cdot \int_{t_0 - \frac{T}{2}}^{t_0 + \frac{T}{2}} [\psi'(\mathbf{x}, t) dt]. \quad (\text{C.3})$$

Hence,

$$\frac{1}{T} \cdot \int_{t_0 - \frac{T}{2}}^{t_0 + \frac{T}{2}} [\psi'(\mathbf{x}, t) dt] = 0, \quad \text{i.e.} \quad \overline{\psi'(\mathbf{x}, t_0)} = 0. \quad (\text{C.4})$$

Applying Reynolds averaging to the general barycentric formulation of budget equations with diffusive mass flux, equation (2.14), gives

$$\begin{aligned} \frac{\partial (\overline{\rho \psi})}{\partial t} + \frac{\partial (\overline{\rho' \psi'})}{\partial t} + \nabla \cdot (\overline{\rho \psi' \cdot \mathbf{v}'^T}) + \nabla \cdot (\overline{\psi \rho' \cdot \mathbf{v}'^T}) + \nabla \cdot (\overline{\rho' \psi' \cdot \mathbf{v}'^T}) + \nabla \cdot (\overline{\rho' \psi' \cdot \mathbf{v}'^T}) \\ = \sum_{\kappa \in \mathcal{M}} \left[ -\nabla \cdot (\overline{\psi_\kappa \mathbf{J}_\kappa^T} + \overline{\psi'_\kappa \mathbf{J}_\kappa'^T} + \overline{\lambda_\kappa}) + \overline{\sigma_\kappa} \right]. \end{aligned} \quad (\text{C.5})$$

The components of equation (C.5) with disturbed quantities are referred to turbulent quantities. In case of no turbulent entries, equation (2.14) is also valid for the mean quantities.

The Reynolds averaging was first published in Reynolds (1895).

## C.2 Favre averaging

Reynolds averaging leads to complicated turbulent quantities, see equation (C.5). This complicates the modelling. In case of modelling only barycentric quantities, i.e.  $\rho(\mathbf{x}, t) \psi(\mathbf{x}, t)$ , the averaging may be formulated with density-weighted averaging. This is known as Favre averaging. Quantity  $\psi(\mathbf{x}, t)$  is split, i.e.

$$\psi(\mathbf{x}, t) = \hat{\psi}(\mathbf{x}, t_0) + \psi''(\mathbf{x}, t), \quad (\text{C.6})$$

such that

$$\overline{\rho(\mathbf{x}, t) \psi(\mathbf{x}, t)} = \frac{1}{T} \cdot \int_{t_0 - \frac{T}{2}}^{t_0 + \frac{T}{2}} \left[ \overline{\rho(\mathbf{x}, t_0) \hat{\psi}(\mathbf{x}, t_0) + \rho(\mathbf{x}, t_0) \psi''(\mathbf{x}, t)} dt \right] = \overline{\rho(\mathbf{x}, t_0)} \hat{\psi}(\mathbf{x}, t_0). \quad (\text{C.7})$$

Thus, equation (2.14) becomes

$$\frac{\partial (\bar{\rho} \hat{\psi})}{\partial t} + \nabla \cdot (\bar{\rho} \hat{\psi} \cdot \hat{\mathbf{v}}^T) + \nabla \cdot (\bar{\rho} \psi'' \cdot \mathbf{v}''^T) = \sum_{\kappa \in \mathcal{M}} \left[ -\nabla \cdot (\bar{\psi}_{\kappa} \mathbf{J}_{\kappa}^T + \bar{\psi}'_{\kappa} \mathbf{J}_{\kappa}^T + \bar{\lambda}_{\kappa}) + \bar{\sigma}_{\kappa} \right] \quad (\text{C.8})$$

requiring only a turbulence closure for approach  $\nabla \cdot (\bar{\rho} \psi'' \cdot \mathbf{v}''^T)$  and  $\nabla \cdot (\bar{\psi}'_{\kappa} \mathbf{J}_{\kappa}^T)$ . However,

$$\frac{1}{T} \cdot \int_{t_0 - \frac{T}{2}}^{t_0 + \frac{T}{2}} [\psi''(\mathbf{x}, t) dt] \neq 0, \quad \text{i.e.} \quad \overline{\psi''(\mathbf{x}, t_0)} \neq 0. \quad (\text{C.9})$$

**Remark:** Reynolds averaging is mainly applied for the incompressible set of equations. On the other hand, Favre averaging is commonly applied for the compressible set of equations.

# Bibliography

- Acosta, Mario C, Sergi Palomas, Stella V. Paronuzzi Ticco, Gladys Utrera, Joachim Biercamp, Pierre-Antoine Bretonniere, Reinhard Budich, Miguel Castrillo, Arnaud Caubel, Francisco Doblas-Reyes, Italo Epicoco, Uwe Fladrich, Sylvie Joussaume, Alok Kumar Gupta, Bryan Lawrence, Philippe Le Sager, Grenville Lister, Marie-Pierre Moine, Jean-Christophe Rioual, Sophie Valcke, Niki Zadeh, and Venkatramani Balaji (2024). “The computational and energy cost of simulation and storage for climate science: lessons from CMIP6”. In: *Geoscientific Model Development* 17.8, pp. 3081–3098. ISSN: 1991-9603. DOI: 10.5194/gmd-17-3081-2024 (cit. on p. 2).
- Arakawa, Akio and Vivian R. Lamb (1977). “Computational Design of the Basic Dynamical Processes of the UCLA General Circulation Model”. In: *General Circulation Models of the Atmosphere*. Ed. by Julius Chang. Vol. 17. Methods in Computational Physics: Advances in Research and Applications. Elsevier, pp. 173–265. DOI: 10.1016/B978-0-12-460817-7.50009-4 (cit. on p. 19).
- Araújo, A. L., A. Murua, and J. M. Sanz-Serna (1997). “Symplectic Methods Based on Decompositions”. In: *SIAM Journal on Numerical Analysis* 34.5, pp. 1926–1947. ISSN: 0036-1429. DOI: 10.1137/S0036142995292128 (cit. on pp. 3, 49).
- Balaji, V., Byron Boville, Samson Cheung, Tom Clune, Nancy Collins, Tony Craig, Carlos Cruz, Arlindo M. Da Silva, Cecelia DeLuca, Rosalinda de Fainchtein, Rocky Dunlap, Brian Eaton, Steve Goldhaber, Robert Hallberg, Tom Henderson, Chris Hill, Mark Iredell, Joseph Jacob, Rob Jacob, Phil Jones, Brian Kauffmann, Erik Kluzek, Ben Koziol, Jay Larson, Peggy Li, Fei Liu, John Michalakes, Raffaele Montuoro, Sylvia Murphy, David Neckels, Ryan O Kuinghtons, Robert Oehmke, Chuck Panaccione, Daniel Rosen, Jim Rosinski, Mathew Rothstein, Kathy Saint, Will Sawyer, Earl Schwab, Shepard Smithline, Walter Spector, Don Stark, Max Suarez, Spencer Swift, Gerhard Theurich, Atanas Trayanov, Silverio Vasquez, Jon Wolfe, Weiyu Yang, Mike Young, and Leonid Zaslavsky (2019). *ESMF Reference Manual for Fortran - Version 8.0.0*. Tech. rep., p. 1349 (cit. on p. 71).
- Bannon, Peter R (2002). “Theoretical Foundations for Models of Moist Convection”. In: *Journal of the Atmospheric Sciences* 59.12, pp. 1967–1982. ISSN: 0022-4928. DOI: 10.1175/1520-0469(2002)059<1967:TFFMOM>2.0.CO;2 (cit. on p. 12).
- Baranowski, Bogdan (1975). *Nichtgleichgewichts-Thermodynamik in der physikalischen Chemie*. 1. Auflage. Leipzig: VEB Deutscher Verlag für Grundstoffindustrie (cit. on pp. 7, 10, 12, iii).

- Bartel, Andreas and Michael Günther (2020). “Inter/Extrapolation-Based Multirate Schemes: A Dynamic-Iteration Perspective”. In: pp. 73–90. DOI: 10.1007/978-3-030-53905-4\_3 (cit. on pp. 21, 94).
- Bauer, Tobias Peter (2024). *Atmosphere-Ocean-Problems with different multirate time integration methods*. DOI: 10.5281/zenodo.10882611 (cit. on p. 84).
- Bauer, Tobias Peter and Oswald Knoth (2021). “Extended multirate infinitesimal step methods: Derivation of order conditions”. In: *Journal of Computational and Applied Mathematics* 387. ISSN: 03770427. DOI: 10.1016/j.cam.2019.112541 (cit. on pp. 35, 37, 40, 42, 53, 60, 62, xxvii).
- Bauer, Tobias Peter, Peter Holtermann, Bernd Heinold, Hagen Radtke, Oswald Knoth, and Knut Klingbeil (2021). “ICONGETM v1.0 flexible NUOPC-driven two-way coupling via ESMF exchange grids between the unstructured-grid atmosphere model ICON and the structured-grid coastal ocean model GETM”. In: *Geoscientific Model Development* 14.8, pp. 4843–4863. ISSN: 1991-9603. DOI: 10.5194/gmd-14-4843-2021 (cit. on pp. 1, 22, 67, 72, 74, 75, 78–80, 83, 93–95, 97, 98, xxvii).
- Bazavov, Alexei (2022). “Commutator-free Lie group methods with minimum storage requirements and reuse of exponentials”. In: *BIT Numerical Mathematics* 62.3, pp. 745–771. ISSN: 0006-3835. DOI: 10.1007/s10543-021-00892-x (cit. on p. 91).
- Beljaars, Anton, Emanuel Dutra, Gianpaolo Balsamo, and Florian Lemarié (2017). “On the numerical stability of surfaceatmosphere coupling in weather and climate models”. In: *Geoscientific Model Development* 10.2, pp. 977–989. ISSN: 1991-9603. DOI: 10.5194/gmd-10-977-2017 (cit. on p. 68).
- Beron-Vera, F.J., J. Ochoa, and P. Ripa (1999). “A note on boundary conditions for salt and fresh-water balances”. In: *Ocean Modelling* 1.2-4, pp. 111–118. ISSN: 14635003. DOI: 10.1016/S1463-5003(00)00003-2 (cit. on p. 66).
- Blumberg, Alan F. and George L. Mellor (1987). “A description of a three-dimensional coastal ocean circulation model”. In: January 1987, pp. 1–16. DOI: 10.1029/C0004p0001 (cit. on pp. 76, 77, 94).
- Bott, Andreas (2008). “Theoretical considerations on the mass and energy consistent treatment of precipitation in cloudy atmospheres”. In: *Atmospheric Research* 89.3, pp. 262–269. ISSN: 01698095. DOI: 10.1016/j.atmosres.2008.02.010 (cit. on pp. 9–13, ii).
- Bremicker-Trübelhorn, Sascha and Sigrun Ortleb (2017). “On Multirate GARK Schemes with Adaptive Micro Step Sizes for FluidStructure Interaction: Order Conditions and Preservation of the Geometric Conservation Law”. In: *Aerospace* 4.4, p. 8. ISSN: 2226-4310. DOI: 10.3390/aerospace4010008 (cit. on pp. 27–29, 33, 52).
- Bryan, Kirk (1969). “A numerical method for the study of the circulation of the world ocean”. In: *Journal of Computational Physics* 4, pp. 347–376. ISSN: 00219991. DOI: 10.1016/0021-9991(69)90004-7 (cit. on p. 76).

- Burchard, Hans (2002). *Applied Turbulence Modelling in Marine Waters*. Vol. 100. Lecture Notes in Earth Sciences. Berlin, Heidelberg: Springer Berlin Heidelberg, p. 218. ISBN: 978-3-540-43795-6. DOI: 10.1007/3-540-45419-5 (cit. on p. 94).
- Burchard, Hans and Karsten Bolding (2002). *GETM – a General Estuarine Transport Model. Scientific Documentation*. Tech. rep. European Commission (cit. on pp. 67, 71, 76, 77).
- Burchard, Hans and Ole Petersen (1999). “Models of turbulence in the marine environment - A comparative study of two-equation turbulence models”. In: *Journal of Marine Systems* 21.1-4, pp. 29–53. ISSN: 09247963. DOI: 10.1016/S0924-7963(99)00004-4 (cit. on pp. 69, 85, 88).
- Burchard, Hans, Karsten Bolding, and Manuel Ruiz Villarreal (1999). *GOTM – a General Ocean Turbulence Model. Theory, implementation and test cases*. Tech. rep. European Commission (cit. on pp. 69, 70, 83, 86, 87).
- (2004). “Three-dimensional modelling of estuarine turbidity maxima in a tidal estuary”. In: *Ocean Dynamics* 54.2, pp. 250–265. ISSN: 1616-7341. DOI: 10.1007/s10236-003-0073-4 (cit. on pp. 77, 94).
- Burchard, Hans, N. Berkay Basdurak, Ulf Gräwe, Michaela Knoll, Volker Mohrholz, and Selina Müller (2017). “Salinity inversions in the thermocline under upwelling favorable winds”. In: *Geophysical Research Letters* 44.3, pp. 1422–1428. ISSN: 00948276. DOI: 10.1002/2016GL072101 (cit. on p. 14).
- Butcher, John C. (2008). *Numerical Methods for Ordinary Differential Equations*. Chichester, UK: John Wiley & Sons, Ltd. ISBN: 9780470753767. DOI: 10.1002/9780470753767 (cit. on p. 24).
- (2010). “Trees, B-series and exponential integrators”. In: *IMA Journal of Numerical Analysis* 30.1, pp. 131–140. ISSN: 0272-4979. DOI: 10.1093/imanum/drn086 (cit. on p. 49).
- Calvin, Katherine, Dipak Dasgupta, Gerhard Krinner, Aditi Mukherji, Peter W. Thorne, Christopher Trisos, José Romero, Paulina Aldunce, Ko Barrett, Gabriel Blanco, William W.L. Cheung, Sarah Connors, Fatima Denton, Aïda Diongue-Niang, David Dodman, Matthias Garschagen, Oliver Geden, Bronwyn Hayward, Christopher Jones, Frank Jotzo, Thelma Krug, Rodel Lasco, Yune-Yi Lee, Valérie Masson-Delmotte, Malte Meinshausen, Katja Mintenbeck, Abdallah Mokssit, Friederike E.L. Otto, Minal Pathak, Anna Pirani, Elvira Poloczanska, Hans-Otto Pörtner, Aromar Revi, Debra C. Roberts, Joyashree Roy, Alex C. Ruane, Jim Skea, Priyadarshi R. Shukla, Raphael Slade, Aimée Slangen, Youba Sokona, Anna A. Sörensson, Melinda Tignor, Detlef van Vuuren, Yi-Ming Wei, Harald Winkler, Panmao Zhai, Zinta Zommers, Jean-Charles Hourcade, Francis X. Johnson, Shonali Pachauri, Nicholas P. Simpson, Chandni Singh, Adelle Thomas, Edmond Totin, Andrés Alegría, Kyle Armour, Birgit Bednar-Friedl, Kornelis Blok, Guéladio Cissé, Frank Dentener, Siri Eriksen, Erich Fischer, Gregory Garner, Céline Guivarch, Marjolijn Haasnoot, Gerrit Hansen, Mathias Hauser, Ed Hawkins, Tim Hermans, Robert Kopp, Noémie Leprince-Ringuet, Jared Lewis, Debora Ley, Chloé Ludden, Leila Niamir, Zebedee Nicholls, Shreya Some, Sophie Szopa, Blair Trewin, Kaj-Ivar van der Wijst, Gundula Winter, Maximilian Witting, Arlene Birt, and Meeyoung Ha (2023). *IPCC*,

- 2023: *Climate Change 2023: Synthesis Report. Contribution of Working Groups I, II and III to the Sixth Assessment Report of the Intergovernmental Panel on Climate Change [Core Writing Team, H. Lee and J. Romero (eds.)]. IPCC, Geneva, Switzerland.* Tech. rep. Intergovernmental Panel on Climate Change. DOI: 10.59327/IPCC/AR6-9789291691647 (cit. on p. 1).
- Chelton, Dudley B. and Shang-Ping Xie (2010). “Coupled Ocean-Atmosphere Interaction at Oceanic Mesoscales”. In: *Oceanography* 23.4, pp. 52–69. ISSN: 10428275. DOI: 10.5670/oceanog.2010.05 (cit. on p. 1).
- Chrysagi, Evridiki, Lars Umlauf, Peter Ludwig Holtermann, Knut Klingbeil, and Hans Burchard (2021). “Highresolution simulations of submesoscale processes in the Baltic Sea: The role of storm events”. In: *Journal of Geophysical Research: Oceans*. ISSN: 2169-9275. DOI: 10.1029/2020JC016411 (cit. on p. 95).
- Connors, Jeffrey M. and Kenneth C. Sockwell (2022). “A Multirate Discontinuous-Galerkin-in-Time Framework for Interface-Coupled Problems”. In: *SIAM Journal on Numerical Analysis* 60.5, pp. 2373–2404. ISSN: 0036-1429. DOI: 10.1137/21M1461149 (cit. on pp. 3, 23).
- Constantinescu, Emil M. and Adrian Sandu (2007). “Multirate Timestepping Methods for Hyperbolic Conservation Laws”. In: *Journal of Scientific Computing* 33.3, pp. 239–278. ISSN: 0885-7474. DOI: 10.1007/s10915-007-9151-y (cit. on p. 3).
- Cotter, Colin J. and D. D. Holm (2013). “A variational formulation of vertical slice models”. In: *Proceedings of the Royal Society A: Mathematical, Physical and Engineering Sciences* 469.2155, pp. 20120678–20120678. ISSN: 1364-5021. DOI: 10.1098/rspa.2012.0678 (cit. on p. 71).
- Csanady, Gabriel T. (2004). *Air-Sea Interaction: Laws and Mechanisms*. ISBN: 0521792592 (cit. on p. 17).
- Cullen, Michael J.P. (2008). “A comparison of numerical solutions to the Eady frontogenesis problem”. In: *Quarterly Journal of the Royal Meteorological Society* 134.637, pp. 2143–2155. ISSN: 00359009. DOI: 10.1002/qj.335 (cit. on p. 71).
- Cushman-Roisin, B and Jean-Marie Beckers (2011). *Introduction to Geophysical Fluid Dynamics: Physical and Numerical Aspects*. Academic Press. Elsevier Science. ISBN: 9780120887590 (cit. on pp. 13, 17, 18, v–vii).
- Cuxart, Joan, A. A. M. Holtslag, R. J. Beare, E. Bazile, A. Beljaars, A. Cheng, L. Conangla, M. Ek, F. Freedman, R. Hamdi, A. Kerstein, H. Kitagawa, G. Lenderink, D. Lewellen, J. Mailhot, T. Mauritsen, V. Perov, G. Schayes, G-J. Steeneveld, G. Svensson, P. Taylor, W. Weng, S. Wunsch, and K-M. Xu (2006). “Single-Column Model Intercomparison for a Stably Stratified Atmospheric Boundary Layer”. In: *Boundary-Layer Meteorology* 118.2, pp. 273–303. ISSN: 0006-8314. DOI: 10.1007/s10546-005-3780-1 (cit. on pp. 84, 86).
- Dangendorf, Sönke, Francisco M. Calafat, Arne Arns, Thomas Wahl, Ivan D. Haigh, and Jürgen Jensen (2014). “Mean sea level variability in the North Sea: Processes and implications”. In: *Journal of Geophysical Research: Oceans* 119.10. ISSN: 21699275. DOI: 10.1002/2014JC009901 (cit. on p. 80).



- Doms, G. and Michael Baldauf (2013). *A description of the Nonhydrostatic Regional COSMOS Model, Part I: Dynamics and Numerics*. Tech. rep. Offenbach: Deutscher Wetterdienst, p. 166. DOI: 10.5676/DWD\_pub/nwv/cosmo-doc\_5.00\_I; (cit. on p. 14).
- Doms, G., Jochen Förstner, E. Heise, Hans-Joachim Herzog, D. Mironov, M. Raschendorfer, T. Reinhardt, B. Ritter, R. Schrodin, J-P. Schulz, and G. Vogel (2013). *A description of the Nonhydrostatic Regional COSMOS Model, Part II: Physical parameterization*. Tech. rep. Offenbach: Deutscher Wetterdienst. DOI: 10.5676/DWD\_pub/nwv/cosmo-doc\_5.00\_II (cit. on pp. 67, 68, 75).
- Döscher, Ralf, U. Willén, C. Jones, Anna Rutgersson, H. E. Markus Meier, U. Hansson, and L. P. Graham (2002). “The development of the coupled regional ocean-atmosphere model RCAO”. In: *Boreal Env. Res.* 7.October, pp. 183–192. ISSN: 1239-6095 (cit. on p. 21).
- Dutton, John A. (1986). *The Ceaseless Wind: An Introduction to the Theory of Atmospheric Motion*. Dover Phoneix Editions. Dover Publications. ISBN: 0486650960 (cit. on p. 23).
- Esau, Igor (2014). “Indirect air-sea interactions simulated with a coupled turbulence-resolving model”. In: *Ocean Dynamics* 64.5, pp. 689–705. ISSN: 16167228. DOI: 10.1007/s10236-014-0712-y (cit. on p. 66).
- Etling, Dieter (2008). *Theoretische Meteorologie*. 3. Auflage. Springer Berlin Heidelberg. ISBN: 9783540759782 (cit. on pp. 10, 14, 23, 68, 69, v–vii).
- Feistel, Rainer (2018). “Thermodynamic properties of seawater, ice and humid air: TEOS-10, before and beyond”. In: *Ocean Science* 14.3, pp. 471–502. ISSN: 1812-0792. DOI: 10.5194/os-14-471-2018 (cit. on pp. 13, 14).
- Gassmann, Almut and Hans-Joachim Herzog (2008). “Towards a consistent numerical compressible non-hydrostatic model using generalized Hamiltonian tools”. In: *Quarterly Journal of the Royal Meteorological Society* 134.635, pp. 1597–1613. ISSN: 00359009. DOI: 10.1002/qj.297 (cit. on p. 74).
- (2015). “How is local material entropy production represented in a numerical model?” In: *Quarterly Journal of the Royal Meteorological Society* 141.688, pp. 854–869. ISSN: 00359009. DOI: 10.1002/qj.2404 (cit. on pp. 8, 12).
- Gear, C. W. and D. R. Wells (1984). “Multirate linear multistep methods”. In: *Bit* 24.4, pp. 484–502. ISSN: 00063835. DOI: 10.1007/BF01934907 (cit. on pp. 3, 23).
- Gräwe, Ulf, Knut Klingbeil, Jessica Kelln, and Sönke Dangendorf (2019). “Decomposing Mean Sea Level Rise in a Semi-Enclosed Basin, the Baltic Sea”. In: *Journal of Climate* 32.11, pp. 3089–3108. ISSN: 0894-8755. DOI: 10.1175/JCLI-D-18-0174.1 (cit. on pp. 80, 95).
- Groot, S R de and P Mazur (1984). *Non-Equilibrium Thermodynamics*. Dover Publications. ISBN: 9780486647418 (cit. on p. iii).
- Grote, Marcus J. and Teodora Mitkova (2010). “Explicit local time-stepping methods for Maxwell’s equations”. In: *Journal of Computational and Applied Mathematics* 234.12, pp. 3283–3302. ISSN: 03770427. DOI: 10.1016/j.cam.2010.04.028 (cit. on p. 3).

- Günther, Michael and Adrian Sandu (2016). “Multirate generalized additive Runge Kutta methods”. In: *Numerische Mathematik* 133.3, pp. 497–524. ISSN: 0029-599X. DOI: 10.1007/s00211-015-0756-z (cit. on pp. 3, 23, 27–29, 31, 33, 40, 43, 52, 58, 60).
- Günther, Michael, A. Kværnø, and P. Rentrop (2001). “Multirate Partitioned Runge-Kutta Methods”. In: *Bit Numerical Mathematics* 41.3, pp. 504–514. ISSN: 00063835. DOI: 10.1023/A:1021967112503 (cit. on pp. 3, 23).
- Hairer, Ernst and Gerhard Wanner (1996). *Solving Ordinary Differential Equations II: Stiff and Differential-Algebraic Problems*. Second Rev. Berlin, Heidelberg: Springer Berlin Heidelberg New York, p. 614. ISBN: 3540604529 (cit. on pp. 25, 57).
- Hairer, Ernst, S P Nørsett, and Gerhard Wanner (1993). *Solving Ordinary Differential Equations I: Nonstiff Problems*. Solving ordinary differential equations. Springer. ISBN: 9783540788621 (cit. on pp. 24, 47, 48, 50).
- Holtermann, Peter Ludwig, Hans Burchard, Ulf Gräwe, Knut Klingbeil, and Lars Umlauf (2014). “Deep-water dynamics and boundary mixing in a nontidal stratified basin: A modeling study of the Baltic Sea”. In: *Journal of Geophysical Research: Oceans* 119.2, pp. 1465–1487. ISSN: 21699275. DOI: 10.1002/2013JC009483 (cit. on p. 95).
- Holton, James R (2004). *An introduction to dynamic meteorology*. Ed. by Renata Dmowska and James R Holton. 4th ed. International Geophysics Series. Burlington, MA: Elsevier Academic Press, p. 535. ISBN: 9780123540157 (cit. on pp. v, vi).
- Ioc, Scor, and Iapso (2010). *The international thermodynamic equation of seawater 2010: Calculation and use of thermodynamic properties*. June, p. 196 (cit. on p. 14).
- Jackiewicz, Zdzisław and Rossana Vermiglio (2000). “Order conditions for partitioned Runge-Kutta methods”. In: *Applications of Mathematics* 45.4, pp. 301–316. ISSN: 0862-7940. DOI: 10.1023/A:1022323529349 (cit. on pp. 3, 25).
- Jähn, Michael, Oswald Knoth, Marcel König, and Ulrike Vogelsberg (2015). “ASAM v2.7: a compressible atmospheric model with a Cartesian cut cell approach”. In: *Geoscientific Model Development* 8.2, pp. 317–340. ISSN: 1991-9603. DOI: 10.5194/gmd-8-317-2015 (cit. on p. 20).
- Jebens, Stefan, Oswald Knoth, and Rüdiger Weiner (2009). “Explicit Two-Step Peer Methods for the Compressible Euler Equations”. In: *Monthly Weather Review* 137.7, pp. 2380–2392. ISSN: 0027-0644. DOI: 10.1175/2008MWR2671.1 (cit. on p. 3).
- Kang, Shinhoo, Alp Dener, Aidan Hamilton, Hong Zhang, Emil M. Constantinescu, and Robert L. Jacob (2023). “Multirate partitioned RungeKutta methods for coupled NavierStokes equations”. In: *Computers & Fluids* 264, p. 105964. ISSN: 00457930. DOI: 10.1016/j.compfluid.2023.105964 (cit. on p. 3).
- Karsten, Sven, Hagen Radtke, Matthias Gröger, Ha T. M. Ho-Hagemann, Hossein Mashayekh, Thomas Neumann, and H. E. Markus Meier (2024). “Flux coupling approach on an exchange grid for the IOW Earth System Model (version 1.04.00) of the Baltic Sea region”. In: *Geoscientific Model Development* 17.4, pp. 1689–1708. ISSN: 1991-9603. DOI: 10.5194/gmd-17-1689-2024 (cit. on p. 67).

- Katsafados, P, A Papadopoulos, G Korres, and G Varlas (2016). “A fully coupled atmosphereocean wave modeling system for the Mediterranean Sea: interactions and sensitivity to the resolved scales and mechanisms”. In: *Geoscientific Model Development* 9.1, pp. 161–173. ISSN: 1991-9603. DOI: 10.5194/gmd-9-161-2016 (cit. on p. 21).
- Kennedy, Christopher A and Mark H Carpenter (2003). “Additive RungeKutta schemes for convectiondiffusionreaction equations”. In: *Applied Numerical Mathematics* 44.1-2, pp. 139–181. ISSN: 01689274. DOI: 10.1016/S0168-9274(02)00138-1 (cit. on pp. 23, 25).
- Klemp, Joseph B., William C. Skamarock, and Jimmy Dudhia (2007). “Conservative split-explicit time integration methods for the compressible nonhydrostatic equations”. In: *Monthly Weather Review* 135.8, pp. 2897–2913. ISSN: 00270644. DOI: 10.1175/MWR3440.1 (cit. on pp. 3, 21).
- Klingbeil, Knut, Florian Lemarié, Laurent Debreu, and Hans Burchard (2018). “The numerics of hydrostatic structured-grid coastal ocean models: State of the art and future perspectives”. In: *Ocean Modelling* 125, pp. 80–105. ISSN: 14635003. DOI: 10.1016/j.ocemod.2018.01.007 (cit. on pp. 9, 17, 19, 21, 67, 77, 94).
- Knoth, Oswald and Jörg Wensch (2014). “Generalized Split-Explicit RungeKutta Methods for the Compressible Euler Equations”. In: *Monthly Weather Review* 142.5, pp. 2067–2081. ISSN: 0027-0644. DOI: 10.1175/MWR-D-13-00068.1 (cit. on pp. 23, 27, 34, 35, 39, 40, 53, 60, 62, 91).
- Knoth, Oswald and Ralf Wolke (1998). “Implicit-explicit Runge-Kutta methods for computing atmospheric reactive flows”. In: *Applied Numerical Mathematics* 28.2-4, pp. 327–341. ISSN: 01689274. DOI: 10.1016/S0168-9274(98)00051-8 (cit. on pp. 3, 23, 34–36, 40, 57).
- Kondo, Junsei (1975). “Air-sea bulk transfer coefficients in diabatic conditions”. In: *Boundary-Layer Meteorology* 9.1, pp. 91–112. ISSN: 00068314. DOI: 10.1007/BF00232256 (cit. on p. 95).
- Kundu, Pijush K., Ira M. Cohen, and David R. Dowling (2001). *Fluid Me.* Fifth Edit. Vol. 40, 6, p. 919. ISBN: 9780123821003. DOI: 10.1002/1521-3773(20010316)40:6<9823::AID-ANIE9823>3.3.CO;2-C (cit. on pp. 7, 9, v, vi).
- Lange, Hans-Joachim (2002). *Die Physik des Wetters und des Klimas: ein Grundkurs zur Theorie des Systems Atmosphäre.* Reimer. ISBN: 9783496027478 (cit. on pp. 7, 10, 68, v, vii).
- Lauritzen, Peter H., Christiane Jablonowski, M. A. Taylor, and Ramachandran D. Nair (2011). *Numerical Techniques for Global Atmospheric Models.* Ed. by Peter Lauritzen, Christiane Jablonowski, Mark Taylor, and Ramachandran Nair. Vol. 80. Lecture Notes in Computational Science and Engineering. Berlin, Heidelberg: Springer Berlin Heidelberg. ISBN: 978-3-642-11639-1. DOI: 10.1007/978-3-642-11640-7 (cit. on pp. 19, 21).
- Lemarié, Florian, Eric Blayo, and Laurent Debreu (2015). “Analysis of Ocean-atmosphere Coupling Algorithms: Consistency and Stability”. In: *Procedia Computer Science* 51, pp. 2066–2075. ISSN: 18770509. DOI: 10.1016/j.procs.2015.05.473 (cit. on pp. 22, 57, 68).
- Linardakis, Leonidas, Daniel Reinert, and Almut Gassmann (2011). *ICON Grid Documentation.* Tech. rep. Hamburg: DKRZ, p. 11 (cit. on p. 75).

- Marchesiello, Patrick, Laurent Debreu, and Eric Blayo (2014). “Sensitivity of Ocean-Atmosphere Coupled Models to the Coupling Method : Example of Tropical Cyclone Erica”. In: (cit. on p. 22).
- Millero, Frank (2010). “History of the Equation of State of Seawater”. In: *Oceanography* 23.3, pp. 18–33. ISSN: 10428275. DOI: 10.5670/oceanog.2010.21 (cit. on p. 14).
- Naumann, Andreas and Jörg Wensch (2019). “Multirate finite step methods”. In: *Numerical Algorithms* 81.4, pp. 1547–1571. ISSN: 1017-1398. DOI: 10.1007/s11075-019-00763-1 (cit. on pp. 56, 57).
- Nurser, A. J. George and Stephen M. Griffies (2019). “Relating the Diffusive Salt Flux just below the Ocean Surface to Boundary Freshwater and Salt Fluxes”. In: *Journal of Physical Oceanography* 49.9, pp. 2365–2376. ISSN: 0022-3670. DOI: 10.1175/JPO-D-19-0037.1 (cit. on p. 66).
- Paulson, Clayton a. and James J. Simpson (1977). *Irradiance measurements in the upper ocean*. DOI: 10.1175/1520-0485(1977)007<0952:IMITU0>2.0.CO;2 (cit. on p. 77).
- Prill, Florian, Daniel Reinert, Daniel Rieger, and Günther Zängl (2019). *Working with the ICON Model*. Tech. rep. Offenbach: DWD, p. 263 (cit. on p. 75).
- Reynolds, Osborne (1895). “IV. On the dynamical theory of incompressible viscous fluids and the determination of the criterion”. In: *Philosophical Transactions of the Royal Society of London*. (A.) 186, pp. 123–164. ISSN: 0264-3820. DOI: 10.1098/rsta.1895.0004 (cit. on p. viii).
- Roquet, F., Gurvan Madec, Trevor J. McDougall, and Paul M. Barker (2015). “Accurate polynomial expressions for the density and specific volume of seawater using the TEOS-10 standard”. In: *Ocean Modelling* 90, pp. 29–43. ISSN: 14635003. DOI: 10.1016/j.ocemod.2015.04.002 (cit. on p. 14).
- Saha, Suranjana, Shrinivas Moorthi, Xingren Wu, Jiande Wang, Sudhir Nadiga, Patrick Tripp, David Behringer, Yu Tai Hou, Hui Ya Chuang, Mark Iredell, Michael Ek, Jesse Meng, Rongqian Yang, Malaquías Pena Mendez, Huug Van Den Dool, Qin Zhang, Wanqiu Wang, Mingyue Chen, and Emily Becker (2014). “The NCEP climate forecast system version 2”. In: *Journal of Climate* 27.6, pp. 2185–2208. ISSN: 08948755. DOI: 10.1175/JCLI-D-12-00823.1 (cit. on p. 95).
- Sandu, Adrian (2019). “A Class of Multirate Infinitesimal GARK Methods”. In: *SIAM Journal on Numerical Analysis* 57.5, pp. 2300–2327. ISSN: 0036-1429. DOI: 10.1137/18M1205492 (cit. on p. 35).
- Sandu, Adrian and Michael Günther (2015). “A Generalized-Structure Approach to Additive Runge–Kutta Methods”. In: *SIAM Journal on Numerical Analysis* 53.1, pp. 17–42. ISSN: 0036-1429. DOI: 10.1137/130943224 (cit. on pp. 3, 25, 26, 30, 40, 43, 49, 50, 58, 59, 91).
- Satoh, Masaki (2003). “Conservative Scheme for a Compressible Nonhydrostatic Model with Moist Processes”. In: *Mon. Wea. Rev.* 131.6, pp. 1033–1050. ISSN: 0027-0644. DOI: 10.1175/1520-0493(2003)131<1033:CSFACN>2.0.CO;2 (cit. on p. 12).
- Schlegel, Martin, Oswald Knoth, Martin Arnold, and Ralf Wolke (2012). “Numerical solution of multiscale problems in atmospheric modeling”. In: *Applied Numerical Mathematics* 62.10,

- pp. 1531–1543. ISSN: 01689274. DOI: 10.1016/j.apnum.2012.06.023 (cit. on pp. 3, 23, 35, 40).
- Sexton, Jean M and Daniel R Reynolds (2018). “Relaxed Multirate Infinitesimal Step Methods”. In: (cit. on pp. 3, 35).
- Shaw, James and Hilary Weller (2016). “Comparison of Terrain-Following and Cut-Cell Grids Using a Nonhydrostatic Model”. In: *Monthly Weather Review* 144.6, pp. 2085–2099. ISSN: 0027-0644. DOI: 10.1175/MWR-D-15-0226.1 (cit. on p. 20).
- Skamarock, William C. and Joseph B. Klemp (1992). “The Stability of Time-Split Numerical Methods for the Hydrostatic and the Nonhydrostatic Elastic Equations”. In: *Monthly Weather Review* 120.9, pp. 2109–2127. ISSN: 0027-0644. DOI: 10.1175/1520-0493(1992)120<2109:TSOTSN>2.0.CO;2 (cit. on pp. 3, 21).
- Staniforth, Andrew N. (2022). *Global Atmospheric and Oceanic Modelling*. Cambridge University Press. ISBN: 9781108974431. DOI: 10.1017/9781108974431 (cit. on pp. 13, 14).
- Strehmel, Karl, Rüdiger Weiner, and Helmut Podhaisky (2012). *Numerik gewöhnlicher Differentialgleichungen*. Wiesbaden: Vieweg+Teubner Verlag. ISBN: 978-3-8348-1847-8. DOI: 10.1007/978-3-8348-2263-5 (cit. on pp. 24, 25, 36, 47–49, 57, 58).
- Stull, Roland B. (1988). *An Introduction to Boundary Layer Meteorology*. Dordrecht: Springer Netherlands. ISBN: 978-90-277-2769-5. DOI: 10.1007/978-94-009-3027-8 (cit. on p. 68).
- Svensson, G., A. A. M. Holtslag, V. Kumar, T. Mauritsen, G. J. Steeneveld, W. M. Angevine, E. Bazile, A. Beljaars, E. I. F. de Bruijn, A. Cheng, L. Conangla, Joan Cuxart, M. Ek, M. J. Falk, F. Freedman, H. Kitagawa, V. E. Larson, A. Lock, J. Mailhot, V. Masson, S. Park, J. Pleim, S. Söderberg, W. Weng, and M. Zampieri (2011). “Evaluation of the Diurnal Cycle in the Atmospheric Boundary Layer Over Land as Represented by a Variety of Single-Column Models: The Second GABLS Experiment”. In: *Boundary-Layer Meteorology* 140.2, pp. 177–206. ISSN: 0006-8314. DOI: 10.1007/s10546-011-9611-7 (cit. on p. 84).
- Tomita, Hirofumi, Masaki Satoh, and Koji Goto (2002). “An Optimization of the Icosahedral Grid Modified by Spring Dynamics”. In: *Journal of Computational Physics* 183.1, pp. 307–331. ISSN: 00219991. DOI: 10.1006/jcph.2002.7193 (cit. on p. 76).
- Ullrich, Paul A., Christiane Jablonowski, James Kent, Peter H. Lauritzen, Ramachandran D. Nair, Kevin A. Reed, Colin M. Zarzycki, David M. Hall, Don Dazlich, Ross Heikes, Celal Konor, David Randall, Thomas Dubos, Yann Meurdesoif, Xi Chen, Lucas Harris, Christian Kühnlein, Vivian Lee, Abdessamad Qaddouri, Claude Girard, Marco A. Giorgetta, Daniel Reinert, Joseph B. Klemp, Sang-Hun Park, William C. Skamarock, Hiroaki Miura, Tomoki Ohno, Ryuji Yoshida, Robert L. Walko, Alex Reinecke, and Kevin Viner (2017). “DCMIP2016: a review of non-hydrostatic dynamical core design and intercomparison of participating models”. In: *Geoscientific Model Development* 10.12, pp. 4477–4509. ISSN: 1991-9603. DOI: 10.5194/gmd-10-4477-2017 (cit. on pp. 9, 19, 74).
- Umlauf, Lars and Hans Burchard (2003). “A generic length-scale equation for geophysical turbulence models”. In: *Journal of Marine Research* 61.2, pp. 235–265. ISSN: 15439542. DOI: 10.1357/002224003322005087 (cit. on p. 70).

- Umlauf, Lars and Hans Burchard (2005). “Second-order turbulence closure models for geophysical boundary layers. A review of recent work”. In: *Continental Shelf Research* 25.7-8 SPEC. ISS. Pp. 795–827. ISSN: 02784343. DOI: 10.1016/j.csr.2004.08.004 (cit. on pp. 83, 84, 86, 87).
- Van Pham, Trang, Jennifer Brauch, Christian Dieterich, Barbara Frueh, and Bodo Ahrens (2014). “New coupled atmosphere-ocean-ice system COSMO-CLM/NEMO: Assessing air temperature sensitivity over the North and Baltic Seas”. In: *Oceanologia* 56.2, pp. 167–189. ISSN: 23007370. DOI: 10.5697/oc.56-2.167 (cit. on p. 21).
- Visram, A. R., Colin J. Cotter, and Michael J.P. Cullen (2014). “A framework for evaluating model error using asymptotic convergence in the Eady model”. In: *Quarterly Journal of the Royal Meteorological Society* 140.682, pp. 1629–1639. ISSN: 00359009. DOI: 10.1002/qj.2244 (cit. on p. 71).
- Wacker, Ulrike, Thomas Frisius, and Fritz Herbert (2006). “Evaporation and Precipitation Surface Effects in Local Mass Continuity Laws of Moist Air”. In: *Journal of the Atmospheric Sciences* 63.10, pp. 2642–2652. ISSN: 0022-4928. DOI: 10.1175/JAS3754.1 (cit. on p. 8).
- Wang, Shiyu, Christian Dieterich, Ralf Döscher, Anders Höglund, Robinson Hordoir, H. E. Markus Meier, Patrick Samuelsson, and Semjon Schimanke (2015). “Development and evaluation of a new regional coupled atmosphereocean model in the North Sea and Baltic Sea”. In: *Tellus A: Dynamic Meteorology and Oceanography* 67.1, p. 24284. ISSN: 1600-0870. DOI: 10.3402/tellusa.v67.24284 (cit. on p. 21).
- Weng, Wensong and Peter A. Taylor (2003). “On Modelling the One-Dimensional Atmospheric Boundary Layer”. In: *Boundary-Layer Meteorology* 107.2, pp. 371–400. ISSN: 0006-8314. DOI: 10.1023/A:1022126511654 (cit. on pp. 69, 70).
- (2006). “Modelling the One-Dimensional Stable Boundary Layer with an E Turbulence Closure Scheme”. In: *Boundary-Layer Meteorology* 118.2, pp. 305–323. ISSN: 0006-8314. DOI: 10.1007/s10546-005-2774-3 (cit. on pp. 70, 83–86).
- Wensch, Jörg, Oswald Knoth, and Alexander Galant (2009). “Multirate infinitesimal step methods for atmospheric flow simulation”. In: *BIT Numerical Mathematics* 49.2, pp. 449–473. ISSN: 0006-3835. DOI: 10.1007/s10543-009-0222-3 (cit. on pp. 23, 27, 34–36, 40, 53, 54, 60).
- Wicker, Louis J. (2009). “A Two-Step AdamsBashforthMoulton Split-Explicit Integrator for Compressible Atmospheric Models”. In: *Monthly Weather Review* 137.10, pp. 3588–3595. ISSN: 0027-0644. DOI: 10.1175/2009MWR2838.1 (cit. on p. 3).
- Wicker, Louis J. and William C. Skamarock (1998). “A Time-Splitting Scheme for the Elastic Equations Incorporating Second-Order RungeKutta Time Differencing”. In: *Monthly Weather Review* 126.7, pp. 1992–1999. ISSN: 0027-0644. DOI: 10.1175/1520-0493(1998)126<1992:ATSSFT>2.0.CO;2 (cit. on p. 3).
- (2002). “Time-Splitting Methods for Elastic Models Using Forward Time Schemes”. In: *Monthly Weather Review* 130.8, pp. 2088–2097. ISSN: 0027-0644. DOI: 10.1175/1520-0493(2002)130<2088:TSMFEM>2.0.CO;2 (cit. on p. 3).

- Yamazaki, Hiroe, Jemma Shipton, Michael J.P. Cullen, Lawrence Mitchell, and Colin J. Cotter (2017). “Vertical slice modelling of nonlinear Eady waves using a compatible finite element method”. In: *Journal of Computational Physics* 343, pp. 130–149. ISSN: 00219991. DOI: 10.1016/j.jcp.2017.04.006 (cit. on p. 71).
- Zängl, Günther, Daniel Reinert, Pilar Rípodas, and Michael Baldauf (2015). “The ICON (ICOsahedral Non-hydrostatic) modelling framework of DWD and MPI-M: Description of the non-hydrostatic dynamical core”. In: *Quarterly Journal of the Royal Meteorological Society* 141.687, pp. 563–579. ISSN: 00359009. DOI: 10.1002/qj.2378 (cit. on pp. 14, 21, 67, 74–76, 93, 94).
- Zdunkowski, Wilford and Andreas Bott (2003). *Dynamics of the Atmosphere: A Course in Theoretical Meteorology*. Cambridge University Press. ISBN: 9780511076480 (cit. on pp. 9, vi).
- (2004). *Thermodynamics of the Atmosphere: A Course in Theoretical Meteorology*. Thermodynamics of the Atmosphere: A Course in Theoretical Meteorology. Cambridge University Press. ISBN: 9780521809535 (cit. on pp. 5, 8, 11–13, iii).
- Zhang, Hong, Zhengyu Liu, Emil Constantinescu, and Robert Jacob (2020). “Stability Analysis of Interface Conditions for OceanAtmosphere Coupling”. In: *Journal of Scientific Computing* 84.3, p. 44. ISSN: 0885-7474. DOI: 10.1007/s10915-020-01293-y (cit. on pp. 57, 68).





# List of Figures

2.1	Physical processes at the boundaries of the atmosphere and ocean which include the mass transfer due to evaporation ( $E$ ) and precipitation ( $P$ ), the momentum transfer between the fluid velocity ( $\mathbf{v}^A, \mathbf{v}^O$ ) profiles and the energy transfer in terms of heat ( $Q$ ) and radiation (sun). . . . .	17
2.2	Horizontal Arakawa C-grid and vertical Lorenz grid staggering in a Cartesian co-ordinate system for one, two and three dimensions. The $\circ$ , $\times$ and $\bullet$ are representing the position of the velocity components in x-, y- and z- direction, respectively, i.e. $u$ , $v$ and $w$ . The $+$ represents other variables, e.g. density, pressure and temperature. . . . .	20
2.3	Schematic 2D representation of a mountain on a flat plane with the first layers of the vertical discretisation with terrain following coordinates (left side) and cut cells (right side). . . . .	20
3.1	Graphical representation of the integration process from $t_n$ to $t_{n+1}$ using a three-stage eRK method. The stage values $Y_i$ are calculated in chronological order. The final $y_{n+1}$ is then given by a linear combination of the increments of each stage. .	25
3.2	Graphical representation of the coupling between the two components of a GARK method in an explicit manner. The coupling is colour coded with <b>green</b> , <b>blue</b> , <b>red</b> , <b>violet</b> and black for the stages and indicate which stages contribute. The stage values $Y_i^k$ are calculated in chronological order. . . . .	27
3.3	Graphical representation of the stage values and their position during the integration of one time step when using a MGARK method. The <b>blue</b> coloured line represents the slow component, while the <b>red</b> coloured the fast component. The fast component is integrated three times in one integration time step of the slow component. The coupling between the two components is not shown. However, for explicit coupling a chronological calculation of the stage values is required. An explicit coupling is graphically represented in Figure 3.2. . . . .	29

3.4	Schematic representation of the coupling and time stepping in an MNGARK method with three components, e.g. asynchronous coupling in atmosphere-ocean models. The time step of the <b>fast</b> component is divided into three parts according to the time step of the slow component. The time step of the <b>super fast</b> component is split into 6 parts. The time steps for each part are shown with curly brackets and described by $m_k^{\{\kappa\}}$ and $h$ . . . . .	33
3.5	Schematic representation of the stage values and time stepping in an MNGARK method with three components. The stage values of each part per component are placed at the corresponding time point. Each part of the slow and <b>fast</b> components is assumed to be integrated with an eRK method with three stages. On the other hand, each part of the <b>super fast</b> component is integrated with an eRK with two stages. The time steps for each part are shown with curly brackets and described by $m_k^{\{\kappa\}}h$ . . . . .	34
3.6	Representation of the integration with a three-stage MIS method from $t_n$ to $t_n + h$ . The four MIS stages are indicated by $Y_i$ , $i = 1, 2, 3, 4$ . The initial values for the IVP of each MIS stage $i$ are given by $Z_i(0)$ , cf. equation (3.19a). The arrows are representing the corresponding integrations. . . . .	36
3.7	Connection of RK type methods to MIS type methods and their generalisations. The different kind of connections are numbered with partitioning ①, generalisation ② with kind (a): additive, (b): interpolation of initial values, (c): multiple components, reformulation (is special case of) ③, applying general RK for inner method ④ with (a): explicit RK . . . . .	40
4.1	Results of MIS54 method . . . . .	63
5.1	Schematic representation of the interpolation between atmosphere and ocean slice models. In the atmosphere and ocean grids active ocean cells are coloured in <b>blue</b> and land cells in <b>green</b> . As shown for the transfer of mean sea level pressure (MSLP in hPa) and sea surface temperature (SST in K), the exchange grid can consist of different cells for each direction. The four possible combinations of land/ocean masks are indicated. On land (cases 1 and 3) an atmosphere-internal SST (here 290K) must be applied. This atmosphere-internal SST is also considered for fractions of ocean cells not covered by the ocean domain (case 2). . . .	72
5.2	Illustration of the grid construction procedure. The original spherical icosahedron is shown in red, denoted as R1B00. In this example, the initial division (black dotted), followed by one subsequent edge bisection yields a R2B01 grid (solid lines), see Prill et al. (2019). . . . .	75

5.3	2D exchange grid formed by a triangular atmosphere (red) and a rectangular ocean (blue) grid. The exchange grid consists of edges from the original triangular and rectangular grids (thick red and blue) and additional edges from the triangulation (black). Assuming that only water cells are shown, the four possible combinations of land/ocean masks are labeled. Here the exchange grid is shown for the interpolation from the ocean to the atmosphere grid, therefore, excluding the elements of case 3. . . . .	78
5.4	Overview of domain for the Central Baltic Sea application and the applied horizontal discretisation in ICON and GETM. . . . .	79
5.5	Schematic overview of the sea level change in comparison to a fixed a vertical discretisation. . . . .	80
6.1	Vertical discretisation at the air-sea interface for the one-dimensional idealised coupled atmosphere-ocean model. . . . .	84
6.2	Results of the one-dimensional atmospheric boundary layer experiment. A stable boundary layer is achieved. . . . .	87
6.3	Results of the implemented entrainment experiment. There are no significant differences to the result from Burchard et al. (1999) and Umlauf and Burchard (2005). . . . .	87
6.4	Results of the implemented entrainment experiment with applied Coriolis frequency and gravitational acceleration from the atmospheric boundary layer experiment. Due to the applied Coriolis frequency, there is a velocity in both directions. The acceleration of the thin near-surface layer is not as deep into the stratified non-turbulent interior region. . . . .	88
6.5	Results of the coupled one-dimensional atmospheric boundary layer experiment. The boundary layer height is significantly lower than for the single experiment. The same holds for the velocity, wet equivalent potential temperature, shear stress and heat flux. . . . .	89
6.6	Results of the coupled one-dimensional entrainment experiment. The acceleration of the thin near-surface layer into the stratified non-turbulent interior region is even less deep than in the single experiment. Close to the air-sea interface, the Brunt-Väisälä frequency becomes negative and, therefore, only the real component of the logarithm is drawn. . . . .	89
6.7	Results of the coupling at the air-sea interface in comparison to the boundary conditions from the original experiments. The no-slip (left panel) and no flux (right panel) condition are also shown as well as the constant cooling (centre panel). The velocity, temperature and various fluxes at the air-sea interface are presented over time. . . . .	90
6.8	Simulation time for each experiment and applied method. . . . .	92

6.9	Daily mean sea surface temperature (SST) from the two-way coupled ICON-GETM run (left panel), and the uncoupled/one-way coupled ICON run (right panel), as well as the difference (central panel; ICONGETM minus ICON) for 16 July 2012. Outside the domain of simulated SST in the Central Baltic Sea, the two-way coupled ICONGETM run also uses the prescribed ICON-internal SST.	96
6.10	Daily mean 2 m air temperature from the two-way coupled ICONGETM simulation (left panel) and the uncoupled/one-way coupled ICON simulation (right panel), as well as the difference (central panel; ICONGETM minus ICON) for 16 July 2012.	96
6.11	Air temperature in the Central Baltic Sea over the period July 1 – 21, 2012 (left panel). Compared are 3-hourly measurements in 29.1 m onboard the RV Meteor, ship track shown on the right panel, with model results from the two-way coupled ICONGETM and uncoupled/one-way coupled ICON simulations, respectively. The white frame shows the island of Gotland, similar to Figure 5.4a.	97
6.12	Daily mean sea surface temperature from satellites (A) and simulated by GETM in the uncoupled (B), one-way (C) and two-way (D) coupled simulation for 16 July 2012. The colourbar is identical to Figure 6.9. The SST derived from satellite data was provided by the Federal Maritime and Hydrographic Agency of Germany (BSH).	98
6.13	Temperature in 5 m depth at station TF271 from CTD measurements and the three model simulations. The one- and two-way coupled simulations are started at 1 July 2012, after the uncoupled spin-up period.	99

# List of Tables

2.1	Corresponding variable description for unified formulation of general set of equations based on the conservation laws, i.e. equations (2.17), (2.22) and (2.25d) . .	15
4.1	Number of conditions up to order $p = 5$ for GARK w/o internal consistency as simplifying assumption. . . . .	50
4.2	MIS method parameters with 5 stages and order four, (MIS54) . . . . .	62



# Selbstständigkeitserklärung

Hiermit erkläre ich, dass ich die vorliegende Dissertation selbständig und ohne unerlaubte fremde Hilfe angefertigt habe. Ich habe keine anderen als die angegebenen Quellen und Hilfsmittel verwendet und die den verwendeten Werken wörtlich oder inhaltlich entnommenen Stellen als solche kenntlich gemacht.

Die vorliegende Dissertation referenziert zwei begutachtete wissenschaftliche Artikel, welche ich als Hauptautor verfasst habe. Der Beitrag aller Autoren ist kurz zusammengefasst:

1. Tobias Peter Bauer and Oswald Knoth (2021). “Extended multirate infinitesimal step methods: Derivation of order conditions”. In: *Journal of Computational and Applied Mathematics* 387. ISSN: 03770427. DOI: 10.1016/j.cam.2019.112541:

TPB entwickelte die Methode Extended multirate infinitesimal step method. TPB führte den Vergleich zu bereits bekannten Methoden durch. Die Ordnungsbedingungen sind durch TPB aufgestellt und durch OK geprüft wurden. TPB berechnete das präsentierte Beispiel der entwickelten Methode. OK stellte die verwendete Software für die Stabilitätsanalysen zur Verfügung. Alle Autoren wirkten ihres Beitrages entsprechend in den jeweiligen Textpassagen mit.

2. Tobias Peter Bauer et al. (2021). “ICONGETM v1.0 flexible NUOPC-driven two-way coupling via ESMF exchange grids between the unstructured-grid atmosphere model ICON and the structured-grid coastal ocean model GETM”. in: *Geoscientific Model Development* 14.8, pp. 4843–4863. ISSN: 1991-9603. DOI: 10.5194/gmd-14-4843-2021:

Der Code wurde von TPB in Zusammenarbeit mit KK entworfen, entwickelt und implementiert. Das Modellsetup wurde von TPB und BH für ICON und von PH und KK für GETM bereitgestellt. Die Kopplungskonfiguration wurde von TPB und KK vorbereitet und mit allen Autoren diskutiert. BH und TPB bewerteten die meteorologischen Ergebnisse der Simulation, d.h. ICON. PH und KK bewerteten die Simulationsergebnisse auf der Ozeanseite, d.h. GETM. HR beriet und diskutierte den Flussaustausch sowie die Kopplungsstrategie. OK beriet bei der Code-Entwicklung und unterstützte die Implementierung mathematischer Hilfsroutinen. Alle Autoren haben in den Abschnitten, die ihrer Rolle während des Arbeitsablaufs entsprechen, zu diesem Artikel beigetragen.





# Lebenslauf

Tobias Peter Bauer

## Wissenschaftlicher Werdegang

- |                 |   |
|-----------------|---|
| seit 07/2020    | <b>Wissenschaftlicher Mitarbeiter</b><br><i>Bundesamt für Kartographie und Geodäsie - Leipzig</i>   |
| 12/2019–03/2020 | <b>Wissenschaftlicher Mitarbeiter</b><br><i>Leibniz Institut für Ostseeforschung Warnemünde - Warnemünde</i>  |
| 07/2015–11/2019 | <b>Wissenschaftlicher Mitarbeiter</b><br><i>Leibniz Institut für Troposphärenforschung - Leipzig</i>  |
| 12/2013–09/2015 | <b>Wissenschaftlicher Mitarbeiter</b><br><i>HTWK Leipzig</i><br>Fakultät für Informatik, Mathematik und Naturwissenschaften<br>ZIM Projekt - Bundesministerium für Wirtschaft und Energie |
| 02/2013–03/2014 | <b>Wissenschaftliche Hilfskraft</b><br><i>Leibniz Institut für Oberflächenmodifizierung - Leipzig</i>   |

## Studium

- |                 |  |
|-----------------|--|
| 10/2012–12/2014 | <b>Masterstudium - Angewandte Mathematik</b><br><i>HTWK Leipzig</i>  |
| 10/2009–09/2012 | <b>Bachelorstudium - Angewandte Mathematik</b><br><i>HTWK Leipzig</i><br>Auslandsstudium: Oxford Brookes University (UK) - 09/2011-06/2012 |
| 07/2005         | <b>Allgemeine Hochschulreife</b><br><i>Johannes-Kepler-Gymnasium Chemnitz</i>  |

## Beruflicher Werdegang

- |                 |   |
|-----------------|---|
| 07/2005–06/2009 | <b>Militärdienst</b><br><i>Bundesministerium für Verteidigung, Bischofswiesen</i> |
|-----------------|---|

